

MESONIC CORRELATION FUNCTIONS
FROM LIGHT QUARKS AND THEIR SPECTRAL
REPRESENTATION IN HOT QUENCHED LATTICE QCD

Dissertation

zur Erlangung des Doktorgrades
der Fakultät für Physik
der Universität Bielefeld

vorgelegt von
SÖNKE WISSEL

Oktober 2006

Mesonic Correlation Functions from Light Quarks and Their Spectral Representation in Hot Quenched Lattice QCD

Dipl.-Phys. (Univ.) Sönke Wissel
geboren am 16.8.1976 in Hannover

Vollständiger Abdruck der von der Fakultät für Physik der Universität Bielefeld zur Erlangung
des akademischen Grades eines

Doktors der Naturwissenschaften (Dr. rer. nat.)

genehmigten Dissertation.

Vorsitzender: Univ.-Prof. Dr. Friederike Schmid
Prüfer der Dissertation (Gutachter):

1. Univ.-Prof. Dr. Edwin Laermann
2. Univ.-Prof. Dr. Mikko Laine

Weitere Mitglieder des Prüfungsausschusses:

3. Univ.-Prof. Dr. Jürgen Engels
4. Dr. Dirk Feldmann

Tag der mündlichen Prüfung (Disputation): 30. November 2006

Die Dissertation wurde am 31. Oktober 2006 bei der Universität Bielefeld eingereicht und
durch die Fakultät der Physik am 31. Oktober 2006 angenommen.

Abstract

In this thesis we investigate thermal in-medium modifications of various mesonic correlation functions by lattice simulations of Quantum Chromodynamics for light valence quark masses and vanishing chemical potential. Mesonic properties are typically extracted from spatial correlation functions. The results presented are based on quenched gauge field configurations generated with the standard Wilson plaquette gauge action. Concerning the fermionic part of the action, we use the non-perturbative $\mathcal{O}(a)$ improved Sheikholeslami-Wohlert as well as the truncated hypercube perfect action. Furthermore we utilize the maximum entropy method in order to determine physically relevant pole masses and to investigate thermal modifications of physical states and possible lattice artefacts in the interacting case.

The analyses of pole and screening masses, dispersion relations, wave functions, decay constants and spectral functions essentially yield no significant modifications of the zero-temperature behavior up to $0.55 T_c$. Close to the phase transition in-medium effects seem to appear, which lead inter alia to significant differences between pole and screening masses. The decay constants are in good agreement with the experimental values. We have simulated above T_c at nearly zero quark masses. At $1.24 T_c$, the occurrence of topological effects, a sign for the presence of a still broken $U(1)_A$ symmetry, prevent a more thorough analyses close to the phase transition.

A complete continuum and infinite volume extrapolation of screening masses, guided by free lattice effective masses is done. It shows that the presence of collective phenomena at 1.5 and $3 T_c$ cannot be explained by pure lattice artefacts. Unlike the vector meson the pion is far from being considered an unbound state.

Zusammenfassung

In dieser Arbeit untersuchen wir anhand von Gittersimulationen der Quantenchromodynamik thermische in-medium Modifikationen für unterschiedliche Mesonkorrelationsfunktionen bei leichten Valenzquarkmassen und verschwindenden chemischen Potentials. Mesonische Eigenschaften werden in der Regel anhand räumlicher Korrelationsfunktionen extrahiert. Die Ergebnisse basieren dabei auf gequenchten Eichfeldkonfiguration, die mit Hilfe der standard Wilson Plaquette Eichwirkung erzeugt werden. Bezüglich des fermionischen Anteil der Wirkung verwenden wir die nicht-störungstheoretische $\mathcal{O}(a)$ verbesserte Sheikholeslami-Wohlert sowie eine auf den Hyperkubus trunkierte perfekte Wirkung. Ferner wird die maximale Entropie Methode verwendet, um anhand von Spektralfunktionen physikalisch relevante Polmassen zu bestimmen und thermische Modifikationen physikalischer Zustände sowie möglicher Gitterartefakte im wechselwirkenden Fall zu untersuchen.

Die Auswertung von Pol- und Screeningmassen, Dispersionsrelationen, Wellenfunktionen, Zerfallskonstanten und Spektralfunktionen hat im wesentlichen ergeben, dass wir bis $0,55 T_c$ keine signifikante Veränderungen zum null Temperatur Verhalten erkennen können. Erst nahe des Phasenübergangs scheinen sich in-medium Effekte bemerkbar zu machen, was u.a. zu einer signifikanten Abweichung zwischen Pol- und Screeningmassen geführt hat. Die Zerfallskonstanten sind in guter Übereinstimmung mit den experimentellen Werten. Oberhalb von T_c haben wir mit einer quasi null Quarkmasse simuliert. Bei $1,24 T_c$ hat das Auftreten topologischer Effekte als ein Zeichen für eine immer noch vorhandene $U(1)_A$ Symmetriebrechung eine eingehendere Analyse in direkter Nähe des Phasenübergang verhindert. Eine vollständige Kontinuums- und Volumen-Extrapolation der Screening Massen orientiert an dem Verhalten freier Gitter effektiven Massen wird durchgeführt. Diese zeigt, dass noch vorhandene kollektive Phänomen bei $1,5$ und $3 T_c$ nicht durch einfache Gittereffekte erklärt werden können. Anders als das Vektormeson ist das pseudoskalare Meson weit davon entfernt ein ungebundener Zustand zu sein.

Contents

Introduction	1
1 Quantum Chromodynamics in the continuum	7
1.1 QCD at finite temperature	8
1.2 Symmetries of the Lagrangian	9
1.3 Phases in finite temperature QCD in theoretical framework	11
1.3.1 Phases at vanishing density	11
1.3.2 Chiral condensate and the Dirac eigenvalue spectrum	13
1.3.3 Phases at finite density	15
1.4 Finite temperature QCD in experimental framework	16
2 QCD on the lattice - A brief introduction	23
2.1 The lattice as a regulator of QCD	23
2.2 Gauge fields on the lattice	24
2.3 Matter fields on the lattice	26
2.3.1 Fermion doublers and Nielsen-Ninomiya theorem	26
2.3.2 Wilson fermions	27
2.3.3 Wilson fermions with Symanzik improvement (Sheikholeslami-Wohlert action)	30
2.3.4 Staggered fermions	33
2.3.5 The Ginsparg-Wilson relation and the overlap operator	33
2.3.6 Hypercube fermions	34
2.4 Simulation techniques	39
2.4.1 Quenched approximation	39
2.4.2 Markov chains and Metropolis	40
2.4.3 Heat bath and overrelaxation	41
2.4.4 Inversion of the fermion matrix	42
2.4.5 Errors and fitting	44
2.5 $Z(3)$ -Symmetry on the lattice	46
2.6 Evaluating physical quantities on the lattice	48
2.6.1 Continuum limit	48
2.7 Simulation details	49
2.7.1 Simulation parameters	49
2.7.2 Determination of the scale	52
2.7.3 Renormalization constants	53
2.8 Mesonic correlation and spectral functions	54
2.8.1 Temporal correlations	54
2.8.2 Spatial correlations	59
2.8.3 Improvements (Fuzzing and Smearing)	60
2.8.4 Determination of meson masses	61

3	Maximum entropy method with free data	65
3.1	Bayes' theorem and maximum entropy method	65
3.1.1	Likelihood and likelihood function	66
3.1.2	Prior probability	66
3.1.3	Outline of the MEM procedure	67
3.2	Free correlation functions in their spectral representation	69
3.2.1	Continuum correlation and spectral functions	69
3.2.2	Wilson fermion correlation and spectral functions	70
3.2.3	Hypercube fermion correlation and spectral functions	72
3.2.4	Binning	74
3.2.5	Summary of observed cut-off effects	75
3.2.6	Probing the MEM on free and interacting model data	75
4	Analysis of mesonic properties below and above T_c	79
4.1	Extracting masses and energies from correlation functions	79
4.1.1	Masses and energies from temporal correlation functions	80
4.1.2	Masses in the chiral limit	80
4.1.3	Dispersion relations	83
4.2	Bethe-Salpeter amplitudes and the pion radius	85
4.3	Quark masses from axial Ward identities	91
4.4	Decay constants	93
4.5	Spectral functions	96
4.6	Cut-off and thermal effects in temporal correlation functions	102
5	Screening masses and correlation functions in the high-temperature phase	107
5.1	Screening masses in infinite volume and continuum extrapolation	107
5.2	Spatial correlation function in the context of chiral and Lorentz symmetry breaking	111
	Summary, conclusions and outlook	115
A	Conventions	119
A.1	$SU(N)$ generators	119
A.1.1	$SU(2)$: Pauli matrices	119
A.1.2	$SU(3)$: Gell-Mann matrices	120
A.1.3	(Euclidean) Dirac matrices	120
B	Tables of results	121
B.1	AWI quark masses below T_c	121
B.2	AWI quark masses above T_c	122
B.3	Renormalization group factors	123
B.4	Screening masses	124
B.5	MEM pole masses	126
C	Auxiliary Functions for the Free Lattice Field Theory	127
D	Storing data - Database SQL with MySQL	129

List of	134
Abbreviations	136
Figures	138
Tables	139
Listings	141
References	143
Acknowledgments	155
Selbstständigkeitserklärung	157
Curriculum vitæ	159

Introduction

Physics is like sex - sure, it may give some practical results, but that's not why we do it.

RICHARD P. FEYNMAN

All of known particle phenomena are well described within the *Standard Model* (SM) of elementary particles and their fundamental interactions, see Tab. 1 and, e.g., text books [1–4]. It provides an elegant theoretical framework and has successfully passed precision tests in the past. Agreeing with both quantum mechanics and special relativity the SM is a quantum field theory (QFT) based on the gauge symmetry $SU(3)_C \times SU(2)_L \times U(1)_Y$. This gauge group includes the symmetry group of strong interactions, $SU(3)_C$, which we will address in this work, as well as the symmetry group of the electroweak interactions, $SU(2)_L \times U(1)_Y$. The corresponding electroweak gauge theory is the *GWS-theory* formulated by GLASHOW, WEINBERG and SALAM. This theory manages to describe the weak and electromagnetic interactions, although they appear very different at everyday low energies, as two different aspects of the same force. The group symmetry, $U(1)_{\text{em}}$, of the QFT describing electromagnetic interactions called *Quantum Electrodynamics* (QED) appears in the SM as a subgroup of $SU(2)_L \times U(1)_Y$ and it is in this sense that the weak and electromagnetic interactions are said to be unified.

The gauge sector of the SM is composed of eight gluons which are the spin-1 gauge bosons of $SU(3)_C$ and the electromagnetic photon γ together with the weak W^\pm and Z particles which are the four gauge bosons of $SU(2)_L \times U(1)_Y$. Except for gravitational interactions, all relevant interactions in particle physics are known to be mediated by exchange of those elementary particles.

The matter sector is composed of fermions of spin $\frac{1}{2}$, which are classified into leptons l and quarks q . The known leptons are: the electron e^- , the muon μ^- and the tau τ^- with electric charge $Q_{\text{em}} = -1$ and their corresponding neutrinos ν_e , ν_μ and ν_τ with $Q_{\text{em}} = 0$. The known quarks come in six different flavors: u, d, s, c, b and t and have fractional electric charge $Q_{\text{em}} = \frac{2}{3}, -\frac{1}{3}, -\frac{1}{3}, \frac{2}{3}, -\frac{1}{3}$ and $\frac{2}{3}$ respectively. Additionally all quarks carry three different color (**red**, **green**, **blue**) or anti-color (**red**, **green**, **blue**) charges. Leptons and quarks are organized in three families with respect to their behavior under electromagnetic and weak forces. Related members of different families are even equivalent under all three SM interactions. The particle content in each family is

$$\begin{aligned} 1^{\text{st}} \text{ family: } & \begin{pmatrix} \nu_e \\ e^- \end{pmatrix}_L, e^-_R, \begin{pmatrix} u \\ d \end{pmatrix}_L, u_R, d_R, \\ 2^{\text{nd}} \text{ family: } & \begin{pmatrix} \nu_\mu \\ \mu^- \end{pmatrix}_L, \mu^-_R, \begin{pmatrix} c \\ s \end{pmatrix}_L, c_R, s_R, \\ 3^{\text{rd}} \text{ family: } & \begin{pmatrix} \nu_\tau \\ \tau^- \end{pmatrix}_L, \tau^-_R, \begin{pmatrix} t \\ b \end{pmatrix}_L, t_R, b_R, \end{aligned}$$

and their corresponding antiparticles. The left-handed and right-handed fields are defined by means of the chirality operator γ_5 as usual.

Since explicit mass terms in the gauge sector of the SM Lagrangian would break the SM gauge symmetry explicitly, weak gauge bosons appear as massless particles. This is in contrast to nature, where we observe massive weak gauge bosons, $m_W^\pm, m_Z \neq 0$. This discrepancy can be resolved by the Higgs mechanism. In the evolution of our universe, i.e., by going to smaller energy scales the SM undergoes a phase transition where its symmetry is spontaneously broken down to

$$SU(3)_C \times SU(2)_L \times U(1)_Y \rightarrow SU(3)_C \times U(1)_{\text{em}}.$$

This mechanism provides not only proper masses to the W^\pm and Z gauge bosons but also to the fermions and leaves as a consequence the prediction of a new particle: The Higgs boson. This scalar and electrically neutral particle has not been seen experimentally so far. However, it is hoped that the Large Hadron Collider at CERN will be able to confirm the existence of the Higgs boson.

Various ideas to fully unify all three symmetries (forces) of the SM to just one common overall gauge symmetry like $SU(5)$, $SO(10)$ or E_8 in a so-called *Grand Unified Theory* (GUT), are supported by the fact that the renormalized running gauge couplings seem to approach each other at high energies. However, no experimental findings in this direction, such as the proton decay, have been made until today. Beyond grand unification, there is also speculation that it may be possible to merge even gravity with the other three gauge symmetries into a *Theory of Everything* (TOE).

interaction	relative strength	range	ex. particle	example
electromagnetic	$\alpha_e = \frac{e^2}{4\pi} \approx \frac{1}{137}$	∞	γ	force between electromagnetic charges
weak	$G_F \approx 10^{-5} m_p^{-2}$ $\Rightarrow \frac{g_W^2}{4\pi} \approx \frac{1}{30}$	$m_W^{-1} \approx 10^{-3} \text{ fm}$	W^\pm, Z^0	β -decay
strong	$\alpha_s \approx 1$	confinement	gluons	forces between quarks
gravity	$G_N \approx 6 \cdot 10^{-39} \text{ GeV}^2$	∞	graviton ?	attraction between matter
GUT	$M_X^{-2} \approx 10^{-30} m_p^{-2}$	$M_X^{-1} \approx 10^{-16} \text{ fm}$	X, Y	p -decay

Tab. 1: Table of the four fundamental forces in nature including a hypohetic GUT interaction at high energy scales. The relative strength of the interaction is given, its range, the exchange particles, and a phenomenological example.

The strong interactions between the color charged quarks and gluons are described by a QFT called Quantum Chromodynamics (QCD). Its simple and elegant Lagrangian is based entirely on the invariance under non-Abelian local gauge transformations, which are elements of $SU(3)_C$. Mediated by gluon exchange at small temperatures the quarks are bound in colorless 'white' hadronic states, i.e., singlets under the color gauge group, which built up nuclear matter. The force between quarks increases with the distance between them until it becomes energetically favorable to create a quark-anti-quark pair (*string breaking*). No quarks can be found individually. This *confinement* property is in opposition to QED where the charge is screened at large distances by vacuum fluctuations. It is supposed to be intimately connected with the non-Abelian nature of QCD, corresponding to the fact that the QCD gauge bosons, unlike photons, carry color charges and thus are self-interacting.

This general accepted picture is supported by the celebrated principle of *asymptotic freedom*. It states that on the other hand the effective (running) coupling constant of QCD falls with increasing momentum transfer or, equivalently, short distances. In a thermal medium, e.g., at

energy densities which have been reached in the early universe or today in large (heavy-ion) colliders, the characteristic momentum transfer between (nearly) massless particles is of the order of the temperature T , and thus the effective coupling between quarks and gluons becomes weak when T grows large. The complicated structure of nuclear matter at low temperatures, where it is composed of a multitude of hadronic particles, baryons and mesons, is expected to give way at asymptotically high temperatures to the relative simplicity of a plasma composed of weakly interacting quarks and gluons (quasi particles), the Quark Gluon Plasma (QGP), often referred to as a new state of matter. At the same time, chiral symmetry – a symmetry of the QCD Lagrangian, which is spontaneously broken in the confined phase – is expected to be restored. This transition from a phase with pions acting as the Goldstone bosons of the broken chiral symmetry, to a chirally symmetric one seems to occur at the same temperature as the confinement-deconfinement transition. Within the confinement

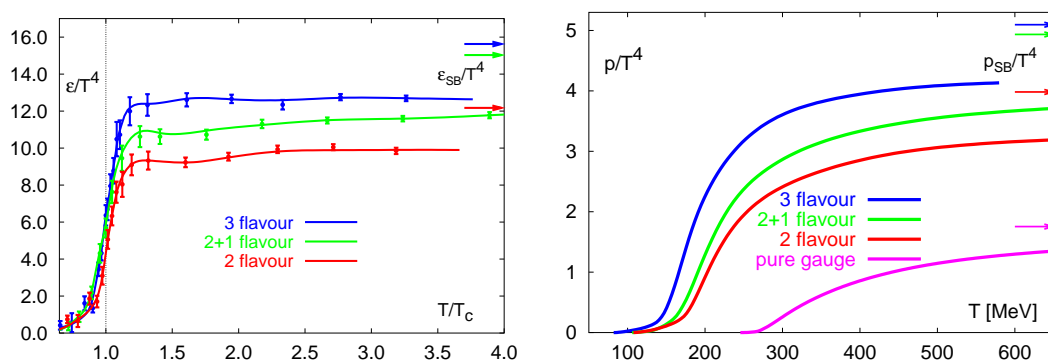


Fig. 1: The LQCD energy (left) and pressure (right) as a function of temperature with staggered fermions and in pure gauge theory. The arrows indicate the continuum ideal gas limits for two and three flavor QCD with quarks of mass $m/T=0.4$ and an additional heavier quark of mass of $m/T=1$, from Ref. [5].

regime and close to the phase transition, where the coupling constant α_s is large, i.e., of order unity, conventional perturbation methods fail. Hence, the investigation of the phase transition or of low energy, static hadron properties is only feasible in a non-perturbatively manner such as a lattice regularized version of QCD, which we address in this work. One introduces a space-time lattice and formulates the theory by a lattice regularized path integral. In numerical simulations of such systems the transition from a hadronic gas to a QGP appears to take place at temperatures between 160 and 190 MeV and is presumably characterized by a crossover behavior. Indeed heavy ion collisions conducted at CERN and BNL give some indication of a QGP formation. However, the precise value of the transition temperature, below called the *critical* temperature T_c , and how high the temperature must rise before the plasma can be considered as weakly coupled, can only be determined by accurate, non-perturbative simulations of the equation-of-state of QCD. Many static properties of the high-temperature phase of QCD, e.g., energy density $\epsilon(T)$ and pressure $p(T)$ (Fig. 1), have already been studied with results consistent with the notion that indeed states with open color are almost liberated above T_c and chiral symmetry is restored. However, explanatory statements for the persistent deviations from the free gas limit even to the highest studied values of T/T_c are of great interest and are still waiting to come. Perturbative calculations based on dimensional reduction exists up to $\mathcal{O}(\alpha_s^3 \ln(1/\alpha_s))$ [6] and results agree with the pressure data at $T \gtrsim 3T_c$. Nowadays there are speculations that the QGP, e.g., studied at RHIC at $T_c < T < 2T_c$ with a center of mass system (CMS) energy of $\sqrt{s} \sim 200$ AGeV, is very different from a plasma of weakly interacting

quarks and gluons [7]. A well defined measure of the interaction strength in a QGP is the ratio between its shear viscosity η (mean free path of particles) and its entropy density s (inter-particle distance). A small ratio within the collision region (fireball) as indicated by experimental findings, has reinforced speculations that the QGP near T_c is a rather strongly coupled one with the properties of a liquid with very low viscosity rather than a dilute gas [8]. Our understanding of the QGP strongly depends on the matter, hadrons (baryons and mesons) and leptons, inside the plasma and their changing properties under such extreme conditions. Studying strongly interacting mesonic matter at finite temperature in the framework of Lattice Gauge Theory (LGT) in the context of light quark masses is the objective of this work.

Among the light vector mesons ρ, ω and ϕ , the ρ is of considerable importance, due to its strong coupling to the $\pi\pi$ and possibly $q\bar{q}$ annihilation channel and its short lifetime of 1.3 fm/c. Hence, its fast decay in thermal dileptons via *virtual* photons might encode information of the early stage of fireball evolution. These properties have given it a key role as *test* particle for studying the QGP by its *in-medium modifications*.

In the heavy quark sector, vector bound states like the charmonium states J/ψ and ψ' are also in the focus of current research as their formation should be suppressed within a QGP background in comparison to a hadronic background due to color screening. This has been predicted by MATSUI and SATZ based on potential models [9]. At what temperatures exactly heavy quarkonia states dissolve is the objective of many present studies.

Finally, due to their negligible final-state interaction with the strongly interacting medium ($\alpha_e \ll \alpha_s$) from the entire reaction volume throughout the evolution of a heavy-ion collision, *real*, so-called direct photons are the ideal candidates to probe the QGP electromagnetically. The corresponding photon spectra are defined as the spectra remaining after subtraction of final-state decays (background or decay photons), whereas in measured dilepton spectra the latter are usually included and assessed separately being referred to as hadronic decay *cocktail*. Unfortunately, the same property that allows photons to escape freely also leads to major experimental challenges – low rates and large backgrounds from the above mentioned hadronic decays.

An important and challenging step towards an understanding of in-medium particle modifications and photon production would be the determination and investigation of spectral functions (SPFs), σ . Especially in the vector channel, where they are directly linked to the lepton pair production rate [10]¹

$$\frac{dW}{d\omega d^3p} = \frac{5\alpha^2}{27\pi^2} \frac{1}{\omega^2 (e^{\omega/T} - 1)} \sigma_V(\omega, \mathbf{p}, T), \quad (0.1)$$

they may offer explanations for the observed enhanced rates of low-mass e^+e^- pairs below the ρ resonance, the suppressed high mass $\mu^+\mu^-$ pairs at J/ψ and ψ' and the excess of direct photons. However, the extraction of SPFs suffers from a lack of information, since measurements on the lattice at imaginary time and finite temperature can only be carried out on a very finite set of discrete points. The Maximum Entropy Method (MEM) [11], applicable in various kinds of research, opened the access to study these modifications from first principles, i.e., without a definite SPF parameterization. However, it still relies on a priori knowledge given by a default model, e.g., the free, $T = \infty$, SPFs.

Especially at high temperatures the physically interesting small energy part of the SPFs might be strongly disturbed by lattice induced effects (artefacts). Hence, a proper disentanglement between physical bound states or resonances and lattice artefacts becomes necessary.

¹For $\omega = |\mathbf{p}|$ one obtains the direct photon rate

In respect thereof we choose two types of actions with small discretization errors and compare their usability with respect to the MEM.

The need for better suitable lattice actions, concerning $\mathcal{O}(a)$ cut-off effects has lead in recent years to miscellaneous improved actions in the fermionic and gluonic sector. Following Wilson's renormalization group theory [12], the so-called fixed point perfect actions, e.g., are per definition free from any cut-off effects. As we will see, for free quarks the perfect action is known analytically and can be obtained with a technique called *blocking from continuum*. In lattice simulations one truncates this action to a unit hypercube to render it ultralocal and one finally gets the on a hypercube truncated fixed point action, also called hypercube fermion (HF) action.

Another approach is given by the Symanzik improvement scheme [13, 14]. Here the convergence to the continuum limit can be accelerated by including counter terms of $\mathcal{O}(a)$ (and higher orders) in the lattice action and the local operators of interest.

One of the central goals of this work is thus to study lattice data, Euclidean meson correlation functions extracted from improved actions, and the corresponding spectral functions using the MEM. Both can provide a better understanding of mesonic properties particularly above the phase transition.

This thesis is organized chapterwise as follows.

In the first chapter, we give a short introduction to QCD, formulated as an $SU(3)$ gauge theory in the FEYNMAN path integral formalism in continuous space-time. We start at zero temperature in real-time and switch over to finite temperature in the imaginary-time formalism. Important symmetries of the QCD Lagrangian, which determine some of the main properties like confinement-deconfinement, broken-restored chiral symmetry or the general particle spectrum are discussed. The chiral condensate as order parameter of chiral symmetry is introduced and its connection to the low eigenvalues is shown. Finally, the phase diagram at zero and/or finite baryon density is given together with a short motivation for studying QCD in the light of present experimental and theoretical findings.

In the second chapter, the discretization of QCD leading to lattice QCD (LQCD) is carried out. Both the gauge and various realizations of the fermionic part of QCD are introduced. Concerning the former, the standard plaquette Wilson action is used. For the latter in particular two fermionic discretization schemes, the non-perturbatively improved Sheikholeslami-Wohlert (SW) and the HF action, are explained. After that, the simulation techniques as well as the data analysis (fitting) and error determination are described. Our chosen parameters and renormalization constants are presented and we show how the scale is set. Next the improvement scheme for the local operators, the corresponding correlation functions (CF) and their connection to the SPFs are given. Finally, the specific particle properties are discussed and various energy extraction methods applied on those CFs are described.

The third chapter is mainly devoted to the MEM and gives an outline of its application. Furthermore, free ($T=\infty$) CFs and SPFs in the continuum as well as in both discretization schemes are calculated (semi-)analytically. They will be used in Chapter 4 as a default model for MEM. This partially builds upon and extends earlier work carried out by S. STICKAN and I. WETZORKE. Finally consistency checks and important properties of the MEM are recapitulated.

The fourth and main chapter combines the findings concerning the temperature dependence of mesonic properties. This includes ground state masses, dispersion relations, current quark masses and wave functions. We also evaluate the pion and rho decay constants. We examine how and whether the application of MEM for reconstructing thermal SPFs works in both

fermion discretizations and present for the first time HF SPF. Furthermore chiral and $U_A(1)$ symmetry restoration is investigated by studying CFs close to and far above the phase transition.

In order to systematically investigate lattice effects, Chapter 5 then describes the infinite volume and continuum extrapolation of effective screening masses. Partial results were presented at the conference *Lattice 2005* in Dublin [15].

The last chapter summarizes the results and provides an outlook on viable directions for future investigations. Several short appendices serve to complete the material presented in the main body of the text and give a short description of the database we used to store our data.

1 Quantum Chromodynamics in the continuum

Symmetry, as wide or as narrow as you may define it, is one idea by which man through the ages has tried to comprehend and create order, beauty, and perfection.

HERMANN WEYL

The strong interactions between quarks and gluons are successfully described by QCD, a local gauge theory introduced over 30 years ago. As part of the SM, it is a QFT based on the unbroken non-Abelian $SU(N_c=3)_C$ color gauge group and seems to be capable of describing the features of its participating particles in a very elegant and compact way. Its dynamics is formally defined by the following Lagrange density

$$\mathcal{L}_{\text{QCD}}[A_\mu, \bar{\psi}, \psi](x, g, m_f, \mu_f) = \mathcal{L}_G(x) + \mathcal{L}_F(x), \quad (1.1)$$

$$\mathcal{L}_G(x, g) = -\frac{1}{4} \sum_{a=1}^{N_c^2-1} F_{\mu\nu}^a(x) F_a^{\mu\nu}(x), \quad (1.2)$$

$$\mathcal{L}_F(x, g, m_f, \mu_f) = \sum_{f=1}^{N_f} \bar{\psi}_f^{a,\alpha}(x) (i\mathcal{D}_{\alpha\beta}^{ab} - m_f \delta_{\alpha\beta} \delta_{ab} + \mu_f \gamma_{\alpha\beta}^0 \delta_{ab}) \psi_f^{b\beta}(x). \quad (1.3)$$

The Grassmann valued four spinor fields ψ_f and $\bar{\psi}_f$ (Dirac bispinors) describing the quarks are members of the $SU(3)_C$ triplet color representation. The index f denotes the $N_f = 6$ quark flavors, while Greek letters will be used as Dirac indices throughout this chapter. The Roman letters are the color indices representing the corresponding color charges of quarks and gluons – thus the name *chromo* in QCD. The quark masses are denoted by m_f and the chemical potentials are given by μ_f . Even though this work is completely dedicated to QCD with vanishing chemical potentials $\mu_f = 0$, we will utilize it in the more phenomenological part of this thesis. The six quarks can be grouped in three flavor families: the u (p)- and d (own)- ($m_{u,d} \simeq 5$ MeV), the s (trange)- and c (harm)- ($m_s \simeq 140$ MeV, $m_c \simeq 1.2$ GeV) and finally the b (ottom)- and t (op)-quark ($m_b \simeq 4$ GeV, $m_t \simeq 175$ GeV). This thesis concentrates on the issue of the light quark sector (1st family), while heavier quark masses are neglected or in other words treated as infinitely heavy.

The dynamics of the N_c^2-1 massless gluons $A_\mu^a(x)$, which transform in the adjoint representation of $SU(3)$,

$$A_\mu(x) = \sum_{a=1}^{N_c^2-1} A_\mu^a(x) T_a, \quad (1.4)$$

is constrained in \mathcal{L}_G via the field strength tensor

$$F_{\mu\nu}(x) = \sum_{a=1}^{N_c^2-1} F_{\mu\nu}^a(x) T_a \quad (1.5)$$

with

$$F_{\mu\nu}^a(x) = \partial_\mu A_\nu^a(x) - \partial_\nu A_\mu^a(x) + gf_{abc}A_\mu^b(x)A_\nu^c(x). \quad (1.6)$$

The matrices $T_a = \lambda_a/2$ are the eight generators of the $SU(3)$ defined in Appendix A.1.2. The gluons couple to the quark fields via the covariant derivative D_μ , equivalently, the massless Dirac operator

$$\mathcal{D} = \gamma^\mu D_\mu = \gamma^\mu (\partial_\mu - igA_\mu(x)) \quad (1.7)$$

with the bare coupling g , where the Dirac matrices are defined by $\{\gamma^\mu, \gamma^\nu\} = 2g^{\mu\nu}$. This ensures the local gauge invariance of the Lagrangian under the $SU(3)$ transformation Eq. (1.22). Finally the theory is defined by its partition function

$$Z(g, m_f, \theta) = \int \prod_\mu \mathcal{D}A_\mu \prod_{f=1}^{N_f} \mathcal{D}\bar{\psi}_f \mathcal{D}\psi_f \exp(-iS_{\text{QCD}}[A_\mu, \bar{\psi}_f, \psi_f] + i\theta\nu[A]) \quad (1.8)$$

with

$$S_{\text{QCD}}[A_\mu, \bar{\psi}, \psi] = \int d^4x \mathcal{L}_{\text{QCD}}[A_\mu, \bar{\psi}_f, \psi_f] \quad (1.9)$$

The real parameter θ is the *vacuum angle* and ν the *topological charge (density Q)* defined by

$$\nu[A_\mu] = \int d^4x Q(x) \quad Q(x) = \frac{g^2}{64\pi^2} \epsilon_{\mu\nu\rho\sigma} \text{Tr}(F^{\rho\sigma} F^{\mu\nu}) \quad (1.10)$$

where $\epsilon_{\mu\nu\rho\sigma}$ is the antisymmetric unit tensor of rank four. The topological charge $\nu[A_\mu]$, sometimes also called the *winding number* of a field configuration, takes integer values for finite action field configurations.

1.1 QCD at finite temperature

Since our investigations are made at finite temperature the main modifications towards a *finite temperature* field theory living in Euclidean space-time is presented below. Again we show the partition function of the Euclidean path-integral formulation

$$Z^E(T, V) = \int \prod_\mu \mathcal{D}A_\mu \prod_{f=1}^{N_f} \mathcal{D}\bar{\psi}_f \mathcal{D}\psi_f \exp(-S_{\text{QCD}}^E[A_\mu, \bar{\psi}_f, \psi_f](T, V)). \quad (1.11)$$

It depends now on temperature T and is considered in volume V . The Euclidean action reads

$$S_{\text{QCD}}^E[A_\mu, \bar{\psi}_f, \psi_f](T, V) = \int_0^{\beta=1/(k_B T)} d\tau \int_V d^3x \mathcal{L}_{\text{QCD}}^E[A_\mu, \bar{\psi}_f, \psi_f]. \quad (1.12)$$

It is derived from Eq. (1.1) by going from Minkowski to Euclidean space, i.e., $g^{\mu\nu} \rightarrow \delta^{\mu\nu}$, or in other words by a (Wick-)rotation from real to imaginary time, i.e., substituting $t \rightarrow -i\tau$ with $\tau \in \mathbb{R}$ [16]. The corresponding Euclidean Lagrangian assuming zero topological charge is then

$$\mathcal{L}_{\text{QCD}}^E = \mathcal{L}_G^E + \mathcal{L}_F^E = \frac{1}{4} \sum_{a=1}^{N_c^2-1} F_{\mu\nu}^a(x) F_a^{\mu\nu}(x) + \sum_{f=1}^{N_f} \bar{\psi}_f^\alpha(x) (\mathcal{D}^E + m_f \mathbf{1}_4 - \mu_f \gamma_4)_{\alpha\beta} \psi_f^\beta(x). \quad (1.13)$$

The Euclidean Dirac operator becomes

$$\mathcal{D}^E = \gamma_\mu^E D_\mu^E = \gamma_\mu^E (\partial_\mu + igA_\mu^a(x)T_a), \quad (1.14)$$

where the γ^E are the Euclidean Dirac matrices defined in the Appendix A.1.3. The temperature is defined through restricting the Euclidean time interval to $[0, 1/(k_B T))$, Eq. (1.12). To make this correspondence more clear one can relate this formal construction to Feynman's path integral formalism of the grand canonical partition function in the framework of statistical quantum mechanics. Consider the thermodynamic expectation value of an operator \mathcal{O} in a system, which is in thermal and chemical equilibrium

$$\langle \mathcal{O}(A_\mu, \bar{\psi}_f, \psi_f) \rangle_{T, \mu_f} = \frac{\text{Tr } \mathcal{O}(A_\mu, \bar{\psi}_f, \psi_f) \hat{\rho}}{\mathcal{Z}} \quad \text{with } \mathcal{Z} = \text{Tr } \hat{\rho}. \quad (1.15)$$

Here \mathcal{Z} is the quantum statistical partition function and $\hat{\rho}$ the *spectral density operator*

$$\hat{\rho} = \exp \left(-\frac{1}{k_B T} \left(\mathcal{H} - \sum_{f=1}^{N_f} \mu_f \mathcal{N}_f \right) \right) \quad (1.16)$$

with the *Hamiltonian* \mathcal{H} , the *baryonic number operator* $\mathcal{N}_f = \int d^3x \bar{\psi}_f(x) \gamma_4 \psi_f(x)$ and the Boltzmann constant k_B . Since $\text{Tr } \hat{\rho}$ can be rewritten in the language of path integral by using a complete set of eigenvectors of the position operators

$$\mathcal{Z} = \int dx \langle x | \hat{\rho} | x \rangle \quad (1.17)$$

one can also interpret $\hat{\rho}$ as an evolution operator in imaginary time from $\tau = 0$ to $\tau = 1/(k_B T)$ and write the expectation value in Eq. (1.15) as path integral

$$\langle \mathcal{O}(A_\mu, \bar{\psi}_f, \psi_f) \rangle_{T, \mu_f} = \frac{1}{\mathcal{Z}^E} \int \prod_{\mu} \mathcal{D}A_\mu \prod_{f=1}^{N_f} \mathcal{D}\bar{\psi}_f \mathcal{D}\psi_f \mathcal{O}(A_\mu, \bar{\psi}_f, \psi_f) \exp(-S^E[A_\mu, \bar{\psi}_f, \psi_f]). \quad (1.18)$$

Because of the trace and in order to satisfy the spin statistics, periodic (antiperiodic) boundary conditions must be imposed on generic bosonic ϕ (fermionic ψ) degrees of freedom in the time direction [17]

$$\begin{aligned} \phi(\tau = 0, \mathbf{x}) &= \phi(\tau = \beta, \mathbf{x}) \\ \psi(\tau = 0, \mathbf{x}) &= -\psi(\tau = \beta, \mathbf{x}). \end{aligned} \quad (1.19)$$

Since only quantities in the Euclidean metric are utilized, we stay in the Euclidean formulation and the index E will be omitted from now on¹.

1.2 Symmetries of the Lagrangian

Symmetries play an important role in physics because they reduce the number of degrees of freedom. Depending on the type of symmetry the theory will have certain conserved currents, corresponding charges, quantum numbers or other related properties. Furthermore it allows for classifying particles as members of irreducible representations. The Poincaré invariance for instance leads to energy, momentum and angular momentum conservation.

The local $SU(3)$ color symmetry, which is given by the invariance of Eq. (1.13) with respect to the local transformation $G(x) \in SU(3)$ (see A.1)

$$\psi(x) \rightarrow G(x)\psi(x) \quad (1.20)$$

$$\bar{\psi}(x) \rightarrow \bar{\psi}(x)G^\dagger(x) \quad (1.21)$$

$$A_\mu(x) \rightarrow G(x)A_\mu(x)G^\dagger(x) - g^{-1}(\partial_\mu G(x))G^\dagger(x), \quad (1.22)$$

¹Note that Lorentz 4-vectors are denoted by x, p and so on, whereas 3-vectors \mathbf{x}, \mathbf{p} are printed in bold font.

leads to the gluons having color charges and thus to interactions among them. For the time being there is no analytic proof, but intuitively confinement is due to these force-carrying color charged gluons.

In flavor space the equality $m_u = m_d$ in Eq. (1.13) implies an exact global $U(2)_V = U(1)_V \otimes SU(2)_V$ flavor symmetry, where $U(1)_V$ expresses the conservation of quark (fermion) number, and $SU(2)_V$ is the isospin symmetry. At zero quark mass, which is a good approximation for the u, d -quark compared to a typical strong interaction scale, e.g., $\Lambda_{\text{QCD}} \simeq 200$ MeV, this symmetry can be extended further to $U(2)_V \otimes U(2)_A = U(1)_V \otimes U(1)_A \otimes SU(2)_V \otimes SU(2)_A$. All symmetry transformations of this *chiral symmetry group* can be described (for a general number of quark flavors N_f) by

$$\psi(x) \longrightarrow \exp(-i\phi T_D \otimes T_F)\psi(x) \quad (1.23)$$

where $T_D = \{\mathbb{1}_4; \gamma_5\}$ acts only on the Dirac indices and $T_F = \{\mathbb{1}_{N_f}, T_a\}$ on the flavor indices. T_D generates the vector (axial-vector) transformation $U(1)_{V,A}$ with $T_F = \mathbb{1}$, while combined with T_a it gives the corresponding $SU(N_f)_{V,A}$ transformations. *Noether's Theorem* gives the corresponding conserved currents and charges

$$j_\mu(x) = \bar{\psi}(x)\gamma_\mu(T_D \otimes T_F)\psi(x) \quad (1.24)$$

$$Q = \int d^3x \bar{\psi}(x)\gamma_0(T_D \otimes T_F)\psi(x). \quad (1.25)$$

The question arises, what impact the physical non-zero masses have.

The axial $SU(2)_A$ symmetry allows the right-handed and left-handed quarks $\psi^{R/L} = 1/2(1 \pm \gamma_5)\psi$ to be rotated independently such that the approximate massless fermions become also parity eigenstates. $SU(2)_A$ symmetry would therefore lead to almost degenerate hadronic isospin multiplets ($a_1 \leftrightarrow \rho$), which is not observed, so that the $SU(2)_A$ must be spontaneously broken. This phenomenon occurs when the Lagrangian possesses a symmetry, but its ground state does not. For massless quarks, the Goldstone theorem [18, 19] then states that the particle spectrum should include $N_f^2 - 1$ massless Goldstone bosons. In reality the finite u, d -masses or u, d, s -masses could make these Goldstones massive, which is actually observed in nature. These 'quasi-Goldstones bosons' are supposed to be the pions $\pi^{\pm,0}$ or pions, kaons and the eta for $N_f = 2, 3$ respectively. The $U(1)_A$ symmetry is broken by the famous Adler-Bell-Jackiw anomaly [20, 21], meaning the symmetry is fulfilled classically, concerning the invariant S , while it is broken on the quantum level due to the non invariance of the measure $\mathcal{D}\bar{\psi}\mathcal{D}\psi$ [22]. Correspondingly, the divergence of the appropriate flavor singlet axial current in the limit of vanishing quark masses is non-zero

$$\partial^\mu j_{A,\mu}^0 = \partial^\mu \bar{\psi}\gamma_\mu(\gamma_5 \otimes \mathbb{1})\psi = N_f \frac{g^2}{32\pi^2} \epsilon_{\mu\nu\rho\sigma} \text{Tr}(F_{\rho\sigma}F_{\mu\nu}) \quad (1.26)$$

and is a consequence of a linear divergence in the triangle graph with an internal fermion loop, and either three axial-vector insertions or one axial and two vector current insertions². The anomaly is governed by a term which is proportional to the topological charge density Eq. (1.10) of the underlying gluon field. Therefore, topologically non-trivial gauge configurations (instantons) break $U(1)_A$ symmetry and are responsible for the large η' meson mass (960 MeV), due to the Witten-Veneziano mechanism [23, 24] following 't Hooft's idea [25, 26].

²On the lattice the fermion doublers encoded in the *anomalous Ward-Takahashi identity* (X in Subsection 2.3.2) contribute to this anomaly.

In a somewhat worse approximation also the strange quark mass can be neglected, leading to the chiral symmetry group $U(3)_V \otimes U(3)_A = U(1)_V \otimes U(1)_A \otimes SU(3)_V \otimes SU(3)_A$. Here again $SU(3)_V$ is expected to be realized for degenerate quark masses leading to Gell-Mann's eightfold way, namely to the irreducible $3 \otimes \bar{3} \rightarrow 1 \oplus 8$ representation, representing the colorless meson multiplet Fig. 1.1 and the $3 \otimes 3 \otimes 3 \rightarrow 10 \oplus 8 \oplus 8 \oplus 1$, representing the baryon-multiplet. The $U_V(1)$ symmetry still implies baryon number conservation, i.e., the number of quarks minus the number of anti-quark is conserved. Thus the net baryon number observed in our Universe cannot solely be explained by QCD.

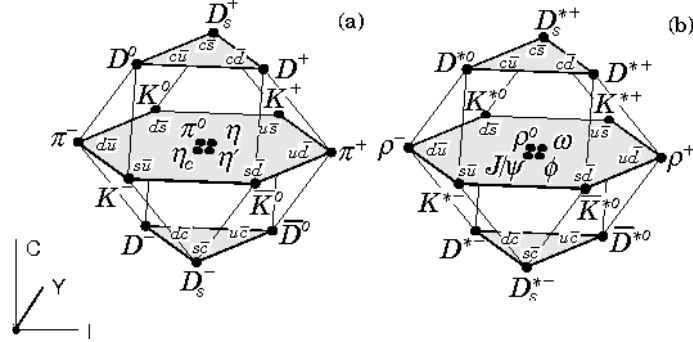


Fig. 1.1: The lightest meson multiplet of the $SU(4)_V$ flavor symmetry group for the pseudoscalar (a) and vector (b) mesons. The nonets of $SU(3)_V$ light mesons occupy the central planes [27].

1.3 Phases in finite temperature QCD in theoretical framework

1.3.1 Phases at vanishing density

The strong interaction at finite temperature and vanishing density is characterized by two qualitatively different phase transitions, which definitely³ occur at different limits of zero and infinitely heavy dynamical (sea) quarks.

The first transition is the confinement-deconfinement transition at T_c . At large separation (small momenta) and low temperatures the coupling strength is strong and the quarks are confined in colorless hadronic bound states $\bar{q}q$ or qqq ((color) *confinement*). In contrast due to *asymptotic freedom* quarks and gluons are only weakly coupled at small distances (large momenta) or high temperatures. Their color charges are screened and they behave at least at asymptotically high temperatures as freely propagating particles (*deconfinement*). Together they build up the QGP, the regime which is believed to be formed a short time (10^{-6} s) after the Big Bang.

In pure gauge (quenched) theory, which corresponds to sea quark masses $m_{u,d,s} \rightarrow \infty$, the phase transition coincides with a spontaneous breaking of the $Z(N_c)$ center symmetry of the

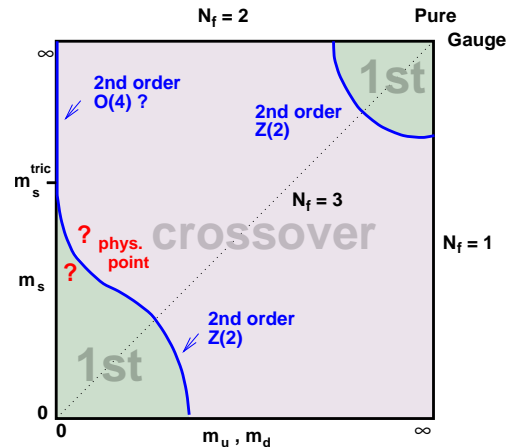


Fig. 1.2: Order of the phase transition for u, d and s ($2 + 1$) sea quark flavor from [28].

³by means of a clean order parameter and in the infinite volume limit

gluonic action. In this regime the *Polyakov loop*, see Section 2.5, serves as an order parameter, which is zero for an infinite volume in the low temperature phase and non-zero in the high temperature phase. The transition is of first order [29] and takes place at $T_c = 270(5)$ MeV [30]. The second transition goes from the chiral symmetric to a non-symmetric phase. At very high temperature the spontaneously broken $SU(N_f)_A$ symmetry gets restored with the chiral condensate $\langle \bar{\psi}\psi \rangle$ for $m_{u,d,s} \rightarrow 0$ as its order parameter. Thus for $N_f = 2$ the pseudoscalar pions are no longer Goldstone bosons and should become degenerate with the scalar singlet meson σ , see Fig. 1.4(a). The same behavior is also anticipated for the flavor triplet (axial-) vector mesons a_1 and ρ .

In the presence of fermions, i.e., in full QCD, the action is no longer $Z(N_c)$ symmetric. Thus the Polyakov loop loses its clean order parameter characteristic. Nevertheless, it still can serve as an indicator of the confinement-deconfinement transition. At the same time the chiral condensate becomes more important as the order parameter of the chiral phase transition, as long as the explicit breaking of the chiral symmetry by the mass is not too strong.

Although deconfinement and chiral symmetry restoration are apparently related to different non-perturbative mechanisms, they seem to be somehow coupled. Lattice computations show a sharp increase of the Polyakov loop around the critical temperature where the chiral condensate vanishes [31], in contrast to quarks in the adjoint representation [32]. However, the interplay between these two effects is not clear yet, and lies in focus of many current studies, see e.g., [33].

The nature of these transitions, i.e., first order, second order or crossover, as studied by lattice simulation and/or effective models, depends strongly on the number of quark flavors N_f and their masses m_f . The corresponding findings are summarized and depicted in Fig. 1.2.

When the sea quark mass is lowered the former (pure gauge) first order transition passes over to a line of a second order phase transition, which belongs to the three dimensional Ising $Z(2)$ universality class. Decreasing the quark masses further, a crossover behavior is expected. As can be seen from Fig. 1.2 the majority of possible quark masses, most likely also the physical ones with very light u - and d -quarks seems to fall into this region.

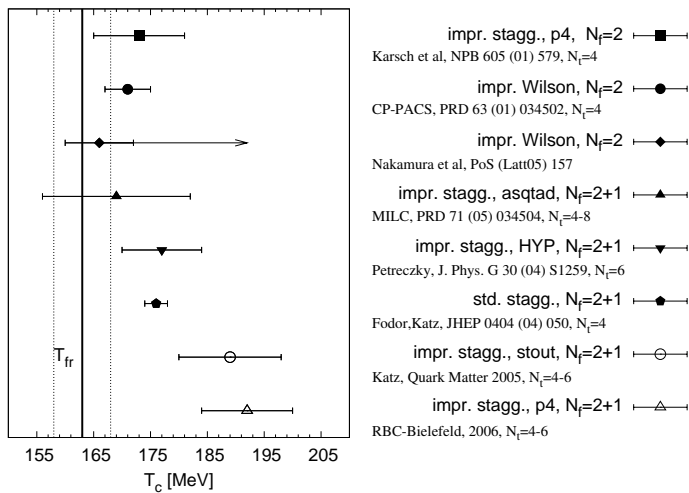


Fig. 1.3: Lattice data on the transition temperature and the chemical freeze-out at RHIC. Picture taken from Ref. [34].

Recent lattice simulations with $N_f = 2 + 1$ staggered fermions with several light u, d -masses and a physical s -mass, using a so called (p3)fat4-action and the RHMC algorithm, give a crossover temperature of $T_c = 192(5)(4)$ MeV [35]⁴. This result was obtained by a combined chiral/continuum extrapolation to the physical pion mass. For a collection of current critical temperatures on the lattice see Fig. 1.3.

The basic features for small quark masses were first investigated by PISARSKI and WILCZEK [36]. They used a Ginsburg-Landau effective theory, called the σ -model, which shares the same global symmetries as QCD. For

⁴This result is somewhat larger compared to former values of $\simeq 170$ MeV, which is mainly due to a different scale-setting.

two massless flavors $m_{u,d} \rightarrow 0$ this model suggests again a transition of second order and of first order for three massless flavors. Lattice simulations confirm this prediction with a transition, which is supposed to fall into the three dimensional $O(4)$ universality class [37] and $T_c = 173(8)$ MeV [38]. In the chiral limit $m_{u,d,s} \rightarrow 0$ lattice results give a first order transition with a transition temperature of $\simeq 154$ MeV [38]. Like in the regime of heavy sea quarks, a second order line, which falls into the three dimensional Ising universality class $Z(2)$ [30], separates the first order from the crossover regime. It ends in a tricritical point and continues according to $m_u, m_d \sim (m_s^{\text{tricrit}} - m_s)^{\frac{5}{2}}$.

At (very) high temperatures also the quantum effects leading to the $U(1)_A$ anomaly become less important and a slow restoration may thus be observed. For $N_f=2$ this should result in a degeneracy of the flavor triplet $\pi \leftrightarrow \delta$ and flavor singlet $\sigma \leftrightarrow \eta'$ [36], see Fig. 1.4(a). Fig. 1.4(b) shows the integrated meson CF (susceptibility χ_H), which corresponds to the inverse of a squared thermal mass $\chi_H \sim m_H^{-2}$ here for staggered fermions [39]. Their masses indicate in fact a $SU(2)_A$ symmetry restoration, while the $U(1)_A$ restoration is only proceeding slowly. The effective $U(1)_A$, i.e., $U(N_f) \times U(N_f)$ restoration seems to be taken place only at very high temperatures. However, the data have to be interpreted with caution, since in the continuum correlations diverge at $\tau = 0$, such that a proper renormalization of χ_H is indispensable.

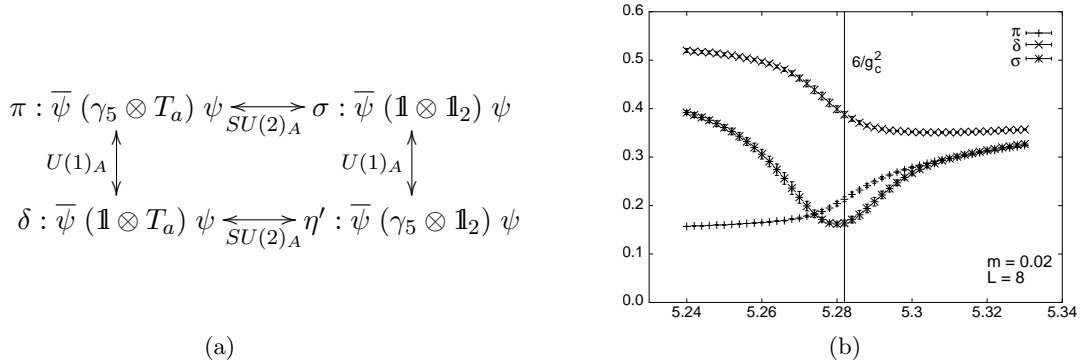


Fig. 1.4: (a) The transformations which relate different particles in the chiral limit. (b) The temperature dependence of the square root of the inverse susceptibilities in different quantum number channels [40].

1.3.2 Chiral condensate and the Dirac eigenvalue spectrum

As stated above, the chiral condensate serves as the order parameter of the chiral phase transition. To make this more clear, we investigate the eigenvalue spectrum of the Dirac operator in real-time formalism. The massless Dirac operator Eq. (1.14) is anti-Hermitian $\mathcal{D}^\dagger = -\mathcal{D}$ and fulfills γ_5 -Hermiticity $\gamma_5 \mathcal{D} \gamma_5 = \mathcal{D}^\dagger$. Hence it satisfies the anticommutator relation

$$\{\gamma_5, \mathcal{D}\} = 0, \quad (1.27)$$

which is a compact expression of chiral symmetry $SU(N_f)_L \otimes SU(N_f)_R$. Namely decomposing ψ and $\bar{\psi}$ in left and righthanded spinors one can easily see that the massless fermionic action

$$S_F = \int d^4x (\bar{\psi}^R \mathcal{D} \psi^R + \bar{\psi}^L \mathcal{D} \psi^L) \quad (1.28)$$

is invariant under the chiral transformation

$$\begin{aligned}\psi^L &\rightarrow L\psi^L, & \bar{\psi}^L &\rightarrow \bar{\psi}^L L^{-1}, \\ \bar{\psi}^R &\rightarrow \bar{\psi}^R R^{-1}, & \psi^R &\rightarrow R\psi^R\end{aligned}\tag{1.29}$$

with $L \in SU(N_f)_L$ and $R \in SU(N_f)_R$. Following the spontaneous symmetry breaking pattern the $SU(N_f)_L \otimes SU(N_f)_R$ symmetry equivalently is broken down to

$$SU(N_f)_L \otimes SU(N_f)_R \rightarrow SU(N_f)_V.\tag{1.30}$$

This implies that the ground state of the quantum system is invariant with respect to the $SU(N_f)_V$, the $SU(N_f)$ subgroup with $L=R$, but not with respect to the $SU(N_f)_A$ symmetry, the axial subgroup of $SU(N_f)$ with $L=R^{-1}$, see Section 1.2. Working on a finite lattice, \mathcal{D} is a finite dimensional matrix and for any given gauge field one can consider its eigenvalues and eigenvectors

$$\mathcal{D}\psi_n = i\lambda_n\psi_n, \quad \lambda_n \in \mathbb{R}.\tag{1.31}$$

Being an anti-Hermitian operator, the eigenvalues of \mathcal{D} are purely imaginary and from Eq. (1.27) it follows further that non-zero eigenvalues occur in pairs $\pm i\lambda_n$ with eigenfunctions $\psi_n, \gamma_5\psi_n$. There can also be eigenvalues equal to zero, $\lambda_n = 0$. Because of Eq. (1.27) the corresponding eigenfunctions can be arranged to be simultaneous eigenfunctions of \mathcal{D} and γ_5 with eigenvalues ± 1 , i.e., these states have a definite chirality. Denoting the number of zero eigenvalues per flavor with positive and negative chirality by N_+ and N_- respectively, the Atiyah-Singer *index theorem* [41, 42] states that

$$\nu = N_f(N_+ - N_-)\tag{1.32}$$

is a topological invariant that does not change under continuous deformations of the gauge field. The spectral density of the Dirac operator is given by

$$\rho(\lambda) = \left\langle \sum_n \delta(\lambda - \lambda_n) \right\rangle\tag{1.33}$$

and is related to the chiral condensate

$$\langle \bar{\psi}\psi \rangle = - \lim_{m_f \rightarrow 0} \lim_{V \rightarrow \infty} \frac{1}{VN_f} \frac{\partial}{\partial m_f} \log Z(T, V).\tag{1.34}$$

Using Eq. (1.11) with fermion degrees of freedom integrated out,

$$Z(T, V) = \int DA_\mu \prod_{f=1}^{N_f} \det(\mathcal{D} + m_f) \exp(-S_{\text{QCD}}[A_\mu]),\tag{1.35}$$

this yields,

$$\langle \bar{\psi}\psi \rangle = - \lim_{m_f \rightarrow 0} \lim_{V \rightarrow \infty} \left\langle \frac{1}{V} \sum_n \frac{1}{i\lambda_n + m_f} \right\rangle = - \lim_{m_f \rightarrow 0} \lim_{V \rightarrow \infty} \left\langle \frac{1}{V} \sum_{n \geq 1} \frac{2m_f}{\lambda_n^2 + m_f^2} \right\rangle\tag{1.36}$$

where the contribution of the zero-modes $|\nu|/mV$ was dropped⁵, assuming that it becomes small in the infinite volume limit. This relation shows that spontaneous breaking of chiral

⁵It is believed that $|\nu| = N_f(N_+ + N_-) \sim \sqrt{V}$.

symmetry is manifest in an accumulation of small Dirac eigenvalues. In the infinite volume limit the sum over eigenvalues can be converted to an integral and this leads to

$$\langle \bar{\psi}\psi \rangle = - \lim_{\epsilon \rightarrow 0} \lim_{m_f \rightarrow 0} \lim_{V \rightarrow \infty} \pi \rho(\epsilon)/V, . \quad (1.37)$$

This connection between eigenvalue density and chiral condensate is known as the Banks and Casher relation [43]. The order parameter is non-zero only if $\rho(0)/V > 0$. It is necessary to take the limits in the order indicated.

Instantons, calorons at finite temperature are topological excitations of the QCD vacuum and seem to be somehow connected to the spontaneous chiral symmetry breaking, for a review see Ref. [44]. In the confining phase, weakly interacting instantons and anti-instantons lead to near-zero eigenvalues, i.e., $\langle \bar{\psi}\psi \rangle \neq 0$, while strongly interacting ‘molecules’ of instantons and anti-instantons in the deconfined phase open a gap in the eigenvalue spectrum, which prevents the spectrum from developing near-zero eigenvalues, thus $\langle \bar{\psi}\psi \rangle = 0$.

1.3.3 Phases at finite density

Although not an issue in this thesis it might be appropriate to also give a general view on the phases with non-vanishing chemical potential or baryon density (Figs. 1.5 and 1.6)⁶.

For non-vanishing chemical potential the line of second order phase transitions in the light quark regime is expected to become a critical surface, which bends over the quark mass plane, still separating first order phase transitions from the crossover regime Fig. 1.5(a). This suggest that a system of strongly interacting quarks and gluons, which has only a smooth crossover transition at $\mu = 0$, will nonetheless undergo a thermal phase transition of first order above a certain critical chemical potential μ_c , which defines the critical point, where the phase transition is of second order (see Fig. 1.5(b)). Its location is still uncertain and lies in the focus of many current lattice investigations. For an alternative scenario see also Ref. [45]. The first order transition corresponds to the occurrence of latent heat and could lead to a production of hadron bubbles in a mixed phases. Thus hadrons might survive the phase transition, still keeping all the information of the primordial system.

Shown in Fig. 1.6 is an additional first order phase transition for small μ , separating the hadron gas with zero baryon density from a liquid phase with density $n_B \simeq 0.17/\text{fm}^3$. At zero temperature this jump in the density is expected to occur at a baryon potential of a nucleus minus its binding energy. The endpoint of this phase transition line was estimated experimentally at GSI to lie in the region of 0.15 – 0.3 times the nuclear density and a temperature of $\simeq 10$ MeV.

An additional interesting and rich phase structure is suggested to appear at high μ and low T [48, 49]. Unlike in electromagnetic superconductivity, where a phonon-induced attractive interaction is needed to form a Bose condensate of electron Cooper pairs by the Bardeen-Cooper-Schrieffer (BCS)-mechanism [50], quarks with different color and anti-parallel spin are already attractive. For instance for $N_f = 2$ they form an energetically favorable diquark condensate and open a gap at the fermi surface. Since a pair of quarks cannot be a color singlet, the local $SU(3)$ color gauge symmetry is broken to $SU(2)$ in this therefore called *color superconductivity* phase (CS, 2SC). Since chiral symmetry is restored and no global symmetry is broken, no order parameter exists, which distinguishes the two flavor superconducting phase from the QGP. At the highest densities, where the strange quark Fermi momentum is close to

⁶Furthermore, a non-vanishing chemical potential in lattice simulations induces severe numerical difficulties, i.e., the sign problem.

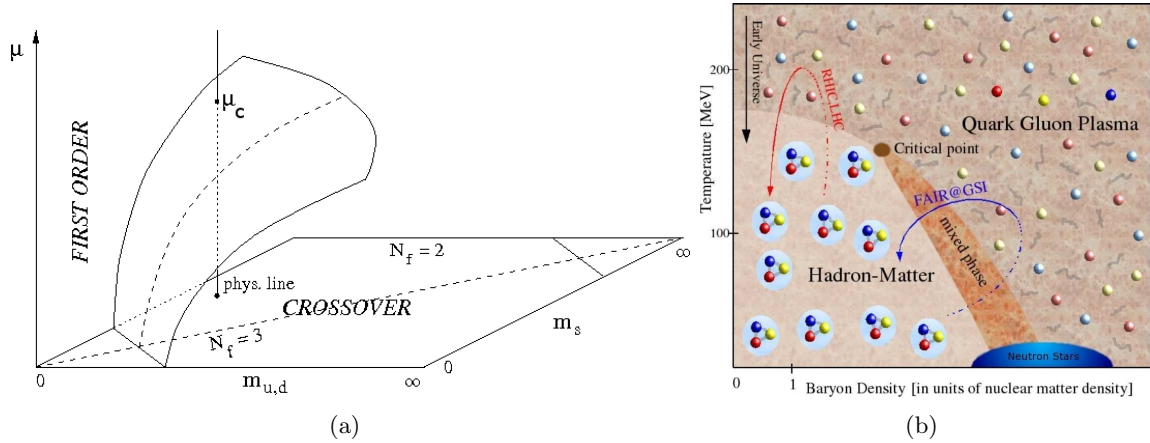


Fig. 1.5: Sketch of first-order/crossover regime and critical surface for non-zero μ_f [46] (a). Phase diagram of QCD for non-vanishing μ_f from [47] (b).

the up and down quark Fermi momenta, the favored phase is the color-flavor-locked (CFL) phase, in which the strange quark participates symmetrically with the up and down quarks. Model calculations, using, e.g., Nambu-Jona-Lasino (NJL) model [51, 52] and gluon-mediated interaction calculations [53], support this scenario. In this phase two global symmetries are broken, the chiral symmetry and baryon number, so there are two gauge-invariant order parameters that distinguish the CFL phase from the QGP. Additionally the NJL model predicts more non-CFL phases. For a review see [54]. In the cores of compact stars, e.g., neutron stars, baryon density and temperature conditions might be appropriate to realize such phases.

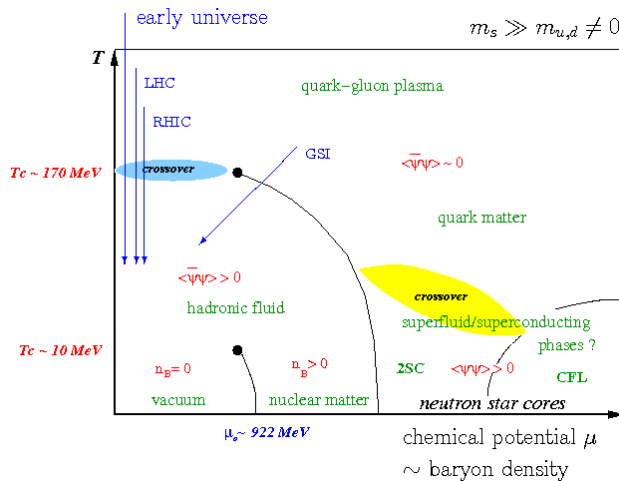


Fig. 1.6: Another more detailed sketch of the QCD phase diagram including also the CS and CFL phases [55].

1.4 Finite temperature QCD in experimental framework

The properties of the nuclear matter at high T and/or various μ have been investigated for quite some time by various experiments at heavy-ion accelerators: SPS at CERN in Geneva

(Switzerland), AGS, RHIC at BNL in Brookhaven (USA) or, e.g., SIS at GSI in Darmstadt (Germany) for lower energies. In order to study the QGP nuclei with a large number of nucleons are accelerated close to speed of light and collided into each other.

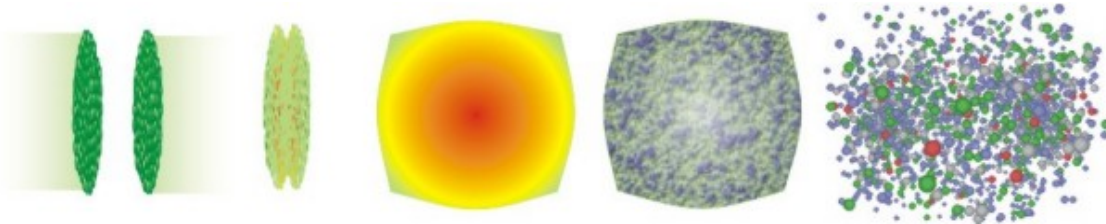


Fig. 1.7: Cartoon of an ultra-relativistic heavy-ion collision. Left to right: the two nuclei approach, collide, form a QGP, the QGP expands and hadronizes, finally hadrons rescatter and freeze out. Source: <http://www.phy.duke.edu/research/NPTheory/transport.ptml>

The understanding of the microscopic structure of thermal QCD matter in the region $T_c \leq T \leq 2T_c$ is of utmost importance for analyzing the results from relativistic heavy ion collisions, at CERN and RHIC. The experimental observation and study of the QGP must be based on signals which can provide evidence for its formation and permit a characterization of its properties. Additionally, our evolving theoretical insight into the nature of this new state has also led to refinements in our understanding of its signals. The experimental quest must proceed in steps: first it should be confirmed that the particles produced in the nuclear reaction really form, at least for a brief period, matter that deserves a description in thermodynamic terms. Second, it needs to be established that this matter has a novel structure and that it is not just a dense gas of hadrons; and third, its main physical properties needs to be characterized.

Important QGP signatures are jet quenching, particle ratios, strangeness enhancement, J/ψ ($\bar{c}c$) suppression or the dilepton and photon production rates. Concerning the latter, vector SPFs with or without a chemical potential are related to the lepton pair production rate in hot and dense matter such as the QGP. They provide the key concept to understand the medium modifications of hadrons. The enhanced low-mass e^+e^- pairs compared to the *cocktail*⁷ below the ρ -resonance at NA45/CERES [56] in Fig. 1.8(b) and the suppressed high mass $\mu^+\mu^-$ pairs at J/ψ and ψ' -resonances at NA38/NA50/HELIOS-3 observed in relativistic heavy ion collisions at CERN-SPS [57] depicted in Fig. 1.8(a) or RHIC⁸ [58, 59] are typical examples which may indicate spectral changes of the $q\bar{q}$ system due to the effect of the surrounding medium.

At low beam energies the target and projectile nuclei will be destroyed and only partially stopped, leading to a non-vanishing baryon number density in the collision region (stopping scenario), see Fig. 1.7. At high beam energies, however, as it is realized at RHIC the particles interpenetrate and finally leave each other partly undisturbed. The collider deposits a high amount of energy density in form of gluons and quark anti-quark pairs in the collision region (transparent scenario). In both scenarios the hot system (fireball) expands and cools down, emitting dominantly pions and other hadrons. The whole process proceeds in steps classified by thermalization, QGP, hadron gas and finally freeze out. During the thermalization time of the order 2 fm/c the system is out of equilibrium, such that LGT is unable to describe the situation. Actually, understanding the mechanisms behind the early equilibration and thermalization is still one of the main unsolved problems in nuclear collisions. Then the QGP

⁷the total of all known sources, e.g., π^0 -, η - and ω -Dalitz-decays, $\pi^+\pi^-$ annihilation and ω -decay.

⁸PHENIX experiment

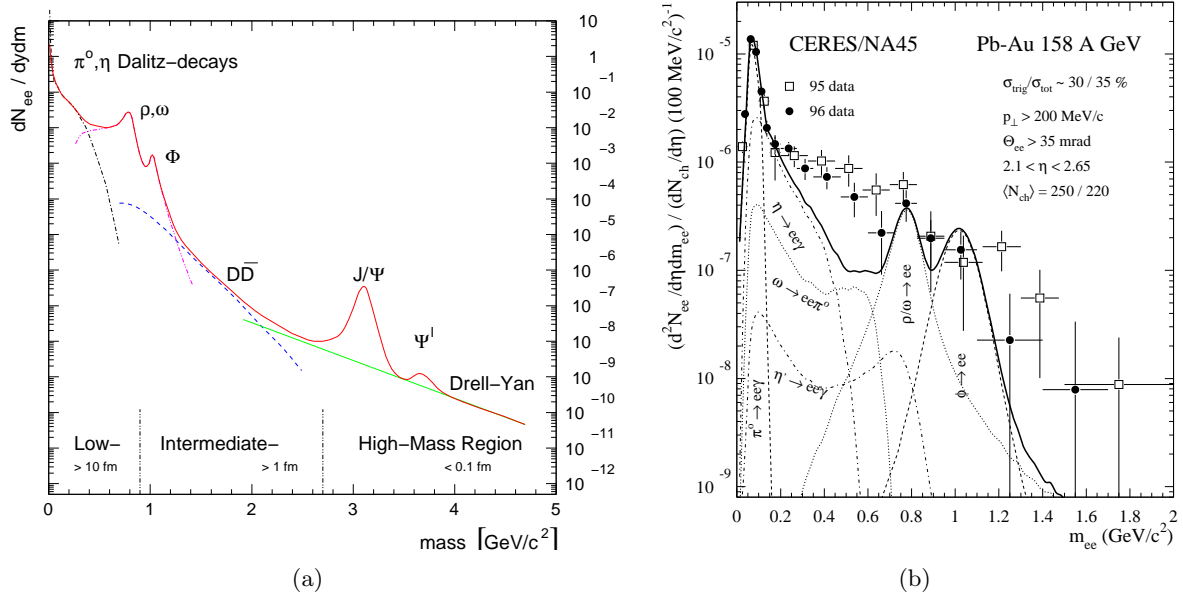


Fig. 1.8: Normalized invariant mass spectra of e^+e^- pairs from CERES in comparison to the known hadronic decay sources (a) and focused on the low mass region (b) [56, 60]. Essentially the low-mass regime is dominated by vector meson decays, the intermediate-mass region by continuum radiation and QGP emission, while the high-mass region by primordial emission and heavy quarkonia.

phase shows up consisting of a gas or liquid of quarks and gluons. Afterwards it cools down through the phase transition and builds up the hadron gas of mostly hot pions, which carry little if any information about the early stage of the formation (soft probes). The mixed phase shown in Fig. 1.9 and 1.5(b) corresponds to the strong first order scenario, where bubbles of hadronic matter are created within the QGP, such that a clear separation between the phases of QGP and the hadron gas is impossible. However, for matter at zero, or small, net baryon density, as is relevant for RHIC, first principle studies indicate that the transition is a smooth (though rapid) crossover. When the expansion reaches a certain extension, the temperature decreases at a point where hadrons stop interacting in-elastically with each other. The particle ratios are fixed and the situation is referred as a *chemical* freeze-out. After further expanding and cooling, the temperature goes down to a point where the final state interactions between hadrons are no longer effective and the particle reach the detector undisturbed, the so-called *thermal* freeze-out.

In contrast to the final low energy hadrons, dileptons, photons or jets (hard probes) directly probe the earlier stage interactions. The energy spectrum of photons for instance may reflect thermal radiation from the hot gas of quarks and gluons. However, the low energy region is heavily contaminated by a background from decays of hadrons, mainly π^0 and η . Therefore, the rate is expected to be two orders of magnitude less sensitive compared to the dilepton rate. In the high momentum region, at high energy, there is a background from “direct” processes such as $g + q$ and $\gamma + q$ reaction and Compton scattering. Current experimental sensitivities are not sufficient enough to observe a clear signal.

Since we will investigate the dilepton spectra from hot QCD in this work, we discuss the experimental results for dileptons from heavy ion collision experiments below. The measured dilepton spectra can be chronologically ordered into several emission phases (see also Fig. 1.9):

- Before the nuclear surfaces actually touch, dileptons are produced through coherent Bremsstrahlung. This part populates very low transverse momenta and has so far not been investigated experimentally.
- Within the first 1 fm/c of the nuclear overlap, the excited hadronic system is far from thermal equilibrium. The pre-equilibrium dilepton radiation emitted at this stage mostly consists of hard processes such as Drell-Yan annihilation $q\bar{q} \rightarrow \gamma \rightarrow l^+l^-$, leaving its trace mainly at large invariant masses $> 3\text{GeV}/c^2$ [61].
- Following deconfinement and rapid thermalization, (thermal) dileptons are produced in the partonic phase via $q\bar{q}$ annihilation with characteristic parameters reflecting the early temperature history of the system.
- After cooling and confinement of the partons to a hot hadron gas, dileptons are created in pion and kaon annihilation processes, e.g., $\pi^+\pi^- \rightarrow \rho \rightarrow \gamma \rightarrow l^+l^-$. This annihilation is dominated by the intermediate formation of light vector mesons ρ, ω, ϕ which directly couple to l^+l^- pairs. The invariant masses of these dileptons directly reflect the SPFs of the vector mesons at the moment of decay. The formation of heavy quark bound states is suppressed. On the other hand, signatures of particles with open charm, D-mesons, should be enhanced.
- Finally, beyond the freeze-out stage, the remaining sources are hadronic resonances and Dalitz decays mostly from π^0, η and ω mesons, e.g., $\pi^0 \rightarrow e^+e^-\gamma$, all contributing to the low mass region with $M < 1\text{GeV}/c^2$.

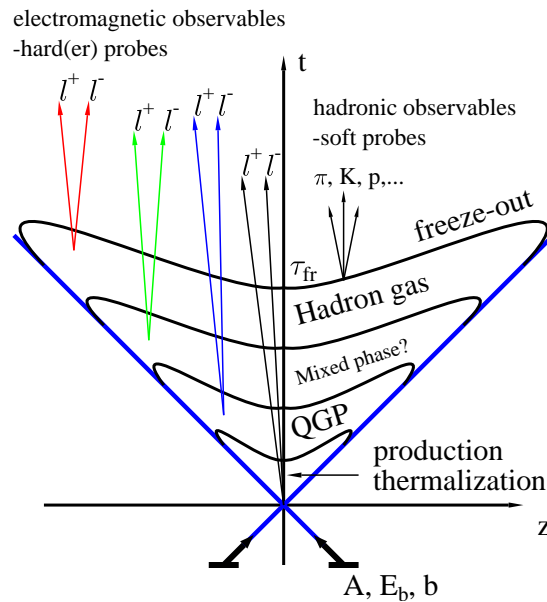


Fig. 1.9: Space-time evolution of an $A+A$ collision [62]. The invariant hyperbola in the space-time diagram allocate the individual stages passed during the heavy-ion collision shown in Fig. 1.7.

Dilepton spectra in the low mass region and the ρ

In the low-intermediate mass region between the $2m_\pi$ threshold and $\sim 1\text{GeV}/c^2$, the dilepton spectrum is dominated by decays of the vector mesons ρ, ω and ϕ . While the vector mesons

predominantly decay hadronically, they have a significant branching ratio for e^+e^- and $\mu^+\mu^-$ decays. The dileptons, once generated, do not interact with the fireball and therefore give information about the hadrons in-media. Of particular interest is the ρ peak, since due to its very small lifetime ~ 1.3 fm/c, the ρ is expected to decay inside the fireball. An in-medium change⁹ of the ρ^* , associated with interactions with thermal pions and/or chiral symmetry restoration, should therefore be manifested in the ρ peak in the dilepton channel.

The early data from heavy ion collisions attracted a lot of interest, since a significant deviation from the expectation based on hadronic decays was seen. This can be seen in Fig. 1.8, which shows the experimental data from CERES [56], together with a ‘cocktail plot’ [60] which includes the prediction based on known hadronic contributions. The clear enhancement in the invariant mass region 0.3–0.6 GeV/c² implies nontrivial medium effects. At least two major scenarios have been put forward to explain the data:

1. In medium “dropping” ρ -mass m_ρ^*

This approach, pursued by BROWN, RHO ET AL. [63], uses effective mean field theory and scaling-based arguments to connect the in-medium hadron masses with chiral symmetry breaking. It links the temperature- and baryon-density dependent reduction of the ρ -mass directly to the corresponding medium-induced change of the chiral condensate (*Brown/Rho scaling*)¹⁰ $m_\rho^*/m_\rho^0 \sim (\langle \bar{q}q \rangle^*/\langle \bar{q}q \rangle)^{1/2}$ [65]. The pion propagation remains unchanged creating a sharp threshold at $2m_\pi$. This scenario is also supported by studies using the QCD sum rules [66].

2. In medium increase in ρ^* -width $\Gamma_\rho(T)$

RAPP and WAMBACH ET AL. [60, 67], using an effective chiral Lagrangian theory, determined the in-medium properties of ρ by calculating the thermal contributions to the current-current correlator. Their calculations show a considerable increase in the width of the rho in-medium (but little mass shift), especially when one includes collisional broadening. Effects of baryons may also be significant [68].

An unmodified ρ , i.e., vacuum SPF, is clearly ruled out. Instead, present experimental data seems to indicate an enhancement of ρ width in heavy ion collisions [69, 70], in agreement with Scenario 2 with little indication of a significant mass shift.

While in the theoretical analyses thermal pions and, in particular, a nonzero baryon density seem to play significant roles, we will investigate here if some modification of the ρ is also seen in a thermal gluonic medium close to the transition temperature.

Dilepton spectra in the high mass region and the J/ψ

J/ψ suppression [9] has been one of the most studied signatures of deconfinement and QGP formation in heavy ion collision experiments [57]. While in a hadronic medium, the potential between a static $\bar{q}q$ can be described by the well-known Cornell potential ($\sim -\alpha/r + \sigma r$), in a QGP medium, perturbation theory predicts that the potential is of a screened Coulomb form (similar to Debye screened potential in an electromagnetic plasma). Lattice studies have also confirmed this. This should in general change the behavior of the in-medium J/ψ significantly and, if the screening radius is sufficiently small, would prevent J/ψ formation altogether. Since it is very difficult to dissolve J/ψ through hadronic interactions, it has been

⁹denoted by the superscripts *

¹⁰Note that the scaling exponent differs from Brown and Rho’s original approach [64] where using Skyrme’s Lagrangian an exponent 1/3 was obtained.

suggested that a substantial suppression of the J/ψ peak in the dilepton channel would be one of the cleanest signals of deconfinement.

Studies based on potentials extracted from lattice studies have predicted that J/ψ should cease to exist above $\approx 1.1T_c$ and the ground state of the $(\bar{b}b)$ system above $\approx 2.3T_c$. However, recent lattice studies, based on a direct analysis of SPFs of the $\bar{c}c$ system in quenched QCD, indicate the survival of a narrow J/ψ state up to at least $\sim 1.7T_c$, or even $\gtrsim 2.25T_c$ [71, 72], respectively. And indeed, more recent results using potentials based on the internal energy U instead of free energy $F = U - TS$ [7] seem to support the spectral analysis with a dissociation temperature of $\gtrsim 2.1T_c$ [73] or $\gtrsim 1.95T_c$ [74]. While the systematics of these studies are not completely under control, and the effect of quenching is not known a-priori, the results seem to indicate that a re-interpretation of NA50 results may be necessary. It has been suggested that a suppression of excited charmonia states, which may have a lower dissolution temperature, can explain the experimental data from both CERN and RHIC [75]. Finally, even if charmonium bound states or narrow resonances survive the phase transition significantly, also inelastic collisions with the constituents of the medium before or after their formation may lead to the observed suppression [76–78].

Dynamical properties

The Au-Au collision experiments in RHIC have produced very interesting results, the interpretation of which would be greatly helped by a first principles calculation of transport coefficients of the QGP. In particular, data for angular distributions of particles seem to require a very low viscosity of the matter produced [79]. Perturbative estimates of the transport coefficients are much higher than is required for RHIC data to be explained in terms of thermalized hot strong matter.

The non-perturbative calculation of phenomenologically relevant transport properties, such as the shear viscosity, collective modes or the electrical conductivity (Kubo formula)

$$\sigma_{el} = \lim_{\omega \rightarrow 0} \frac{\sigma_V(\omega, \mathbf{P})}{6\omega}, \quad (1.38)$$

thus pose an important challenge. Up to now, lattice simulations which can provide information are unable to make reliable predictions of most dynamical properties of the QGP. Attempts to determine the SFPs in various color-singlet channels [80, 81] are still limited by the need to use the quenched approximation and the systematics are not well understood, especially for low frequencies [82]. For further discussion of the difficulty of extracting transport coefficients from Euclidean lattice correlators, see [83].

However, many dynamical properties have been studied in the framework of so-called hard thermal loop (HTL) effective theory. There are good arguments in support of the notion that these techniques work reliable for temperatures $T > 3T_c$ [84, 85], but it is not known precisely, whether they can be applied also closer to the phase transition. Also the divergent vector SPFs at small energies due to cut contributions may be seen as a hint for their inconsistency [82].

Outlook

In the very near future, the Large Hadron Collider (LHC) at CERN will be commissioned for high energy proton-proton and heavy ion lead-lead reactions. These heavy ion collisions will be at a total CMS energy of $\sqrt{s} = 5.5$ ATeV, where A is the nucleon number, thus bringing 1144 TeV in total kinetic energy into the collision. At this highest energy all parameters

relevant for the formation of the QGP, such as energy density, size and lifetime of the fireball and relaxation time, will be more favorable.

2 QCD on the lattice - A brief introduction

The mathematical sciences particularly exhibit order, symmetry, and limitation; and these are the greatest forms of the beautiful.

ARISTOTLE

As already mentioned in Chapter 1, QCD exhibits the crucial character of asymptotic freedom. Thus the associated coupling constant g decreases and perturbation theory becomes applicable in the limit of high energies, i.e., at small distances or high momenta. In contrast, at low energies g is too large ($\mathcal{O}(1)$) to evaluate physical quantities using perturbation theory. LQCD was introduced as a method to overcome this problem.

In these two different regimes the value of the coupling as a function of the length scale or momentum transfer q is well known and described through the *running* of the coupling or the associated *fine structure constant* $\alpha_s = g^2(q)/(4\pi)$, respectively. To lowest order in perturbation theory, i.e., in the weak coupling regime, it is given by

$$\alpha_s(q) = \frac{\alpha_s(\Lambda_{\text{QCD}})}{1 + \alpha_s(\Lambda_{\text{QCD}}) \frac{33 - 3N_f}{12\pi} \ln \left(\frac{q^2}{\Lambda_{\text{QCD}}^2} \right)}. \quad (2.1)$$

$\alpha_s(q)$ has been determined in various experimental measurements at $q \gg \Lambda_{\text{QCD}}$ [27]. In order to compare α_s measured at different energy scales they must be evolved to a common scale using renormalization group theory. For convenience, this is taken to be the mass of the Z boson ($m_Z = 91$ GeV), which results in $\alpha_s(m_Z) = 0.1172(20)$.

LQCD is based on the path integral method, see e.g., [86–88]. Since its introduction by FEYNMAN [89] it has become a very important tool for elementary particle physics. Unfortunately, like any QFT QCD suffers from divergences and a regularization is needed to treat them in a proper way, e.g., Pauli-Villars regularization. While these regularizations mostly work only in the perturbative regime, LQCD allows to study QCD also in the non-perturbative regime.

In what follows, we will focus mainly on a proposal, first presented by WILSON [90], which is discussed in more detail in various text books, e.g., [86, 91] and review articles e.g., [31, 88].

2.1 The lattice as a regulator of QCD

LQCD is a theory regularized on a 4-dimensional Euclidean discrete space-time lattice so that one can carry out path integrals like Eq. (1.11) directly, though approximately, on a computer with Monte Carlo methods. To formulate the theory on the lattice one has to take care of preserving the symmetries, like the local gauge invariance and more difficult chiral symmetry. The Poincaré symmetry is reduced to a cubic symmetry, but this poses no real problem, since the original symmetry will be restored in the continuum limit.

To construct LQCD, one introduces a hyper-cubic lattice of size $N_\sigma^3 \times N_\tau$ and a lattice spacing a . N_σ and N_τ correspond to the number of points in spatial and temporal direction respectively. Volume and temperature are related to these values by

$$V = L^3 = (aN_\sigma)^3, \quad T = \frac{1}{\beta} = (aN_\tau)^{-1}. \quad (2.2)$$

In order to obtain continuum physics again one has to remove the discretization by taking the limit $a \rightarrow 0$ at constant V and T ($N_\mu \rightarrow \infty$). At the same time the momentum cutoff $\Lambda = \pi/a$ goes to infinity and renormalization is necessary to obtain finite physical quantities, see Sec. 2.7.3.

For LQCD calculations to be sensible, N_σ and a have to meet mainly two requirements:

- the spacing should be small in order to keep discretization effects small
- the physical lattice size should be large enough to ensure that, for instance, the particle one wants to study fits in the box (small finite-volume effects), and the momentum resolution $\frac{2\pi}{N_\sigma a} \leq |p_\mu| \leq \frac{\pi}{a}$ is suitable.

Since the particle mass is connected to the correlation length by $\xi = 1/m$ the lattice should therefore obey the following inequality

$$a \ll \xi \ll aN_\sigma \quad (\text{e.g., } m_\pi L \gg 1). \quad (2.3)$$

Here we have assumed – and we will further do so – natural units $\hbar = c = 1^1$, so that all quantities with nontrivial dimension have the dimension of some power of mass or inverse length. Thus we can rewrite S_{QCD}^E in Eq. (1.12) in terms of dimensionless lattice variables, denoted with a hat, by scaling x , m and ψ with a according to their canonical dimension.

$$\begin{aligned} x \rightarrow an = a(\mathbf{n}, n_4) = a(n_1, n_2, n_3, n_4) & \quad m \rightarrow \frac{1}{a}\hat{m}, \\ \psi_\alpha(x = na) \rightarrow \frac{1}{a^{3/2}}\hat{\psi}_\alpha(n) & \quad \int d^4x \rightarrow a^4 \sum_n \end{aligned} \quad (2.4)$$

$\partial_\mu \mathcal{O}(x)$ can be defined in various ways, e.g.,

$$\partial_\mu \mathcal{O}(x) \rightarrow \begin{cases} \Delta_\mu^f \mathcal{O}(n) := \frac{1}{a}(\mathcal{O}(n + \hat{\mu}) - \mathcal{O}(n)), & \text{forward derivative} \\ \Delta_\mu^b \mathcal{O}(n) := \frac{1}{a}(\mathcal{O}(n) - \mathcal{O}(n - \hat{\mu})), & \text{backward derivative} \\ \Delta_\mu^s \mathcal{O}(n) := \frac{1}{2a}(\mathcal{O}(n + \hat{\mu}) - \mathcal{O}(n - \hat{\mu})), & \text{symmetric derivative} \end{cases} \quad (2.5)$$

Here, $\hat{\mu}$ represents the unit vector in the direction indicated by μ . In what follows we will set $a = 1$, if it is not explicitly given. These different definitions show already the ambiguity in choosing a discretization. It is by far not unique and, in particular for the fermion action, we will see different discretizations with different kinds of lattice artifacts, which reproduce the correct continuum QCD in the naïve (continuum) limit $a \rightarrow 0$.

2.2 Gauge fields on the lattice

The insertion of, e.g., $\Delta_\mu^s \psi(n)$ in the QCD Lagrangian needs now link variables $U_\mu(x) \in SU(3)$. They are associated with the link connecting x to $x + a\hat{\mu}$, in order to keep the gauge invariance

¹197.33 MeV \doteq 1 fm⁻¹

of the quark bilinears. This is the analog to the covariant derivative in the continuum. They are defined in terms of the gauge fields $A_\mu = A_\mu^a T_a$ as

$$\begin{aligned} U_\mu(x = na) &= U(x, x + a\hat{\mu}) \equiv \mathcal{P} \exp \left\{ ig \int_x^{x+a\hat{\mu}} dz_\nu A_\nu(z) \right\} \simeq \exp \{ iga A_\mu(x + a\hat{\mu}/2) \} \\ &= 1 + iga A_\mu(x + a\hat{\mu}/2) + \mathcal{O}(a^2 g^2) \\ &\rightarrow U_\mu(n) = \bullet \xrightarrow{\mu} \bullet \mu(n) \end{aligned} \quad (2.6)$$

where \mathcal{P} denotes path-ordering. Note that the $U_\mu(n)$ are elements of the $SU(3)$ transformation group, i.e., under a local gauge transformation $G(n) \in SU(3)$ they transform according to

$$U_\mu(n) \rightarrow G(n) U_\mu(n) G^{-1}(n + \hat{\mu}) \quad (2.7)$$

and have the following useful properties

$$U_\mu(n) = U_{-\mu}^{-1}(n + \hat{\mu}) = U_{-\mu}^\dagger(n + \hat{\mu}) \quad (2.8)$$

$$U_\mu(n) = \mathbb{1} \quad \text{as } g \rightarrow 0. \quad (2.9)$$

Wilson's action for the gauge field [90, 92] is given by a sum over *plaquette variables* $U_{\mu\nu}(x)$

$$\begin{aligned} S_G &= \beta \sum_n \sum_{\mu < \nu} \left[1 - \frac{1}{3} \text{Re Tr } U_{\mu\nu}(n) \right] \\ &= \beta \sum_n \sum_{\mu < \nu} \left[1 - \frac{1}{3} \text{Re Tr } \boxed{\square}_{\mu\nu}(n) \right] \quad \beta = 2N_c/g^2 = 6/g^2 \end{aligned} \quad (2.10)$$

The plaquettes (1×1 Wilson loop) are composed of four link variables

$$U_{\mu\nu}(n) \equiv U_\mu(n) U_\nu(n + \hat{\mu}) U_{-\mu}(n + \hat{\mu} + \hat{\nu}) U_{-\nu}(n + \hat{\nu}) = \boxed{\square}, \quad (2.11)$$

such, that $\text{Tr } U_{\mu\nu}(n)$ is invariant under the gauge transformation Eq. (2.7). Using the Baker-Campbell-Hausdorff formula $e^A e^B = e^{A+B+1/2[A,B]+\dots}$ and the Taylor expansion of the gauge fields $A_\mu(x)$ around the center of the plaquette, $U_{\mu\nu}(n)$ becomes

$$U_{\mu\nu}(n) \rightarrow U_{\mu\nu}(x) = \exp \{ iga^2 (\partial_\mu A_\nu(x) - \partial_\nu A_\mu(x) + ig[A_\mu(x), A_\nu(x)]) + \mathcal{O}(a^4) \}, \quad (2.12)$$

so that in the naïve continuum limit of $a \rightarrow 0$ the Wilson action approaches the usual Yang-Mills gauge action

$$\begin{aligned} S_G &= a^4 \sum_{x, \mu < \nu} [\text{Tr } (F_{\mu\nu}(x) F_{\mu\nu}(x)) + \mathcal{O}(a^2)] + \mathcal{O}(g^2 a^2) \\ &\xrightarrow{a \rightarrow 0} \frac{1}{2} \int_V d^3x \int_0^{1/T} d\tau \text{Tr } (F_{\mu\nu}(x) F_{\mu\nu}(x)) + \mathcal{O}(g^2). \end{aligned} \quad (2.13)$$

Using suitable larger planar Wilson loops one can even better reproduce the continuum action up to $\mathcal{O}(a^4)$ in lowest order of g (tree-level 1×2 -Improvement). The problem that additional quantum effects induce $\mathcal{O}(a^4)$ and higher order corrections in lowest order perturbation theory can be overcome by using non-planar loops. For gauge theories LÜSCHER and WEISZ [93] developed such an improvement scheme following Symanzik's *improvement program* [94, 95] (see 2.3.3). By adding further gauge invariant terms they showed that it is in principle possible to reduce the cut-off effects to any order. But this comes along with a higher computational effort and does not improve the overall error of the complete action, which in case of Sheikholeslami-Wohlert-Fermions is of order $\mathcal{O}(a^2)$. So we have used the simple Wilson gauge action Eq. (2.10).

2.3 Matter fields on the lattice

The fermionic part of the action given in Eq. (1.13) can now be discretized in a straightforward way. The Grassmann fields ψ on the lattice obey periodic boundary conditions in spatial directions and according to Eq. (1.19) antiperiodic boundary conditions in temporal direction. The derivative in the continuum will be replaced by the symmetric finite difference scheme Δ_μ^s and gauge links are inserted to maintain the local gauge invariance. This ensures the correct transformation properties according to the gauge group $SU(3)$. The naïve action then reads

$$S_F = \sum_{n,m} \hat{\psi}(n) M_F(n, m) \hat{\psi}(m), \quad (2.14)$$

where the naïve fermion matrix M_F^N is defined as

$$M_F^N(n, m) = \hat{m} \delta_{n,m} + \frac{1}{2} \sum_{\mu} (\gamma_{\mu}) \left\{ U_{\mu}(n) \delta_{n+\hat{\mu},m} - U_{\mu}^{\dagger}(n - \hat{\mu}) \delta_{n-\hat{\mu},m} \right\}. \quad (2.15)$$

Using dimensionful quantities, the action Eq. (2.14) reproduces the correct continuum action for $a \rightarrow 0$, which then respects the global chiral $U(N_f) \times U(N_f)$ symmetry of QCD. In order to see this one has to expand the action in powers of the lattice spacing. For a gauge link we obtain

$$U_{\mu}(n) \rightarrow \mathbb{1} + i g a \left[A_{\mu}(n a) + \frac{1}{2} a \partial_{\mu} A_{\mu}(n a) + \frac{1}{6} a^2 \partial_{\mu}^2 A_{\mu}(n a) + \mathcal{O}(a^3) \right] + \mathcal{O}(a^2 g^2) \quad (2.16)$$

Plugging this expression into the lattice action in Eq. (2.14) with dimensionful variables

$$\begin{aligned} S_F &= a^4 \sum_n \left[\sum_{\mu} (\gamma_{\mu}^{\alpha\beta}) \bar{\psi}_{\alpha}(n a) \frac{1}{2a} \left\{ \psi_{\beta}((n + \hat{\mu})a) - \psi_{\beta}((n - \hat{\mu})a) \right. \right. \\ &\quad \left. \left. + i g a (A_{\mu}(n a) \psi_{\beta}((n + \hat{\mu})a) + A_{\mu}((n - \hat{\mu})a) \psi_{\beta}((n - \hat{\mu})a)) \right\} \right. \\ &\quad \left. + m \psi_{\alpha}(n a) \psi_{\beta}(n a) \delta^{\alpha\beta} \right] + \mathcal{O}(a^6) \end{aligned} \quad (2.17)$$

$$\xrightarrow{a \rightarrow 0} \int_V d^3 x \int_0^{1/T} d\tau \bar{\psi}^{\alpha}(x) (\mathcal{D}_{\mu;\alpha\beta} + m)_{\alpha\beta} \psi^{\beta}(x) \quad (2.18)$$

the continuum fermion action is reproduced up to order $\mathcal{O}(a^2)$.

2.3.1 Fermion doublers and Nielsen-Ninomiya theorem

Describing fermionic fields on the lattice by a translationally invariant, i.e., $M_F(x, y) = M_F(x - y)$, Hermitian and local² matrix and preserving chiral symmetry at the same time, one inevitably runs into the problem of *fermion doubling*. This was formulated in the *no-go theorem* by NIELSEN and NINOMIYA [96, 97]. This property can easily be seen by looking at the (naïve) quark propagator Δ_F , namely the inverse of the fermion matrix of the non-interacting theory. In momentum space it is given by

$$\Delta_F^N(\hat{p}) = (M_F^N(\hat{p}))^{-1} = \frac{-i \sum_{\mu} \gamma_{\mu} \sin \hat{p}_{\mu} + \hat{m}}{\sum_{\mu} \sin^2 \hat{p}_{\mu} + \hat{m}^2} \quad (2.19)$$

²couplings in the corresponding action need to decay at least exponentially with the distance in order to guarantee universality, i.e., to obtain the correct continuum limit. More precisely it requires the lattice Dirac operator $M_F(p)$ to satisfy the inequality, $\|M_F(x)\| < C e^{-d|x|}$, where $\|\cdot\|$ denotes a matrix norm for the kernel $M_F(x)$. C and d are some positive numbers.

The *dispersion relation* is then obtained from the pole of this propagator ($\hat{E} = -i\hat{p}_4$)

$$\sinh^2 \hat{E} = \sum_{i=1}^3 \sin^2 \hat{p}_i + \hat{m}^2 \quad (2.20)$$

with

$$\hat{p}_i = \frac{2\pi}{N_\sigma} n_i, \quad 0 \leq n_i < N_\sigma \quad (2.21)$$

Thus the propagator does not only have a pole at $\hat{\mathbf{p}} = (0, 0, 0)$, or $\hat{E}(0) = \hat{m}$, but also $2^d - 1$ further ones at every corner of the Brillouin Zone (BZ). In each dimension the number of fermions doubles, hence the name 'doublers'. Since locality is a mandatory property and because of the no-go theorem, all lattice actions have finally to be a compromise between breaking chiral symmetry and allowing doublers.

2.3.2 Wilson fermions

Constructing a lattice action one has the freedom to choose additional operators, which vanish in the continuum limit. Wilson used this property to avoid doublers in the continuum and introduced a new dimension 5-operator, namely $\frac{r}{2}\bar{\psi}D_\mu^2\psi = \frac{r}{2}\bar{\psi}\square\psi$,

$$\hat{\psi}(n)\square\hat{\psi}(n) = \hat{\psi}(n) \sum_{\mu} \left\{ U_{\mu}(n)\delta_{n+\hat{\mu},m} + U_{\mu}^{\dagger}(n-\hat{\mu})\delta_{n-\hat{\mu},m} - 2\delta_{n,m} \right\} \hat{\psi}(m) \quad (2.22)$$

with the Wilson parameter r ($0 < r \leq 1$)³. Actually r is usually set to 1 to benefit from numerical advantages. The new fermion matrix M_W then reads

$$M_W^{\alpha\beta}(n, m) = (\hat{m} + 4r)\delta_{n,m}\delta_{\alpha\beta} - \frac{1}{2} \sum_{\mu} \left[(r - \gamma_{\mu})_{\alpha\beta} U_{\mu}(n)\delta_{n+\hat{\mu},m} + (r + \gamma_{\mu})_{\alpha\beta} U_{\mu}^{\dagger}(n-\hat{\mu})\delta_{n-\hat{\mu},m} \right]. \quad (2.23)$$

With a redefinition of the dimensionless fermion fields $\sqrt{\hat{m} + 4r}\hat{\psi}(n) \rightarrow \hat{\psi}(n)$ the matrix reads

$$M_W^{\alpha\beta}(n, m) = \delta_{n,m}\delta_{\alpha\beta} - \kappa \sum_{\mu} \left[(\mathbb{1} - \gamma_{\mu})_{\alpha\beta} U_{\mu}(n)\delta_{n+\hat{\mu},m} + (\mathbb{1} + \gamma_{\mu})_{\alpha\beta} U_{\mu}^{\dagger}(n-\hat{\mu})\delta_{n-\hat{\mu},m} \right], \quad (2.24)$$

where we have introduced the dimensionless *hopping parameter* $\kappa = 1/(2\hat{m} + 8r)$. The consequence of Wilson's construction can again be demonstrated by looking at the new propagator analog to Eq. (2.19) in dimensionful quantities

$$\Delta_W(p) = (M_W(p))^{-1} = \frac{-i \sum_{\mu} \gamma_{\mu} \frac{1}{a} \sin p_{\mu} a + m(p)}{\sum_{\mu} \frac{1}{a^2} \sin^2 p_{\mu} a + m^2(p)} \quad (2.25)$$

with

$$m(p) = m + \frac{2r}{a} \sum_{\mu} \sin^2(p_{\mu} a/2). \quad (2.26)$$

From this we see that for any fixed p_{μ} the physical quark mass remains unchanged ($m(\mathbf{p}) = m$) in the continuum limit, while the doublers with p_{μ} near the corners of the BZ receive an infinitely heavy mass due to the additional $1/a$ -term. Hence, they decouple from the theory. However, this procedure exhibits also some unpleasant disadvantages: First, at finite a , the

³this constraint follows from reflection positivity

doublers still exist and may interact, secondly, discretization errors already start at $\mathcal{O}(a)$ instead at $\mathcal{O}(a^2)$ as for the former naïve action and thirdly chiral symmetry is explicitly broken, even for $m \rightarrow 0$. Nevertheless, in our simulation – at least below T_c – a is small enough, so that the doublers are sufficiently heavy and should not disturb the extraction of ground state masses. Note that via Symanzik improvement (see 2.3.3) one can eliminate the $\mathcal{O}(a)$ deviations from the continuum limit.

The *critical value* of the hopping parameter κ_c is defined as the limit in which the pion mass vanishes. Unlike for interacting quarks, the fermion mass for free quarks receives no additional mass renormalization ($m_q = m$) and $\kappa_c = 1/(8r)$. When interactions are switched on this value has to be determined numerically in advance (fine-tuning). In this case a quark mass can be defined as

$$\hat{m}_q = \frac{1}{2} \left(\frac{1}{\kappa} - \frac{1}{\kappa_c} \right). \quad (2.27)$$

This mass is sometimes also called the Vector Ward Identity (VWI) quark mass (see below), since the divergence of the vector current is proportional to the mass difference of quark flavors in the current, which looks similar to Eq. (2.27). Another way to define a quark mass m_q is to use the axial-vector current in combination with the pseudoscalar density. By transferring the axial current to its naïve local

$$j_{A,\mu}^a \rightarrow \frac{1}{a^3} \mathcal{J}_{A,\mu}^{a(loc)} = \frac{1}{a^3} \hat{\psi}(n) \gamma_\mu (T_a \gamma_5) \hat{\psi}(n) \quad (2.28)$$

or non-local lattice version

$$j_{A,\mu}^a \rightarrow \frac{1}{a^3} \mathcal{J}_{A,\mu}^a = \frac{1}{a^3} \frac{1}{2} \left\{ \left(\hat{\psi}(n+\mu) \gamma_\mu (T_a \gamma_5) U_\mu(n) \hat{\psi}(n) \right) + \left(\hat{\psi}(n) \gamma_\mu (T_a \gamma_5) U_\mu^\dagger(n) \hat{\psi}(n+\mu) \right) \right\} \quad (2.29)$$

its (former) conservation at $m_{u,d}=0$ in the flavor non-singlet case (Section 1.2) is no longer valid and $\mathcal{J}_{A,\mu}^a$ needs to be redefined. This can be done by using a *Ward-Takahashi identity*, which states, that variations of operators \mathcal{O} with respect to the symmetry transformation phase ϕ , Eq. (1.23), together with an action which obeys the same symmetry should vanish

$$\left\langle \mathcal{O} \frac{\delta S_W}{\delta \phi} \right\rangle - \left\langle \frac{\delta \mathcal{O}}{\delta \phi} \right\rangle = 0. \quad (2.30)$$

Inserting Eq. (2.29) in this identity with $\mathcal{O} = 1$ gives the *Axial Ward Identity* (AWI) [86, 98]

$$\langle \alpha | \Delta_\mu^b \mathcal{J}_{A,\mu}^a | \beta \rangle = \langle \alpha | \bar{\psi} \{ T_a, m \} \gamma_5 \psi + X^a | \beta \rangle \quad (2.31)$$

with the dimension 5-operator X^a

$$X^a = -\frac{r}{2} \sum_\mu \left[\bar{\psi}(n) T_a \gamma_5 U_\mu(n) \psi(n+\mu) + \bar{\psi}(n+\mu) T_a \gamma_5 U_\mu^\dagger(n) \psi(n+\mu) \right] + (n \rightarrow n-\mu) - 4\bar{\psi}(n) T_a \gamma_5 \psi(n). \quad (2.32)$$

Its vanishing in the continuum $\lim_{a \rightarrow 0} a^{-4} X^a$ is no longer guaranteed, because of mixing with the lower dimensional operators $\mathcal{J}_P^a = \bar{\psi} T_a \gamma_5 \psi$ (dimension 3) and $\Delta_\mu^b \mathcal{J}_{A,\mu}^a$ (dimension 4) and ultraviolet divergences in loops emerging beyond tree level. Explicitly X^a reads

$$X^a = \bar{X}^a - \bar{\psi} \{ T_a, m' \} \gamma_5 \psi - (Z_A - 1) \Delta_\mu^b \mathcal{J}_{A,\mu}^a \quad (2.33)$$

with a new mass parameter m' and renormalization constant Z_A . It might be the source of the anomalies in the continuum limit of the divergence of the singlet axial current Eq. (1.26).

However, in case of a flavor non-singlet, such anomalies are not present for $m_f=0$ and still \mathcal{J}_A^a is not conserved. Now, by definition, \bar{X}^a is decoupled from the lower dimensional operators, such that $\langle\alpha|\bar{X}^a|\beta\rangle \xrightarrow{a\rightarrow 0} 0$. Using Eq. (2.33) one obtains

$$\langle\alpha|\Delta_\mu^b(Z_A\mathcal{J}_{A,\mu}^a)|\beta\rangle = \langle\alpha|\bar{\psi}\{T_a, m_q\}\gamma_5\psi + \bar{X}^a|\beta\rangle. \quad (2.34)$$

Hence, the lattice axial current $Z_A\mathcal{J}_{A,\mu}^a$ is conserved for a vanishing quark mass $m_q=m-m'$ and $a\rightarrow 0$.

Using $\langle\alpha| = \langle 0|$ and $|\beta\rangle = |\mathcal{J}_P(0)\rangle$ and integrating over space leads to

$$\frac{m_q(\tau)}{Z_A} = \frac{\sum_{\mathbf{x}}\langle\Delta_\mu\mathcal{J}_{A,\mu}(x)\mathcal{J}_P^\dagger(0)\rangle}{2\sum_{\mathbf{x}}\langle\mathcal{J}_P(x)\mathcal{J}_P^\dagger(0)\rangle}. \quad (2.35)$$

This defines the so-called *AWI current quark mass*⁴. Instead of $\mathcal{J}_{A,\mu}$ one can also consider the local axial vector current in Eq. (2.28) and define a renormalization factor $Z_A^{(loc)}$, such that

$$Z_A\mathcal{J}_{A,\mu} = Z_A^{(loc)}\mathcal{J}_{A,\mu}^{(loc)} + \mathcal{O}(a^4). \quad (2.36)$$

A similar definition also holds for the vector current. All finite vector and axial-vector renormalization factors tend to 1 in the continuum limit. In the remaining part of this thesis we will implicitly use local currents and renormalization factors. Concerning our analysis, the fourth component of the axial current has the largest overlap with the pion state, i.e., it is the single contribution for $\mathbf{p}=\mathbf{0}$, so we only need to determine Eq. (2.35) for $\mu=4$. We further improved the signal by using a higher lattice derivative to $\mathcal{O}(a^4)$ as suggested in [99].

For non-vanishing m_q the chiral $SU(N_f)_A$ symmetry is broken explicitly, which leads to the Partially Conserved Axial Current (PCAC)-*hypothesis*, which states that the divergence of the axial current serves as interpolating field of the pseudoscalar density

$$\partial_\mu\mathcal{J}_{A,\mu}^a(n) = f_P m_P^2 \mathcal{J}_P^a(n), \quad (2.37)$$

where m_P is the mass of the pseudoscalar particle and f_P the pseudoscalar decay constant. In case of u and d quark this is the pion π with $f_\pi=93$ MeV. It is connected to the chiral condensate $\langle\bar{\psi}\psi\rangle$ via the Gell-Mann-Oaks-Renner (GMOR) relation [100]

$$m_\pi^2 f_\pi^2 = -2m_q \langle\bar{\psi}\psi\rangle. \quad (2.38)$$

With this relation the definition of Eq. (2.27) can be justified in the limit of broken chirality $\langle\bar{\psi}\psi\rangle \neq 0$ below T_c , while Eq. (2.35) remains also valid above T_c . One can parameterize the matrix element of $\mathcal{J}_{A,\mu}^a$ between the vacuum and an on-shell pion by writing

$$\langle 0|\mathcal{J}_{A,\mu}^a(n)|\mathcal{J}_\pi^b(p)\rangle = i\delta^{ab} f_\pi p^\mu e^{-ipn}. \quad (2.39)$$

Together with the AWI for $N_F=2$ in momentum space

$$\langle 0|\partial_\mu\mathcal{J}_{A,\mu}^a(0)|\mathcal{J}_\pi^b(p)\rangle = p^2 f_\pi \delta^{ab} = \langle 0|\bar{\psi}\{T_a, m_q\}\gamma_5\psi|\mathcal{J}_\pi^b(p)\rangle \quad (2.40)$$

with $\text{Tr}[\{T_a, m_q\}T_b] = \frac{1}{2}\delta^{ab}(m_u + m_d)$ and $\mathbf{p}=\mathbf{0}$ gives

$$m_\pi^2 = (m_u + m_d) \frac{M^2}{f_\pi} \propto m_q. \quad (2.41)$$

The mass parameter M has been estimated to be of order 400 MeV [101]. Thus $(m_u + m_d) \simeq 10$ MeV is enough to give the pion its observed mass of 140 MeV.

⁴sometimes also called PCAC quark mass

2.3.3 Wilson fermions with Symanzik improvement (Sheikholeslami-Wohlert action)

The problem with the leading cutoff effects has found a clean solution via SYMANZIK's improvement program. Its underlying idea is given in [13, 14] and has been applied originally to the ϕ^4 theory on the lattice. He used additional counter terms of dimension $d > 4$ to the pure Lagrangian and tuned their coefficients such that all contributions of order $\mathcal{O}(a^{d-4})$ could be eliminated. SHEIKHOESLAMI and WOHLERT [102] used this procedure to reduce the errors of the Wilson fermion action to $\mathcal{O}(a^2)$. Thereby they used correction terms of dimension 5, \mathcal{O}_i , i.e.,

$$\mathcal{L}_{\text{cont}} = \mathcal{L}_{\text{latt}} + a \sum_i c_i \mathcal{O}_i + \mathcal{O}(a^2). \quad (2.42)$$

Their number is finite, because they have to be invariant under the same symmetry as the original action (e.g., $U(1) \times SU(N_f)$) and can be further eliminated by applying a partial integration. By doing so one ends up with the following five terms

$$\mathcal{O}_1 = \bar{\psi} i \sigma_{\mu\nu} F_{\mu\nu} \psi \quad (2.43)$$

$$\mathcal{O}_2 = \bar{\psi} D_\mu D_\mu \psi \quad (2.44)$$

$$\mathcal{O}_3 = m \text{Tr} (F_{\mu\nu} F_{\mu\nu}) \quad (2.45)$$

$$\mathcal{O}_4 = m \bar{\psi} \gamma_\mu D_\mu \psi \quad (2.46)$$

$$\mathcal{O}_5 = m^2 \bar{\psi} \psi \quad (2.47)$$

These terms can be reduced further if one is interested only in on shell quantities. Then the equations of motion show that $\mathcal{O}_{2,4}$ are redundant. Finally the operators $\mathcal{O}_{3,5}$ already appear in the Wilson Lagrangian and the utilization of a mass independent renormalization scheme leads to an absorption of these terms by rescaling the bare mass and coupling. The $\mathcal{O}(a)$ -improved Sheikholeslami-Wohlert action S_F^{SW} then reads

$$S_F^{SW} = \sum_{n,m} \hat{\psi}(n) M_{SW}(n,m) \hat{\psi}(m) \quad (2.48)$$

with

$$M_{SW}(n,m) = A(n) \delta_{n,m} - \kappa \Delta_{n,m}. \quad (2.49)$$

It is divided in a diagonal and non-diagonal part, which are given by

$$\Delta_{n,m} = \frac{1}{2} \sum_{\mu} (\mathbb{1} - \gamma_\mu) U_\mu(n) \delta_{n+\mu,m} + (\mathbb{1} + \gamma_\mu) U_\mu^\dagger(n-\mu) \delta_{n-\mu,m} \quad (2.50)$$

and

$$A(n) = \mathbb{1} - igc_{SW} \frac{\kappa}{2} \sigma_{\mu\nu} F_{\mu\nu}(n) \quad (2.51)$$

where

$$F_{\mu\nu}(n) = \frac{1}{8ig} \sum_j \left(U_{\mu\nu}^j(n) - U_{\mu\nu}^{j\dagger}(n) \right). \quad (2.52)$$

These terms can be depicted as

$$S_F^{SW} = \sum_{n,m} \hat{\psi}(n) \left\{ \left[\mathbb{1} - \frac{\kappa c_{SW}}{2} \sum_{\mu,\nu} \text{Im} \begin{array}{|c|c|} \hline \square & \square \\ \hline \square & \square \\ \hline \end{array} (n) \sigma_{\mu\nu}(n) \right] \delta_{n,m} - \kappa \sum_{\mu} \left[(\mathbb{1} - \gamma_\mu) \delta_{n+\hat{\mu},m} \begin{array}{c} \bullet \\ \longrightarrow \\ \bullet \end{array} \mu(n) + (\mathbb{1} + \gamma_\mu) \delta_{n-\hat{\mu},m} \begin{array}{c} \bullet \\ \longleftarrow \\ \bullet \end{array} \mu(m) \right] \right\} \hat{\psi}(m). \quad (2.53)$$

The correction term is also called the *clover term* and it is obvious why this action often is referred to as *clover action*. For the tree level (tadpole) improvement c_{SW} can simply be set to one. A perturbative and non-perturbative evaluation of the coefficient $c_{SW}(g)$ has been performed by LÜSCHER ET AL. [103]. They required that the Ward-Identity of a controlled quantity, in this case the PCAC-Relation, should be satisfied up to $\mathcal{O}(a^2)$ corrections within the Schrödinger Functional formalism. The results for c_{SW} were found to be well fitted by

$$c_{SW} = \frac{1 - 0.656g^2 - 0.152g^4 - 0.054g^6}{1 - 0.922g^2} \quad \text{for } 0 \leq g \leq 1. \quad (2.54)$$

Calculating CFs of local fields as, e.g., given in Eq. (2.35) one has to improve additionally the operators in the same way as has been done for the action. This leads to improved currents

$$\mathcal{J}_{A,\mu}^I = \mathcal{J}_{A,\mu} + ac_A \tilde{\nabla}_\mu \mathcal{J}_P \quad (2.55)$$

$$\mathcal{J}_{V,\mu}^I = \mathcal{J}_{V,\mu} + ac_V \tilde{\nabla}_\nu T_{\mu\nu} \quad (2.56)$$

with $\tilde{\nabla}_\mu = \frac{1}{2}(\Delta_\mu^f + \Delta_\mu^b)$ and the tensor current $T_{\mu\nu} = \bar{\psi} \sigma_{\mu\nu} \psi$. The coefficient c_A has also been determined by the ALPHA-Collaboration non-perturbatively [103]

$$c_A = -0.00756g^2 \cdot \frac{1 - 0.748g^2}{1 - 0.977g^2} \quad \text{with } 0 \leq g \leq 1. \quad (2.57)$$

In case of $\mathcal{J}_{V,\mu}^I$ it could be shown [104] that c_V almost vanishes for $\beta \geq 6.4$. These new definitions can be used to improve the PCAC-Relation Eq. (2.35). All necessary currents have been measured. One major drawback of the SW improvement scheme is a bigger susceptibility to *exceptional configurations* (see Section 2.7.1) compared to the unimproved case. In quenched simulations on relatively coarse lattices and for moderately light quark flavors, gauge configurations can be sampled where the Wilson matrix has one or few real eigenvalues with norm exceptionally close to zero, i.e., much smaller than the other configurations. The corresponding eigenvectors of the operator are referred to as ‘spurious’ zero modes, because in a chirally invariant formulation, the Dirac matrix can have zero modes only if some quark flavor is massless.⁵ On gauge configurations with spurious quark zero modes, fermionic observables (quark propagator) in a chirally broken phase may undergo fluctuations that exceed typical ones by orders of magnitudes, see Fig. 2.1. Increasing the statistics does not reduce in general the standard deviation, even larger fluctuations may occur. Using the non-perturbatively improved action, it could be shown that this problem occurs at values of m of about half of the strange quark mass if $a \simeq 0.1$ fm [107]. With unimproved Wilson fermions this limit is pushed to somewhat lower quark masses.

One rather new approach, which could be very helpful to avoid exceptional configurations, especially also for low quark masses below and close to the phase transition is the *twisted mass* formulation. Here one writes the fermion action with a twisted mass μ -term proportional to $\gamma_5 \tau_3$ where τ_3 acts in flavor space and bounds the fermion spectrum from below. For large enough μ exceptional configurations are absent, Fig. 2.2. Additionally for $\kappa_c^{\text{extra}} \neq \kappa_c(\mu = 0)$ extrapolated from $\kappa_c(\mu)$ by PCAC masses to $\mu = 0$ (maximal twist), see e.g. [108, 109], the action is automatically $\mathcal{O}(a)$ improved [110]. The twisted mass theory has its own problems, though. The appearance of τ^3 in the twisted mass term means that the up- and down-type

⁵In unquenched simulations configurations with spurious or genuine zero-modes play almost no role, due to their vanishing or small fermion determinant, which determines their weight or probability respectively, see however [105].

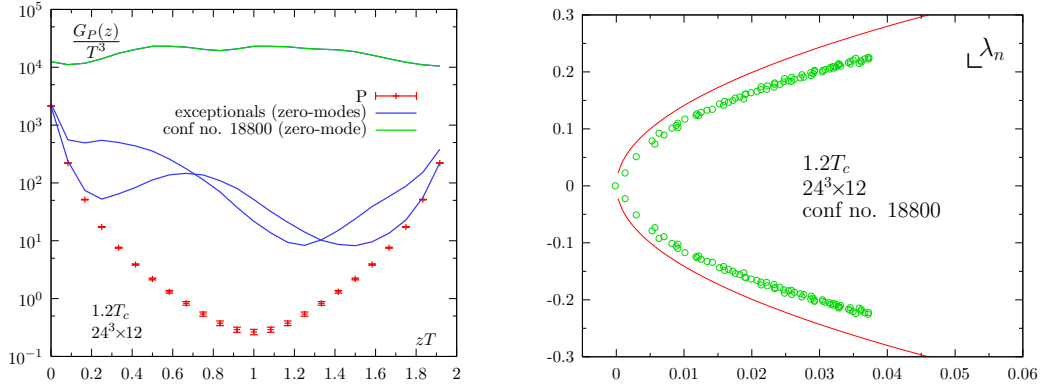


Fig. 2.1: Examples of exceptional configurations close to (above) T_c in the P CF (left) and the corresponding SW-Dirac eigenvalue spectrum with the apparent zero mode [106] (right). Configuration 18800 (green) is somewhat extreme, since the real part of its Polyakov loop is very small and one might speculate that it is still located in the chiral broken phase. For comparison also the zero-mass Ginsparg-Wilson circle, see Section 2.3.5, is shown (solid red curve).

quarks have opposite signs for the twisted mass term, and hence isospin is no longer conserved as long as $\mu \neq 0$. Whether and how this effects physical properties is an open question. Furthermore dynamical simulation show a first order phase transition and metastability characterized by a jump in the plaquette expectation value. This prevents a proper simulation close to the chiral limit. However, the metastability weakens using improved gauge actions.

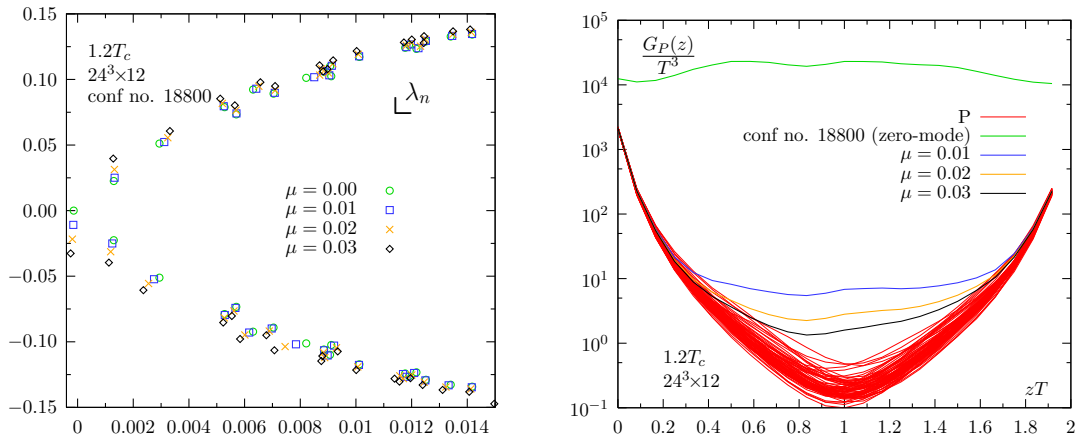


Fig. 2.2: Impact of the twisted mass term on the (exceptional) configuration number 18800 at $1.2 T_c$. We have chosen $\kappa_c(\mu = 0) = 0.13558$. The twisted mass term forbids the strip $\text{Im } \lambda_n \in [-\mu, \mu]$ to be filled with eigenvalues. Note the tiny different shifts of λ_n with increasing μ in real and imaginary direction, see [111]. They probably explain the necessity to use κ_c^{extra} for $\mathcal{O}(a)$ -improvement, see also [112]. The topological eigenvalue is shifted to negative imaginary direction. In case of a chiral perfect Ginsparg-Wilson operator this would imply $Q = +1$.

2.3.4 Staggered fermions

Another way to handle the fermion doublers is to introduce staggered fermions (or Kogut-Susskind fermions) [113, 114]. They are obtained by so-called *spin diagonalization* of the Dirac matrices, where a local change of fermionic variable

$$\psi(n) \rightarrow \Gamma(n)\psi(n), \quad \bar{\psi}(n) = \bar{\psi}(n)\Gamma^\dagger(n) \quad (2.58)$$

$$\Gamma^\dagger(n)\gamma_\mu\Gamma(n + \hat{\mu}) = \eta_\mu(n)\mathbb{1} = \Delta_\mu(n) \in U(1)^{\otimes d} \quad (2.59)$$

is performed. Here $\Gamma(n)$ is a $d \times d$ unitary matrix leading to the spin diagonalization and Δ_μ is a diagonal unitary matrix belonging to the direct product of $U(1)$ groups denoted by $U(1)^{\otimes d}$. One possible choice is $\Gamma(n) = \gamma_1^{n_1}\gamma_2^{n_2}\gamma_3^{n_3}\gamma_4^{n_4}$, which leads to the staggered phases $\eta_\mu(n) = (-1)^{n_1 + \dots + n_\mu - 1}$. The resulting fermion action is now diagonal in the Dirac components. The number of degenerate flavors can then be reduced by taking only one component of the new action into account. By doing this one can reduce the fermion multiplication factor 2^d to $2^d/4$. The 4 remaining degenerate fermion states for $d=4$ are interpreted as states of different fermion species (pseudo-flavors).

Due to a remnant chiral symmetry ($U(1)_{\text{even}} \times U(1)_{\text{odd}}$) for fermions on the even and odd sites⁶ of the lattice separately, staggered fermions are protected against additive mass renormalization and exceptional configurations (see 2.3.2 and 2.3.3), which are genuine problems for the Wilson operator. The discretization errors behave like $\mathcal{O}(a^2)$, instead of $\mathcal{O}(a)$ for pure Wilson-Fermions. However, a great disadvantage is that one always has to deal with exactly four flavors, conventionally called *tastes* in the continuum. At least for sea quarks in unquenched simulations one can overcome this problem by taking the fourth root of the staggered Dirac operator (*fourth-root trick*). This operation, however, is dangerous, since the locality of the resulting action is questionable, e.g., CREUTZ argued, that it is flawed for theories with an odd number of flavors [115]. For a current status report on the validity of this procedure see Ref. [116].

2.3.5 The Ginsparg-Wilson relation and the overlap operator

In 1982 GINSPARG and WILSON [117] were the first who found a way to circumvent the Nielsen-Ninomiya no-go theorem. They proposed to give up chiral symmetry in its conventional formulation Eq. (1.27)

$$\{M, \gamma_5\} = 0, \quad (2.60)$$

and to use an operator which fulfills a remnant chiral symmetry condition instead

$$M\gamma_5 + \gamma_5M = (a/\mu)M\gamma_5RM \quad \Rightarrow \quad M^{-1}\gamma_5 + \gamma_5M^{-1} = (a/\mu)\gamma_5R. \quad (2.61)$$

In this *Ginsparg-Wilson relation* (GWR), the continuum condition that the right hand side of Eq. (2.60) vanishes is now transferred to a term of $\mathcal{O}(a)$. $R(x, y)$ is a local operator, whose structure in Dirac space is constrained by $\{\gamma_5, R\} = 0$ and μ a mass parameter of order $\mathcal{O}(1)$. Since the GWR is a formulation of chiral symmetry after performing a Wilson *renormalization group transformation* (RGT) from the continuum to the lattice, it is supposed to have exact zero modes with positive and negative chirality. Following the continuum index theorem Eq. (1.32), any operator fulfilling the GWR can be used to determine the topological charge ν . The domain wall approach [118, 119] is one of the solutions of the GWR. An additional fifth dimension with the extent L_5 is introduced. It suppresses the chiral symmetry breaking exponentially with L_5 , so that the operator is chirally symmetric in the limit $L_5 \rightarrow \infty$.

⁶A site n is called even if $n_1 + n_2 + n_3 + n_4$ is even and it is called odd otherwise

The other solution of the GWR is the overlap operator

$$M_{ov} = \frac{\mu}{a} \left[1 + A/\sqrt{A^\dagger A} \right], \quad A = a\hat{M} - \mu \quad (2.62)$$

With the special choice $\hat{M} = M_W$ with zero bare mass and $r = 1$ this operator is called the *Neuberger overlap operator*. Then μ represents a negative Wilson fermion mass. M_{ov} also obeys γ_5 -Hermiticity. Note that the operator $A/\sqrt{A^\dagger A}$ is unitary, hence the spectrum of M_{ov} in the complex plane lies on a circle, with center and radius μ/a , which is the GW circle [120]. Most important is the exact chiral symmetry under the transformations

$$\begin{aligned} \psi &\rightarrow e^{i\theta T_a \gamma_5 (1 - \frac{a}{\mu} M_{ov})} \psi \\ \bar{\psi} &\rightarrow e^{i\theta T_a \gamma_5 (1 - \frac{a}{\mu} M_{ov})} \bar{\psi} \end{aligned} \quad (2.63)$$

The axial anomaly in this formulation comes again from a non-invariance of the fermion measure $D\bar{\psi}D\psi$ [121], similar to the continuum derivations. In this way Ginsparg-Wilson fermions also correctly reproduce the axial anomaly.

Although these realizations of chiral fermions seem to be very promising, they suffer from the increase in computer time.

2.3.6 Hypercube fermions

There is another natural way to proceed from the continuum formulation of the action to a lattice form. In this *blocking from continuum*, one defines the lattice fermion fields as block averages of the continuum ones integrated over hypercubes. The lattice action of these new lattice fermion fields is then connected to the continuum one by the Wilson RGT. The resulting lattice theory with so-called *perfect lattice fermions*, is equivalent to the underlying continuum theory with respect to long distance physics and is free of lattice artifacts. In the same manner one can also start from a given lattice formulation on a fine lattice and - by using the RGT - arrive at another lattice formulation at a coarser lattice which is physically equivalent. Iterating this procedure infinitely many times we arrive at the fixed point action (FPA), where we assume that this limit exists. The FPA of the quantum renormalization group trajectory represents perfect lattice fermions since it is insensitive to a change of the lattice spacing.

In general, a FPA may have an infinite number of local terms in the action. For practical cases, one usually introduces a scheme for truncating the action after some time. The hypercube Dirac operator is a free FPA with its couplings being truncated to the unit hypercube. In this subsection we consider the construction of the hypercube Dirac operator. The discussion will closely follow Refs. [122, 123]. We start from the case of free fermions and explain how gauge fields can be introduced.

Let us divide the (infinite) lattice into disjoint hypercubic blocks of n^d sites each and introduce new variables living at the centers of these blocks (block factor n RGT). Then the RGT relates

$$\psi'_{x'} \sim \sum_{x \in x'} \psi_x, \quad (2.64)$$

where ψ represents the fermions on the fine lattice and the ψ' represents fermions on the coarser lattice. The points $x \in \mathbb{Z}^d$ are the sites of the original fine lattice and x' are those of the new lattice with spacing n . $x \in x'$ means that the site x belongs to the block with center x' .

Now the original action $S[\bar{\psi}, \psi]$ transforms into a new action $S'[\bar{\psi}', \psi']$ on the coarse lattice. The latter is determined by the functional integral

$$e^{-S'[\bar{\psi}', \psi']} = \int D\bar{\psi} D\psi K[\bar{\psi}', \psi', \bar{\psi}, \psi] e^{-S[\bar{\psi}, \psi]} . \quad (2.65)$$

The kernel $K[\bar{\psi}', \psi', \bar{\psi}, \psi]$ has to be chosen such that the partition function and all expectation values remain invariant under the RGT. At the end, one usually rescales the lattice spacing back to 1. The correlation length in lattice units gets divided by n .

For the kernel functional there are many possible choices [124, 125]. We will use the Gaussian type kernel

$$K[\bar{\psi}', \psi', \bar{\psi}, \psi] = \exp \left\{ -\frac{1}{\alpha_{HF}} \sum_{x'} \left[\bar{\psi}'_{x'} - \frac{1}{n^{(d+1)/2}} \sum_{x \in x'} \bar{\psi}_x \right] \left[\psi'_{x'} - \frac{1}{n^{(d+1)/2}} \sum_{x \in x'} \psi_x \right] \right\} . \quad (2.66)$$

This type of transformation with non-vanishing $\alpha_{HF} > 0$ is not chirally invariant, which will lead to the formulation with broken chiral symmetry in its standard form given by $\{D, \gamma_5\} = 0$. Assume that we are on a 'critical surface', where the correlation length is infinite. After an infinite number of RGT iterations we obtain a finite FPA $S^*[\bar{\psi}, \psi]$. The critical surface needs a fermion mass $m=0$ in order to obtain a divergent correlation length, but one can generalize the consideration to a finite mass.

Assume that we want to perform a number N of RGT iterations. If we start from a small mass $m/(nN)$, then the final mass will be m . In the limit $nN \rightarrow \infty$, i.e. we start from an infinitesimal mass, we obtain a perfect action at finite mass. In this context, 'perfect' means that dimensionless quantities do not depend on the lattice spacing, hence they are identical to the continuum values.

For the block transformation in Eqs. (2.65) and (2.66), this perfect action can be computed analytically in momentum space [126]. The computation simplifies if we let $n \rightarrow \infty$, so that $N=1$ is sufficient. Hence starting from the continuum action (with no momentum cut-off), we integrate out all momenta above π/a to get the perfect action

$$\begin{aligned} S^*[\bar{\psi}, \psi] &= \frac{1}{(2\pi)^d} \int_{-\pi}^{\pi} d^d p \bar{\psi}(-p) \Delta^*(p)^{-1} \psi(p) , \\ \Delta^*(p) &= \sum_{l \in \mathbb{Z}^d} \frac{\Pi(p + 2\pi l)^2}{i(p_\mu + 2\pi l_\mu) \gamma_\mu + m} + \alpha_{HF} , \\ \Pi(p) &= \prod_{\mu=1}^d \frac{2 \sin(p_\mu/2)}{p_\mu} , \end{aligned} \quad (2.67)$$

where Δ^* is the free perfect propagator. The same perfect action is obtained starting from a variety of lattice actions [127], in particular from the Wilson fermion action. In coordinate space the action can be written as

$$S^*[\bar{\psi}, \psi] = \sum_{x,r} \bar{\psi}_x [\rho_\mu(r) \gamma_\mu + \lambda(r)] \psi_{x+r} . \quad (2.68)$$

At the cost of broken chiral symmetry we obtain a theory with its couplings ρ_μ and λ decaying exponentially as $|r|$ increases. An exception is the case $d=1$, where they are confined to one lattice spacing for the special choice

$$\alpha_{HF} = \frac{e^m - m - 1}{m^2} . \quad (2.69)$$

This is still in agreement with the Nielsen-Ninomiya theorem (Section 2.3.1): to obtain a local perfect action, one must break chiral symmetry explicitly. Although the chiral symmetry is not manifest in the perfect action, all chiral properties are still correctly reproduced by it. This is due to the GWR, introduced before in (2.61), which the perfect action obeys,

$$\{\Delta^*(p), \gamma_5\} = 2\alpha_{HF}\gamma_5 . \quad (2.70)$$

Here we can identify α_{HF} with the mass parameter μ , namely,

$$\alpha_{HF} = \frac{1}{2\mu} . \quad (2.71)$$

It turns out that for the choice of α in Eq. (2.69) the locality is also excellent in higher dimensions, i.e., the exponential decay of the couplings is very fast. This is important, because for practical purposes the couplings have to be truncated to a short range, and the truncation should not distort the perfect properties too much. Ref. [128] proposed a truncation scheme that uses periodic boundary conditions over 3 lattice spacings and thus confines the couplings to a unit hypercube

$$\begin{aligned} \rho_\mu(x-y) &= \rho_1(\delta_{y,x+\hat{\mu}} - \delta_{y,x-\hat{\mu}}) + \sum_{\hat{\nu} \neq \hat{\mu}} \rho_2(\delta_{y,x+\hat{\mu}+\hat{\nu}} - \delta_{y,x-\hat{\mu}+\hat{\nu}}) \\ &\quad + \sum_{\substack{\hat{\nu} \neq \hat{\mu} \\ \hat{\rho} \neq \hat{\mu}, \hat{\nu}}} \rho_3(\delta_{y,x+\hat{\mu}+\hat{\nu}+\hat{\rho}} - \delta_{y,x-\hat{\mu}+\hat{\nu}+\hat{\rho}}) \\ &\quad + \sum_{\substack{\hat{\nu} \neq \hat{\mu} \\ \hat{\rho} \neq \hat{\nu}, \hat{\sigma} \neq \hat{\rho}}} \rho_4(\delta_{y,x+\hat{\mu}+\hat{\nu}+\hat{\rho}+\hat{\sigma}} - \delta_{y,x-\hat{\mu}+\hat{\nu}+\hat{\rho}+\hat{\sigma}}) , \\ \lambda(x-y) &= \lambda_0\delta_{y,x} + \sum_{\mu} \lambda_1(\delta_{y,x+\hat{\mu}} + \delta_{y,x-\hat{\mu}}) + \sum_{\hat{\nu} \neq \hat{\mu}} \lambda_2(\delta_{y,x+\hat{\mu}+\hat{\nu}} + \delta_{y,x-\hat{\mu}+\hat{\nu}}) \\ &\quad + \sum_{\substack{\hat{\nu} \neq \hat{\mu} \\ \hat{\rho} \neq \hat{\mu}, \hat{\nu}}} \lambda_3(\delta_{y,x+\hat{\mu}+\hat{\nu}+\hat{\rho}} + \delta_{y,x-\hat{\mu}+\hat{\nu}+\hat{\rho}}) \\ &\quad + \sum_{\substack{\hat{\nu} \neq \hat{\mu} \\ \hat{\rho} \neq \hat{\nu}, \hat{\sigma} \neq \hat{\rho}}} \lambda_4(\delta_{y,x+\hat{\mu}+\hat{\nu}+\hat{\rho}+\hat{\sigma}} + \delta_{y,x-\hat{\mu}+\hat{\nu}+\hat{\rho}+\hat{\sigma}}) . \end{aligned} \quad (2.72)$$

The couplings λ_i and ρ_i are tabulated in Tab. 2.1.

It was pointed out that the spectral and thermodynamic properties of the HF are still drastically improved compared to Wilson fermions [128], see Section 3.2.

It is far more difficult to construct an approximately perfect action for a complicated interacting theory like QCD. However, it was proposed in Refs. [122, 128, 129] that one can just use this simple ansatz for HF together with the standard gauge link variables. Apart from nearest neighbors, one also has couplings over 2, 3 and 4-space diagonals in the unit hypercube. One connects all these coupled sites by all possible *shortest* lattice paths, by multiplying the compact gauge fields on the path links. This procedure was called *minimal gauging* or *gauging the HF by hand*. Note that one can connect the diagonal points of the d -dimensional hypercube via $d!$ such shortest lattice paths. One averages over all of them to construct the hyper-link, see Fig. 2.3. We identify the hyper-link between site x and $x + \hat{\mu}$ with $U_\mu^{(1)}(x)$ and the hyper-link in plane, cube and hyper-cube as $U_{\mu+\nu}^{(2)}(x)$, $U_{\mu+\nu+\rho}^{(3)}(x)$, and $U_{\mu+\nu+\rho+\sigma}^{(4)}(x)$,

respectively. Then we can write the corresponding fermion matrix in terms of the hyper-links which are constructed recursively starting from the gauge links $U_\mu^{(1)}$ ($\mu_1 \neq \mu_2 \neq \dots \neq \mu_d$),

$$\begin{aligned}
U_{\mu_1+\mu_2+\dots+\mu_d}^{(d)}(x) = & \frac{1}{d} \left[U_{\mu_1}^{(1)}(x) U_{\mu_2+\mu_3+\dots+\mu_d}^{(d-1)}(x + \hat{\mu}_1) \right. \\
& + U_{\mu_2}^{(1)}(x) U_{\mu_1+\mu_3+\dots+\mu_d}^{(d-1)}(x + \hat{\mu}_2) \\
& + \dots \\
& \left. + U_{\mu_d}^{(1)}(x) U_{\mu_1+\mu_2+\dots+\mu_{d-1}}^{(d-1)}(x + \hat{\mu}_d) \right]. \quad (2.73)
\end{aligned}$$

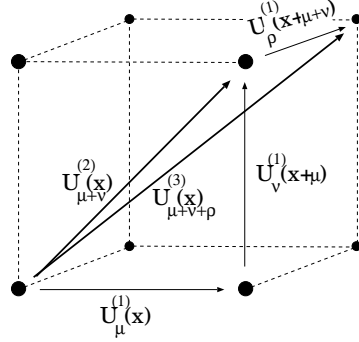


Fig. 2.3: 1-space, 2-space and 3-space hyper-links from Ref. [122].

It is convenient to introduce prefactors which are functions of the HF hopping parameters κ_i and λ_i , $i=1, \dots, 4$, and sums of γ -matrices

$$\begin{aligned}
\Gamma_{\pm\mu} &= \lambda_1 + \rho_1(\pm\gamma_\mu) \\
\Gamma_{\pm\mu\pm\nu} &= \lambda_2 + \rho_2(\pm\gamma_\mu \pm \gamma_\nu) \\
\Gamma_{\pm\mu\pm\nu\pm\rho} &= \lambda_3 + \rho_3(\pm\gamma_\mu \pm \gamma_\nu \pm \gamma_\rho) \\
\Gamma_{\pm\mu\pm\nu\pm\rho\pm\sigma} &= \lambda_4 + \rho_4(\pm\gamma_\mu \pm \gamma_\nu \pm \gamma_\rho \pm \gamma_\sigma). \quad (2.74)
\end{aligned}$$

The hypercube operator is organized in sums which run over four different directions for two 1-space links, six directions for four 2-space links, four directions for eight 3-space links, and one direction for the sixteen 4-space links. Altogether 80 hyper-links plus the term δ_{xy} contribute. With each path of the free HF, a γ -matrix is associated. The γ -matrices are

action	FP			W	Naive
mass	0.0	1.0	2.0	m	m
λ_0	1.852720547	1.26885069540	0.8442376349	m+4r	m
λ_1	-0.060757866	-0.03008271460	-0.0119736477	-r/2	0.0
λ_2	-0.030036032	-0.01082956270	-0.0032647950	0.0	0.0
λ_3	-0.015967620	-0.00471575763	-0.0011445684	0.0	0.0
λ_4	-0.008426812	-0.00221240767	-0.0004622883	0.0	0.0
ρ_1	0.136846794	0.05457967484	0.0185415007	0.5	0.5
ρ_2	0.032077284	0.01101007028	0.0031625467	0.0	0.0
ρ_3	0.011058131	0.00325481234	0.0007898101	0.0	0.0
ρ_4	0.004748991	0.00120632489	0.0002501304	0.0	0.0

Tab. 2.1: The coefficients for the fixed point action are taken from [128, 129].

chosen such that they add up to produce a prefactor Γ , see Eq. (2.74), which is associated with a given hyper-link.

The feature Eq. (2.8) also holds for the hyper-links, e.g.,

$$U_{\mu_1+\mu_2+\dots+\mu_d}^{\dagger(d)}(x) = U_{-\mu_1-\mu_2-\dots-\mu_d}^{(d)}(x + \hat{\mu}_1 + \hat{\mu}_2 + \dots + \hat{\mu}_d). \quad (2.75)$$

Therefore, only one half of the $3^d - 1$ hyper-links has to be computed and stored in the implementation of the HF.

The HF matrix can now be written as [122]

$$\begin{aligned} M_{HF}(x, y) &= \lambda_0 \delta_{x,y} \\ &+ \sum_{\mu} \left[\Gamma_{+\mu} U_{\mu}^{(1)}(x) \delta_{x,y-\hat{\mu}} + \Gamma_{-\mu} U_{-\mu}^{(1)}(x) \delta_{x,y+\hat{\mu}} \right] \\ &+ \sum_{\mu} \sum_{\nu > \mu} \left[\Gamma_{+\mu+\nu} U_{+\mu+\nu}^{(2)}(x) \delta_{x,y-\hat{\mu}-\hat{\nu}} + \Gamma_{+\mu-\nu} U_{+\mu-\nu}^{(2)}(x) \delta_{x,y-\hat{\mu}+\hat{\nu}} \right. \\ &+ \Gamma_{-\mu+\nu} U_{-\mu+\nu}^{(2)}(x) \delta_{x,y+\hat{\mu}-\hat{\nu}} + \left. \Gamma_{-\mu-\nu} U_{-\mu-\nu}^{(2)}(x) \delta_{x,y+\hat{\mu}+\hat{\nu}} \right] \\ &+ \sum_{\mu} \sum_{\nu > \mu} \sum_{\rho > \nu} \left[\Gamma_{+\mu+\nu+\rho} U_{+\mu+\nu+\rho}^{(3)}(x) \delta_{x,y-\hat{\mu}-\hat{\nu}-\hat{\rho}} + \Gamma_{+\mu+\nu-\rho} U_{+\mu+\nu-\rho}^{(3)}(x) \delta_{x,y-\hat{\mu}-\hat{\nu}+\hat{\rho}} \right. \\ &+ \Gamma_{+\mu-\nu+\rho} U_{+\mu-\nu+\rho}^{(3)}(x) \delta_{x,y-\hat{\mu}+\hat{\nu}+\hat{\rho}} + \Gamma_{+\mu-\nu-\rho} U_{+\mu-\nu-\rho}^{(3)}(x) \delta_{x,y-\hat{\mu}+\hat{\nu}-\hat{\rho}} \\ &+ \Gamma_{-\mu+\nu+\rho} U_{-\mu+\nu+\rho}^{(3)}(x) \delta_{x,y+\hat{\mu}-\hat{\nu}-\hat{\rho}} + \Gamma_{-\mu+\nu-\rho} U_{-\mu+\nu-\rho}^{(3)}(x) \delta_{x,y+\hat{\mu}-\hat{\nu}+\hat{\rho}} \\ &+ \left. \Gamma_{-\mu-\nu+\rho} U_{-\mu-\nu+\rho}^{(3)}(x) \delta_{x,y+\hat{\mu}+\hat{\nu}-\hat{\rho}} + \Gamma_{-\mu-\nu-\rho} U_{-\mu-\nu-\rho}^{(3)}(x) \delta_{x,y+\hat{\mu}+\hat{\nu}+\hat{\rho}} \right] \\ &+ \sum_{\mu} \sum_{\nu > \mu} \sum_{\rho > \nu} \sum_{\sigma > \rho} \left[\Gamma_{+\mu+\nu+\rho+\sigma} U_{+\mu+\nu+\rho+\sigma}^{(4)}(x) \delta_{x,y-\hat{\mu}-\hat{\nu}-\hat{\rho}-\hat{\sigma}} + \Gamma_{+\mu+\nu+\rho-\sigma} U_{+\mu+\nu+\rho-\sigma}^{(4)}(x) \delta_{x,y-\hat{\mu}-\hat{\nu}-\hat{\rho}+\hat{\sigma}} \right. \\ &+ \Gamma_{+\mu+\nu-\rho+\sigma} U_{+\mu+\nu-\rho+\sigma}^{(4)}(x) \delta_{x,y-\hat{\mu}-\hat{\nu}+\hat{\rho}-\hat{\sigma}} + \Gamma_{+\mu+\nu-\rho-\sigma} U_{+\mu+\nu-\rho-\sigma}^{(4)}(x) \delta_{x,y-\hat{\mu}-\hat{\nu}+\hat{\rho}+\hat{\sigma}} \\ &+ \Gamma_{+\mu-\nu+\rho+\sigma} U_{+\mu-\nu+\rho+\sigma}^{(4)}(x) \delta_{x,y-\hat{\mu}+\hat{\nu}-\hat{\rho}-\hat{\sigma}} + \Gamma_{+\mu-\nu+\rho-\sigma} U_{+\mu-\nu+\rho-\sigma}^{(4)}(x) \delta_{x,y-\hat{\mu}+\hat{\nu}-\hat{\rho}+\hat{\sigma}} \\ &+ \Gamma_{+\mu-\nu-\rho+\sigma} U_{+\mu-\nu-\rho+\sigma}^{(4)}(x) \delta_{x,y-\hat{\mu}+\hat{\nu}+\hat{\rho}-\hat{\sigma}} + \Gamma_{+\mu-\nu-\rho-\sigma} U_{+\mu-\nu-\rho-\sigma}^{(4)}(x) \delta_{x,y-\hat{\mu}+\hat{\nu}+\hat{\rho}+\hat{\sigma}} \\ &+ \Gamma_{-\mu+\nu+\rho+\sigma} U_{-\mu+\nu+\rho+\sigma}^{(4)}(x) \delta_{x,y+\hat{\mu}-\hat{\nu}-\hat{\rho}-\hat{\sigma}} + \Gamma_{-\mu+\nu+\rho-\sigma} U_{-\mu+\nu+\rho-\sigma}^{(4)}(x) \delta_{x,y+\hat{\mu}-\hat{\nu}-\hat{\rho}+\hat{\sigma}} \\ &+ \Gamma_{-\mu+\nu-\rho+\sigma} U_{-\mu+\nu-\rho+\sigma}^{(4)}(x) \delta_{x,y+\hat{\mu}-\hat{\nu}+\hat{\rho}-\hat{\sigma}} + \Gamma_{-\mu+\nu-\rho-\sigma} U_{-\mu+\nu-\rho-\sigma}^{(4)}(x) \delta_{x,y+\hat{\mu}-\hat{\nu}+\hat{\rho}+\hat{\sigma}} \\ &+ \Gamma_{-\mu-\nu+\rho+\sigma} U_{-\mu-\nu+\rho+\sigma}^{(4)}(x) \delta_{x,y+\hat{\mu}+\hat{\nu}-\hat{\rho}-\hat{\sigma}} + \Gamma_{-\mu-\nu+\rho-\sigma} U_{-\mu-\nu+\rho-\sigma}^{(4)}(x) \delta_{x,y+\hat{\mu}+\hat{\nu}-\hat{\rho}+\hat{\sigma}} \\ &+ \left. \Gamma_{-\mu-\nu-\rho+\sigma} U_{-\mu-\nu-\rho+\sigma}^{(4)}(x) \delta_{x,y+\hat{\mu}+\hat{\nu}+\hat{\rho}-\hat{\sigma}} + \Gamma_{-\mu-\nu-\rho-\sigma} U_{-\mu-\nu-\rho-\sigma}^{(4)}(x) \delta_{x,y+\hat{\mu}+\hat{\nu}+\hat{\rho}+\hat{\sigma}} \right]. \quad (2.76) \end{aligned}$$

Like Wilson fermions the HF matrix exhibits the ' γ_5 -Hermiticity', $\gamma_5 M_{HF} \gamma_5 = M_{HF}^{\dagger}$ ⁷, i.e. M_{HF} is indeed non-Hermitian but its eigenvalues come in complex-conjugate pairs.

⁷for Wilson fermions see Eq. (2.102)

2.4 Simulation techniques

In this section, the numerical methods which have been used to obtain our results are described. First, a basic approximation, the so-called *quenched* or *valence quark approximation* [130, 131] is discussed, leading to a path integral measure which solely depends on gluonic degrees of freedom. Next the algorithm for generating the gauge configurations and computing the quark propagator are explained. For a more detailed discussion see [132, 133]

2.4.1 Quenched approximation

Let us consider the expectation value of the following (general) operator

$$\mathcal{O} = \psi_{A_1} \bar{\psi}_{B_1} \psi_{A_2} \bar{\psi}_{B_2} \dots \psi_{A_n} \bar{\psi}_{B_n} F[U], \quad (2.77)$$

where each of the indices $A_1, \dots, A_n, B_1, \dots, B_n$ represents a set of color, flavor and Dirac indices together with the lattice point positions, and $F(U)$ is an arbitrary function of link variables U . The expectation value is then written as

$$\langle \mathcal{O} \rangle = \frac{\int DU D\bar{\psi} D\psi e^{-S} \mathcal{O}}{\int DU D\bar{\psi} D\psi e^{-S}} \quad (2.78)$$

where DU , $D\bar{\psi}$ and $D\psi$ are defined by

$$DU = \prod_{\mu, n} dU_{\mu}(n), \quad D\bar{\psi} = \prod_n d\bar{\psi}(n), \quad D\psi = \prod_n d\psi(n). \quad (2.79)$$

and $S = S_G + S_F$ is the total action. S_G being the purely gluonic part of the action and fermion fields appear in S_F . For all the actions considered in the previous sections, S_F is bilinear in the fermionic fields:

$$S_F(U, \psi, \bar{\psi}) = \sum_{A_1, B_1} \bar{\psi}_{B_1} M(U)_{B_1, A_1} \psi_{A_1}. \quad (2.80)$$

After the integral over the fermionic Grassmann variables is performed, the expectation value contains two point functions $\langle \bar{\psi}_A \psi_B \rangle = M(U)_{BA}^{-1}$ (*Wick's theorem*), and can be written in the following form with the effective action $S_{eff}(U) \equiv S_G(U) - \log \det M(U) = S_G(U) - \text{Tr} \log M(U)$

$$\begin{aligned} \langle \mathcal{O} \rangle &= Z^{-1} \int DU e^{-S_{eff}(U)} F(U) \sum_{C_1 \dots C_n} \epsilon_{B_1 \dots B_n}^{C_1 \dots C_n} M(U)_{C_1 A_1}^{-1} \dots M(U)_{C_n A_n}^{-1} \\ &= Z^{-1} \int DU e^{-S_G(U)} \det(M(U)) F(U) \sum_{C_1 \dots C_n} \epsilon_{B_1 \dots B_n}^{C_1 \dots C_n} M(U)_{C_1 A_1}^{-1} \dots M(U)_{C_n A_n}^{-1} \end{aligned} \quad (2.81)$$

where the generalized Levi-Civita symbol $\epsilon_{B_1 \dots B_n}^{C_1 \dots C_n}$ is defined by

$$\epsilon_{B_1 \dots B_n}^{C_1 \dots C_n} = \begin{vmatrix} \delta_{B_1}^{C_1} & \dots & \delta_{B_1}^{C_n} \\ \vdots & \ddots & \vdots \\ \delta_{B_n}^{C_1} & \dots & \delta_{B_n}^{C_n} \end{vmatrix} \quad (2.82)$$

and the partition function Z is

$$Z \equiv \int DU e^{-S_{eff}(U)} = \int DU e^{-S_G(U)} \det M(U). \quad (2.83)$$

An enormous gain in the computing time can be obtained by setting $\det(M(U)) = 1$ in the expressions above. This approximation, quite common in LGT calculations, is known as the quenched approximation. Physically, this amounts to ignoring all internal fermion loops in the calculation: fermion fields can appear only as external ('valence') fields. Experiences in zero temperature calculations tell us that this approximation works very well for a qualitative understanding of most features of QCD like confinement, asymptotic freedom, spontaneous chiral symmetry breaking etc, since most of the interesting dynamics is caused by the gluon fields. Even quantitatively, it has been found that the quenched approximation works to $\sim 10\%$ accuracy for spectrum and decay constant calculations [134, 135]. It is important to keep in mind, however, that it is just an approximation: there is no effective field theory description of the quenched theory. For a numerically accurate calculation of QCD observables, one has to go beyond the quenched approximation (for a recent summary of results for QCD observables from the lattice, and comparison with quenched results, see Ref. [136]). Also, qualitative questions where fermionic loops play an important role clearly cannot be studied by using the quenched approximation, for example, the 'breaking' of the QCD string.

Similarly, in finite temperature calculations for studying some questions, in particular issues in the low temperature phase where the thermal excitations of the pion gas play an important role, the quenched approximation is clearly inadequate. Also the nature of the transition is different as has been illustrated in Section 1.3.1. However, for investigating qualitative issues related to the deconfined phase, in particular the question of strong and/or non-perturbative interactions above T_c and viscosity of the plasma, that are important for understanding many puzzling features of the RHIC results, it is the gluonic degrees of freedom that are expected to play the major role. Since our main interest in this work will be to answer such questions, we will restrict ourselves to the quenched approximation.

2.4.2 Markov chains and Metropolis

Although a large number of degrees of freedom are eliminated, the path integral Eq. (2.81) is still high dimensional and usual numerical integration methods are not applicable. Instead, one has to turn to a *Monte-Carlo integration*. The aim is to find a representative sequence of field configurations $\{\Omega_i\}$ on which the observable \mathcal{O} is evaluated,

$$\langle \mathcal{O}(\Omega) \rangle_{\Omega} \simeq \frac{1}{Z} \sum_i e^{-S_G(\Omega_i)} \mathcal{O}(\Omega_i). \quad (2.84)$$

Since the number of possible gauge field configurations is large, but the weight factor $e^{-S_G(\Omega_i)}$ is very tiny for almost all Ω_i , a simple selection by just randomly picking gauge fields out of a uniform distribution would only lead to a small contribution, i.e., to a slow convergence

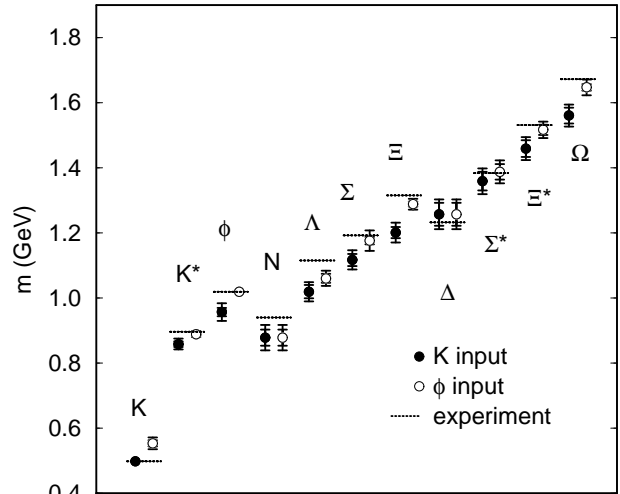


Fig. 2.4: Quenched light hadron spectrum compared to the experimental values. The statistical error and the sum of systematic and statistical errors are indicated. [134]

of Eq. (2.84). What is required therefore is *importance sampling*, which means to generate sequences of equilibrium gauge configurations with a probability distribution $P(\Omega)$ equal to their weight factor in Eq. (2.84), thus

$$P(\Omega) = \frac{1}{Z} \exp(-S_G(\Omega)). \quad (2.85)$$

One way to generate such configurations is via a Markov process. The idea is to select a new configuration Ω' by a transition probability $P_T(\Omega, \Omega')$, which depends solely on the new and the previous configuration (Ω). This update is then repeated (chain), so that after some time of thermalization the equilibrium distribution, Eq. (2.85), of $\{\Omega_i\}$ is reached. For $P_T(\Omega, \Omega')$ to be a Markov chain, it has to possess two important properties. First, every configuration should in principle be reachable in a finite number of steps N (irreducibility), which ensures the so-called *strong ergodicity*

$$P_T^N(\Omega, \Omega') > 0 \quad \forall \Omega, \Omega' \quad (2.86)$$

Secondly the transition probability must map the distribution $P(\Omega)$ on itself

$$P(\Omega') = \int d\Omega P(\Omega) P_T(\Omega, \Omega') \quad \forall \Omega'. \quad (2.87)$$

This guarantees that the appropriate distribution is realized irrespective of the starting configuration. A sufficient (but not necessary) condition for Eq. (2.87) to hold is *detailed balance*,

$$P(\Omega') P_T(\Omega', \Omega) = P(\Omega) P_T(\Omega, \Omega') \quad \forall \Omega. \quad (2.88)$$

It can be shown, see e.g. [91], that $\langle \mathcal{O}(\Omega) \rangle_\Omega$ evaluated with such a Markov chain indeed approaches the ensemble average $\langle \mathcal{O} \rangle$ with a statistical uncertainty of order $\mathcal{O}(1/\sqrt{n})$.

METROPOLIS ET AL. [137] found that a probability P_A of changing configurations Ω to a randomly chosen Ω' defined via

$$P_A(\Omega, \Omega') = \min \left(1, \frac{P(\Omega')}{P(\Omega)} \right). \quad (2.89)$$

satisfies indeed the required ergodicity and detailed balance. However, if the trial configuration Ω' is chosen randomly, i.e., completely independent of Ω , an acceptance becomes rather unlikely, which results in a very small acceptance rate and the system will move only slowly through configuration space. This problem can be solved by using configurations Ω' , that are closer to the former Ω , for instance by a local (link) update. However, such algorithms then suffer from large autocorrelation times τ . These grow exponentially with the lattice correlation length $\hat{\xi}$, i.e., $\tau \sim \hat{\xi}^z$ with $z=2$ for the Metropolis algorithm. ξ itself depends on the simulated system and the observables of interest. Since its physical length is fixed $\hat{\xi}$ and thus τ increases dramatically by going to finer lattices. This is known as *critical slowing down*.

2.4.3 Heat bath and overrelaxation

One important feature of S_G is its locality, meaning that a change δS_G due to an update of one single link U can be calculated very fast.

$$\delta S_G = -\frac{\beta}{3} \text{Re Tr } \delta UV + \text{terms not involving } U, \quad (2.90)$$

with V being the remaining links in the plaquettes containing U . Thus a single link update can easily be carried out several times before one proceeds to the next link. This method is called the *multi-hit Metropolis*. The *pseudo heat bath* algorithm [138, 139] on the other hand, updates individual links by putting them into a local equilibrium with their neighboring links (heat bath) using the probability distribution

$$dP(U) = \exp\left(-\frac{\beta}{3}\text{Re Tr } UV\right) dU. \quad (2.91)$$

In one heat bath iteration this is done again successively for every lattice link, sweeping over the whole lattice. The crucial difference between the heat bath and the Metropolis algorithm is that the new link is less correlated with the old one, which reduces ξ , while z is still approximately 2. This algorithm works fine with $SU(2)$, but for $SU(3)$ it is rather slow [140].

CABIBBO and MARINARI [138] circumvented this problem, by doing the updates in the $SU(2)$ subgroups of the $SU(3)$ link. Together with an improved way to (approximately) do the integral over the group manifold this leads to the FHKP updating scheme [139, 141], which has been used in our work.

One further step to reduce the correlations between updated configurations is the *overrelaxation update* [142, 143]. After some sweeps with FHKP one takes the opposite in the parameter space of the $SU(2)$ submatrices, to change U while keeping S fixed. With this combination of FHKP and overrelaxation one is then able to reduce z to nearly one. In our simulation, we have used, depending on the temperature, 3 – 5 overrelaxation steps per heat bath step.

2.4.4 Inversion of the fermion matrix

The most fundamental fermionic quantity in LQCD is the quark propagator, $\langle\psi(x)\bar{\psi}(y)\rangle$. It describes the propagation of a quark from x to y and is equivalent to an element of the inverse of the fermion matrix, $M^{-1}(x, y)$ Eq. (2.81). This corresponds to finding the solution of the inhomogeneous equation

$$\sum_{m,B} M_{A,B}(n, m)\psi_B(m) = \phi_A(n) \quad (2.92)$$

with a point-like source $\phi_A(n)$ for every color-spin combination A . Choosing $n=0$, $A=(a, \alpha)$, $\psi_B(m)$ represents the $(a, \alpha, 0)$ -th column of $M_{B,A}^{-1}(m, 0)$ and contains all propagators from the origin to all other points m and color-spin combinations.

Since M is sparse and its dimension $N = N_\sigma^3 \cdot N_\tau \cdot N_c \cdot N_d \cdot N_f$ is very large, Eq. (2.92) can only be solved approximatively by an iterative method, e.g., minimizing the error function of residuals r , $\langle r, r \rangle = \langle M\psi - \phi, M\psi - \phi \rangle$, below some certain value ϵ . The algorithms we have used are based on the conjugate residual method [144]. Starting with a trial residual vector r_0 , one uses conjugate search directions p_k within the Krylov space $\mathcal{K}(M, r_0, k) = \text{span}\{r_0, Mr_0, \dots, M^{k-1}r_0\}$ instead of local gradients for finding a minimum of $\langle\psi-\phi, M(\psi-\phi)\rangle$. This guarantees convergence in N iterative steps. The conjugate gradient (CG) algorithm [145] needs M to be Hermitian and positive definite, a condition which can be fulfilled by using the equation

$$M^\dagger M\psi = M^\dagger \phi \quad (2.93)$$

instead of Eq. (2.92). This means, however, that the number of operations 'matrix times vector' doubles. An alternative is the application of algorithms which do not require Hermiticity like the minimal residue (MR) algorithm [144] or the stabilized biconjugate gradients (BiCGStab) algorithm [146]. Both need larger memory resources and the latter has an unorthodox

convergence behavior, see e.g. [147]. We have found that the CG is fast for large quark masses or above T_c while the BiCGStabl performs best for small quark masses below T_c . The convergence time of such methods is governed by the *condition number*, which is the ratio of the largest to the smallest eigenvalue of the matrix. Since the smallest eigenvalue approaches zero for $\kappa \rightarrow \kappa_c$, i.e., if a zero-mode exists, light quark masses for $T < T_c$ result in large condition numbers and correspondingly larger inversion times. In order to decrease the condition number of the matrix to accelerate the inversion, we used *even-odd preconditioning* [148]. The idea is to divide the lattice in even and odd points and to calculate first the inverse just on the even points. Afterwards one can reconstruct the inverse on the odd points by one matrix multiplication. The system of equation can thus be written as

$$\begin{pmatrix} A_{ee} & -\kappa\Delta_{eo} \\ -\kappa\Delta_{oe} & A_{oo} \end{pmatrix} \begin{pmatrix} \psi_e \\ \psi_o \end{pmatrix} = \begin{pmatrix} \phi_e \\ \phi_o \end{pmatrix} \quad (2.94)$$

where A and Δ are defined in Eq. (2.51) and Eq. (2.50). Multiplying this with

$$\begin{pmatrix} \mathbb{1}_{ee} & \kappa\Delta_{eo}A_{oo}^{-1} \\ 0 & 0 \end{pmatrix} \quad (2.95)$$

one gets

$$\widetilde{M}_{ee}\psi_e = (A_{ee} - \kappa^2\Delta_{eo}A_{oo}^{-1}\Delta_{oe})\psi_e = \phi_e + \kappa\Delta_{eo}A_{oo}^{-1}\phi_o = \widetilde{\phi}_e \quad (2.96)$$

$$\psi_o = A_{oo}^{-1}(\phi_o + \kappa\Delta_{oe}\psi_e). \quad (2.97)$$

And indeed substituting ψ_e into Eq. (2.97) ψ_o can be deduced. While the number of operations per iteration is preserved by this procedure, the non-diagonal part of \widetilde{M} contains κ^2 instead of κ and M comes closer to the unit matrix for small κ . In practice the smallest eigenvalue of \widetilde{M} increases compared to M by a factor of about two.

The computational effort can be further reduced by setting $r = 1$. In this case the term $(r \pm \gamma_\mu)/2$ becomes a projector, which decomposes the four spinor ψ into two two-spinors and saves computing time in the inversion [149].

Another very important property of M^{-1} is its γ_5 -Hermiticity. Using the charge conjugation operator $C = \gamma_4\gamma_2$ and $\widetilde{C} = C\gamma_5$

$$C\gamma_\mu C^{-1} = -\gamma_\mu^T \quad C\gamma_5 C^{-1} = -\gamma_5^T \quad (2.98)$$

$$\widetilde{C}\gamma_\mu \widetilde{C}^{-1} = \gamma_\mu^T \quad \widetilde{C}\gamma_5 \widetilde{C}^{-1} = \gamma_5^T \quad (2.99)$$

one finds

$$CM^{-1}(x, y; \Omega)C^{-1} = (M^{-1})^T(y, x; \Omega^*) \quad (2.100)$$

$$\widetilde{C}M^{-1}(x, y; \Omega)\widetilde{C}^{-1} = (M^{-1})^*(x, y; \Omega^*), \quad (2.101)$$

where Ω^* denotes all complex conjugate U . Combining Eq. (2.100) and Eq. (2.101) therefore gives

$$\begin{aligned} \gamma_5 M^{-1}(x, y; \Omega) \gamma_5 &= CC\gamma_5 (M^{-1})(x, y; \Omega) \gamma_5^{-1} C^{-1} C^{-1} \\ &= C\widetilde{C} (M^{-1})(x, y; \Omega) \widetilde{C}^{-1} C^{-1} \\ &= C (M^{-1})(x, y; \Omega)^* C^{-1} \\ &= (M^{-1})^\dagger(y, x; \Omega) \end{aligned} \quad (2.102)$$

This relation between forward and backward propagators is rewarding since the inversion of the fermion matrix is the most time consuming step in the complete calculation. Rewriting the backward propagator for degenerate flavors, e.g., in Eq. (2.152) $(M^{-1}(x_f, x_i) = (M^{-1})^\dagger(x_i, x_f))$, we need to invert the matrix only once.

2.4.5 Errors and fitting

Unfortunately every physical quantity determined by numerical simulations on the lattice suffers from statistical as well as from systematic errors. The latter may come from finite volume or finite lattice spacing effects due to the discretization or the fact that one uses quenched simulations. These errors can be reduced by studying different lattice sizes keeping the lattice spacing fixed or vice versa.

The statistical errors on the other hand are due to the finite number of measurements, i.e., only a finite set of configurations has been used to sample the path integral. Both are unavoidable and a clear systematic study has to be undertaken. Finally it is always desirable to keep the systematic error below the statistical. Now we will discuss how to obtain estimates for the statistical errors.

Statistical error for primary quantities

Let A be the exact expectation for primary quantities, and A_n , $n=1, \dots, N$ the finite set of measurements. For large enough statistics ($N \gg 1$), one can use \bar{A} as an estimate for A :

$$A \simeq \bar{A} \equiv \frac{1}{N} \sum_{i=1}^N A_i. \quad (2.103)$$

In case of independent configurations with respect to the measured quantities, \bar{A} is normally distributed around A with the simple variance

$$\sigma(\bar{A})^2 = \frac{\sigma(A)^2}{N-1} = \frac{\overline{(A-\bar{A})^2}}{N-1} = \frac{\overline{A^2} - \bar{A}^2}{N-1}, \quad (2.104)$$

which is a consequence of the central limit theorem and gives a reliable error estimate $A = \bar{A} \pm \sigma(\bar{A})$. Otherwise one has to consider the autocorrelation of the measured quantity. The error is then given by

$$\sigma(\bar{A})^2 = \lim_{N \rightarrow \infty} \frac{2\tau_{int}}{N} \left(\overline{A^2} - \bar{A}^2 \right), \quad (2.105)$$

where the (*integrated*) *autocorrelation time* τ_{int} is taken from the normalized autocorrelation function

$$C_{AA}(t) = \frac{\langle A_i A_{i+t} \rangle}{\langle A_i A_i \rangle}. \quad (2.106)$$

For large t it typically decays exponentially

$$C_{AA}(t) \rightarrow e^{-\frac{|t|}{\tau(A)}} \quad (2.107)$$

which immediately leads to the definition of the (*exponential*) *autocorrelation time* $\tau_{exp}(A)$:

$$\tau_{exp}(A) = - \limsup_{t \rightarrow \infty} \frac{|t|}{\ln |C_{AA}(t)|}. \quad (2.108)$$

This quantity naturally lends itself to the interpretation of being the decay time of the slowest mode in A . The integrated autocorrelation time on the other hand is defined as

$$\tau_{int} = \frac{1}{2} \sum_{t=-\infty}^{\infty} C_{AA}(t) = \frac{1}{2} + \sum_{t=1}^{\infty} C_{AA}(t). \quad (2.109)$$

In case of independent measurements τ_{int} is equal to $\frac{1}{2}$ and Eq. (2.105) reduces to the simple variance. However, in practice it is not always possible to compute $\tau_{int}(A)$ reliably, due to low statistics, and there is no straightforward way of its determination for secondary quantities $y(A)$, e.g. masses or wave functions. In both cases a jackknife analysis is suitable.

Statistical error for secondary quantities: Jackknife error estimation

If $y(A)$ is given explicitly, the best estimate is $\bar{y} = y(\bar{A})$ (not $\overline{y(A)}$) and the corresponding error can be deduced by a simple Gaussian error propagation. The idea of Jackknife-blocking [150] is to treat the process of measurement and subsequently the transformation of primary quantities to secondary ones as a black box. From that perspective one can get a more stable estimate of the error by simply deleting one measurement from the sample and determine its impact on the average value. Let A^j be the average over the sample with the j -th measurement removed on which the secondary quantity is going to be extracted, e.g. by the fitting procedure presented below,

$$A^j = \frac{1}{N-1} \sum_{i \neq j} A_i \quad \text{and} \quad \bar{A}^j = \frac{1}{N} \sum_{j=1}^N A^j. \quad (2.110)$$

Then $\mathcal{A}^j = N\bar{A} - (N-1)A^j$ are members of the so-called pseudo jackknife dataset. They yield *improved* jackknife estimators $y_j = y(\mathcal{A}^j)$, instead of $y_j = y(A^j)$, of the secondary quantity y with its improved mean and variance

$$\bar{y} = \frac{1}{N} \sum_{j=1}^N y_j \quad \text{and} \quad \sigma^2(\bar{y}) = \frac{1}{N(N-1)} \sum_{j=1}^N (y_j - \bar{y})^2. \quad (2.111)$$

For primary quantities, $y(A) = A$, $\sigma^2(\bar{y})$ coincides with the Gaussian standard deviation (Eq. (2.104)):

$$\bar{\mathcal{A}} = \frac{1}{N} \sum_{j=1}^N \mathcal{A}^j = N\bar{A} - (N-1)\bar{A}^j \quad (2.112)$$

$$\sigma^2(\bar{\mathcal{A}}) = \frac{\overline{(\mathcal{A}^j - \bar{\mathcal{A}})^2}}{(N-1)} = \frac{N-1}{N} \sum_{j=1}^N (A^j - \bar{A}^j)^2. \quad (2.113)$$

Using the improved mean of the observable \bar{y} , one corrects for a possible bias in the sample data, i.e. $\bar{A} \neq \bar{A}^j$. So far we have achieved nothing more than getting a stable estimate of the error of secondary quantities, although still implicitly assuming uncorrelated measurements and thus underestimating the true error. The missing enhancement to this method is to aggregate n subsequent measurements into a block and treat the average of that block as one measurement, repeating the same procedure on the blocked data. The block size is then to be increased successively until the measured error approaches a plateau from below. In the limit of an infinite number of measurements, the stabilized error is the correct one for completely uncorrelated measurements. It can easily be seen that this method also serves as an implicit determination of the correlation time $\tau_{int}(y(\mathcal{A}))$. In fact, it can be extracted via

$$\tau_{int}(y(\mathcal{A})) = \frac{1}{2} \frac{\sigma_{n_u}^2(\bar{y})}{\sigma_1^2(\bar{y})}, \quad (2.114)$$

where $\sigma_n^2(\bar{y})$ denotes the obtained error at block size n and n_u being the block size at which the blocked data appears uncorrelated. Concerning this work, we have seen just minor or no

significant increase of jackknife errors for n ranging between 1 and 5. Thus we consider our gauge configuration each separated by 300 – 500 update steps to have almost no correlations left. In order to be on a safe side we choose a block size of 5, namely $y = \bar{y} \pm \sigma_5(\bar{y})$ which should in any case be large enough to avoid correlations.

Fitting

A standard procedure to fit a function $g(t, \mathbf{a})$ with parameters \mathbf{a} to a set of data points $((f_k(t_i), t_i); k=1, \dots, N_{\text{sample}}; i=1, \dots, N_{\text{points}})$ is to minimize the $\chi^2(\mathbf{a})$ -measure⁸

$$\chi^2(g(\mathbf{a})) = \sum_{t_i, t_j} (\bar{f}(t_i) - g(t_i, \mathbf{a})) C^{-1}(t_i, t_j) (\bar{f}(t_j) - g(t_j, \mathbf{a})), \quad (2.115)$$

$$C^{-1}(t_i, t_j) = \frac{1}{N_{\text{sample}}(N_{\text{sample}} - 1)} \sum_{k=1}^{N_{\text{sample}}} (f_k(t_i) - \bar{f}(t_i))(f_k(t_j) - \bar{f}(t_j)). \quad (2.116)$$

A meaningful number of samples N_{sample} with respect to Eq. (2.115) must at least be larger than the dimension of the symmetric covariance matrix C in order to prevent its singularity. However, for an insufficient number, small eigenvalues in the covariance matrix can appear, which lead to unreasonable large values in the inverse. In this case *eigenvalue smoothing* proposed by MICHAEL and MCKERREL [152] can be applied. Consider N_{points} eigenvalues λ_i with $\lambda_i \geq \lambda_{i+1}$, then the smoothing method leads to λ' new eigenvalues with

$$\lambda'_i = \max(\lambda_i, \lambda_{\min}) \quad \text{with} \quad \lambda_{\min} = \frac{1}{N_{\text{points}} - N_R} \sum_{i=N_R+1}^{N_{\text{points}}} \lambda_i. \quad (2.117)$$

and N_R denotes the number of retained eigenvalues. This procedure increases the stability of the fit, and is particularly important for the MEM, see Section 3.2.6.

For a perfect Gaussian distributed set of data, one can show that χ^2 in fact should have a value which corresponds to the number of degrees of freedom $N_{\text{dof}} = N_{\text{points}} - N_{\text{parameter}}$. In this respect, χ^2/N_{dof} can be used as an indicator of the quality of fit. $\chi^2/N_{\text{dof}} \gg 1$ is a sign that $g(t, \mathbf{a})$ is a poor model for describing the data while $\chi^2/N_{\text{dof}} \ll 1$ shows overestimated errors. As Eq. (2.116) is just an estimation of the 'true' covariance matrix, we will also use a simplified version of χ^2

$$\chi^2(g(\mathbf{a})) = \sum_{t_i} \left(\frac{\bar{f}(t_i) - g(t_i, \mathbf{a})}{\sigma(t_i)} \right)^2, \quad (2.118)$$

which takes just the diagonal elements of C^{-1} , i.e., the standard deviation into account.

2.5 $Z(3)$ -Symmetry on the lattice

The action of the pure gauge theory has an exact global symmetry associated with the center of the gauge group, $Z(3)$ ($Z(N)$ for $SU(N)$). This is the symmetry under the simultaneous transformation of all time-like gauge links on a given three dimensional hypersurface with n_4 fixed

$$U_4(n) \rightarrow zU_4(n) \quad \text{with} \quad z = \exp(il2\pi/3) \in Z(3) \quad (l = 0, 1, 2). \quad (2.119)$$

⁸we have used a C-version of the minimization program minuit [151] using the MIGrad method.

This $Z(3)$ symmetry plays an important role in our picture of confinement [153, 154]. One gauge field observable that is not invariant under this gauge transformation is the *Polyakov loop* [155]

$$L(\mathbf{n}) = \frac{1}{N_c} \text{Tr} \prod_{n_4=0}^{N_\tau-1} U_4(\mathbf{n}, n_4) \quad \text{with} \quad L(\mathbf{n}) \rightarrow zL(\mathbf{n}). \quad (2.120)$$

This operator acts as an order parameter for the deconfinement transition:

$$\lim_{V \rightarrow \infty} \langle |L| \rangle = \lim_{N_\sigma \rightarrow \infty} \left\langle \left| \frac{1}{N_\sigma^3} \sum_{\mathbf{n}} L(\mathbf{n}) \right| \right\rangle \begin{cases} = 0 & \Leftrightarrow \text{confined phase, } T < T_c \\ > 0 & \Leftrightarrow \text{deconfined phase, } T > T_c \end{cases}. \quad (2.121)$$

Below T_c , $\lim_{V \rightarrow \infty} \langle |L| \rangle = 0$, so the vacuum is $Z(3)$ symmetric. Above T_c it acquires a nonzero expectation value, signifying a spontaneous breaking of the $Z(3)$ symmetry. The system above T_c can exist in one of three identical vacua, corresponding to the three values of z (see Fig. 2.5(c)).

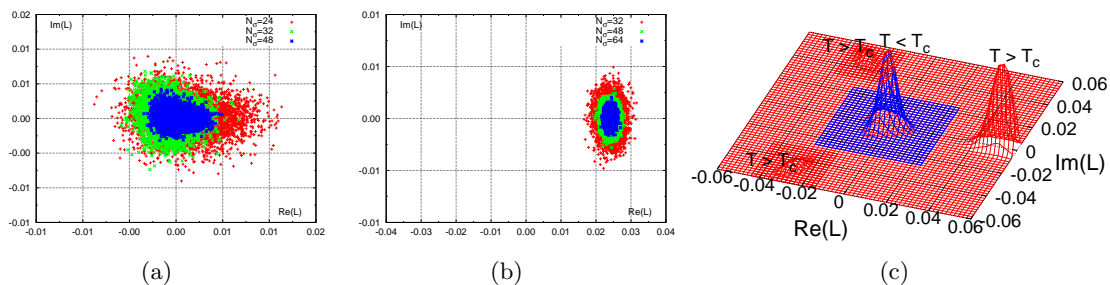


Fig. 2.5: $Z(3)$ -symmetry: Polyakov loops L in the complex plane for our simulations at $0.9 T_c$ (a) and at $3 T_c$ (b) and various volumes. (c) Distribution of the Polyakov loop in the symmetric phase (blue) and the spontaneous broken phase (red) from [156].

The expectation value of L is related with the excess in free energy $\Delta F_q(T)$ of putting one static color triplet test charge in the gluonic heat bath [86, 157]:

$$e^{-\beta \Delta F_q(T)} = \langle |L| \rangle. \quad (2.122)$$

Thus, a single static quark is associated with an infinite free energy below T_c , as would be expected for a confining vacuum. Above T_c , the free energy associated with a single static quark is finite, signifying deconfinement.

Fermions break the $Z(3)$ symmetry, so the full theory does not have the symmetry: in the full theory, the $l = 0$ vacuum (corresponding to a real $\langle L \rangle$) is preferred. In the quenched approximation, the configurations are generated with the measure of the pure gauge theory. However, since we then measure expectation values of fermionic observables, the three vacua are not identical. For example, while the chiral condensate vanishes above T_c for the $l = 0$ vacuum, a nonzero value is seen in the other vacua for some temperatures [158, 159]. Also screening masses depend on the specific $Z(3)$ sector, as has been checked by P.SCHMIDT [156]. Note that a change by a $Z(3)$ transformation can also be interpreted as a change in the boundary conditions of the fermions [160]. The usual anti-periodic boundary conditions Eq. (1.19) are twisted to

$$\psi(0, \mathbf{x}) = -z\psi(1/T, \mathbf{x}). \quad (2.123)$$

This affects the discrete Matsubara frequencies for fermions and hence the screening masses. Instead of

$$\omega_n = (2n + 1)\pi T \quad (2.124)$$

we have

$$\omega_n = ((2n + 1)\pi - \arg L)T. \quad (2.125)$$

Thus in the free-field case the lowest eigenvalue of the Dirac operator in the real sector, πT , is three times larger than in the complex sector.

For obvious reasons, we prefer to work with configurations around the $l = 0$ vacuum. In finite volumes one can see tunnelings between the three vacua; however, at the temperatures and lattice sizes that we work with, such tunnelings are extremely rare. If in some of our simulations such tunnelings occur, we discontinue the gauge field update and start a new run. Alternately, we also use a $Z(3)$ -transformation on one time slice of the gauge fields to take us back to the (real) $l=0$ sector.

2.6 Evaluating physical quantities on the lattice

2.6.1 Continuum limit

The issue of how to connect LQCD expectation values to the corresponding physical observables, will be addressed in this subsection. As already mentioned, the dimensionless quantity $\hat{\mathcal{O}}$ can be rescaled to the physical one by

$$\mathcal{O}(g(a), a) = a^{-\dim[\mathcal{O}]} \hat{\mathcal{O}}(g(a), a) \quad (2.126)$$

and leads to the continuum form with

$$\mathcal{O}_{\text{cont}} = \lim_{a \rightarrow 0} \mathcal{O}(g(a), a). \quad (2.127)$$

Concerning particle masses, e.g., $m_\pi = \hat{m}_\pi/a$ this relation gives a finite result only if the coupling on the lattice $g(a \rightarrow 0)$ approaches its critical value g^* , where the correlation length $\xi \sim \frac{1}{\hat{m}_\pi}$ must diverge, in order to keep m_π finite. In statistical models this situation corresponds to a second order phase transition and due to *universality* the system forgets about details in the underlying lattice. In QCD this limit should be realized at $g^* = 0$ ($\beta = \infty$) due to asymptotic freedom. At first sight the theory seems to have no interactions in the continuum, but this is not the case, since the renormalized coupling does not vanish.

Additionally close to the continuum the observable should be independent of the lattice spacing, leading to the *renormalization group equation* (RGE)

$$\left[a \frac{\partial}{\partial a} - \beta(g) \frac{\partial}{\partial g} \right] \mathcal{O}(g(a), a) = 0, \quad (2.128)$$

with the β -function defined as

$$\beta(g) = -a \frac{\partial g}{\partial a} \quad (2.129)$$

Thus it follows, that a change in a can be compensated by rescaling g .

However, for finite a the r.h.s of Eq. (2.128) is no longer 0 and becomes subject to modifications depending on the observable (*scaling violation*). The range where Eq. (2.128) holds approximately is called *scaling region*. The β -function has been calculated perturbatively up to four-loop order

$$\beta(g) = -\beta_0 g^3 - \beta_1 g^5 - \beta_2 g^7 - \beta_3 g^9 + \mathcal{O}(g^{11}) \quad (2.130)$$

giving the first two (universal)⁹ coefficients¹⁰

$$\beta_0 = \frac{1}{16\pi^2} \left(\frac{11}{3} N_c - \frac{2}{3} N_f \right) \quad \text{and} \quad (2.131)$$

$$\beta_1 = \frac{1}{(16\pi^2)^2} \left(\frac{34}{3} N_c^2 - \frac{10}{3} N_f N_c - \frac{N_c^2 - 1}{N_c} \right). \quad (2.132)$$

The solution of Eq. (2.128) with the two-loop β -function, valid for $a \ll 1/\Lambda$, and hence the dependence of a on g is then given by

$$g^{-2}(a) \equiv 2\beta_0 \ln \left(\frac{1}{a\Lambda} \right) + \frac{\beta_1}{\beta_0} \ln \left(2 \ln \left(\frac{1}{a\Lambda} \right) \right) \quad (2.133)$$

$$\Rightarrow a\Lambda = \lim_{g^2 \rightarrow 0} \left\{ R(g^2) = (\beta_0 g^2)^{-\frac{\beta_1}{2\beta_0^2}} \exp \left(-\frac{1}{2\beta_0 g^2} \right) \right\}. \quad (2.134)$$

Here Λ is an integration constant and depends on the renormalization scheme. It has a mass dimension one and must be inferred by experimental measurements. $R(g^2)$ is just the integrated β -function.

Inserting Eq. (2.134) in Eq. (2.126) one gets

$$\hat{\mathcal{O}} \rightarrow \frac{\mathcal{O}_{\text{cont}}}{\Lambda^d} \cdot (R(g^2))^d \quad \text{as } a \rightarrow 0 \quad (g \rightarrow g^*). \quad (2.135)$$

Quantities which behave like this are said to show *asymptotic scaling*. For small enough a the ratio of two such quantities \mathcal{O}^1 and \mathcal{O}^2 with the same mass dimension approximately converges to its continuum value, i.e., the system is in the scaling region,

$$\frac{\hat{\mathcal{O}}^1}{\hat{\mathcal{O}}^2} = \frac{\mathcal{O}_{\text{cont}}^1}{\mathcal{O}_{\text{cont}}^2} + \mathcal{O}(a). \quad (2.136)$$

The approximate independence of the ratio from the lattice spacing is called *scaling*.

2.7 Simulation details

In this section an overview of the simulation parameters for the pure gauge as well as for the fermion sector, both in the Wilson and the HF case will be given. Furthermore we give the lattice spacings a in physical units and the renormalization constants we used. In addition, the procedure to determine the HF parameters is described and the results are shown.

2.7.1 Simulation parameters

All computations with double-precision numbers have been performed on the IBM-Jump¹¹ computer at NIC Jülich. For our analysis we allow, depending on the lattice size, between 2000-5000 sweeps for thermalization. All subsequent configurations are separated by 300-500 sweeps, each with 3-5 overrelaxation steps per heat bath. A cold (unit) configuration was used as starting configuration above T_c , in order to guarantee that the Polyakov loop falls into the 'right' real sector, see Section 2.5, of the configuration space from the beginning. On large lattices it stays in this sector, while for smaller lattices and close to the phase transition, we had to transform the gauge configuration in order to rotate the Polyakov loop back again.

⁹independent of the renormalization scheme

¹⁰Since both coefficients are positive, the β -function itself is negative up to this order. This means that upon decreasing a the coupling constant reduces, again confirming the fixed point to be $g^* = 0$.

¹¹JUelich Multi Processor (see <http://jumpdoc.fz-juelich.de>)

β	N_τ	T/T_c	$a[\text{fm}]$	$a^{-1}[\text{GeV}]$	κ_c	c_{SW}
6.000	16	0.441	0.104	1.905	0.13520	1.769231
6.136	16	0.553	0.083	2.389	0.13571	1.653008
6.499	16	0.929	0.049	4.012	0.13558	1.494176
6.205	8	1.229	0.074	2.654	0.13580	1.610974
6.499	12	1.238	0.049	4.012	0.13558	1.494176
6.721	16	1.235	0.037	5.338	0.13522	1.440388
6.338	8	1.491	0.061	3.221	0.13580	1.548725
6.640	12	1.487	0.041	4.817	0.13536	1.457898
6.872	16	1.489	0.031	6.432	0.13495	1.412488
7.192	24	1.456	0.021	9.435	0.13437	1.367261
6.872	8	2.978	0.031	6.432	0.13495	1.412488
7.192	12	2.912	0.021	9.435	0.13437	1.367261
7.457	16	2.977	0.015	12.86	0.13396	1.338927
7.457	8	5.955	0.015	12.86	0.13396	1.338927

Tab. 2.2: Estimated scales, temperatures and κ_c for the parameters used.

For the determination of the scales a, a^{-1} and temperature T quoted see Section 2.7.2. The critical hopping parameters and the non-perturbatively determined c_{SW} shown in Tab. 2.2 stem from an interpolation of values from a $T = 0$ study by LÜSCHER ET AL. [103]. The authors have studied the vanishing of the current quark mass over a large range of β values. For the inversion algorithm we have chosen stopping criterions ϵ in the range of $10^{-12} - 10^{-15}$. The numerical parameters and statistics we have used below T_c are shown in Tab. 2.3. In

T/T_c	β	$N_\sigma^3 \times N_\tau$	N_{conf}	κ
0.44	6.000	$24^3 \times 16$	60	0.13240 0.13320 0.13420 0.13480
0.55	6.136	$24^3 \times 16$	60	0.13300 0.13400 0.13460 0.13540
		$32^3 \times 16$	120	0.13300 0.13400 0.13460 0.13495 0.13540
		$48^3 \times 16$	60	0.13300 0.13400 0.13460 0.13495
0.62	6.499	$32^3 \times 24$	120	0.13300 0.13460
0.93	6.499	$24^3 \times 16$	120	0.13300 0.13400 0.13460 0.13540
		$32^3 \times 16$	120	0.13300 0.13400 0.13460 0.13531 0.13540
		$48^3 \times 16$	60	0.13300 0.13400 0.13460 0.13531

Tab. 2.3: Lattice parameter and number of configurations for the SW-action below T_c .

order to study finite volume and lattice spacing effects above T_c , we have used at least three different volumes and lattice spacings per temperature, see Tab. 2.4.

In the vicinity of the phase transition we are faced with non-trivial topological activities, e.g., zero-modes or exceptional configurations. In the deconfined phase we left them out for our analysis to avoid unphysical results or, expressed differently, we mimic the role of suppression of such objects by the fermion determinant in dynamical simulations. In order to gain some further insight into the topological properties of the gauge configurations and to give a justification for this approach we studied the eigenvalues λ_n and eigenvectors ψ_n of the Dirac operator utilizing the SW-Operator, the hypercube operator as well as the overlap hypercube operator, which has the advantage to respect the index relation and thus shows exact zero modes. We observe that the exceptional configurations we encounter at $1.2 T_c$ indeed have zero-modes $\lambda_n = 0$ with chirality $\langle \bar{\psi}_n \gamma_5 \psi_n \rangle = \pm 1$ of the overlap operator. The

investigation further showed that the SW-Operator is sometimes blind for zero-modes. In this case no or very small fluctuations appear in the CF.

As can be seen in Fig. 2.1 the CF of an exceptional configuration is usually peaked at a certain spatial position. Around this position the lowest eigenmodes of the SW-Operator are localized. As expected their number seems to grow with volume close to the phase transition, see N_{excp} in Tab. 2.4. Fortunately at higher temperature the number of these exceptionals is vastly reduced as shown in Tab. 2.4, which according to the anomaly in Eq. (1.26) confirms that the $U(1)_A$ symmetry gets restored effectively. A detailed analysis deserves further investigation but goes beyond the scope of this thesis.

T/T_c	β	$N_\sigma^3 \times N_\tau$	N_{conf}	N_{excp}	κ
1.24	6.205	$(64 32 24 16)^3 \times 8$	$(46 61 85 118)$	$(>15 11 18 19)$	0.13599
1.24	6.499	$(48 36 24)^3 \times 12$	$(81 81 70)$	$(14 10 3)$	0.13558
1.24	6.721	$(64 48 32)^3 \times 16$	$(84 96 81)$	$(22 2 1)$	0.13507
1.49	6.338	$(96 64 32 24 16)^3 \times 8$	$(36 46 62 59 60)$	$(1 0 0 0 2)$	0.13581
1.49	6.640	$(48^* 36 24)^3 \times 12$	$(61 59 68)$	$(3 0 0)$	0.13536
1.49	6.872	$(64 48 32)^3 \times 16$	$(66 62 60)$	$(0 0 0)$	0.13495
1.46	7.192	$64^3 \times 24$	80	2	0.13440
2.98	6.872	$(96 64 32 24 16)^3 \times 8$	$(37 43 65 80 80)$	$(0 0 0 0 0)$	0.13494
2.91	7.192	$(48 36 24)^3 \times 12$	$(85 80 80)$	$(1 0 0)$	0.13440
2.98	7.457	$(64 48 32)^3 \times 16$	$(80 80 60)$	$(0 0 0)$	0.13390
5.96	7.457	$32^3 \times 8$	70	0	0.13390

Tab. 2.4: Lattice parameter and number of configurations for the SW-action above T_c (* data at $\kappa=0.13525$ available).

For the hypercube operator the parameters $(\lambda_0, \dots, \lambda_4, \rho_1, \dots, \rho_4)$ are known in the free case and have been given in Tab. 2.1. In the interacting case we utilized *minimal gauging* (see 2.3.6) and compensated the resulting additive mass renormalization [161] by rescaling the parameters

$$\begin{aligned}
\lambda_0 &\rightarrow \lambda_0, \\
\lambda_1 &\rightarrow u\lambda_1, \quad \rho_1 \rightarrow uv\rho_1, \\
\lambda_2 &\rightarrow u^2\lambda_2, \quad \rho_2 \rightarrow (uv)^2\rho_2, \\
\lambda_3 &\rightarrow u^3\lambda_3, \quad \rho_3 \rightarrow (uv)^3\rho_3, \\
\lambda_4 &\rightarrow u^4\lambda_4, \quad \rho_4 \rightarrow (uv)^4\rho_4,
\end{aligned} \tag{2.137}$$

with u and w , where $1/u \leq v \leq 1$. Increasing u towards its critical value corresponds to decreasing the current quark mass. The factor v controls mostly the imaginary part of the eigenvalues, i.e., the width of the eigenvalue bulk spectrum.

To further control the chiral quality of this operator following Ref. [161] we used so called *fat links*:

$$U_\mu^{\text{new}}(x) = (1 - \alpha)U_\mu^{\text{old}}(x) + \frac{\alpha}{6} \sum_{\pm\nu \neq \mu < 4} U_{\mu\nu}^{\text{staple}}(x) \tag{2.138}$$

$$U_{\mu\nu}^{\text{staple}}(x) = U_\nu^{\text{old}}(x)U_\mu^{\text{old}}(x + \hat{\nu}) U_\nu^{\text{old}\dagger}(x + \hat{\mu}). \tag{2.139}$$

All those parameters have been adjusted such that the eigenvalues follow the GW circle closely, c.f. Fig. 2.6. The resulting parameters are shown in Tab. 2.5.

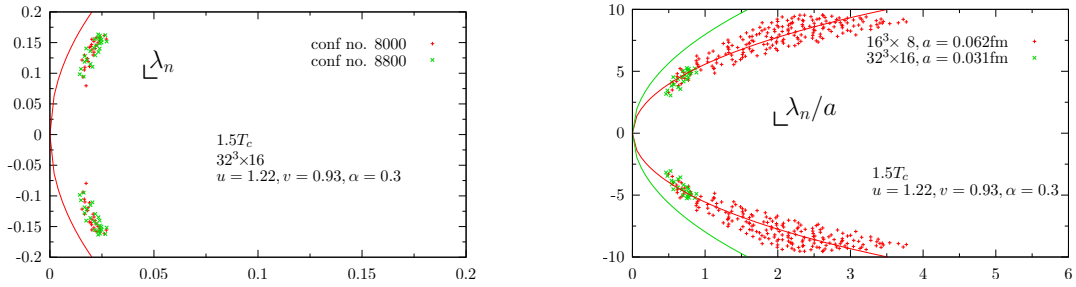


Fig. 2.6: The 80 lowest eigenvalues of the HF-action on a $32^3 \times 16$ lattice at $1.5 T_c$ [162]. For comparison also the GW circle is shown. The right picture shows that the gap scales for the coarse and fine lattice spacings at the same temperature.

T/T_c	β	$N_\sigma^3 \times N_\tau$	N_{conf}	α	u	v
1.49	6.872	$(48 32)^3 \times 16$	(108 74)	0.3	1.22	0.93
2.98	7.457	$(48 32)^3 \times 16$	(135 188)	0.3	1.19	0.93
	7.192	$48^3 \times 12$	85	0.3	1.20	0.90

Tab. 2.5: Parameters for the HF-action above T_c .

2.7.2 Determination of the scale

As seen from Eq. (2.135) and Eq. (2.134), once one has determined the lattice spacing a or Λ respectively by comparing a quantity on the lattice with the corresponding quantity measured experimentally, the scale is fixed. Often this is done by using the ρ -mass, $m_\rho = 770$ MeV, the nucleon mass, $m_N = 940$ MeV, or the square root of the string tension, $\sqrt{\sigma}$. The latter characterizes the long distance behavior of heavy quarkonia (static) potentials $V_{q\bar{q}}(r) = -\alpha/r + \sigma r$ at $T = 0$. It is somewhat model dependent, but has the advantage to be insensitive to the quark mass in the quenched case. Therefore it has been used in this work. Otherwise one has to ensure that the bare quark masses considered are sufficiently small. Normally one has to extrapolate.

EDWARDS ET AL. [163] parameterized the string tension in the range $5.6 \leq \beta \leq 6.5$ using [164]

$$(a\sqrt{\sigma})(g) = R(g^2)(1 + c_2\hat{a}^2(g) + c_4\hat{a}^4(g) + c_6\hat{a}^6(g)^6)/\frac{\lambda}{\sqrt{\sigma}} \quad (2.140)$$

$$\hat{a}(g) \equiv \frac{R(g^2)}{R(g^2(\beta = 6.0))} \quad (2.141)$$

with the constants $c_2 = 0.2371$, $c_4 = 0.01545$, $c_6 = 0.01975$ and $\lambda = 0.01364$ and the function $R(g^2)$ defined by Eq. (2.134). Using $T_c/\sqrt{\sigma} = 0.630(5)$ [165] and fixing the critical temperature to $T_c = 270$ MeV [31] a can be set and is given in Tab. 2.2.

An alternative method to introduce a scale by means of potential models uses the *Sommer parameter* r_0 [166]. This length scale is defined in terms of the force $F(r)$ of the potential, where

$$r_0^2 F(r_0) = r_0^2 \left. \frac{\partial V_{q\bar{q}}(r)}{\partial r} \right|_{r=r_0} = 1.65. \quad (2.142)$$

The constant on the right hand side was chosen such that r_0 has a value of approximately 0.49 fm by phenomenological models. The ALPHA-collaboration [167] found a good description of their data in the range $5.7 \leq \beta \leq 6.57$ with

$$\ln(a/r_0) = -1.6805 - 1.7139(\beta - 6) + 0.8155(\beta - 6)^2 - 0.6667(\beta - 6)^3. \quad (2.143)$$

The corresponding a and a^{-1} values show a deviation of at most 10%. Because of this we mostly show data scaled with temperature. Whenever we quote values on a physical scale we use the string tension values, $\sqrt{\sigma} = 420$ MeV, for definiteness. However, one should always keep in mind this uncertainty.

2.7.3 Renormalization constants

The calculation of the renormalization constants Z_H for the currents \mathcal{J}_H is presented here. They can be defined perturbatively and non-perturbatively. From lattice perturbation theory the expression for the renormalization constants to one loop order and in the chiral limit is known to be

$$Z_H(g^2, a\mu) = 1 - \frac{g^2}{12\pi^2} [\gamma_H \ln(a\mu) + C_F \Delta_H], \quad (2.144)$$

where γ_H is the one loop coefficient of the anomalous dimension and $C_F = \frac{1}{2} (N - \frac{1}{N}) = \frac{4}{3}$ is the value of the *quadratic Casimir operator* in the fundamental representation of $SU(3)$. Δ_H has been determined [168] using the SW-action Eq. (2.48) and is listed in Tab. 2.6 for various channels.

Note that in the channels A and V the renormalization factors are scale independent, as they only arise from the use of non-conserved (local) currents (see Section 2.3.2). Renormalization constants, calculated in bare lattice perturbation theory, often show large deviations from the non-perturbatively determined ones. LEPAGE and MACKENZIE [169] explained these deviations by ultraviolet divergencies appearing in tadpole loops. They suggested [168–170] to use 'renormalized' coupling constants, which greatly enhance the predictive power of lattice perturbation theory. Using this tadpole improvement (TI) the renormalization constants are given as

$$Z_H(g^2, a\mu) = u^4(g^2) \left\{ 1 - \frac{g_P^2}{12\pi^2} [\gamma_{H0} \ln(a\mu) + C_F \Delta_H] \right\} \quad (2.145)$$

with the plaquette expectation value

$$u^4 \equiv \frac{1}{N_\sigma^3 N_\tau} \left\langle \frac{1}{3} \sum_x \text{Re Tr } U_{\mu\nu}(x) \right\rangle \quad (2.146)$$

which is calculated non-perturbatively on the lattice. One way to define the tadpole improved coupling [171] is given by $g_P^2 = g^2/u^4$. To obtain, however, results in the more common $\overline{\text{MS}}$ scheme the coupling $g_{\overline{\text{MS}}}^2$ in this scheme has to be evaluated. This computation starts with the determination of the coupling g_V which is defined by the potential $V(\mu) \equiv C_F \frac{g_V^2(\mu)}{\mu^2}$. This is related to the plaquette expectation value through

$$-\ln \langle u^4(g^2) \rangle = \frac{g_V^2(\mu^*)}{3} \left\{ 1 - \frac{g_V^2(\mu^*)}{4\pi} \left[\frac{66}{12\pi} \ln(6.7117/\mu^*) \right] \right\} \quad (2.147)$$

at the scale $\mu^* = 3.4018$, where the matching should be most accurate [169, 172]. Using now the non-perturbatively calculated plaquette values, listed in Table B.5, the equation can be used to compute the coupling $g_V^2(\mu^*)$. The evolution to the scale $\mu = 1/a$ can then be carried

H	Δ_H	γ_{H0}	b_H
S	7.08031	-8	0.14434
P	9.38431	-8	0.11484
V	4.09381	0	0.11492
A	2.94256	0	0.11414

Tab. 2.6: The values Δ_H , b_h , γ_{H0} as given in the table in [168–170].

out with the standard two loop renormalization group equation given by Eq. (2.133). The conversion to the $\overline{\text{MS}}$ -scheme can be achieved with the relation between the scale parameters $\Lambda_{\overline{\text{MS}}} = 0.6252\Lambda_V$. The results are also listed in Tab. B.5. Now the renormalization factors can be calculated by using $g_{\overline{\text{MS}}}^2$ instead of g_P in Eq. (2.145).

The influence of non-vanishing quark masses is given by

$$Z_H(am_q, g_{\overline{\text{MS}}}^2) = Z_H(g_{\overline{\text{MS}}}^2, a\mu = 1)(1 + b_H(g_{\overline{\text{MS}}}^2) am_q). \quad (2.148)$$

Here the coefficients b_H can be expanded again in powers of the coupling,

$$b_H(g_{\overline{\text{MS}}}^2) = 1 + C_F b_H g_{\overline{\text{MS}}}^2, \quad (2.149)$$

and have been calculated at one loop level [170]. The results, b_H , are also listed in Tab. 2.6. More reliable renormalization constants have to be determined non-perturbatively. In the vector and axial-vector channel the validity of the Ward identities, Eq. (2.30), can be used as a criterion to determine the renormalization constants Z_V, Z_A and b_V . Using the Schrödinger functional scheme, LÜSCHER ET AL. [173] calculated these factors near zero quark mass at various couplings $0 < g^2 \leq 1$ and reached an error of less than 1%. Fitting these data leads to the parameterizations

$$\begin{aligned} Z_V &= \frac{1 - 0.7663g^2 + 0.0488g^4}{1 - 0.6369g^2} & Z_A &= \frac{1 - 0.8496g^2 + 0.0610g^4}{1 - 0.7332g^2} \\ b_V &= \frac{1 - 0.6518g^2 - 0.1226g^4}{1 - 0.8467g^2}. \end{aligned} \quad (2.150)$$

In these channels (V,AV), the non-perturbatively determined renormalization constants will be used from now on, whereas in other channels (P,S) we rely on the values obtained from the TI perturbation theory presented above. A complete list of these perturbatively and non-perturbatively determined constants for the particular couplings and quark masses can be found in Appendix B (Tabs. B.3 and B.4). They differ at most by 2% in those channels where both values are available. Concerning the HF action we still did not determine the renormalization constants.

2.8 Mesonic correlation and spectral functions

In this section the formulation of temporal as well as spatial hadronic correlations and their relation to the SPF is given. Additionally some of their properties are discussed. The local and flavor non-singlet operators are given and some of their properties are described.

2.8.1 Temporal correlations

Hadronic properties like masses or decay constants of various particles can be extracted from the CFs of their associated currents \mathcal{J}_H ,

$$\begin{aligned} \mathcal{J}_H^M(x) &= \bar{\psi}_A(x)\Gamma_H^M\psi_B(x) && \text{for mesons,} \\ \mathcal{J}_H^B(x) &= \epsilon_{ijk}\Gamma_H^{B(1)}\psi_A^k(x)\left(\psi_B^i(x)\Gamma_H^{B(2)}\psi_C^j(x)\right) && \text{for baryons.} \end{aligned} \quad (2.151)$$

Here Γ_H^M can be any linear combination of the 16 independent Dirac-matrices ($\Gamma \in \text{Span}\{\mathbf{1}, \gamma_5, \gamma_\mu, \gamma_\mu\gamma_5, \sigma_{\mu\nu}\}$) and fixes the quantum number of the channel to scalar, pseudoscalar, vector, axial-vector and tensor channels correspondingly, while $\Gamma_H^{B(1,2)} \in \{\mathbf{1}, i\mathbf{1}, \gamma_5, C, C\gamma_5, C\gamma_\mu, C\gamma_4\gamma_5\}$.

The correlators in quenched formulation Eq. (2.81) and Euclidian time $\tau \in [0, 1/T]$ ($\langle \dots \rangle$ denotes the expectation value at finite T) have the form

$$\begin{aligned} G_H(x_f, x_i) &= \langle \mathcal{J}_H(x_f) \mathcal{J}_H^\dagger(x_i) \rangle \\ &= \frac{1}{Z} \int dU d\bar{\psi} d\psi (\bar{\psi}_A(x_f) \Gamma_H \psi_B(x_f)) (\bar{\psi}_B(x_i) \Gamma_H^\dagger \psi_A(x_i)) e^{-S} \\ &= \frac{1}{Z} \int dU \text{Tr} \left(M^{-1}(x_f, x_i) \Gamma_H M^{-1}(x_i, x_f) \Gamma_H^\dagger \right) \\ &\quad - \text{Tr} \left(\Gamma_H M^{-1}(x_f, x_f) \right) \text{Tr} \left(\Gamma_H^\dagger M^{-1}(x_i, x_i) \right) e^{-S_G(U)} \end{aligned} \quad (2.152)$$

$$= x_i \text{---} \text{---} x_f - x_i \text{---} \text{---} x_f, \quad (2.153)$$

where A and B are the different quark flavors, while Tr implies the trace over color and Dirac indices. The second term describes disconnected diagrams in which each of the quark line starts and ends at the same point. In case of the correlators with $A \neq B$ the contributions from the disconnected diagram vanishes. Taking advantage of Eq. (2.102) we then find our two-point function

$$G_H(x_f, x_i) = \left\langle \text{Tr} \left(M^{-1}(x_f, x_i) \Gamma_H \gamma_5 (M^{-1})^\dagger(x_f, x_i) \gamma_5 \Gamma_H^\dagger \right) \right\rangle_{\mathcal{U}}. \quad (2.154)$$

This corresponds to non-singlet (isovector) channels ($I = 1$), which we consider from now on, see Tab. 2.7. Due to translation invariance, we can write $G_H(x_f, x_i) = G_H(x_f - x_i, 0) = G_H(x, 0) = G_H(x)$. Note that this Euclidean correlator is an analytic continuation of the real time correlator $D_H^>(t) = \langle \mathcal{J}_H(t) \mathcal{J}_H(0) \rangle$, $G_H(\tau, T) = D_H^>(-i\tau, T)$. In spatial momentum space this correlator is

$$\begin{aligned} G_H(\tau, \mathbf{p}) &= \sum_{\mathbf{x}} G_H(\tau, \mathbf{x}) e^{-i\mathbf{p} \cdot \mathbf{x}} \\ &= \sum_{\mathbf{x}} \langle 0 | \mathcal{J}_H(x) \mathcal{J}_H^\dagger(0) | 0 \rangle e^{-i\mathbf{p} \cdot \mathbf{x}} \\ &= \sum_{\mathbf{x}} \langle 0 | e^{\hat{\tau} \hat{H} - i\hat{\mathbf{q}} \cdot \hat{\mathbf{x}}} \mathcal{J}_H(0) e^{-\hat{\tau} \hat{H} + i\hat{\mathbf{q}} \cdot \hat{\mathbf{x}}} \mathcal{J}_H^\dagger(0) | 0 \rangle e^{-i\mathbf{p} \cdot \mathbf{x}} \\ &= \sum_{\mathbf{x}} \sum_n \int \frac{d^3 \mathbf{q}}{(2\pi)^3 2E_H^n(\mathbf{q})} \langle 0 | e^{\hat{\tau} \hat{H} - i\hat{\mathbf{q}} \cdot \hat{\mathbf{x}}} \mathcal{J}_H(0) e^{-\hat{\tau} \hat{H} + i\hat{\mathbf{q}} \cdot \hat{\mathbf{x}}} | n, \mathbf{q} \rangle \langle n, \mathbf{q} | \mathcal{J}_H^\dagger(0) | 0 \rangle e^{-i\mathbf{p} \cdot \mathbf{x}} \\ &= \sum_n \int \frac{d^3 \mathbf{q}}{(2\pi)^3 2E_H^n(\mathbf{q})} \langle 0 | \mathcal{J}_H(0) | n, \mathbf{q} \rangle \langle n, \mathbf{q} | \mathcal{J}_H^\dagger(0) | 0 \rangle e^{-E_H^n(\mathbf{q})\tau} \sum_{\mathbf{x}} e^{-i\mathbf{q}\mathbf{x}} e^{-i\mathbf{p} \cdot \mathbf{x}} \\ &= \sum_n \int \frac{d^3 \mathbf{q}}{(2\pi)^3} \frac{A_H^n(\mathbf{q}) A_H^{n\dagger}(\mathbf{q})}{2E_H^n(\mathbf{q})} e^{-E_H^n(\mathbf{p})\tau} (2\pi)^3 \delta(\mathbf{q} - \mathbf{p}) \\ &= \sum_n \frac{|A_H^n(\mathbf{p})|^3}{2E_H^n(\mathbf{p})} e^{-E_H^n(\mathbf{p})\tau}. \end{aligned} \quad (2.155)$$

Here $A_H^n(\mathbf{p}) = \langle 0 | \mathcal{J}_H(0) | n, \mathbf{p} \rangle$ is the so called *Bethe-Salpeter amplitude*, which represents the overlap of the operator $\mathcal{J}_H(0)$ with the hadron state $|n\rangle$ and momentum \mathbf{p} . Note that the one-meson states having spatial momentum \mathbf{p} are normalized as

$$\langle n, \mathbf{p} | n, \mathbf{p}' \rangle = (2\pi)^3 2E_H^n \delta(\mathbf{p} - \mathbf{p}'). \quad (2.156)$$

The use of periodic boundary conditions gives rise to another term, describing a backward propagating particle and we arrive at

$$\begin{aligned} G_H(\tau, \mathbf{p}) &= \sum_n \frac{A_H^n(\mathbf{p})A_H^{n\dagger}(\mathbf{p})}{2E_H^n(\mathbf{p})} \left(e^{-E_H^n(\mathbf{p})\tau} + e^{-E_H^n(\mathbf{p})[N_\tau-\tau]} \right) \\ &= \sum_n \frac{A_H^n(\mathbf{p})A_H^{n\dagger}(\mathbf{p})}{E_H^n(\mathbf{p})} e^{-E_H^n(\mathbf{p})\frac{N_\tau}{2}} \cosh \left[E_H^n(\mathbf{p}) \left(\frac{N_\tau}{2} - \tau \right) \right]. \end{aligned} \quad (2.157)$$

Another way of looking at these CFs, *Matsubara Green's function*, is given by its Fourier transform [174]. Because they satisfy Eq. (1.19)

$$\begin{aligned} G_H(0, \mathbf{x}) &= G_H(\beta, \mathbf{x}) && \text{bosonic operators} \\ G_H(0, \mathbf{x}) &= -G_H(\beta, \mathbf{x}) && \text{fermionic operators} \end{aligned} \quad (2.158)$$

their Fourier transform is written with the Matsubara frequency $\omega_n = 2n\pi T$ for bosonic operators, or $\omega_n = (2n+1)\pi T$ for fermionic operators ($n=0, \pm 1, \pm 2, \dots$):

$$G_H(\tau, \mathbf{p}) = T \sum_{n=-\infty}^{\infty} \int_{-\infty}^{\infty} \frac{d^3p}{(2\pi)^3} e^{-i(\omega_n\tau - \mathbf{p}\mathbf{x})} G_H(\omega_n, \mathbf{x}). \quad (2.159)$$

$G_H(\omega_n, \mathbf{p})$ depends on the discrete Matsubara modes. The SPF $\sigma_H(\omega, \mathbf{p}, T)$ is the imaginary part of the momentum space operator

$$G_H(\omega_n, \mathbf{p}) = \int_{-\infty}^{\infty} \frac{\sigma_H(\omega, \mathbf{p}, T)}{\omega - i\omega_n + i\epsilon} d\omega \quad \Longrightarrow \quad \sigma_H(\omega, \mathbf{p}, T) = \frac{1}{\pi} \text{Im} G_H(\omega_n, \mathbf{p}). \quad (2.160)$$

Using equations Eq. (2.159) and Eq. (2.160) together with the identity

$$T \sum_n \frac{e^{-i\omega_n\tau}}{\omega - i\omega_n} = \frac{e^{-\tau\omega}}{1 - e^{-\omega/T}} \quad \text{with} \quad 0 < \tau < \frac{1}{T} \quad (2.161)$$

and the property of the SPF $\sigma(-\omega) = -\sigma(\omega)$,¹² the CF can then be written as

$$\begin{aligned} G_H(\tau, \mathbf{p}) &= T \sum_{n=-\infty}^{\infty} e^{-i\omega_n\tau} G_H(\omega_n, \mathbf{p}) \\ &= \int_{-\infty}^{\infty} T \sum_n \frac{e^{-i\omega_n\tau}}{\omega - i\omega_n} \sigma_H(\omega, \mathbf{p}, T) d\omega \\ &= \int_{-\infty}^{\infty} \frac{e^{-\tau\omega}}{1 - e^{-\omega/T}} \sigma_H(\omega, \mathbf{p}, T) d\omega \\ &= \int_0^{\infty} \frac{e^{-\tau\omega} + e^{(\tau-1/T)\omega}}{1 - e^{-\omega/T}} \sigma_H(\omega, \mathbf{p}, T) d\omega \\ &= \int_0^{\infty} \frac{\cosh(\omega(\tau - 1/(2T)))}{\sinh(\omega/(2T))} \sigma_H(\omega, \mathbf{p}, T) d\omega \\ &\equiv \int_0^{\infty} K(\tau, \omega, T) \sigma_H(\omega, \mathbf{p}, T) d\omega. \end{aligned} \quad (2.162)$$

The function $K(\tau, \omega, T)$ is the integration kernel in the continuum representation which is essential for the MEM analysis. For $T \rightarrow 0$ this function reduces to $K(\tau, \omega) = e^{-\tau\omega}$.

¹²this is a consequence of $D_H^>(-\omega) = D_H^<(\omega)$ derived from Eq. (1.19) and known as Kubo-Martin-Schwinger relation [175]

To get a rough idea how a zero temperature 'pole+continuum' parameterization for the SPF looks like, we show a SPF with a ground state energy $E_H = \sqrt{m_H^2 + \mathbf{p}^2}$ and continuum threshold $E_{H,c}$ ¹³

$$\sigma_H(\omega, \mathbf{p}) \equiv |\langle 0 | \mathcal{J}_H | H(\mathbf{p}) \rangle|^2 \text{sgn}(\omega) \delta(\omega^2 - E_H^2(\mathbf{p})) + \sigma_c \omega^2 \Theta(\omega^2 - E_{H,c}^2). \quad (2.164)$$

The correct form of the SPF could, however, be quite complicated. However, the continuum contribution reaches this behavior perturbatively due to asymptotic freedom. Nevertheless studying $G_H(\tau)$ without any closer specified ansätze is one of the aims of this thesis.

Inserting Eq. (2.164) into Eq. (2.162) with the kernel at zero temperature, it follows that at large distance (large τ) the exponential damping is dominated by the pole contribution. On the other hand, at short distance (small τ), the power behavior $1/\tau \exp(-E_{H,c}^2 \tau)$ from the continuum contribution leads to a divergent CF for $\tau=0$. Just taking the pole contribution into account, one gets the low temperature and large distance behavior of G_H

$$G_H(\tau, \mathbf{p}) = \frac{|\langle 0 | \mathcal{J}_H | H(\mathbf{p}) \rangle|^2 \cosh(E_H(\mathbf{p})(\tau - 1/(2T)))}{2E_H(\mathbf{p}) \sinh(E_H(\mathbf{p})/(2T))}. \quad (2.165)$$

In order to increase the number of points in time direction, e.g., for studying various temperatures or to get a better time resolution, but keeping the physical lattice size fixed, e.g., to avoid finite size effects, one can introduce *anisotropic lattices* with $a_\tau \neq a_\sigma$. However, this has the great disadvantage that the anisotropy factor a_σ/a_τ has to be tuned through additional simulations and a scale analysis becomes necessary. To avoid these additional computational efforts, we use only isotropic lattices.

In the high-temperature limit, where quarks and anti-quarks are supposed to move rather freely, their dynamics can be described to leading order by a modified SPF for massless quarks [174]

$$\sigma_H(\omega, \mathbf{p}) = \sigma_c \omega^2 \tanh(\omega/4T), \quad (2.166)$$

see also Section 3.2.

In the following we give a list of meson channels we examine in this thesis and their physical properties, i.e., decay constants f_H , masses m_H and thresholds $E_{H,c}$, on the basis of their lowest states.

Pseudoscalar channel ($H = P, \pi$): $\mathcal{J}_P = \bar{\psi} \gamma_5 \psi$

The current \mathcal{J}_P projects onto the $J^{PC} = 0^{-+}$ state. For a u- and d-quark combination this current corresponds to the pion, the Goldstone particle in the phase of spontaneously broken chiral symmetry. Thus, its ground state mass and excitation vanishes in the chiral limit. At zero temperature its amplitude is given by

$$\langle 0 | \mathcal{J}_P | P(\mathbf{p}) \rangle = f_P \frac{E_P^2}{2m_q} \Big|_{\mathbf{p}=\mathbf{0}} = f_P \frac{m_P^2}{2m_q}. \quad (2.167)$$

¹³This simple parameterization of SPF has been commonly used in QCD sum rules [176]. For a more realistic (relativistic Breit-Wigner) form of parameterization (see [177])

$$\sigma_V(\omega) = \frac{2}{\pi} \left[F_V^2 \frac{\Gamma_\rho m_\rho}{(\omega^2 - m_\rho^2)^2 + \Gamma_\rho^2 m_\rho^2} + \frac{1}{8\pi} \left(1 + \frac{\alpha_s}{\pi} \right) \frac{1}{1 + e^{2(\omega_0 - \omega)/\delta}} \right]. \quad (2.163)$$

Lowest order perturbation theory predicts for the pion state $\sigma_c = \frac{N_c}{8\pi^2}$. The corresponding experimental values at $T = 0$ are given as $f_\pi = 132$ MeV, $m_\pi = 139$ MeV and $E_{P,c} = 1.3$ GeV [27, 177] and with Eq. (2.165) one gets for the large τ behavior

$$G_P(\tau, \mathbf{p} = \mathbf{0}) = \frac{f_P^2 m_P^3}{8m_q^2} \frac{\cosh(m_P(\tau - 1/(2T)))}{\sinh(m_P/(2T))}. \quad (2.168)$$

Scalar channel ($H = S, a_0$): $\mathcal{J}_S = \bar{\psi}\psi$

The current \mathcal{J}_S projects onto $J^{PC} = 0^{++}$ quantum numbers. The identification of the scalar mesons is a long-standing puzzle. The reasons are their large decay widths and the many inelastic thresholds in the neighborhood of which scalar mesons lie. The established scalars are the $a_0(980)$ and $f_0(980)$ [27]. It is believed that the a_0 is not a regular $\bar{q}q$ meson but that it couples to $\bar{u}d\bar{s}s$ more than to $\bar{u}d$, since it can decay in $K\bar{K}$ pairs. Because of these uncertainties we parameterize the scalar CF simply as

$$G_S(\tau, \mathbf{p} = \mathbf{0}) = \lambda_S \frac{\cosh(m_S(\tau - 1/(2T)))}{\sinh(m_S/(2T))}. \quad (2.169)$$

Vector channel ($H = V, \rho$): $\mathcal{J}_V = \sum_{i=1}^3 \bar{\psi}\gamma_i\psi$

The current $\mathcal{J}_{V,\mu}$ projects onto a polarization state of a vector meson $J^{PC} = 1^{--}$. In this channel one has to take care of the polarization ϵ_μ

$$\langle 0 | \mathcal{J}_{V;\mu} | V(\mathbf{p}) \rangle = \frac{E_V^2(\mathbf{p})}{Z_V f_V} \epsilon_\mu \quad (2.170)$$

Summing over the polarizations leads to

$$|A_V(\mathbf{p})|^2 = \sum_{\mu=1}^3 |\langle 0 | \mathcal{J}_{V;\mu} | V(\mathbf{p}) \rangle|^2 = - \left(\frac{E_V^2(\mathbf{p})}{f_V} \right)^2 \sum_{\mu=1}^3 \left(g_{\mu\mu} - \frac{p_\mu^2}{p^2} \right) \stackrel{\mathbf{p}=\mathbf{0}}{=} 3 \frac{m_V^4}{f_V^2}. \quad (2.171)$$

and therefore using Eq. (2.165)

$$G_V(\tau, \mathbf{p} = \mathbf{0}) = 3 \frac{m_V^3}{2f_V^2} \frac{\cosh(m_V(\tau - 1/(2T)))}{\sinh(m_V/(2T))}. \quad (2.172)$$

Perturbation theory and the experiment give $\sigma_c = \frac{N_c}{4\pi^2}$ and $E_{V,c} = 1.6$ GeV, $m_\rho = 771(1)$ MeV, $f_\rho^{-1} = 0.2$ [27, 177].

Axial-vector channel ($H = AV, a_1$): $\mathcal{J}_A = \sum_{i=1}^3 \bar{\psi}\gamma_i\gamma_5\psi$

The lightest hadron found with the quantum numbers $J^{PC} = 1^{++}$ is $a_1(1260)$. The experimental measured mass for the a_1 is 1230(40) GeV and $f_{a_1} \simeq f_\rho$. Its temporal component mixes also with the pseudoscalar state with a different sign. The ansatz for the SPF is therefore

$$\sigma_A(\omega, \mathbf{p}) = + |\langle 0 | \mathcal{J}_A | A(\mathbf{p}) \rangle|^2 \delta(\omega^2 - E_A^2(\mathbf{p})) - |\langle 0 | \mathcal{J}_A | P(\mathbf{p}) \rangle|^2 \delta(\omega^2 - E_P^2(\mathbf{p})) + \sigma_c \omega^2 \Theta(\omega^2 - E_{A,P,c}^2(\mathbf{p})) \quad (2.173)$$

and the matrix element

$$\langle 0 | \mathcal{J}_{A,\mu} | A_\mu(\mathbf{p}) \rangle = \frac{E_A^2(\mathbf{p})}{f_A} \epsilon_\mu. \quad (2.174)$$

This allows in principle for a negative SPF and has to be taken into account for the fit ansatz.

Channel	Correlator	J^{PC}	$I = 1$	$I = 0$
PS	$\sum_{\mathbf{x}} \langle 0 \bar{u}(x) \gamma_5 d(x) [\bar{u}(0) \gamma_5 d(0)]^\dagger 0 \rangle e^{-i\mathbf{p}\cdot\mathbf{x}}$	0^{-+}	$\pi^{0,\pm}(138), (\pi)$	$\eta(547), (\eta')$
S	$\sum_{\mathbf{x}} \langle 0 \bar{u}(x) d(x) [\bar{u}(0) d(0)]^\dagger 0 \rangle e^{-i\mathbf{p}\cdot\mathbf{x}}$	0^{++}	$a_0(980), (\delta)$	$f_0(980?), (\sigma)$
V	$\sum_{\mathbf{x}} \langle 0 \bar{u}(x) \gamma_i d(x) [\bar{u}(0) \gamma_i d(0)]^\dagger 0 \rangle e^{-i\mathbf{p}\cdot\mathbf{x}}$	1^{--}	$\rho(770)^{0,\pm}$	$\omega(782)$
AV	$\sum_{\mathbf{x}} \langle 0 \bar{u}(x) \gamma_5 \gamma_i d(x) [\bar{u}(0) \gamma_5 \gamma_i d(0)]^\dagger 0 \rangle e^{-i\mathbf{p}\cdot\mathbf{x}}$	1^{++}	$a_1(1260)$	$f_1(1285)$

Tab. 2.7: CFs and corresponding quantum numbers for spin (J), parity (P) and charge conjugation (C) used in this thesis. The last two columns show the particles associated with the flavor triplet ($I=1$) and singlet ($I=0$) ground states.

2.8.2 Spatial correlations

Another method to extract hadronic information especially at non-zero temperature is to analyze the spatial correlators. They are obtained via an integration over the so-called *funny space* \tilde{V} [178], which includes the Euclidean time and two spatial directions, say $\tilde{\mathbf{x}} = (\mathbf{x}_\perp, \tau)$ and $\tilde{\mathbf{p}} = (\mathbf{p}_\perp, p_4 = \omega_n)$

$$G_H(z, \mathbf{p}_\perp, \omega_n) = \int_0^{1/T} d\tau \int d\mathbf{x}_\perp e^{-i(\tilde{\mathbf{p}}\cdot\tilde{\mathbf{x}})} G_H(z, \mathbf{x}_\perp, \tau) \quad (2.175)$$

with $\mathbf{p}_\perp = (p_x, p_y)$ and $\mathbf{x}_\perp = (x, y)$. Its connection to the temporal correlator can again be shown by the SPF. As we have seen at zero-temperature the SPF depends on p^2 only, which is a consequence of the equivalence between temporal and spatial direction in Euclidean time. At non-zero temperature the temporal direction is distinguishable from the spatial one by its finite extent. Physically this corresponds to a four-velocity of a (static) heat bath in n_4 -direction. The presence of such a heat bath introduces modification to the dispersion relation, so that in general $p^2 \neq m_H^2$. Correspondingly the SPF depends on p_4 and \mathbf{p} separately. The corresponding ground state mass in spatial direction, called *screening mass*, may thus differ from the one in time direction, called *pole mass*, which is in contrast to $T=0$. The propagator in momentum space is then modified by the vacuum polarization tensor $\Pi(p, T)$, which contains the modifications to the heat bath

$$\begin{aligned} G_H(\mathbf{p}, \omega_n) &= \int_0^{1/T} d\tau \int d^3\mathbf{x} G_H(x) e^{-i\omega_n\tau - i\mathbf{p}\mathbf{x}} \\ &= \frac{1}{\omega_n^2 + m_H^2 + \mathbf{p}^2 + \Pi(p, T)} \end{aligned} \quad (2.176)$$

To illustrate such modifications a simple model can be assumed [179], where the dispersion relation in Eq. (2.176) is written as

$$E_H^2(\mathbf{p}, T) = m_H^2 + \mathbf{p}^2 + \Pi(p, T) = m_H^2(T) + A^2(T)\mathbf{p}^2. \quad (2.177)$$

In this parameterization the whole temperature dependence is absorbed in the mass $m_H(T)$ and an additional factor $A(T)$, which is equal to one at zero temperature. This should be a valid description at least for low temperatures. Using Eq. (2.176) one gets

$$\begin{aligned} G_H(z, \mathbf{p}_\perp, \omega_n) &= \int_{-\infty}^{\infty} \frac{dp_z}{2\pi} e^{ip_z z} G_H(\mathbf{p}, \omega_n) \\ &= \frac{1}{2\omega_z A^2(T)} e^{-\omega_z z} \end{aligned} \quad (2.178)$$

where

$$\omega_z^2 = E_z^2(\tilde{\mathbf{p}}, T) = \frac{\omega_n^2}{A^2(T)} + m_H^z{}^2(T) + \mathbf{p}_\perp^2 \quad (2.179)$$

and $E_z(\tilde{\mathbf{0}}, T) = m_H^z(T) = m_H(T)/A(T)$ the thermal screening mass. Obviously one still obtains an exponential decreasing CF with an energy, which is dominated by the thermal screening mass, that is actually the pole mass divided by $A(T)$. From the evaluation of the meson screening mass, governing the large distance behavior of the correlator, one can extract informations on the nature of the excitations characterizing the QGP. In the high-temperature limit, where mesonic bound state are supposed to be dissolved, their energies are dominated by the (almost) massless quarks and $E_z(\mathbf{p}_\perp) = 2\sqrt{\omega_n^2 + \mathbf{p}_\perp^2}$. Thus at zero momentum and in the infinite volume the ground state screening mass should be identical to twice the lowest quark Matsubara frequency, namely $2\pi T a = 2\pi/N_\tau$ [180].

2.8.3 Improvements (Fuzzing and Smearing)

To improve the overlap of our operators with their ground states and therefore to extract more reliable results of the corresponding masses, we use a technique, first introduced by R. GUPTA ET AL. [181] and further investigated by LACKOCK ET AL. [182]. The idea is to make the operators more physical in the sense that one introduces a spatial extension. The former local operators $\mathcal{J}_H(x)$ become now nonlocal $\mathcal{J}_H^R(x) = \tilde{\psi}^R(x)\Gamma_H\psi(x)$ by averaging over quarks separated by a distance Ra . To preserve gauge invariance these new quarks are connected by gauge links so one ends up with

$$\begin{aligned} \tilde{\psi}^R(x) = \frac{1}{6} \sum_{\mu=1}^3 (U_\mu^\dagger(x-\mu) \dots U_\mu^\dagger(x-R\hat{\mu})\psi(x-R\hat{\mu}) \\ + U_\mu(x) \dots U_\mu(x+(R-1)\hat{\mu})\psi(x+R\hat{\mu})) \end{aligned} \quad (2.180)$$

The new operator is depicted in Fig. 2.7(a) and leads to $G_H^R(x) = \langle \mathcal{J}_H^R(x)\mathcal{J}_H^\dagger(0) \rangle$. In our case we have used one quark fuzzed operator in the sink not only due to computational reasons (the source is fixed at $x=0$), but also because it has been argued by the authors in [182] that contributions from quark and anti-quark fuzzed operators would partially cancel and give rise to purely local terms. R is varied from 0 to 8.

Another way to mimic the mesonic spatial extent in more appropriate but unfortunately not gauge invariant way is to use *exponential fuzzing*. $G_H(\tau, \mathbf{x})$ with $\mathcal{J}(x; y) = \bar{\psi}(x)\Gamma_H\psi(y)$ becomes

$$G_H(\tau, \mathbf{x}) = \int \int dy_1 dy_2 w_1(y_1)w_2(y_2) \langle \mathcal{J}(\tau, \mathbf{x}; \mathbf{y}_1, 0)\mathcal{J}^\dagger(\mathbf{y}_2, 0; \tau, \mathbf{x}) \rangle \quad (2.181)$$

and

$$w_1(y_1)w_2(y_2) = \begin{cases} \delta(\mathbf{y}_1)\delta(\mathbf{y}_2), & \text{point-point} \\ \delta(\mathbf{y}_1)e^{-a|\mathbf{y}_2|^b}, & \text{point-exp} \\ e^{-a|\mathbf{y}_1|^b}e^{-a|\mathbf{y}_2|^b}, & \text{exp-exp} \end{cases} \quad (2.182)$$

Here a and b have to be adjusted such that the overlap with the ground state is maximized. This improvement scheme has not been implemented, because it needs an additional gauge fixing, which would enhance the computational effort.

To further enhance the contribution stemming from the gluonic cloud, we also spread the links in space. This is done by a technique called *APE-smearing* [183]. The old links U^{old} are replaced by new links U^{new} via

$$U_{\mu}^{new}(x) = \mathcal{P}_{SU(3)} \left(cU_{\mu}^{old}(x) + \sum_{\pm\nu \neq \mu < 4} U_{\mu\nu}^{staple}(x) \right), \quad (2.183)$$

see Fig. 2.7(b). $\mathcal{P}_{SU(3)}$ projects back to the $SU(3)$ group and c is an arbitrary parameter. For lattice cut-offs similar to those used in our calculations, it could be shown [182] that an optimum is gained by iterating this procedure eight times using $c=2$. We used 0, 4 and 8 smearing iterations (SI).

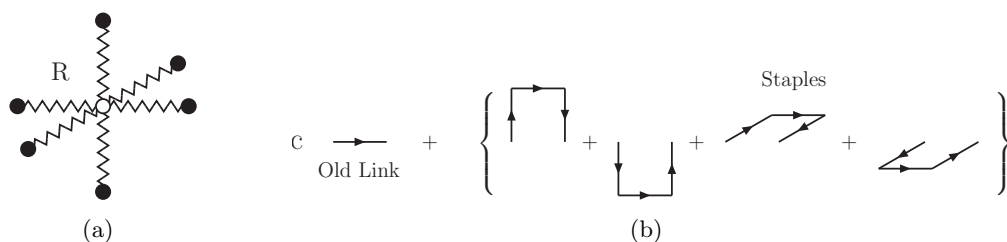


Fig. 2.7: Operator improvements: Fuzzing (a) and Smearing (b).

2.8.4 Determination of meson masses

The meson masses can be extracted from the exponential fall-off of the CFs at zero momentum $G_H(\tau, \mathbf{p}=\mathbf{0})$, which is governed by the Energy $E_H(\mathbf{p}=\mathbf{0})=m_H$. In this thesis we have used formally three different methods to determine the ground state masses of the particles.

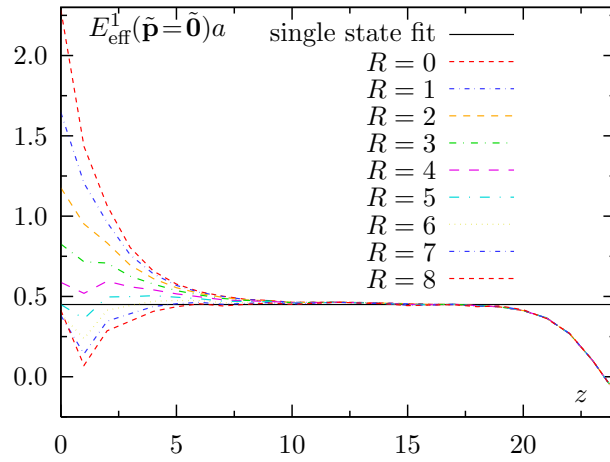
The easiest way and a first estimate to determine a ground state mass is to use the so-called *effective energy* definition, which is

$$E_{\text{eff}}^1(\tau, \mathbf{p}) = \ln \left(\frac{G_H^R(\tau, \mathbf{p})}{G_H^R(\tau + 1, \mathbf{p})} \right) \quad (2.184)$$

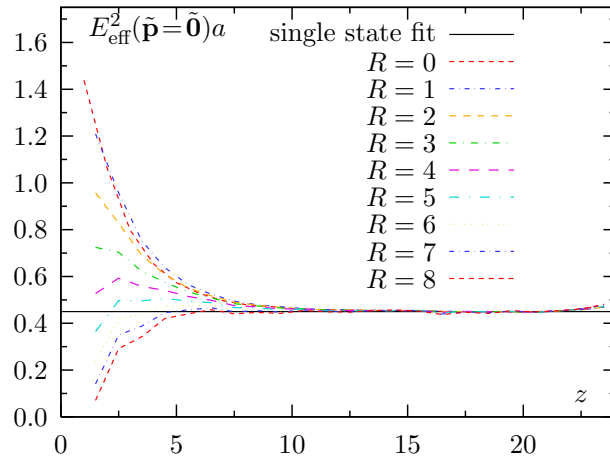
with the fuzzing radius R . For small distances this energy is strongly affected by higher excited states until it reaches a plateau. Here excited states have died out and a proper determination of the energy of the lowest state for $\mathbf{p}=\mathbf{0}$ becomes feasible. However, afterwards it falls down again due to the periodicity (hyperbolic cosine). Another way of defining an effective energy [184] now in accordance with the temporal periodicity at finite temperatures is to find a solution of the equation

$$\frac{G_H^R(\tau, \mathbf{p})}{G_H^R(\tau + 1, \mathbf{p})} = \frac{\cosh [E_{\text{eff}}^2(\tau, \mathbf{p})(\tau - N_\tau/2)]}{\cosh [E_{\text{eff}}^2(\tau, \mathbf{p})(\tau + 1 - N_\tau/2)]}, \quad (2.185)$$

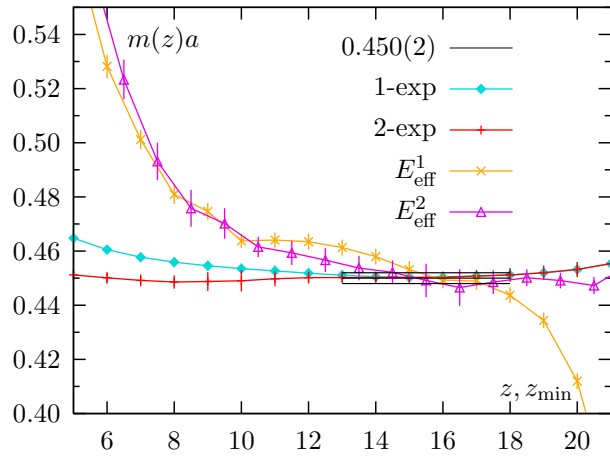
e.g., with Newton-Raphson's method. This choice extends the plateau to larger distances. In both cases it is seen that fuzzing and smearing indeed suppresses higher states, so that the plateau sets in at smaller distances. From Fig. 2.8 on can conclude $R=4-5$ to be most suitable, although it depends slightly on the momentum, the mass as well as on the temperature. However, for definiteness we decided to take $R=5$ as an optimal value. The number of smearing iterations plays only a minor role and has no influence on the final result. The third choice to determine the ground state mass is to fit the CFs via one- or two state fit



(a)



(b)



(c)

Fig. 2.8: Effective screening energy (mass) for a 'smeared' P at $T = 0.55$, $48^3 \times 16$ and $\kappa = 0.13300$ with Eq. (2.184) (a) and Eq. (2.185) (b) at various radii $0 \leq R \leq 8$. For better visibility the errors have been omitted but shown in (c). Comparison of various methods on the same data at $R=0$ (c). The plateau from the coincidence of one- and two state mass fits is shown by black lines.

ansätze Eq. (2.157) ($n = 1, 2$). The fit range of τ_{min} up to $N_\tau - \tau_{min}$ is then varied. This allows also to extract the amplitudes and, by varying R , also the Bethe-Salpeter amplitudes (see Section 4.2). We used all three methods concurrently as a cross-check where possible. However, final quotes on mass values are mostly obtained from the global fits of correlators since, in most cases, the effective mass estimates become noisier and less stable. The same methods are also applicable to spatial correlators.

3 Maximum entropy method with free data

A reasonable probability is the only certainty.

E.W. Howe

In this chapter we will outline the *Maximum Entropy Method* (MEM), which we will use to tackle the ill-posed problem of Eq. (2.162). Namely we need to reconstruct SPFs $\sigma_H(\omega)$, which consist of $\mathcal{O}(10^3)$ points from lattice correlations $G_H(\tau, \mathbf{p})$ available at $\mathcal{O}(10)$ points

$$\begin{aligned} G_H(\tau_i, \mathbf{p}) &= \int_0^\infty K(\tau_i, \omega) \sigma_H(\omega, \mathbf{p}) d\omega = \sum_{j=0}^{N_\omega} K(\tau_i, \omega_j) \sigma_H(\omega_j, \mathbf{p}) \Delta\omega \\ &= \sum_{j=0}^{N_\omega} K_{ij} \sigma_j^H \Delta\omega \quad \omega_j = j \cdot \Delta\omega, \end{aligned} \quad (3.1)$$

where N_ω is the number of $\Delta\omega$ intervals within $[0, \omega_{max}]$. The MEM is based on Bayes' rule and has been successfully used over the past years in various fields of research. In LQCD the MEM has been applied at zero as well as at finite temperature. It was found to work very well for extracting masses and decay constants of ground and even excited states from CFs at zero temperature [185]. Hence, it was also used for analyzing temperature correlators using Eq. (3.1) to investigate properties of mesonic observable in heat bath, see e.g. [11, 186]. Here we will describe its functionality and discuss several features.

The second section of this chapter is devoted to the analytic derivation of the free continuum and lattice CFs and SPFs for the Wilson and the truncated FPA. The latter can be utilized as an input (default) model for the MEM in our later analysis in Chapter 4. On the lattice free means $g \rightarrow 0 \Leftrightarrow \beta \rightarrow \infty$, which corresponds to setting all gauge links to unity. The free SPFs are considered to better represent the high energy part of the SPF in comparison to the commonly used continuum form $\sigma_c \omega^2$ with an additionally fixed ω_{max} .

Already the first studies of the MEM in an interacting theory, see e.g. [11, 72, 185], revealed the presence of lattice artifacts in the SPF, which are quite different from the cut-off effects in the free case. Additional bumps in ω observed at $T = 0$ showed a scaling with a (provided ω is in physical units), which is not physical for higher excited states and lead to the interpretation as bound states of doublers. We will focus on that also in Chapter 4. The next sections serve as a short summary of what was found and described in more detail in [187, 188], with a small but important correction to the high energy part of the free hypercube SPF. Finally the dependencies of the MEM on the input parameters is briefly reviewed.

3.1 Bayes' theorem and maximum entropy method

According to a theorem by BAYES [189] the joint probability of two events $P[A, B]$ can be written in terms of a conditional probability as

$$P[A, B] = P[A|B]P[B] = P[B|A]P[A] \quad \Leftrightarrow \quad P[A|B] = \frac{P[B|A]P[A]}{P[B]}, \quad (3.2)$$

where $P[A|B]$ is the conditional probability of A given B , and $P[A]$ is the probability of A , and $P[B|A]$ vice versa. This theorem is used to infer the probability of an SPF denoted by σ given the lattice correlator G and prior knowledge parameterized in H :

$$P[\sigma|GH] = \frac{P[G|\sigma H]P[\sigma|H]}{P[G|H]}. \quad (3.3)$$

Here $P[\sigma|GH]$, $P[G|\sigma H]$, and $P[\sigma|H]$ are called the *posterior probability*, the *likelihood*, and the *prior probability*, respectively.

3.1.1 Likelihood and likelihood function

Following the central limit theorem, which states that for a large number of measurements the data obey a Gaussian distribution, the functional form of $P[G|\sigma H]$ is well known and can be expressed via usual χ^2 by

$$P[G|\sigma H] \sim \exp(-L) = \exp\left(-\frac{\chi^2}{2}\right) \quad (3.4)$$

with

$$\chi^2 = \sum_{ij} (G(\tau_i) - G^t(\tau_i)) C_{ij}^{-1} (G(\tau_j) - G^t(\tau_j)), \quad (3.5)$$

where $G(\tau_i)$ is the average over all measurements and $G^t(\tau_i) = \sum_j K_{ij} \sigma_j^t \Delta\omega$ is the CF of a trial SPF $\sigma^t(\omega_j)$. C_{ij} denotes the symmetric covariance matrix, which has already been described in Eq. (2.116). Without any prior knowledge H , $P[\sigma] = \text{constant}$ and maximizing $P[\sigma|G]$ is equivalent to maximizing $P[G|\sigma]$ (Eq. (3.3)). This results in the standard χ^2 -fitting procedure in Section 2.4.5. However, it requires more data points than fit parameters and is therefore not appropriate for our problem.

3.1.2 Prior probability

The extra ingredient of the MEM is its prior probability $P[\sigma|H]$. It is obtained by introducing external information (prior knowledge) H on σ , such as $\sigma \geq 0$ or even a functional form for σ denoted by $m(\omega)$ (default model). Using the axioms locality, coordinate invariance, system independence and scaling [11, 190–192] a functional $S(\sigma)$, which gives

$$\sigma_1 \text{ is a more plausible image than } \sigma_2 \Leftrightarrow S(\sigma_1) > S(\sigma_2) \quad (3.6)$$

can uniquely be fixed as the Shannon-Jaynes entropy

$$S(\sigma) = \int_0^\infty \left[\sigma(\omega) - m(\omega) - \sigma(\omega) \ln \left(\frac{\sigma(\omega)}{m(\omega)} \right) \right] d\omega \quad (3.7)$$

$$= \sum_{j=0}^{N_\omega} \left[\sigma(\omega_j) - m(\omega_j) - \sigma(\omega_j) \ln \left(\frac{\sigma(\omega_j)}{m(\omega_j)} \right) \right] \Delta\omega. \quad (3.8)$$

The prior probability can then be written as

$$P[\sigma|H] = P[\sigma|\alpha m] \sim \exp(\alpha S(\sigma)). \quad (3.9)$$

Here the real and positive factor α controls the weight between entropy and likelihood function and will be integrated out in the final result. For large α the resulting SPF is dominated by

the default model, while small α corresponds to best fitting the lattice data. A critical remark might already be added: because even small differences between a trial SPF and the default model function make the entropy term large, the default model function strongly affects the outcome of the MEM when the data quality is not sufficient. Therefore the default model should include only reliable information we know beforehand. If not, there is a risk the result might be controlled by hand [193].

3.1.3 Outline of the MEM procedure

In principle there are three different methods, which differ in the way they handle α : The historical, the classical [190] and R.K. BRYAN's method [194]. The latter is superior to the other two in searching for the maximum of $P[\sigma|G\alpha m]$ and can be divided into mainly three parts.

Searching for the most probable image σ_α for a given α

The most probable SPF with given α , σ_α , is obtained by maximizing $P[\sigma|G\alpha m]$ thus

$$\left. \frac{\delta P[\sigma|G\alpha m]}{\delta \sigma} \right|_{\sigma=\sigma_\alpha} \propto \left. \frac{\delta P[\sigma|\alpha m]P[\sigma|G]}{\delta \sigma} \right|_{\sigma=\sigma_\alpha} = 0 \quad \Leftrightarrow \quad (\alpha \nabla_\sigma S - \nabla_\sigma L)|_{\sigma=\sigma_\alpha} = 0 \quad (3.10)$$

with

$$\nabla_\sigma S = - \sum_j \ln \left(\frac{\sigma(\omega_j)}{m(\omega_j)} \right) \quad \text{and} \quad \nabla_\sigma L = \frac{\partial L}{\partial G^t} \frac{\partial G^t}{\partial \sigma} = \frac{\partial L}{\partial G^t} K^T. \quad (3.11)$$

Since $\sigma(\omega_i)$ is of $\mathcal{O}(10^3)$, $K(\tau_i, \omega_j)$ is a large matrix, whose dimension can be reduced substantially using the so-called *singular value decomposition*. K can be written as product $K = V \Xi U^T$ with U and V being orthogonal matrices and Ξ a diagonal matrix with ordered singular values ξ_i . Since most ξ_i are very small or even zero, the space can be reduced to the 'singular space' with dimension $N_s \leq N_\tau$ by a criterion, e.g., $\xi_{min} > 10^{-6} \xi_{max}$. Its basis is spanned by the first N_s columns of U containing the $N_\omega \times N_s$ matrix $U^{(s)}$ and the $N_\tau \times N_s$ matrix $V^{(s)}$. Due to the fact that the SPF σ is positive semi-definite, it can thus be parameterized using the orthogonal matrix U^s and a vector u in this singular space:

$$\sigma(\omega_j) = m(\omega_j) \exp \sum_{k=1}^{N_s} U_{jk}^{(s)} u_k. \quad (3.12)$$

Substituting the decomposition of K and Eq. (3.12) into Eq. (3.10) gives

$$f(u) = -\alpha u - \frac{\partial L}{\partial G^t} \Xi V^T = 0, \quad (3.13)$$

an equation, which can be solved by a standard Newton search. For a more detailed description see [186] or BRYAN [194].

Averaging over α

The final SPF is then determined by a weighted ($P[\sigma|Gm]$) average over all possible $\sigma(\omega)$

$$\begin{aligned} \bar{\sigma}(\omega) &= \int \mathcal{D}\sigma \sigma(\omega) P[\sigma|Gm] \\ &= \int d\alpha \int \mathcal{D}\sigma \sigma(\omega) P[\sigma|G\alpha m] P[\alpha|Gm] \\ &\approx \int d\alpha \sigma_\alpha(\omega) P[\alpha|Gm]. \end{aligned} \quad (3.14)$$

Here we have assumed that $P[\sigma|G\alpha m]$ is sharply peaked around σ_α which is considered to be a valid approximation for data with small errors. Using the identity

$$P[G|m\alpha] = \int \mathcal{D}\sigma P[G|\sigma m\alpha]P[\sigma|m\alpha] \quad (3.15)$$

and again Bayes' theorem leads to

$$\begin{aligned} P[\alpha|Gm] &= \int \mathcal{D}\sigma P[G|\sigma m\alpha]P[\sigma|m\alpha] \cdot \frac{P[\alpha|m]}{P[G|m]} \\ &\propto P[\alpha|m] \int \mathcal{D}\sigma e^{Q(\alpha,\sigma)} \end{aligned} \quad (3.16)$$

with $Q(\alpha, \sigma) = \alpha S(\sigma) - L(\sigma)$. Again the same approximation as in Eq. (3.14) has been made for the second line. For $P[\alpha|m]$ any flat function can be used. We use $P[\alpha|m] = 1/\alpha$ in Eq. (3.14) as proposed by JEFFREY [195] on grounds of scale invariance¹. Since σ_α maximizes Q and $P[\alpha|Gm]$ turns out to be sharply peaked around some value α (see Fig. 3.5), a Gaussian approximation of the integral in Eq. (3.16) [186, 196] by expanding Q with respect to $\delta\sigma_i = \sigma_i - (\sigma_\alpha)_i$,

$$Q(\alpha, \sigma) \simeq Q(\alpha, \sigma_\alpha) - \frac{1}{2} \sum_{i,j} \delta\sigma_i (\alpha\delta_{ij} + \Lambda_{ij}) \delta\sigma_j \quad (3.17)$$

becomes suitable. This gives

$$P[\alpha|Gm] \simeq \frac{1}{\alpha} \exp \left\{ \frac{1}{2} \sum_i \ln \left(\frac{\alpha}{\alpha + \lambda_i} \right) + Q(\alpha, \sigma_\alpha) \right\} \quad (3.18)$$

with the eigenvalues λ_i of the real symmetric matrix

$$\Lambda_{ij} = \left. \frac{\partial^2 L}{\partial\sigma_i \partial\sigma_j} \right|_{\sigma=\sigma_\alpha} \quad (3.19)$$

and simplifies the computational effort. Normalizing $P[\alpha|Gm]$, such that $\int P[\alpha|Gm]d\alpha = 1$, the SPF can thus be determined.

Error analysis

Since $\sigma(\omega)$ for successive ω bins are highly correlated, an error can only be estimated over a certain range of ω , $I = [\omega_i, \omega_f]$. Then

$$\langle \sigma_\alpha \rangle_I \simeq \frac{\int_I d\omega \sigma_\alpha(\omega)}{\int_I d\omega} \approx \frac{\sum_{j \in I} \sigma_\alpha(\omega) \Delta\omega}{(\omega_f - \omega_i)} \quad (3.20)$$

$$\langle (\delta\sigma_\alpha)^2 \rangle_I = \frac{1}{(\omega_f - \omega_i)^2} \int d\sigma \int_{I \times I} d\omega d\omega' \delta\sigma(\omega) \delta\sigma(\omega') P[\sigma|Gm\alpha] \quad (3.21)$$

with $\delta\sigma = \sigma(\omega) - \sigma_\alpha(\omega)$. Again the final result is obtained by integrating over α like in Eq. (3.14).

¹a factor, which can be absorbed in the integration measure ($d\alpha \rightarrow d\ln(\alpha)$) in Eq. (3.14)

3.2 Free correlation functions in their spectral representation

In this section a complete definition of the free CF and their spectral representation in the continuum is reviewed. Due to asymptotic freedom of QCD the free-field limit is approached at infinite temperature. Then a discretized version of these for the Wilson and the truncated FPA is formulated on the lattice. This follows closely the calculations, which have already been presented in [187, 197] with only minor modifications. These definitions are necessary for a complete understanding of the MEM result and the comparisons to the continuum theory presented in Chapters 4 and 5.

3.2.1 Continuum correlation and spectral functions

The computation of the continuum CF starts with the free fermion spectral function $\sigma_F(k_0, \mathbf{k})$ and the free fermion propagator $S_F(i\omega_n, \mathbf{k})$ in momentum space,

$$S_F(i\omega_n, \mathbf{k}) = \int_{-\infty}^{\infty} \frac{dk_0}{2\pi} \frac{\sigma_F(k_0, \mathbf{k})}{i\omega_n - k_0} \quad (3.22)$$

$$\sigma_F(k) = 2\pi \text{sgn}(k_0) [k_\mu \gamma_\mu + m_q] \delta(k^2 - m_q^2) \quad (3.23)$$

with the fermionic Matsubara frequencies $\omega_n = (2n + 1)\pi T$. With these, one obtains the meson SPF as the imaginary part of the momentum space correlator Eq. (2.160)

$$\sigma_H^{cont}(\omega, \mathbf{p} = \mathbf{0}) = \frac{1}{\pi} \text{Im} \ T N_c \sum_{n=-\infty}^{\infty} \iiint_{-\infty}^{\infty} \frac{d^3 k}{(2\pi)^3} \text{Tr} [\gamma_5 \Gamma_H S_F(i\omega_n, \mathbf{k}) \Gamma_H^\dagger \gamma_5 S_F(i\omega_n - \omega, \mathbf{k})], \quad (3.24)$$

which leads to [174, 187, 198, 199]

$$\begin{aligned} \sigma_H^{cont}(\omega) &= \frac{N_c}{8\pi^2} \Theta(\omega - 2m_q) \omega^2 \tanh(\omega/4T) \sqrt{1 - \left(\frac{2m_q}{\omega}\right)^2} \left(a_H + b_H \left(\frac{2m_q}{\omega}\right)^2 \right) + \\ &\quad \frac{N_c}{\pi^2 T} \omega \delta(\omega) \int_m^\infty dp_0 p_0^2 \sqrt{1 - \frac{m^2}{p_0^2}} \left(f_H^1 + f_H^2 \frac{m^2}{p_0^2} \right) e^{p_0/T} n_F^2(p_0), \end{aligned}$$

where $n_F(\omega) = 1/(e^{\omega/T} + 1)$ is the Fermi distribution. Further SPFs always implicitly assume zero momentum $\mathbf{p} = \mathbf{0}$. The factors a_H, b_H, f_H^1 and f_H^2 , introduced here, are given for different quantum number channels in Tab. 3.1. In the massless limit SPFs are chirally symmetric, $|\sigma_P| = |\sigma_S|$ and $|\sigma_V| = |\sigma_{AV}|$. The first term is the leading order perturbation result for the continuum and Eq. (3.25) leads to the constants σ_c for $\omega \rightarrow \infty$ as introduced in Section 2.8. The continuum CFs for instance for the P case in the chiral limit can be obtained from this SPF by using Eq. (2.157) and equal those derived in Ref. [180]:

$$\frac{G_P^c(\tau T)}{T^3} = \pi N_c (1 - 2\tau T) \frac{1 + \cos^2(2\pi\tau T)}{\sin^3(2\pi\tau T)} + 2N_c \frac{\cos(2\pi\tau T)}{\sin^2(2\pi\tau T)}. \quad (3.25)$$

Here G_P^c is rescaled with the temperature to obtain a dimensionless quantity. As in the high-temperature limit T is the only relevant scale, all quantities with a nontrivial dimension in this chapter will be rescaled from now on, i.e.,

$$\omega \rightarrow \tilde{\omega} = \frac{\omega}{T} \quad \sigma \rightarrow \tilde{\sigma} = \frac{\sigma}{T^2} \quad G_H \rightarrow \tilde{G}_H = \frac{G_H}{T^3} \quad \tau \rightarrow \tilde{\tau} = \tau T. \quad (3.26)$$

Thus we have

$$\tilde{G}_H(\tilde{\tau}) = \int_0^\infty d\tilde{\omega} \tilde{\sigma}(\tilde{\omega}, T) \tilde{K}(\tilde{\omega}, \tilde{\tau}, T) \quad (3.27)$$

with the dimensionless kernel

$$K \rightarrow \tilde{K} = \cosh(\tilde{\omega}(\tilde{\tau} - 1/2)) / \sinh(\tilde{\omega}/2). \quad (3.28)$$

However, it is sometimes also useful to maintain the explicit temperature dependence of the distance, i.e., the notation τT or zT for discussing the cut-off dependence.

3.2.2 Wilson fermion correlation and spectral functions

The starting point for our discussion is the Wilson fermion propagator in momentum space generalized to anisotropic lattices $\xi = a_\sigma/a_\tau \geq 1$ and for the moment arbitrary r_τ and $r_\sigma = r$. It is given by

$$\Delta^W(k) = \frac{-i\gamma_4 \sin(k_4) - i\mathcal{K} + [r_\tau(1 - \cos(k_4)) + \mathcal{M}]}{\sin^2(k_4) + \mathcal{K}^2 + [r_\tau(1 - \cos(k_4)) + \mathcal{M}]^2}, \quad (3.29)$$

$$\mathcal{M} = \frac{1}{\xi} \left[r \sum_{i=1}^3 (1 - \cos(k_i)) + m_q \right], \quad (3.30)$$

$$\mathcal{K} = \frac{1}{\xi} \sum_{i=1}^3 \gamma_i \sin(k_i), \quad (3.31)$$

where we have set $a_\tau = 1 \Rightarrow a_\sigma = \xi$. The corresponding dispersion relation is defined by the two poles $k_4 = iE_-$ and $k_4 = \pi + iE_+$ of the propagator

$$\begin{aligned} \cosh(E_\pm(\mathbf{k})) &= \frac{\mathcal{U} \pm r_\tau(r_\tau + \mathcal{M})}{1 - r_\tau^2} \\ \mathcal{U}^2 &= (1 + r_\tau \mathcal{M})^2 + (1 - r_\tau^2)(\mathcal{K}^2 + \mathcal{M}^2). \end{aligned} \quad (3.32)$$

In the limit $m, \mathbf{k} \rightarrow 0$ and $r \neq 0 \neq r_\tau$ Eq. (3.32) simplifies and leads to $\cosh(E_\pm) = \frac{1 \pm r^2}{1 - r^2}$. If additionally the limit $r_\tau \rightarrow 1$ is taken, the contribution of the negative pole E_- corresponding to physical quark mass m at $\mathbf{k} = \mathbf{0}$ is zero, as it should be, while E_+ as the corresponding mass for the doublers diverges. However, also for finite \mathbf{k} the limit $r_\tau \rightarrow 1$ eliminates the ghost branch by changing the dispersion relation to

$$\cosh E_-(\mathbf{k}) = 1 + \frac{\mathcal{K}^2 + \mathcal{M}^2}{2(1 + \mathcal{M})}, \quad E_+(\mathbf{k}) \rightarrow \infty \quad (3.33)$$

(see Fig. 3.2(a)). In the next step we derive an analytic expression for the quark propagator $S^W(\tau, \mathbf{k})$ in a discretized time. This can be done by analytic continuation of $\Delta^W(k)$ in k_4 and by taking the limit $N_\tau \rightarrow \infty$. This allows to compute the Fourier transform of the quark propagator

$$S_\infty^W(\tau, \mathbf{k}) = \int_{-\pi}^{\pi} \frac{dk_4}{2\pi} \Delta^W(k) e^{ik_4\tau} \quad (3.34)$$

analytically [200] by an integration over the contour shown in Fig. 3.1. Returning now to finite N_τ and using the identities given in Appendix C, Eq. (C.1), leads to the desired form of the quark propagator² ($E = E_-$)

$$\begin{aligned} S^W(\tau, \mathbf{k}) &= \sum_{m=-\infty}^{\infty} (-1)^{|m|} S_\infty^W(\tau + m, \mathbf{k}) \\ &= \sum_{i=1}^3 \frac{i \sin k_i}{2(1 + \mathcal{M}) \sinh E} \frac{\sinh[E(\mathbf{k})N_\tau(\tilde{\tau} - 1/2)]}{\cosh(E/2T)} \gamma_i \\ &\quad + \frac{\sinh E}{2(1 + \mathcal{M}) \sinh E} \frac{\cosh[E(\mathbf{k})N_\tau(\tilde{\tau} - 1/2)]}{\cosh(E/2T)} \gamma_4 \\ &\quad + \frac{1 - \cosh E + \mathcal{M}}{2(1 + \mathcal{M}) \sinh E} \frac{\sinh[E(\mathbf{k})N_\tau(\tilde{\tau} - 1/2)]}{\cosh(E/2T)} \mathbb{1}. \end{aligned} \quad (3.35)$$

It can be used to obtain the analytic expression for the meson CFs

$$\begin{aligned} \tilde{G}_H^W(\tilde{\tau}) &= N_c \left(\frac{N_\tau}{\xi N_\sigma} \right)^3 \sum_{\mathbf{k}} \text{Tr} \left[\gamma_5 \Gamma_H S^W(\tau, \mathbf{k}) \Gamma_H^\dagger \gamma_5 S^{W\dagger}(\tau, \mathbf{k}) \right] \\ &= N_c \left(\frac{N_\tau}{\xi N_\sigma} \right)^3 \sum_{\mathbf{k}} \frac{c_H^W(\mathbf{k}) \cosh[2E(\mathbf{k})N_\tau(\tilde{\tau} - 1/2)] + d_H^W(\mathbf{k})}{(1 + \mathcal{M})^2 \cosh^2(E(\mathbf{k})/2T)}, \end{aligned} \quad (3.36)$$

where the coefficients

$$c_H^W = \frac{1}{2} \left[T_4^H + \frac{\sum_i T_i^H \sin^2 k_i}{\sinh^2 E} + T_u^H - T_u^H \frac{\mathcal{K}^2}{\sinh^2 E} \right], \quad (3.37)$$

$$d_H^W = \frac{1}{2} \left[T_4^H + \frac{\sum_i T_i^H \sin^2 k_i}{\sinh^2 E} - T_u^H + T_u^H \frac{\mathcal{K}^2}{\sinh^2 E} \right], \quad (3.38)$$

are given by

$$T_\mu^H = \frac{1}{4} \text{Tr} \left[\Gamma_H \gamma_\mu \Gamma_H^\dagger \gamma_5 \gamma_\mu \gamma_5 \right], \quad T_u^H = \frac{1}{4} \text{Tr} \left[\Gamma_H \Gamma_H^\dagger \right]. \quad (3.39)$$

With the abbreviation

$$d^W \equiv d^W(\mathbf{k}) = \frac{\mathcal{K}^2}{\sinh^2 E} \quad (3.40)$$

these parameters can be evaluated with Tab. 3.1. Note that $\sinh^2 E \rightarrow \mathcal{K}^2$ in the massless continuum limit. Thus d^W approaches one for massless quarks.

Now the analytic quark and meson propagators are known, Eq. (3.37) needs to be transformed into Eq. (2.157), in order to evaluate (compute) the SPFs. In other words one has to reduce the three dimensional momentum integral (sum) into a one dimensional energy ω integral. This transformation is only possible for a one-to-one relation between momentum and energy, thus $r_\tau = 1$ is needed. These transformations are described in [187, 197] and one ends up mainly with two numerical integrations within specified boundaries giving $\tilde{\sigma}_H^W(\tilde{\omega})$, which is bounded by

$$\tilde{\omega}_{min} = 2N_\tau \ln(1 + m/\xi), \quad \tilde{\omega}_{max} = 2N_\tau \ln(1 + (6 + m)/\xi). \quad (3.41)$$

Alternatively one has to use the binning procedure described in Section 3.2.4.

²Here the contact term [200] appearing due to a remanent E_+ contribution, which is proportional to $\delta(\tau)$, is neglected.

H	a_H	b_H	f_H^1	f_H^2	c_H^W	d_H^W	c_H^{FP}	d_H^{FP}
P	1	0	0	0	1	0	δ^2	0
S	-1	1	0	-1	$-d^W$	$d^W - 1$	$-d^{FP}$	$d^{FP} - \delta^2$
$\sum_{i=1}^3 V_i$	2	1	1	-1	$3 - d^W$	d^W	$3\delta^2 - d^{FP}$	d^{FP}
V_4	0	0	-1	0	0	-1	0	$-\delta^2$
$V \equiv \sum_{\mu=1}^4 V_\mu$	2	1	0	-1	$3 - d^W$	$d^W - 1$	$3\delta^2 - d^{FP}$	$d^{FP} - \delta^2$
$\sum_{i=1}^3 A_i$	-2	2	-1	-2	$-2d^W$	$2d^W - 3$	$-2d^{FP}$	$d^{FP} - \delta^2$
A_4	0	1	1	-1	$1 - d^W$	d^W	$\delta^2 - d^{FP}$	d^{FP}
$A \equiv \sum_{\mu=1}^4 A_\mu$	-2	3	0	-3	$1 - 3d^W$	$3(d^W - 1)$	$\delta^2 - 3d^{FP}$	$3(d^{FP} - \delta^2)$

Tab. 3.1: The coefficients a_H , b_H , f_H^1 and f_H^2 for the free continuum spectral functions σ_H^{cont} and the coefficients c_H and d_H for the Wilson CF, Eq. (3.37), and the corresponding ones for the truncated FPA, Eq. (3.49).

3.2.3 Hypercube fermion correlation and spectral functions

Although technically more involved, one can follow the same path for the hypercube action. Like in the Wilson case we start to derive the free FP SPF with the free FP propagator, which in momentum space is given by a Fourier transformation of Eq. (2.68) and (2.72):

$$S_F^{FP}(k) = \frac{-i\gamma_4 \delta \sin k_4 - i\mathcal{K}_1 - i\mathcal{K}_2 \cos k_4 + \kappa_1 + \kappa_2 \cos k_4}{(\mathcal{K}_1^2 + \kappa_1^2 + \delta^2) + 2 \cos k_4 (\mathcal{K}_1 \mathcal{K}_2 + \kappa_1 \kappa_2) + \cos^2 k_4 (\mathcal{K}_2^2 + \kappa_2^2 - \delta^2)}, \quad (3.43)$$

with

$$\mathcal{K}_1 = \sum_{i=1}^3 \gamma_i \alpha_i, \quad \mathcal{K}_2 = \sum_{i=1}^3 \gamma_i \beta_i, \quad (3.44)$$

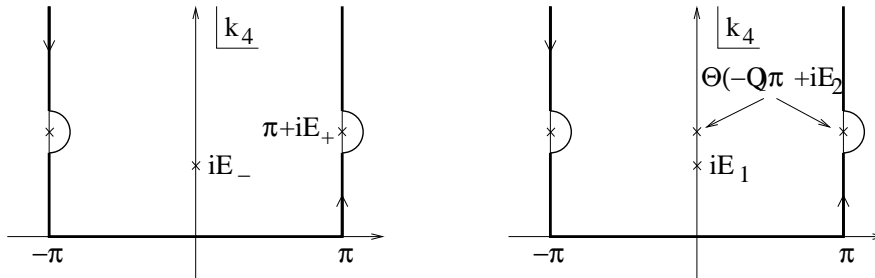


Fig. 3.1: Integration contour and poles in the complex k_4 plane for the Wilson action (left) and for the FP-action (right).

and $\alpha_i(\mathbf{k}), \beta(\mathbf{k}), \kappa_i(\mathbf{k})$ and $\delta(\mathbf{k})$ listed in the Appendix C. The two poles of the propagator can be written as

$$\cosh E_1 = \frac{-P - \sqrt{(P^2 - QR)}}{Q}, \quad (3.45)$$

$$\text{sgn}(Q) \cosh E_2 = \frac{-P + \sqrt{(P^2 - QR)}}{Q}, \quad (3.46)$$

with the functions

$$P(\mathbf{k}) = \mathcal{K}_1 \mathcal{K}_2 + \kappa_1 \kappa_2, \quad Q(\mathbf{k}) = \mathcal{K}_2^2 + \kappa_2^2 - \delta^2, \quad R(\mathbf{k}) = \mathcal{K}_1^2 + \kappa_1^2 + \delta^2. \quad (3.47)$$

The resulting dispersion relation, shown in Fig. 3.2(b), along the different lattice directions $\hat{\mathbf{k}}$, is greatly improved with respect to the Wilson action Fig. 3.2(a). It stays close to the continuum one up to $|\mathbf{k}| \approx 2.5/a$ whereas the Wilson dispersion relation starts to deviate significantly already at $|\mathbf{k}| \approx 1.5/a$. This is also true for the rotational symmetry as can be seen by comparing the dispersion relations along different axes.

The second step is again the computation of the fermionic propagator in the $N_\tau \rightarrow \infty$ limit which can be performed analytically by an integration along the contour shown in Fig. 3.1. The two different poles appear as two different contributions, where the second contribution from $E_2(\mathbf{k})$ is a ghost (doubler) branch similar to the Wilson case with $r_\tau \neq 1$ [200]

$$S_\infty^{FP}(\tau, \mathbf{k}) = \frac{1}{2\sqrt{P^2 - QR} \sinh E_1} e^{-E_1 \tau} \left[(\kappa_1 - i\mathcal{K}_1) + (\kappa_2 - i\mathcal{K}_2) \cosh E_1 + \gamma_4 \delta \text{sgn}(\tau) \sinh E_1 \right] - \frac{(-1)^{\tau\theta(-Q)}}{2\sqrt{P^2 - QR} \sinh E_2} e^{-E_2 \tau} \left[(\kappa_1 - i\mathcal{K}_1) \text{sgn}(Q) + (\kappa_2 - i\mathcal{K}_2) \cosh E_2 + \gamma_4 \delta \text{sgn}(\tau) \sinh E_2 \right]. \quad (3.48)$$

The ghost branch results in an oscillating contribution only for large momenta, where $Q(\mathbf{k}) < 0$. At small momenta the entire contribution is suppressed because $E_2 \gg E_1$. Therefore, the

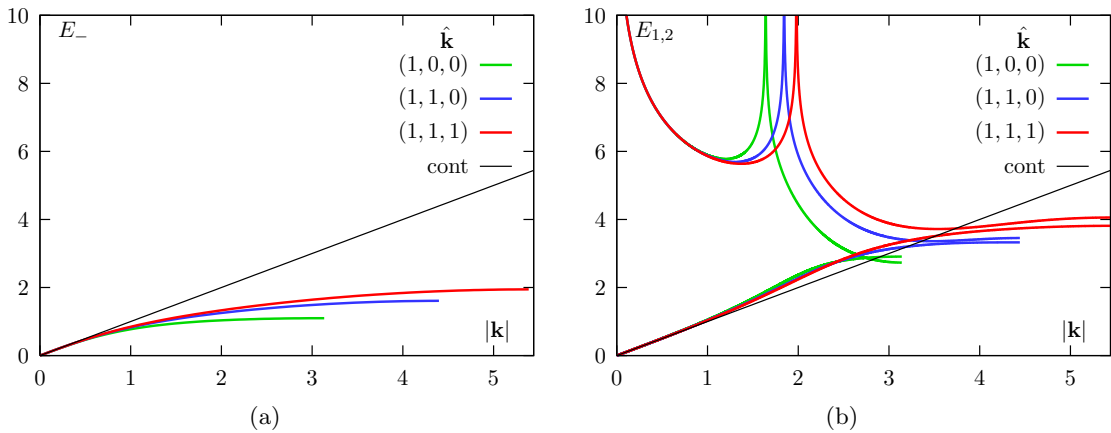


Fig. 3.2: Dispersion relation of the Wilson action ($r_\tau=1$) (a) and of the truncated FP action (b). The higher energy branch of the dispersion relation for the truncated FPA results from the pole E_2 and the lower energy branch from the pole E_1 .

second branch contributes only to the short distance part of the CF. Returning again to finite N_τ via Eq. (3.35) leads to the mesonic CF for the truncated FPA

$$\begin{aligned} \tilde{G}_H^{FP}(\tilde{\tau}) &= N_c \left(\frac{N_\tau}{N_\sigma} \right)^3 \sum_{\mathbf{k}} \frac{c_H^{FP}(\mathbf{k}) \cosh[2E_1(\mathbf{k})N_\tau(\tilde{\tau} - 1/2)] + d_H^{FP}(\mathbf{k})}{(P^2 - QR) \cosh^2(E_1(\mathbf{k})N_\tau/2)} \\ &\quad + \Delta G_H^{E_2}(\tilde{\tau}). \end{aligned} \quad (3.49)$$

where the functions c_H^{FP} and d_H^{FP} are given by

$$\begin{aligned} c_H^{FP} &= \frac{1}{8} \left[\frac{\sum_i T_i^H (\alpha_i + \beta_i \cosh E_1)^2}{\sinh^2 E_1} + \frac{T_u^H (\kappa_1 + \kappa_2 \cosh E_1)^2}{\sinh^2 E_1} + T_4^H \delta^2 \right] \\ d_H^{FP} &= \frac{1}{8} \left[-\frac{\sum_i T_i^H (\alpha_i + \beta_i \cosh E_1)^2}{\sinh^2 E_1} - \frac{T_u^H (\kappa_1 + \kappa_2 \cosh E_1)^2}{\sinh^2 E_1} + T_4^H \delta^2 \right]. \end{aligned} \quad (3.50)$$

They are listed in Tab. 3.1 for different channels. In contrast to the Wilson fermion case they depend on two different functions $d^{FP}(\mathbf{k})$ and $\delta(\mathbf{k})$. The first one is given by

$$d^{FP}(\mathbf{k}) = \frac{(\mathcal{K}_1 + \mathcal{K}_2 \cosh E_1)^2}{\sinh^2 E_1} \quad (3.51)$$

and the second one is defined in Appendix C. Both approach one for massless quarks in the continuum limit. The contribution arising from the second pole is denoted by $\Delta G_H^{E_2}$ and is also given in Appendix C. An analytic expression for the free FP SPF with only the ‘physical’ pole taken into account is given again in [187, 197]. Here, for the hypercube action we have derived the SPFs by the binning procedure described in the following section.

3.2.4 Binning

As already mentioned, to transform the three dimensional momentum integral analytically into a one dimensional integral over the energy, the dispersion relation has to be bijective, namely a strictly increasing function of the momenta. For the case of Wilson fermions with $r \neq 1$ or the contribution from the second pole of the truncated FPA this is no longer true for the entire BZ. Hence, one needs to divide the zone into intervals in which this condition is fulfilled and perform the transformation in every interval separately. This can be avoided if one assumes the validity of the continuum kernel and transforms the integral with the delta function. Then one can write the meson CF generically in the form

$$\tilde{G}_H(\tilde{\tau}) = \int d^3k \mathcal{F}(\mathbf{k}) \cosh(2E(\mathbf{k})N_\tau(\tilde{\tau} - 1/2)), \quad (3.52)$$

with the known dispersion relation $E(\mathbf{k})$. Then one rewrites the integral as

$$\tilde{G}_H(\tilde{\tau}) = \int_0^\infty d\tilde{\omega} \tilde{\sigma}^{lat}(\tilde{\omega}) \frac{\cosh(\tilde{\omega}(\tilde{\tau} - 1/2))}{\sinh(\tilde{\omega}/2)}, \quad (3.53)$$

with

$$\tilde{\sigma}^{lat}(\tilde{\omega}) = \int d^3k \delta(\tilde{\omega} - 2E(\mathbf{k})N_\tau) [\mathcal{F}(\mathbf{k}) \sinh(N_\tau E(\mathbf{k}))]. \quad (3.54)$$

For the actual computations, one smears the delta function by partitioning the energy interval into finite elements ω_n with $\omega_{n+1} - \omega_n = \Delta\omega$ to obtain

$$\tilde{\sigma}_n = \sum_{\mathbf{k}} \Theta(2N_\tau E(\mathbf{k}) - \omega_{n-1}) \Theta(\omega_n - 2N_\tau E(\mathbf{k})) [\mathcal{F}(\mathbf{k}) \sinh(N_\tau E(\mathbf{k}))], \quad (3.55)$$

where $\tilde{\sigma}^{lat}(\tilde{\omega}) \doteq \tilde{\sigma}_n$ for $\tilde{\omega} \in [\tilde{\omega}_{n-1}, \tilde{\omega}_n]$. In the limit of $\Delta\tilde{\omega} \rightarrow 0$ this equation becomes exact. The SPFs presented in Fig. 3.2 have been obtained using 500 bins where each bin contains on average 10^5 different momenta. The results with only taking the first physical pole into account have been successfully cross-checked with the integration method. Due to a small error in the numerical implementation, which did not distinguish correctly between the different energy contributions, the cut-off effects in the SPF for the truncated FPA have changed somewhat in the high frequency region compared to [187].

3.2.5 Summary of observed cut-off effects

In [197] cut-off effects of the free CF as well as of the SPF have been studied extensively. Some of the findings, which are important for our analysis are recapitulated here:

- Deviations from the free continuum SPF of more than 15% occur already at $\omega a = 1.5$ for Wilson fermions, while the truncated FPA stays close to the continuum SPF up to $\omega a \approx 4.8$, see Figs. 3.4(a) and 3.4(b).
- A comparison of $G_P(\tilde{\tau} = 0.5)/T^3$, which is most strongly effected by finite lattice size effects, at different volumes (*aspect ratios* N_σ/N_τ) indicates that for $N_\tau = 16$ fixed, both formulations achieve the infinite volume behavior $N_\sigma \rightarrow \infty$ for an aspect ratio $N_\sigma/N_\tau \gtrsim 4$.
- Comparing the ratios of free CFs G_P/G_S at zero quark mass, which should be 1 for a chirally symmetric action, indicates that the truncated FPA is better suited for larger distances, i.e., has better chiral properties, than the Wilson action.
- For massive quarks the optimal Wilson parameter for the infrared part of the free SPF is given by $r = 1/\xi$ with small deviations at large distances, but huge cut-off effects at short distances.

3.2.6 Probing the MEM on free and interacting model data

A lot of tests have been performed on MEM, e.g., Refs. [11, 186, 188] for its dependence on various input parameters like N_τ , ω_{max} and σ_c . They have been done by using for instance mock data: Free or interacting CFs $G(\tau)$ have been constructed by various SPF ansätze like Delta-, Gaussian- or Breit-Wigner Peaks and continuum contributions. On these Gaussian distributed data with a variance

$$\sigma(\tau) = \begin{cases} b G(\tau) \tau & \text{if } \tau \leq N_\tau/2 \\ b G(\tau) (N_\tau - \tau) & \text{if } \tau > N_\tau/2 \end{cases} \quad (3.56)$$

have been generated to mimic the noise level of lattice data. Here b controls the noise and is chosen in the range 0.0001–0.1. Finally the output of the MEM was compared with the original SPF. The following list tries to collect the main findings.

- Using Wilson free data, one can reconstruct the (free) continuum SPF Eq. (2.166), if one uses the lattice kernel $K^{lat}(\tau, \omega, N_\tau)$ [186]

$$K(\tau, \omega) = \frac{\cosh(\omega(\tau - \frac{1}{2T}))}{\sinh(\frac{\omega}{2T})} \rightarrow K^{lat}(\tau, \omega, N_\tau) = \frac{2\omega}{N_\tau} \sum_{n=0}^{N_\tau-1} \frac{\exp(-i2n\pi\tau/N_\tau)}{4 \sin^2(n\pi/N_\tau) + \omega^2}. \quad (3.57)$$

However, calculations for the free theory show that cut-off effects show up in the SPF rather than in the kernel [187]. So we use the continuum kernel and the free lattice SPF as our default model.

- Peak height and widths are influenced by
 - the number of configuration N_C : insufficient N_C leads to a flattening and broadening of the peak [186],
 - the number of time slices N_τ : This could only be studied by leaving out some data for larger time separation [11],
 - the discretization of ω ($\Delta\omega$): peaks broaden and reduce in height for a decreasing number of N_ω [186]. In what follows we choose for consistency N_ω in the range 500-700.
- The MEM is able to correctly reproduce the free W [188] as well as the FP lattice SPFs now with the modified UV-part for $N_\tau = 12, 16, 24$, c.f. Figs. 3.4(a) and 3.4(b). In the AV channel of the Wilson SPF, one has to modify the default SPF in the UV part to avoid a non positive definite SPF. Thus the tiny deviations between the free and reproduced SPF (green).
- Once ω_{max} is larger as the ultraviolet lattice cut-off for Wilson fermions Eq. (3.42), i.e., $\tilde{\omega}_{max} \gtrsim 4N_\tau$ no ω_{max} dependence in the SPFs for $T < T_c$ is found anymore.
- Fuzzing leads to a vanishing of the second bump, but induces also a bump in the free spectral function [201, 202]. Thus we solely use point-to-point correlators.
- In order to handle the problem of very tiny eigenvalues of the covariance matrix due to limited statistics, which sometimes induces small entries in the first bin of the SPF [186] and leads to significant shifts in the first peak position, one can use the eigenvalue smoothing procedure, described in Section 2.4.5. However, a definite criterion for finding the ‘correct’ SPF cannot be given. Thus we adopt the way this problem is handled in [188], which starts with the lowest smoothing level $N_R = 0$ until the SPF is insensitive under small changes of the smoothing level or the entry in the first bin is minimized (mostly $N_R = 2$ or $N_R = 3$), see e.g Fig. 3.3. In particular above T_c smearing becomes relevant, since it leads to shifts of $\gtrsim 2$ in units of ω/T in the first peak position.

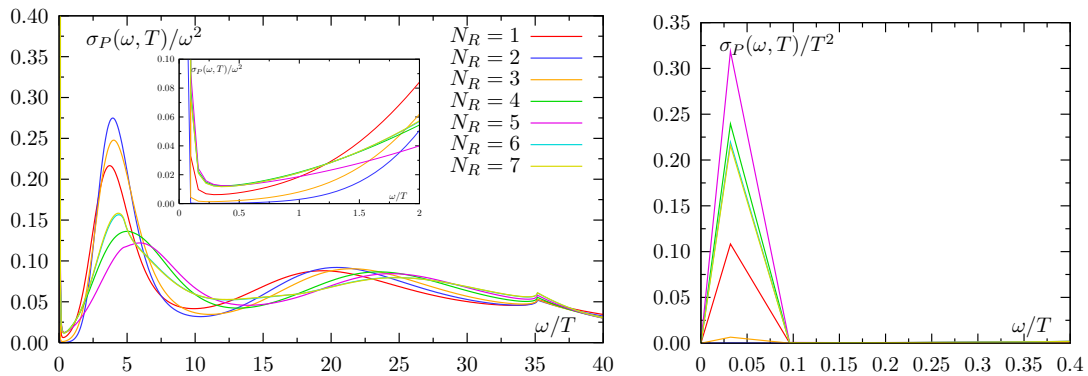


Fig. 3.3: Dependency of the SPF on the smearing level N_R at $0.9T_c$ with $\kappa = 0.13460$ on a $48^3 \times 16$ lattice. The right figure is scaled for a better visibility of the entry in the first bin. In this case the optimal smearing level is $N_R = 2$.

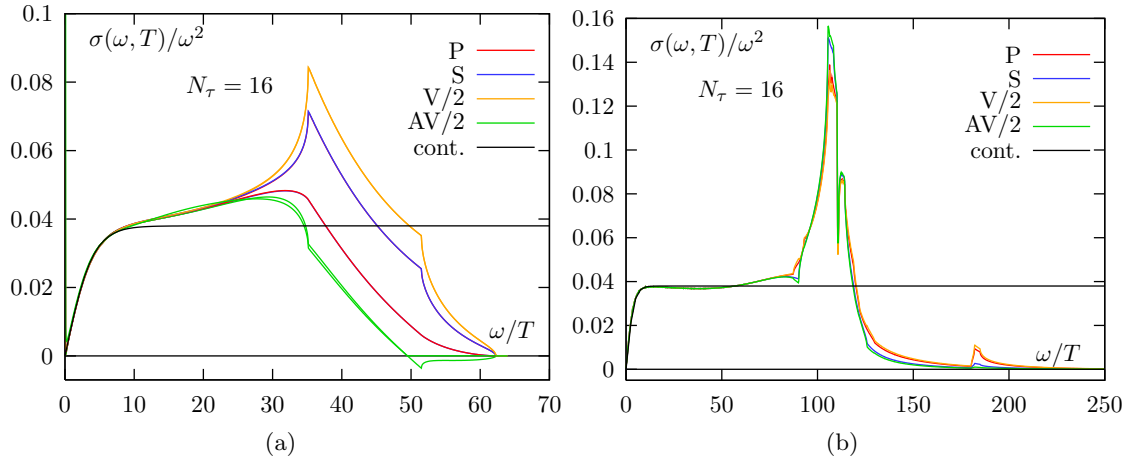


Fig. 3.4: Reconstructed free SPF of the Wilson (a) and the truncated FPA (b) using the MEM with $b = 0.01$ and $N_C = 100$. They fall exactly on top of the corresponding free SPF derived by numerical integration and Binning respectively.

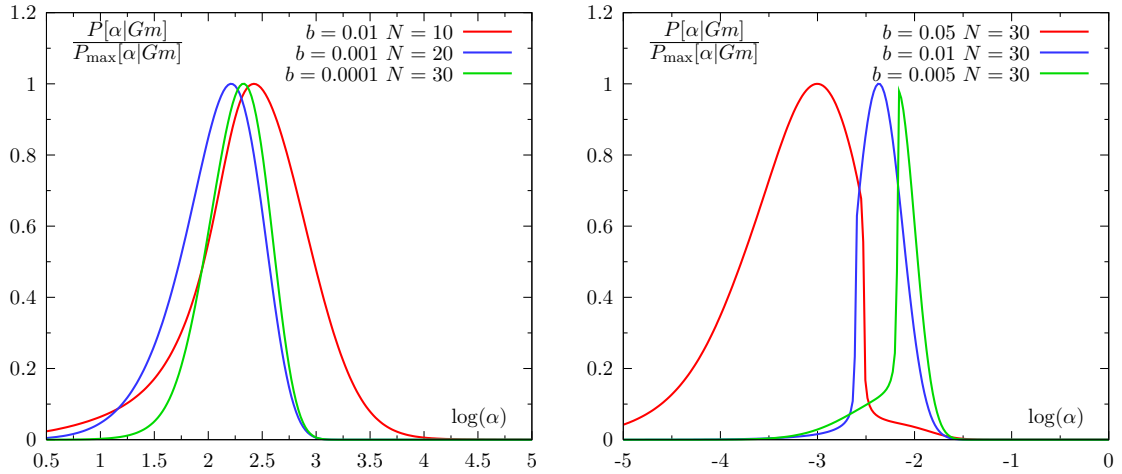


Fig. 3.5: The posterior probability distribution $P[\alpha|Gm]$ normalized by its maximum for various combinations of mock data N and b for free Wilson fermions (pseudoscalar) on a $64^3 \times 16$ lattice (left) and at $0.9T_c$ on a $48^3 \times 16$ lattice with $\kappa = 0.13300$ both with the free SPF as default model. The better the quality of data the narrower the distribution is.

4 Analysis of mesonic properties below and above T_c

In this chapter the data concerning CFs and SPFs, are analyzed and interpreted. Using a fit to the spatial and the MEM analysis of the temporal CFs, we extract screening and pole energies (masses), Bethe-Salpeter amplitudes (wave functions) and decay constants. Based on the energies, we discuss various forms of dispersion relations and possible temperature dependencies. Furthermore, the SPFs for the hypercube action in the interacting case especially above T_c are considered using MEM. They are inter alia compared to the former Wilson SPFs. The cut-off dependence of Wilson and HF CFs is investigated by studying their ratio to the free CFs at $1.5 T_c$ and $3 T_c$. Except for the MEM results, many of our statements rely on spatial CFs since here the signals can be followed to much larger distances. Even though they are not directly related to physical observables and their connection to SPFs is more involved, Section 2.8.2, they still will provide useful physical insight.

4.1 Extracting masses and energies from correlation functions

To extract mesonic properties from spatial CFs, both a single ($m=1$) as well as a two-state ($m=\{1,2\}$) parameterization as Eq. (2.157), here in spatial direction, is used:

$$G_H^R(z, \tilde{\mathbf{p}}) = \sum_m \frac{A_H^m(R, \tilde{\mathbf{p}}) A_H^m(0, \tilde{\mathbf{p}})}{2E^m(\tilde{\mathbf{p}})} [\exp(-E^m(\tilde{\mathbf{p}})z) + \exp(-E^m(\tilde{\mathbf{p}})(N_\sigma - z))], \quad (4.1)$$

where $\tilde{\mathbf{p}}$ lies in funny space and $A_H^m(R, \tilde{\mathbf{p}}) \equiv \langle 0 | \mathcal{J}_H^R | m, \tilde{\mathbf{p}} \rangle$ corresponds to the overlap of the (improved) operator with the meson. The strategy is then to increase the starting point of the fit interval $z_i = z_{initial}$ successively, where the large z value $z_f = z_{final} = N_\sigma/2$ is kept fixed, until the fit stabilizes to a plateau of the fit parameters. The only significant signal remaining in $G_H(z)$ from a large enough z_i onwards will be the one from the lightest state. Using symmetrized CFs leads thereby to more stable fits, especially for noisy correlators. Having established further the optimal smearing and fuzzing level for large enough lattices both parameterizations often lead to common plateau values for the ground state screening masses listed in Tab. B.7 and Tab. B.6 (see also [188]). However, for small lattices or quark masses contamination by higher states or small signal/noise ratios respectively is still present. It often happened that both fits showed a slightly different plateau value. In Tab. B.7 we list both the single energy value, supported also by the local effective energy Eq. (2.185), and an averaged energy of both fits. Unfortunately for some lattice configurations measurements in the AV channel do not exist (n.e.), since they have not been measured in the past. As can be clearly seen in the tables the error increases with decreasing pion mass as expected, since the correlation length in the chiral limit induces larger fluctuations to the CF. Furthermore, exceptionals lead to even larger errors in the vicinity of the phase transition below T_c . As already mentioned, close to but above T_c we have omitted the corresponding configurations. Some of the data, especially from small lattices, have been reanalyzed and show only minor

deviations to Refs. [186, 188] which are explainable by the new statistics and/or by the use of a new fitting program *minuit*. However, the values coincide mostly within the given errors.

4.1.1 Masses and energies from temporal correlation functions

To extract the pole energies we use the SPF, i.e., the location of the maximum of the first (ground state) peak, gained by the MEM with the free lattice SPF as default model. Whereas here we are focused solely on the masses, we investigate SPFs on the whole in more detail in Section 4.5. The results below T_c are listed in Tab. B.8. In order to get an error estimate, we use the simple Jackknife procedure. However, due to our low statistics these errors seem to be rather small compared to the decay widths, which are sometimes also taken as an error estimate. Systematical errors, introduced e.g., by the eigenvalue smearing procedure are much larger than the statistical ones.

4.1.2 Masses in the chiral limit

The particle masses for different κ values have to be extrapolated to the chiral limit, i.e., to the physical quark mass value. The critical values of κ below T_c have been determined by a linear extrapolation of the squared pion mass vs. $1/\kappa$ via

$$m_P^2(\kappa) = c_P m_q \quad (4.2)$$

with the VWI quark mass m_q defined in Eq. (2.27). Additionally, quenched chiral perturbation theory ($q\chi PT$) recommends using

$$m_P^2(\kappa) = c_P m_q^{\frac{1}{1+\delta}} \quad (4.3)$$

with δ small and positive [203]. Phenomenologically also an ansatz

$$m_P^2(\kappa) + c_P^1 m_P^3(\kappa) = c_P^2 m_q \quad (4.4)$$

is suggested [204]. However, all three ansätze lead to similar values of κ_c , so no significant improvement to Eq. (4.2) can be observed.

Once κ_c is fixed, Tab. 4.1, the V and S masses can then be obtained by

$$m_{V,S}(\kappa) = m_{V,S}(\kappa_c) + c_{V,S} \left(\frac{1}{\kappa} - \frac{1}{\kappa_c} \right). \quad (4.5)$$

Again this has been done with screening (Tab. B.7) and pole (Tab. B.8) masses, see Fig. 4.1. Deviation from the linear behavior in Eqs. (4.2) or (4.5) can formally have three reasons. First, for very heavy quark masses the binding energy can be approximately neglected and the screening masses in all channels should be equal to twice the quark mass. Secondly, for small quark masses $q\chi PT$ predicts the occurrence of the so-called *quenched chiral logs* [203] arising from so-called hairpin diagrams. And thirdly as the bare quark mass decreases, the contribution of topological zero modes to the P and S susceptibilities rises as¹ $|\nu|/(m_q^2 V)$. On the other hand $|\nu| \propto \sqrt{V}$. While in unquenched simulations zero modes are suppressed, they induce a systematic error in quenched simulations, which increases for smaller m_q and decreases with V . As can be easily shown, the contributions of these zero modes are positive for the P and negative for the S. In Ref. [205] the authors suggest therefore to add the S to

¹This relation holds solely for chiral fermions, but its impact can also be observed with our data. This might be explained by the smallness of our a .

the P CF, which leads to a cancellation of the zero modes in the P+S channel. Albeit this gives an additional contribution to the P CF, it should be suppressed like higher states by its larger (scalar) mass compared to the pion. Thus a clean pion mass extraction becomes possible. Although this approach is in principle applicable, this behavior is expected only for chiral fermions². However, in our case the problems with exceptional configurations due to the additive mass renormalization of Wilson fermion still persist. While the P+S remains almost unchanged compared to the P the negative contributions to S are so large, relative to the S values, that the CFs even become negative for small quark masses and large distances. Like the S SPFs the mass fits have small signal/noise ratios, and plateaux, if any, are seen only for small distances. Hence, any mass values from S CFs quoted should be taken with caution. Finally we decided to omit the lowest pion masses for the extrapolation in Figs. 4.1(e) and 4.1(f).

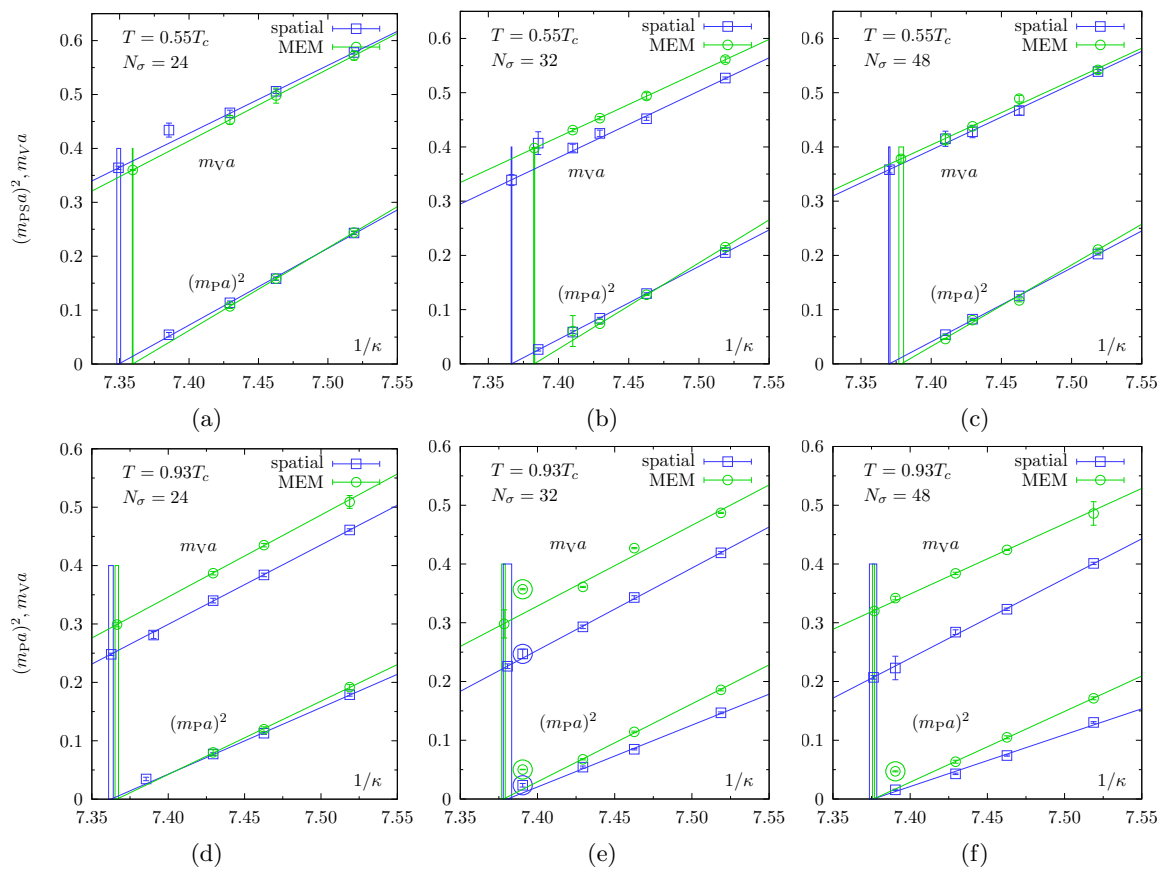


Fig. 4.1: Comparison between MEM pole masses and screening masses of the two-exponential fit in the P and V channel with $N_\tau = 16$ fixed at $T = 0.55 T_c$ (a,b,c) and $T = 0.93 T_c$ (d,e,f). The bars denote the error ranges in κ_c . Values omitted for the chiral extrapolation are marked with circles.

Masses below T_c

We start with the investigation of the particle masses below T_c . As can be seen in Tab. 4.1 differences between the critical κ^z of screening masses and κ of the pole masses are very small.

²The reason for the different behavior in the case of Wilson (non-chiral) fermions is that the real eigenmodes of the Dirac operator are not eigenfunctions of γ_5 with eigenvalues ± 1 in general.

T/T_c	N_σ	κ_c^z	$m_V^z a$	$m_V^z [\text{GeV}]$	$m_S^z a$	$m_S^z [\text{GeV}]$	L[fm]
0.93	48	0.13557(8)	0.214(4)	0.859(16)	0.345(10)	1.384(40)	2.35
	32	0.13549(10)	0.219(8)	0.879(32)	0.353(10)	1.416(40)	1.57
	24	0.13582(6)	0.246(12)	0.986(48)	0.260(8)	1.023(32)	1.18
0.55	48	0.13568(2)	0.361(6)	0.862(14)	-	-	3.98
	32	0.13575(1)	0.349(8)	0.834(19)	0.531(8)	1.269(19)	2.66
	24	0.13606(5)	0.385(8)	0.920(19)	0.404(7)	0.965(17)	1.99
0.44	24	0.13551(5)	0.399(5)	0.760(10)	0.850(30)	1.619(60)	2.50

T/T_c	N_σ	κ_c	$m_V a$	$m_V [\text{GeV}]$	$m_S a$	$m_S [\text{GeV}]$	L[fm]
0.93	48	0.13556(3)	0.327(1)	1.312(4)	0.338(17)	1.356(68)	2.35
	32	0.13555(5)	0.297(24)	1.192(96)	0.339(8)	1.360(32)	1.59
	24	0.13574(4)	0.299(4)	1.199(16)	0.280(10)	1.123(40)	1.18
0.55	48	0.13552(7)	0.378(6)	0.903(14)	0.478(22)	1.142(53)	3.98
	32	0.13546(4)	0.398(1)	0.948(2)	0.614(11)	1.467(26)	2.66
	24	0.13588(1)	0.360(1)	0.860(7)	0.558(14)	1.333(33)	1.99
0.44	24	0.13553(12)	0.428(5)	0.815(10)	-	-	2.50

Tab. 4.1: Screening (above) and pole masses (below) in the chiral limit together with κ_c^z (κ_c) as obtained from $N_\tau = 16$ lattices with the different volumes and temperatures below T_c .

At $0.93 T_c$ and $0.44 T_c$ they coincide within the errors, whereas at $0.55 T_c$ the discrepancies are up to 30%. Finite size effects in κ_c^z are at most 2.5%. As we will still see in Section 4.3, the same holds for the κ_c values using the VWI together with the AWI current quark mass definition.

At the lowest temperature of $0.44 T_c$ the extrapolated screening V mass 760(10) MeV coincides with its physical value of 770 MeV. At $0.55 T_c$ and $0.93 T_c$ this mass is significantly larger, 834–920 MeV and 859–986 MeV, respectively. This could indicate either a temperature or finite size effect, since the spatial extension shrinks with temperature, if N_τ is kept fixed. In contrast the V mass on the $48^3 \times 16$ lattice at $0.55 T_c$ is larger than on the $32^3 \times 16$ lattice, which is however not significant. Keeping the physical lattice size roughly fixed at all three temperatures, the V screening masses still increase with temperature.

In Fig. 4.2 we show the finite volume extrapolation of the vector screening masses with $m_V^z(V) = m_V^z(\infty) (1 + c/V)$ motivated by FUKUGITA ET AL. [206]. This description works for volumes lower than $\lesssim (2.5 \text{ fm})^3$, while a leveling-off might set in for larger volumes. The final results with 834(32) MeV at $0.55 T_c$ and 840(14) MeV at $0.93 T_c$ still lie somewhat above the zero temperature result. Earlier theoretical predictions made by LÜSCHER in 1983 offer an exponential fall-off of the hadron masses [207]. The common explanation for the apparent discrepancy is that Lüscher’s formula deals with asymptotic large lattice volumes where finite-size effects arise from interac-

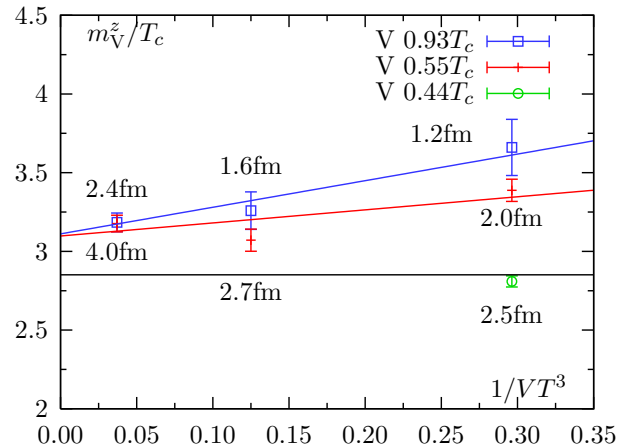


Fig. 4.2: Finite volume extrapolation of vector screening masses. The $T = 0$ vector mass is indicated by the black line.

tions between copies of virtual pion clouds surrounding the hadron in a box with periodic boundary conditions. In contrast, FUKUGITA ET AL. ascribe the power-like behavior of their data to a distortion of the hadron wave-function itself (as it would occur for rather small lattice volumes). Taking both pictures together one would expect a power-like dependence for sub-asymptotic lattice volumes that gradually changes into an exponential fall-off towards larger box sizes.

The fact that the AV CFs have not always been measured in the past, prevent a systematical study of the AV screening masses.

Concerning pole energies, it is hard to give definite values of the V and S masses and errors, i.e., the peak position depends on the smearing level. In a reasonable range ($N_R = 1-4$) fluctuations and thus systematic errors are of the order of 10%, c.f Fig. 3.3. Using the Jackknife procedure for optimal N_R gives much smaller statistical errors. The V pole masses are with one exception somewhat larger ($\simeq 10\%$), i.e., within the above mentioned systematic error range, than the screening masses at $0.44 T_c$ and $0.55 T_c$ and significant larger ($\simeq 40\%$) at $0.93 T_c$. In contrast the S pole masses match the screening ones at $0.93 T_c$ and are again larger $\leq 16\%$ at $0.55 T_c$. Such a behavior is shared also by the P. For $0.44 T_c$ the chiral extrapolation in the S mass was impossible, since no peaks show up for the two smallest quark masses. By looking at the corresponding CFs this is not unexpected since the long distance data is fully disturbed by zero modes.

Masses above T_c

Above the critical temperature, close inspection of the masses extracted from fits to spatial CFs do not reveal a definite plateau behavior. The fit results listed in the Appendix B.4 are determined by a plateau fit on few large z_f mass parameters. Although the masses are close to the free limit ($2\pi T$) down to 5^0_{00} for $6 T_c$, they can only serve as mere estimates. We defer the discussion therefore to Chapter 5, in which a systematic analysis of finite lattice spacing and finite volume effects is carried out. Here we list only the general features which become already clear from the fits. In both discretizations the P/S masses approach $2\pi T$ from below with increasing temperature, while the V/AV masses are always larger and lie even above the free value. The effective chiral $SU(2)_A$ and $U(1)_A$ symmetry restoration shows up in degenerate P/S and V/AV masses, see also Section 5.2. The influence of changes in quark masses here from 5 MeV to 30 MeV at $1.5 T_c$ is only weak and within the errors.

4.1.3 Dispersion relations

In this section we study the dispersion relation of the P with non-zero momentum. In contrast to the continuum, the momenta are discretized and limited on the lattice. Since we study pole and screening energies at finite temperature, where Lorentz invariance is broken, we restrict our analysis to projections of meson CFs on truly spatial momenta only, i.e., $\mathbf{p}_\perp = (p_1, p_2)$, with $p_i = 2\pi n_i / N_\sigma \in [-\pi/a, \pi/a]$ and $n_i \in [-N_\sigma/2, N_\sigma/2]$. The bosonic Matsubara frequencies are set to zero, since the first non-zero one $\omega_1 = 2\pi / N_\tau a$ is rather large. The energies are extracted again via fits to CFs, Eq. (4.1), or utilizing the MEM, respectively. Their functional dependence on the momenta is compared to various relations on the lattice. Besides the known continuum relation

$$E^2 = \mathbf{p}^2 + m^2 \quad (\text{A})$$

we further check three forms

$$\sinh^2 E = \sum_i \sin^2 p_i + \sinh^2 m \quad (\text{B}),$$

$$\sinh^2 \frac{E}{2} = \sum_i \sin^2 \frac{p_i}{2} + \sinh^2 \frac{m}{2} \quad (\text{C}),$$

$$\sinh^2 \frac{E}{4} = \sum_i \sin^2 \frac{p_i}{4} + \sinh^2 \frac{m}{4} \quad (\text{D}),$$

which are all justified by different lattice actions (discretizations) of an free effective meson (scalar) theory at $T=0$. The correct relation is not known a priori and there exist of course more such relations, but they will not be considered here. It has been found that at $T=0$ Eq. C describes the data best for pure Wilson [208], as well as for TI Wilson fermions [156, 209]. Our results concerning the screening energies are shown in Fig. 4.3. For small quark masses or momenta one can hardly decide which form is preferred by the data. However, for the heaviest pion mass also in spatial direction Eq. C seems to be favored, while Eq. B is ruled out by the data.

The data at $1.5 T_c$ in both fermion formulations lie somewhat above the dispersion relations and get closer to them at $3 T_c$. However, the energies of the hypercube fermions even at $3 T_c$ still lie somewhat above the expectations and have smaller errors. Again no definite conclusion about the correct form of the dispersion relation can be made. In Figs. 4.3(c) and 4.3(d), we plot the free effective screening energies at $z = N_\sigma/4$, since no energy plateau can be found (see Chapter 5). They fall significantly above the bound state forms Eq. B-D. Concerning screening energies we have also checked the V channel, but found no qualitative difference. The same analysis has been carried out using energies extracted by MEM for the Wilson action. In contrast to $0.55 T_c$, where the dispersion relation matches the spatial one, the P pole energies at $0.93 T_c$ lie significantly above the expected form. Assuming a temperature effect described as in Section 2.8.2

$$E^2 = m^2 + A^2(T)\mathbf{p}^2 \quad \text{and} \quad (E^z)^2 = \frac{m^2}{A^2(T)} + \mathbf{p}_\perp^2 = (m^z)^2 + \mathbf{p}_\perp^2 \quad (4.6)$$

the ratios $(E^2/(E^z)^2)(\mathbf{p}_\perp) = A^2(T, \mathbf{p}_\perp)$ and $m^2/(m^z)^2 = A^2(T, m)$ with $\mathbf{p} = 0$ allow for quantifying $A(T)$ as function of momenta or quark mass (see Figs. 4.3(e) and 4.3(f)). For the heaviest quark mass we find the averaged $A^2(T)$ to be 1.32(1) and 1.35(4), respectively. These ratios obviously increase with decreasing quark mass. For lighter quark masses the error bars are too large to decide whether $A^2(T, \mathbf{p}_\perp)$ is a constant in \mathbf{p}_\perp .

Assuming the validity of Eq. C for $0.55 T_c$ allows to quantify the discretization error since in the continuum, Eq. A, the *kinetic* mass

$$m_{kin} = (\partial^2 E / \partial p^2 |_{p=0})^{-1} = \sinh m \quad (4.7)$$

equals the *static* mass $m = E(\mathbf{p}=0)$. Even for the heaviest pion at $0.55 T_c$ this corresponds to $m = 0.446(3)$ and $m_{kin} = 0.460(4)$, which is a difference of just 3% and supports the assumption that we basically see continuum dynamics.

To summarize, no definite conclusion of the correct form of the dispersion relation can be drawn from the data. Considering our very small a values they all, except Eq. B, are indistinguishable and match the continuum dispersion relation like our data do. However, Eq. C seems to be favored for heavy quark masses. Furthermore no temperature effect can be seen at $0.55 T_c$.

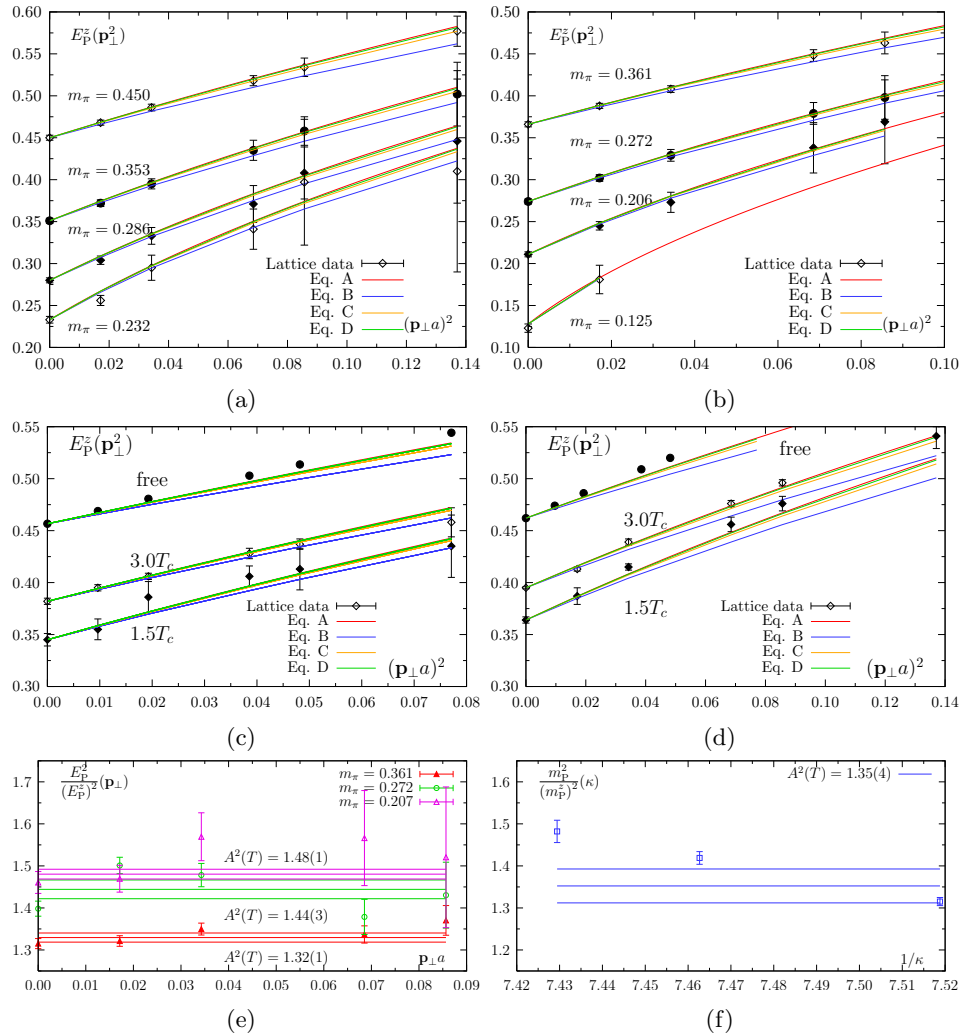


Fig. 4.3: Screening energies E_z of the P at $0.55 T_c$ (a), $0.93 T_c$ (b) on $48^3 \times 16$ lattices and above T_c on a $64^3 \times 16$ lattice (c) for Wilson fermions. (d) shows the energies of the Hypercube fermions above T_c on a $48^3 \times 16$ lattice. Estimates for the temperature modification factor $A(T)$ for the P at $0.93 T_c$ (e,f).

In contrast comparing temporal and spatial dispersion relations at $0.93 T_c$ indeed shows a temperature effect, which can be described by model assumptions with $A^2(T) \simeq 1.3-1.5$. Above T_c the screening energies follow the same behavior. Especially the Hypercube fermion energies lie somewhat above the expected forms.

4.2 Bethe-Salpeter amplitudes and the pion radius

As a by-product of the smearing procedure described in Section 2.8.3 the Bethe-Salpeter amplitudes defined in Eq. (2.155) allow to determine rough approximations about the mesonic particle extent or the electromagnetic charge radius. Basically they are a measure of the *wave function* $\phi_m(R, \mathbf{p})$, i.e., the probability of creating a particular quark-anti-quark state m, \mathbf{p}

with spatial extent R . As in the case of the energies we take the parameterization of Eq. (4.1) for fitting our CFs. Following [210] the corresponding wave function is then given by

$$\phi_m(R, \mathbf{p}) = \frac{A_H^m(R, \mathbf{p})}{A_H^m(0, \mathbf{p})}. \quad (4.8)$$

The extraction of the amplitudes $A_H^m(R, \mathbf{p})$ is by far not unique. Fitting CFs for each value of R separately would be a poor strategy, since spurious dependencies of the ground state mass on R make it difficult to relate the amplitudes to each other. Alternatively one can use simultaneous two-state fits at all R values with one common ground state energy. Unfortunately this fitting procedure was not stable enough to resolve the remaining R dependence of the excited state energies, so we proceed by setting ground as well as excited mass fixed as has been done already in, e.g. [132, 211]. For this analysis it is necessary to ensure that solely the ground and one excited state is present. Therefore we checked for stabilities of both energies by skipping step by step the first points of the CF. Since the excited state contribution reduces with the fit range, one should be careful not to omit too many points. Stability was found for the ground state parameters by omitting the first 3 points. Since we have no such criteria for the first excited states and indeed a stable excited state was not found, we simply use the same interval. Nevertheless, all quoted results concerning excited states have larger systematic errors, such that any conclusions on these are not reliable. In the following we focus on spatial Bethe-Salpeter amplitudes on $N_\sigma = 48$ lattices, where full fuzzed and smeared data sets below as well as above T_c are available. As in the last section we restrict the analysis to spatial momenta up to $|\mathbf{p}_\perp| \leq 2\frac{2\pi}{N_\sigma}$.

As an additional cross check we have used another method for extracting the ground state wave function namely

$$\phi_0(R) = \frac{G_H^R(z, \mathbf{p}_\perp)}{G_H^0(z, \mathbf{p}_\perp)}, \quad (4.9)$$

which holds only if all excited states have completely died out. However, it is not possible to use this method for extracting excited wave functions. Below T_c the ground state parameters turned out to agree within errors, whereas above T_c the deviations are much larger, c.f. the second row of Tab. 4.3. Obviously a clear separation between ground and excited state is not possible. For extracting a pion radius we describe the Bethe-Salpeter wave function through modified hydrogen S wave functions [212]

$$\phi_0(R) \propto \exp\left(-\left(\frac{R}{R_0}\right)^\nu\right) \quad (4.10)$$

$$\phi_1(R) \propto \left(1 - \frac{R}{R_n}\right) \exp\left(-\left(\frac{R}{R_1}\right)^\nu\right) \quad (4.11)$$

for the ground and the first excited state. The parameters R_0 , R_1 , R_n and ν are again determined from fits. For a Coulomb potential one would assume to have $\nu=1$, whereas for a purely linear potential one gets $\nu=1.5$. A quark anti-quark bound state is expected to have a value somewhere in between. We use this parameterization to obtain an estimate of the mean square radius, the second moment of the electromagnetic form factor. According to [212, 213] it can be calculated with

$$\langle R^2 \rangle_{BS}^0 = \frac{1}{\omega} \frac{\int d^3\vec{R} \vec{R}^2 \phi_0^2(|\vec{R}|)}{\int d^3\vec{R} \phi_0^2(|\vec{R}|)} = \frac{1}{\omega} \frac{R_0^2 \Gamma(\frac{5}{\nu})}{4^{1/\nu} \Gamma(\frac{3}{\nu})} \quad (4.12)$$

or equivalently for ϕ_1

$$\langle R^2 \rangle_{BS}^1 = \frac{1}{\omega} \frac{P(5) - \frac{2}{R_n} P(6) + \frac{1}{R_n^2} P(7)}{P(3) - \frac{2}{R_n} P(4) + \frac{1}{R_n^2} P(5)} \quad (4.13)$$

with

$$P(m) = 2^{-\frac{m}{\nu}} R_1^m \Gamma\left(\frac{m}{\nu}\right). \quad (4.14)$$

Here ω is a factor which accounts for the quark anti-quark position relative to the CM, where the latter depends also on the gluon motion [181]. If one assumes that both particles are always fixed on the opposite sides of the CM at $R/2$, one has $\omega=4$, while $\omega=2$ for particles moving uncorrelated.

Analyzing the pseudoscalar data below T_c , Tab. 4.2, a continuous shrinking of the particle radius with increasing mass and rising momenta is observable, as expected [214]. It has been claimed that fast moving particles with high momenta are Lorentz contracted and show therefore a smaller radius. However, since the momentum directions $2\pi/N_\sigma(1, 1, 0)$ and permutations thereof mix contracted with non-contracted directions, while our smearing is done in a rotational symmetric way, this cannot be a pure Lorentz contraction effect and such a claim cannot be fully justified by this study. The increase of the ν parameter indicates a more linear behavior of the potential. Thereby the radius as well as the errors extracted from the ratio method are significantly smaller than the ones extracted from the simultaneous fits method.

Comparing the almost mass independent radius values in the chiral limit $\langle R^2 \rangle^0 \simeq 0.142 \text{ fm}^2$ ($0.55T_c$) and 0.103 fm^2 ($0.93T_c$) with the experimental result $0.439(8) \text{ fm}^2$ [215] shows large deviations. Even an ω value in Eq. (4.12), which we have chosen to be 2 to produce the largest values, cannot remove this discrepancy. This observation is in agreement with earlier findings in e.g., Ref. [211], where it has been argued that the Bethe-Salpeter amplitudes might not capture the charge distribution of mesons as e.g. determined by form factors.

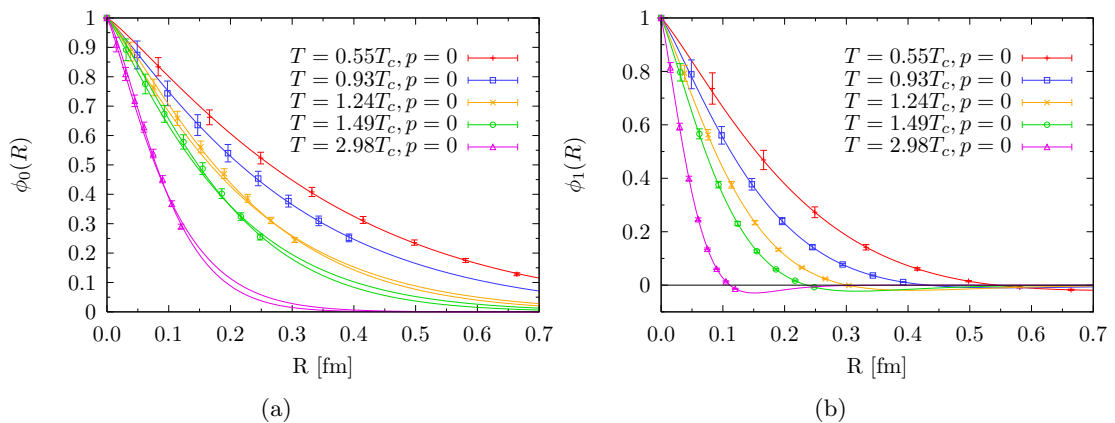


Fig. 4.4: Ground and excited state wave function of the P at all considered temperatures and $N_\sigma = 48$ ($m_\pi = 1 \text{ GeV}$ below T_c). Thin curves in (a) represent the results of the ratio method.

Above the critical temperature, Tabs. 4.3 and 4.4, we focus on the ground state wave function, since it gives more precise results and ambiguities regarding the excited state are absent. Again the radius shrinks with increasing momentum, while nothing can be said about its mass dependence. On $32^3 \times 8$ lattices in Tab. 4.4 the data do not fit anymore to the functional dependence of Eqs. (4.10) and (4.11) over the whole range of R and we had to restrict our

$T = 0.55T_c, 48^3 \times 16, \beta = 6.136, a = 0.083\text{fm}$								
		ground state			excited state			
m_π	p^2	R_0	ν	$\langle R^2 \rangle_{BS}^0$	R_1	ν	R_n	$\langle R^2 \rangle_{BS}^1$
0.450	0	4.36(6)	1.17(4)	17.8(17)	3.98(17)	1.33(10)	6.55(8)	6.5(30)
	1	4.29(6)	1.20(3)	16.2(11)	3.91(16)	1.34(10)	6.52(8)	5.9(24)
	2	4.22(6)	1.21(3)	15.3(10)	3.85(17)	1.35(10)	6.46(7)	5.5(21)
	4	4.10(6)	1.24(3)	13.6(9)	3.70(24)	1.36(13)	6.37(8)	4.7(21)
0.353	0	4.44(6)	1.16(3)	18.9(14)	3.98(20)	1.31(14)	7.08(9)	6.0(31)
	1	4.36(4)	1.18(2)	17.5(8)	3.90(19)	1.32(12)	7.02(8)	5.5(22)
	2	4.29(10)	1.20(6)	16.2(22)	3.84(26)	1.33(18)	6.90(9)	5.2(30)
	4	4.17(5)	1.23(3)	14.4(9)	3.69(30)	1.35(20)	6.76(16)	4.5(23)
0.286	0	4.47(6)	1.15(3)	19.6(15)	3.95(24)	1.29(17)	7.51(10)	5.8(31)
	1	4.39(7)	1.18(4)	17.7(16)	3.89(20)	1.30(14)	7.40(10)	5.5(23)
	2	4.32(10)	1.20(6)	16.4(22)	3.84(30)	1.32(15)	6.90(13)	5.4(29)
	4	4.21(4)	1.22(2)	15.0(7)	3.66(34)	1.33(23)	7.13(19)	4.4(22)
0.232	0	4.49(7)	1.15(4)	19.8(20)	3.93(37)	1.28(29)	7.85(23)	5.6(44)
	1	4.40(6)	1.17(3)	18.2(13)	3.87(32)	1.30(24)	7.56(16)	5.3(33)
	2	4.32(12)	1.20(7)	16.4(25)	3.84(41)	1.32(28)	6.91(21)	5.3(50)
	4	4.23(5)	1.23(3)	14.8(9)	3.65(44)	1.33(29)	7.37(20)	4.4(23)

$T = 0.93T_c, 48^3 \times 16, \beta = 6.499, a = 0.049\text{fm}$								
		ground state			excited state			
m_π	p^2	R_0	ν	$\langle R^2 \rangle_{BS}^0$	R_1	ν	R_n	$\langle R^2 \rangle_{BS}^1$
0.361	0	5.89(10)	1.15(6)	34.1(49)	4.67(14)	1.38(13)	7.98(10)	7.1(26)
	1	5.73(8)	1.18(5)	30.1(34)	4.59(12)	1.39(11)	7.83(6)	6.7(20)
	2	5.58(8)	1.21(6)	26.8(34)	4.52(10)	1.41(9)	7.69(5)	6.2(13)
	4	5.35(10)	1.25(7)	22.8(31)	4.31(15)	1.44(13)	7.49(9)	5.3(12)
0.272	0	6.07(12)	1.14(8)	37.1(72)	4.62(19)	1.34(14)	8.82(30)	7.0(21)
	1	5.89(12)	1.16(8)	33.3(63)	4.56(19)	1.37(14)	8.57(27)	6.5(17)
	2	5.73(13)	1.20(10)	28.9(62)	4.50(19)	1.39(17)	8.27(19)	6.1(19)
	4	5.50(12)	1.26(9)	23.7(40)	4.27(15)	1.42(14)	7.91(18)	5.3(11)
0.206	0	6.17(14)	1.13(8)	39.3(79)	4.53(22)	1.32(11)	9.56(56)	6.9(12)
	1	6.00(10)	1.16(7)	34.6(57)	4.49(18)	1.35(10)	9.18(40)	6.4(10)
	2	5.83(13)	1.22(9)	28.7(53)	4.44(22)	1.37(19)	8.60(30)	6.1(19)
	4	5.60(19)	1.31(15)	22.5(58)	4.17(13)	1.40(12)	7.86(16)	5.2(9)
0.125	0	6.18(12)	1.11(7)	41.4(76)	4.36(37)	1.28(19)	9.97(119)	6.8(20)
	1	6.00(10)	1.16(7)	34.6(57)	4.50(18)	1.35(10)	9.18(40)	6.4(10)
	2	5.83(13)	1.22(9)	28.7(53)	4.44(22)	1.37(19)	8.61(30)	6.1(18)
	4	5.60(20)	1.31(15)	22.5(58)	4.16(13)	1.23(12)	7.86(16)	8.1(45)

Tab. 4.2: Parameters of the Bethe-Salpeter wave functions of the P below T_c with $\omega=2$. R_0 , ν and $\langle R^2 \rangle_{BS}^0$ are given for the ground state and R_1 , ν , R_n , $\langle R^2 \rangle_{BS}^1$ for the excited mass.

$T = 1.24T_c, 48^3 \times 16, \beta = 6.721, a = 0.038\text{fm}$								
		ground state			excited state			
m_π	p^2	R_0	ν	$\langle R^2 \rangle_{BS}^0$	R_1	ν	R_n	$\langle R^2 \rangle_{BS}^1$
0.342	0	6.15(7)	1.24(5)	30.7(30)	4.93(10)	1.37(9)	7.93(7)	9.1(31)
	0	6.07(1)	1.147(1)	36.4(2)				
	1	5.94(8)	1.28(6)	26.6(29)	4.82(10)	1.40(10)	7.76(6)	7.9(25)
	1	5.86(1)	1.171(1)	32.1(1)				
	2	5.74(8)	1.33(6)	22.8(23)	4.67(8)	1.42(7)	7.47(4)	7.1(19)
	2	5.65(2)	1.197(1)	28.3(2)				
	4	5.45(10)	1.40(9)	18.6(24)	4.41(10)	1.45(9)	7.09(6)	5.8(13)
	4	5.37(2)	1.227(2)	24.0(2)				

$T = 1.49T_c, 48^3 \times 16, \beta = 6.872, a = 0.031\text{fm}$								
		ground state			excited state			
m_π	p^2	R_0	ν	$\langle R^2 \rangle_{BS}^0$	R_1	ν	R_n	$\langle R^2 \rangle_{BS}^1$
0.365	0	6.34(9)	1.28(7)	30.3(38)	5.04(11)	1.42(9)	7.61(6)	9.3(31)
	0	6.34(1)	1.160(1)	38.6(2)				
	1	6.11(4)	1.32(4)	26.3(17)	4.93(7)	1.44(7)	7.41(4)	8.4(20)
	1	6.11(1)	1.187(1)	33.8(2)				
	2	5.89(8)	1.37(7)	22.6(24)	4.78(10)	1.46(10)	7.19(6)	7.4(23)
	2	5.87(1)	1.217(1)	29.2(1)				
	4	5.55(9)	1.45(8)	18.0(19)	4.45(9)	1.51(8)	6.81(7)	5.5(10)
	4	5.51(2)	1.261(3)	23.7(2)				
0.361	0	6.73(2)	1.325(1)	31.6(2)				
	1	6.50(1)	1.350(1)	28.4(1)				
	2	6.27(1)	1.380(2)	25.3(1)				
	4	5.93(2)	1.416(3)	21.5(2)				

$T = 2.98T_c, 48^3 \times 16, \beta = 7.457, a = 0.015\text{fm}$								
		ground state			excited state			
m_π	p^2	R_0	ν	$\langle R^2 \rangle_{BS}^0$	R_1	ν	R_n	$\langle R^2 \rangle_{BS}^1$
0.394	0	6.95(7)	1.36(5)	32.0(24)	5.49(9)	1.51(7)	7.42(5)	11.0(27)
	0	7.04(2)	1.217(2)	42.1(3)				
	1	6.66(4)	1.41(4)	27.4(15)	5.33(5)	1.51(5)	7.24(2)	10.9(20)
	1	6.73(1)	1.251(2)	36.0(2)				
	2	6.39(4)	1.48(4)	23.0(11)	5.16(6)	1.54(6)	7.07(3)	8.5(15)
	2	6.47(2)	1.283(2)	31.4(2)				
	4	6.00(6)	1.56(6)	18.6(12)	4.81(7)	1.58(7)	6.70(4)	6.4(11)
	4	6.05(2)	1.331(3)	25.3(2)				
0.390	0	7.37(1)	1.383(2)	34.8(1)				
	1	7.09(2)	1.414(2)	30.8(2)				
	2	6.81(2)	1.448(2)	27.2(2)				
	4	6.45(3)	1.482(3)	23.4(2)				

Tab. 4.3: Parameters of the Bethe-Salpeter wave functions of the P above T_c with $\omega=2$. R_0 , ν and $\langle R^2 \rangle_{BS}^0$ are given for the ground state and R_1 , ν , R_n , $\langle R^2 \rangle_{BS}^1$ for the excited mass. Each second row list the fit results by the ratio method Eq. (4.9).

data to the $R \in [0, 5]$ or $R \in [0, 7]$ interval, respectively, in order to extract meaningful results.

$T = 1.49T_c, 48^3 \times 12, \beta = 6.640, a = 0.041\text{fm}$								
		ground state			excited state			
m_π	p^2	R_0	ν	$\langle R^2 \rangle_{BS}^0$	R_1	ν	R_n	$\langle R^2 \rangle_{BS}^1$
0.485	0	5.15(5)	1.41(3)	16.4(7)	5.14(11)	1.28(9)	6.50(4)	33.6(157)
	0	5.10(1)	1.263(2)	20.3(7)				

$T = 1.49T_c, 32^3 \times 8, \beta = 6.338, a = 0.062\text{fm}$									
		ground state			excited state				
m_π	p^2	R_0	ν	$\langle R^2 \rangle_{BS}^0$	R_1	ν	R_n	$\langle R^2 \rangle_{BS}^1$	
0.713	$R = 5$	0	3.80(2)	1.41(3)	8.90(36)	4.51(20)	1.34(2)	4.56(4)	33.1(55)
	$R = 7$	0	3.687(4)	1.444(1)	8.06(10)				

$T = 2.98T_c, 32^3 \times 8, \beta = 6.872, a = 0.031\text{fm}$									
		ground state			excited state				
m_π	p^2	R_0	ν	$\langle R^2 \rangle_{BS}^0$	R_1	ν	R_n	$\langle R^2 \rangle_{BS}^1$	
0.736	$R = 5$	0	4.06(5)	1.55(7)	8.56(63)	5.05(64)	0.97(5)	4.33(9)	146.6(448)
	$R = 7$	0	3.92(2)	1.596(6)	7.66(9)				

Tab. 4.4: Parameters of the Bethe-Salpeter wave functions of the P above T_c with $\omega = 2$. R_0 , ν and $\langle R^2 \rangle_{BS}^0$ are given for the ground state and R_1 , ν , R_n , $\langle R^2 \rangle_{BS}^1$ for the excited mass. Each second row list the fit results by the ratio method Eq. (4.9).

By looking at the data at $1.5 T_c$, R_0 and $\langle R^2 \rangle^0$ in lattice units increase with β . One might argue that the gauge links for larger β are closer to the unit matrix and an insertion of links in the fuzzing procedure increases the wave-function width. However, $\langle R^2 \rangle^0$ stays constant in physical units. Taking on the other hand a constant a at 1.5 and $3 T_c$, R_0 shows that the broadness of the wave functions shrinks. Thus the shrinking of the wave function can be interpreted as a pure temperature effect.

To also make contact with the temporal Bethe-Salpeter amplitudes, in Fig. 4.5 we have plotted both spatial and temporal amplitudes extracted by the ratio method at different small distance points. While they are indistinguishable below T_c clear differences between these amplitudes appear above T_c . The spatial wave functions are smaller than the temporal ones. This effect might be explained by a confining potential in spatial directions with a string tension, which increases with temperature as has been found in Ref. [30] in studying the (3+1)-dimensional $SU(3)$ pure gauge theory

$$\sqrt{\sigma_s(T)} = (0.566 \pm 0.013)g^2(T)T \quad \text{for } T \gtrsim 2T_c. \quad (4.15)$$

Furthermore KOCH ET AL. [178] used a modified Coulomb

$$V_{q\bar{q}}(r) = a[-1/r + 2T \ln(rT)] \quad (4.16)$$

and a confining (string) effective potential

$$V_{q\bar{q}}(r) = -a/r + \sigma_s r + \text{const.} \quad (4.17)$$

They plugged both into a two-dimensional Schrödinger equation, solved it numerically and compared the wave functions to the actual LQCD data. The results suggest that the confining effective potential reproduces the data well while the Coulomb potential, favored perturbatively, is definitely too weak at large distances.

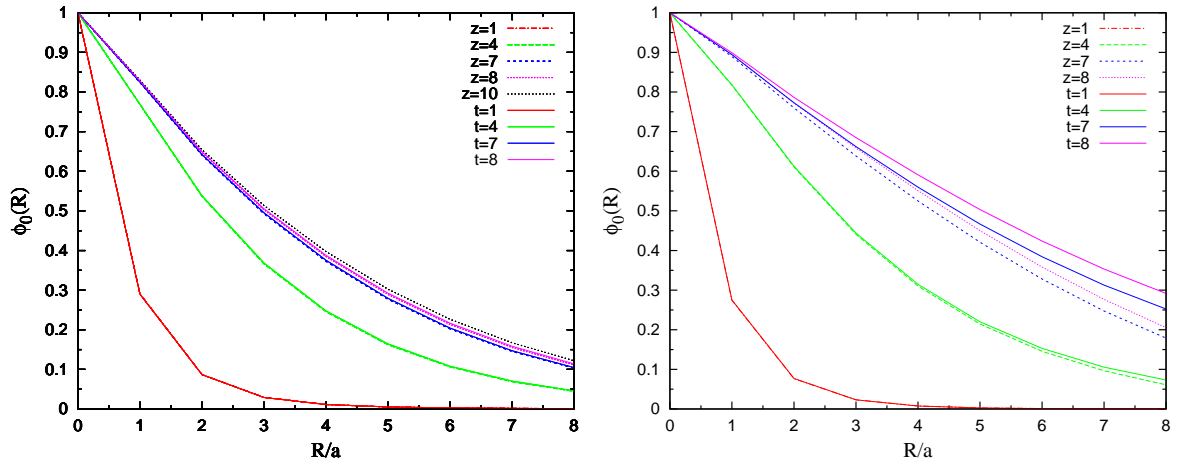


Fig. 4.5: Bethe-Salpeter amplitudes by the ratio method at 0.55 (left) and $3 T_c$ (right) on $48^3 \times 16$ lattices for small distances z and t in CFs by the ratio method.

4.3 Quark masses from axial Ward identities

When chiral symmetry is restored the pion is no longer a Goldstone boson and has a non-vanishing mass. Therefore the determination of bare quark masses m_b by searching the critical hopping parameter κ_c , where the pion mass vanishes, is obviously not valid above the critical temperature. Instead one can use the current quark mass definition Eq. (2.35) using the $\mathcal{O}(a)$ non-perturbatively improved currents Eq. (2.55). Since Eq. (2.35) is an operator identity, which holds in principle for all distances, it should also be independent of temporal or spatial direction. In Figs. 4.6(a) we show m_{AWI} for both directions and at temperature below and above T_c and find indeed no difference. However, since the mass plateaux for spatial correlators are larger we have used spatial correlators for our calculations only. In Tabs. B.1 and B.2 we quote our results. Both, m_b and m_{AWI} , are connected to the renormalized quark mass m_R via

$$m_R = \frac{Z_A(1 + b_A m_b)}{Z_P(1 + b_P m_b)} m_{AWI} = Z_m(1 + b_m m_b) m_b \quad (4.18)$$

from which it follows expanding in powers of a

$$m_{AWI} = Z \{1 + [b_m + (b_P - b_A)] a m_b\} m_b + \mathcal{O}(a^2) = Z(m_b) m_b + \mathcal{O}(a^2) \quad (4.19)$$

with $Z = Z_m Z_P / Z_A$. The factors b_m , $b_P - b_A$ and Z are known and have been calculated non-perturbatively by GUAGNELLI ET AL. [216] at zero temperature.

In Tab. B.1 we show the κ_c^z values below T_c , i.e., the extrapolated κ parameter, where the AWI quark masses vanish. They are in good agreement with the κ^z values in Section 4.1.2. Using m_b and κ one can also obtain the corresponding κ_c^z above T_c via the VWI, Eq. (2.27), which are listed in Tab. B.2. These values coincide fairly well with the interpolated values from Ref. [103] in Section 2.7.1, see Fig. 4.6(b). At some temperatures, especially for $N_\tau = 8$ at 1.5 and $3 T_c$, the tendency to smaller quark masses with increasing volume becomes apparent. This finite volume effect might explain the rather large deviations at $3 T_c$ and $\beta = 6.872$ in Fig. 4.6(b). At $1.5 T_c$ and $\beta = 6.640$ the critical hopping parameters at two different simulated κ values agree with each other. Hence quark mass effects can be neglected.

All in all these results confirm the findings in [188] that no clear temperature effect above T_c is observable.

To compare the quark masses obtained at different scales $\mu=1/a$ with each other, they have to be transformed to their physical value at a common scale. This can be done by using a mass independent renormalization scheme, e.g., $\overline{\text{MS}}$ where the renormalized quark mass m_R is only a function of the scale μ or accordingly $g_R(\mu)$. Including a mass into the RGE Eq. (2.133) one obtains

$$\mu \frac{\partial m_R}{\partial \mu} = \tau(g_R) m_R. \quad (4.20)$$

$\tau(g_R)$ is the renormalization group function, which can be determined perturbatively

$$\tau(g_R) = -g_R^2 \{d_0 + d_1 g_R^2 + \dots\}, \quad (4.21)$$

where only the first coefficient $d_0 = 8/(4\pi^2)$ is renormalization scheme independent. This allows to relate the running of the quark mass to the one of the coupling up to order g_R^4 with

$$m_R(\mu) = M(2\beta_0 g_R^2(\mu))^{d_0/2\beta_0}, \quad \beta_0 = \frac{11}{16\pi^2}. \quad (4.22)$$

M is the renormalization group invariant and scale independent mass, which in contrast to Λ in Eq. (2.133) is also renormalization scheme independent [217]. The common scale for quoting quark masses is $\mu = 2 \text{ GeV}$, which is approximately the inverse lattice spacing at $\beta = 6.0$. There the coupling is $g_{\overline{\text{MS}}}^2 = 2.4288$ (Tab. B.5) and allows now to compute the quark mass at this scale via

$$m_{\overline{\text{MS}}}(2\text{GeV}) = \left(\frac{g_{\overline{\text{MS}}}^2(2\text{GeV})}{g_{\overline{\text{MS}}}^2(1/a)} \right)^{d_0/2\beta_0} \frac{Z_A(m_b, g_{\overline{\text{MS}}}^2(1/a))}{Z_P(m_b, g_{\overline{\text{MS}}}^2(1/a), 1/a)} m_{AWI}(a). \quad (4.23)$$

The perturbative renormalization constants Z_A and Z_P stem from Eq. (2.148). The final renormalized quark masses can be found in the last column of Tab. B.1 and Tab. B.2. Different values at the same temperature might be due to somewhat different scales, i.e., slightly different temperatures, or effects of order g^4 , neglected in the RGE or in the renormalization constant.

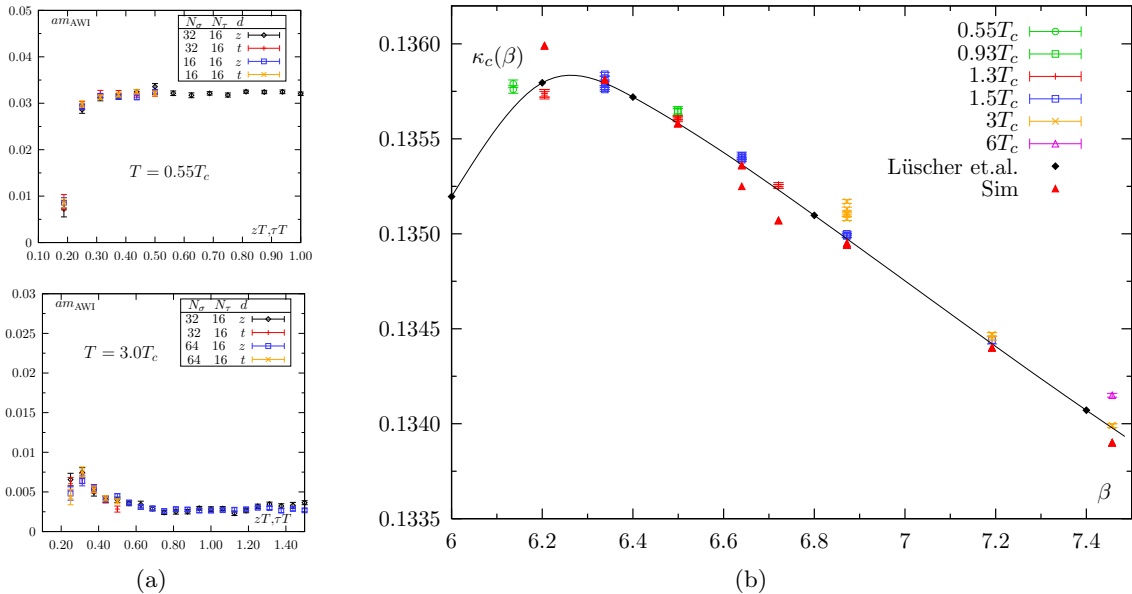


Fig. 4.6: AWI quark masses below and above T_c (a). Critical hopping parameter compared to those of Ref. [103] at different couplings and temperatures (b). The black curve is an interpolation of those points. 'sim' marks the κ values we used in our simulations.

In Tab. B.2 one can also find the AWI quark masses of the HF action. Since improved currents are not yet known for this action, those have been determined with $c_A = 0$, which might explain why they are negative for some lattice parameters.

4.4 Decay constants

Mesonic resonances are described by a limited number of parameters, which may vary with temperature or in-medium. After the investigation of meson masses and energies, amplitudes, (AWI-) quarkmasses and their temperature dependence, we focus in this section on the decay constants f_H ($H = P, V$). They are of considerable importance by themselves, but also enter the couplings of the ρ -meson, see e.g. Ref. [132],

$$g_{\rho\pi\pi} \simeq \frac{m_\rho}{f_\pi}, \quad g_{\rho\gamma} = \frac{m_\rho^2}{f_\rho}. \quad (4.24)$$

Correspondingly they have influence via the process

$$\pi^+\pi^- \xrightarrow{g_{\rho\pi\pi}} \rho^* \xrightarrow{g_{\rho\gamma}} e^+e^- \quad (4.25)$$

on the decay width³ $\Gamma_{\rho^*}(T)$ and might explain the ρ^* width broadening and the enhanced dilepton rate as discussed in Section 1.4.

Of special interest in this respect is the vector meson decay constant f_V . Experimentally it can be determined by the ρ^0 meson decay into electron-positron pairs $\rho^0 \rightarrow e^+e^-$ [27, 218], which rate is given by

$$\Gamma_{\rho \rightarrow e^+e^-} \approx \frac{4\pi}{3} \frac{\alpha_e^2}{m_\rho^3} g_{\rho\gamma}^2 = \frac{4\pi}{3} \frac{\alpha_e^2}{m_\rho^3} \left(\frac{m_\rho^2}{f_\rho} \right)^2 = \frac{4\pi}{3} \frac{\alpha_e^2}{m_\rho} F_V^2 = 7.02(11) \text{ keV}. \quad (4.26)$$

Here α_e is the fine structure constant of QED (Tab. 1).

The phenomenologically more important decay constant of the pion as defined in Eq. (2.39) can be determined from the leptonic decay of charged pions $\pi^\pm \rightarrow \mu^\pm + \nu$ and is the experimentally most accurately known decay constant. One finds $f_\pi(T=0) \simeq 132 \text{ MeV}$. Again a change of f_π with temperature would change the decay width $\Gamma_{\rho \rightarrow \pi\pi}$ in pion states.

Using the PCAC Eq. (2.39) together with the AWI definition Eq. (2.35) and Eq. (4.19) one can extract the P decay constant f_P on the lattice by means of

$$\begin{aligned} Z_A \langle 0 | \Delta_\mu \mathcal{J}_{A,\mu}^I(n) \mathcal{J}_P^\dagger(0) | 0 \rangle &= Z_A \Delta_\mu \left\{ \langle 0 | \mathcal{J}_{A,\mu}(n) | \mathcal{J}_P \rangle \langle \mathcal{J}_P | \mathcal{J}_P^\dagger(0) | 0 \rangle \right\} \\ &= f_P m_P^2 e^{ipn} \langle \mathcal{J}_P | \mathcal{J}_P^\dagger(0) | 0 \rangle \end{aligned} \quad (4.27)$$

and

$$\begin{aligned} Z_A \langle 0 | \Delta_\mu \mathcal{J}_{A,\mu}^I(n) \mathcal{J}_P^\dagger(0) | 0 \rangle &= 2m_{AWI} \langle 0 | \mathcal{J}_P(n) \mathcal{J}_P^\dagger(0) | 0 \rangle \\ &= 2m_{AWI} e^{ipn} \langle 0 | \mathcal{J}_P(0) | \mathcal{J}_P \rangle \langle \mathcal{J}_P | \mathcal{J}_P^\dagger(0) | 0 \rangle \end{aligned} \quad (4.28)$$

such that

$$\Rightarrow \frac{f_P}{Z(m_b)} = \frac{2A_P(\mathbf{0})m_b}{m_P^2}. \quad (4.29)$$

³ $\Gamma_\rho = 149.2(7) \text{ MeV}$ at zero temperature.

It is this relation we have used with spatial amplitudes $A_P(\tilde{\mathbf{0}})$ and screening masses m_P^z in order to determine $f_P/Z(m_b)$. At first sight f_P or $A_P(\mathbf{0})$ respectively seems to be very sensitive to the physical quark masses m_u and m_d , since they are much smaller than m_π . Naïvely Eq. (4.29) should vanish in the chiral limit. This is however not the case, since using the GMOR relation in Eq. (2.38) gives $f_P = |\langle \bar{\psi}\psi \rangle| / (Z(m_b)A_P(\mathbf{0}))$, which is then independent of quark masses but dependent on the quark condensate. This relation indicates that f_P or $A_P(\mathbf{0})$ extrapolated to $m_u = m_d = 0$ is still finite and not very different from its value at physical quark masses. f_P can also be studied (in temporal direction) by the fourth component of the axial-vector current as it couples to the pion state Eq. (2.39). At vanishing momenta its CF looks as follows

$$\sum_{\mathbf{n}} \langle 0 | \mathcal{J}_{A,4}(n) \mathcal{J}_{A,4}^\dagger(0) | 0 \rangle = \frac{f_P^2 m_P}{2Z_A^2} [\exp(-m_P t) + \exp(-m_P(N_\tau - t))] \quad (4.30)$$

and we have again

$$\Rightarrow \frac{f_P}{Z_A} = \frac{A_{A_4}(\mathbf{0})}{m_P}. \quad (4.31)$$

This relation can be safely used below T_c . However, above T_c our fitting program did not converge, which indicates that the overlap with the pion state significantly decreases. This suggests that the coupling to the pseudoscalar state is lost and the corresponding matrix element, i.e., f_P vanishes. On the theoretical side, Ward Identities imply that the axial current is degenerate with the vector current when chiral symmetry is restored. Moreover A_μ and V_μ are conserved currents, i.e., A_4 and V_4 are operators for a conserved charge. Thus, fitting their CFs fails, since they are constant for large distances, namely

$$Q_{A,4}(\tau) = \text{const.} \Rightarrow \sum_{\mathbf{n}} \langle 0 | \mathcal{J}_{A,4}(n) \mathcal{J}_{A,4}^\dagger(0) | 0 \rangle = \langle 0 | Q_{A,4}(\tau) \mathcal{J}_{A,4}^\dagger(0) | 0 \rangle = \text{const.} \quad (4.32)$$

The evaluation of the V meson constant equivalently is

$$\begin{aligned} Z_V A_{V,\mu}(\mathbf{0}) &= Z_V \langle 0 | \mathcal{J}_{V,\mu}^I(0) | V(\mathbf{p} = 0) \rangle = F_V m_V \epsilon_\mu = \frac{m_V^2}{f_V} \epsilon_\mu \\ \Rightarrow (Z_V f_V)^{-1} &= \frac{1}{m_V^2} \sqrt{\frac{|A_V(\mathbf{0})|^2}{3}} \end{aligned} \quad (4.33)$$

The experimental value for the ρ meson, Eq. (4.26), is $F_\rho = 220(5)$ MeV.

First the behavior of the pion decay constant shall be studied. This we have done using single state fits to the pseudoscalar CFs in spatial direction and utilizing Eq. (4.29) as well as fits to the fourth (temporal) component of the axial-vector CFs in temporal direction together with Eq. (4.31). The main focus lies thereby on its value in the chiral extrapolation. Our analysis is based on the assumption that its dependence on the quark mass is simply linear. In fact as seen in the figures the linear fit is likely to be appropriate. Below T_c Fig. 4.7(a) f_P clearly decreases with respect to the bare quark mass. Since the renormalization constants are known a direct comparison with the experiment becomes possible and is in a surprisingly good accordance to the measured value of 132 MeV (Tab. 4.5 (top)). Also concerning the time direction, we have found with 142(2) MeV at $0.55 T_c$ and 143(6) at $0.93 T_c$ values which are only somewhat ($\simeq 8\%$) larger, see Tab. 4.5 (middle).

Like the screening masses f_P changes significantly above the phase transition compared to the findings below T_c . However, only our data at $1.5 T_c$ on a $48^3 \times 12$ lattice allow a chiral

extrapolation which gives a value that is compatible with zero Tab. 4.5 (bottom). Effectively it shows the restoration of chiral symmetry $\langle\bar{\psi}\psi\rangle=0$ in the limit of vanishing quark mass. Similar conclusions can be made for the V decay constant, here only from spatial CFs. In the confined phase the extrapolated value of F_V matches the experimental value within the errors, which additionally may indicate the reliability of the renormalization constant. In contrast to f_P , however, F_V stays finite above T_c and no definite mass and temperature dependence is seen (Fig. 4.7(b)). Note that above T_c the connection of the decay constant as the decay width of a rudiment V resonance becomes doubtful. Instead it might give a signature of the overlap of the operator to a mesonic state of a quark-anti-quark.

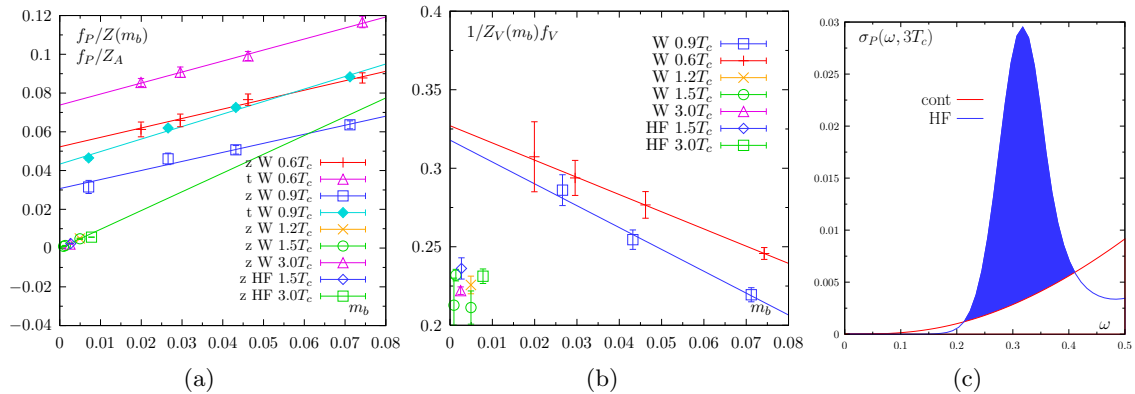


Fig. 4.7: Decay constants $f_P/Z(m_b)$ 'z' (Eq. (4.29)) and f_P/Z_A 't' (Eq. (4.31)) (a) and $1/f_V Z_V$ from Eq. (4.33) (b) above and below T_c on $48^3 \times 16$ lattices. Area under the ground state peak (c), which corresponds to the amplitude, see Eq. (4.34).

Once the SPF are determined one might think of extracting the physical width by directly fitting the ground state peak in the SPF. In this regard a short remark on the finite width of the SPF: In quenched approximation, where only interactions of the fermions with the gluonic background are considered, the ground state peak should be zero for the π and very small for the ρ meson. However, this holds then only for an infinite statistics and an infinite temporal lattice extent. Thus the width if non-zero is likely to be an artifact of MEM, or more precisely due to our limited statistics. We will come back to this in the following section.

Advocated by the authors of [11, 185], another way to determine the decay constant is by its relation to the area below the first peak of the SPF Eq. (2.164). This relation is given as

$$\int_{\omega_{\min}}^{\omega_{\max}} \sigma_H(\omega) d\omega = \frac{|\langle 0 | \mathcal{J}_H(n) | H(\mathbf{p} = 0) \rangle|^2}{2m_H} = \frac{A_H^2(\mathbf{0})}{2m_H}, \quad (4.34)$$

where $[\omega_{\min}, \omega_{\max}]$ is chosen to bound the one-meson particle state. In our analyses these are the intersection points with the finite T continuum SPF Eq. (2.166). This approach was applied to the HF data and gives similar results like fitting the spatial CF, see Tab. 4.5. It can be seen as a cross check to the SPF extracted with MEM and more importantly further supports the fact that the amplitudes of the spatial compared to the temporal CFs almost coincide if somewhat smaller. It should be mentioned again that concerning the HF data no clear connection to physical values due to the unknown renormalization constants can be given.

The final conclusion at these fairly large quark mass extrapolations and without a proper infinite volume and continuum extrapolation ($a \rightarrow 0$) is that no temperature dependence of decay constants in the confined phase neither in temporal nor in spatial direction is visible.

	T/T_c	m_b, m_{AWI}	$m_{\overline{MS}}[\text{MeV}]$	Z_V	Z	f_P/Z	$f_P[\text{MeV}]$	$1/Z_V f_V$	$F_V[\text{GeV}]$
W	0.55	0	0	0.788	1.090	0.052(2)	135(5)	0.327(1)	0.221(4)
	0.93	0	0	0.811	1.105	0.031(3)	137(8)	0.318(9)	0.221(7)
	1.2	0.00492	37.4(12)	0.827	1.105	0.0049(1)	28.8(5)	0.226(6)	0.370(10)
	1.5	0.001372	12.8(9)	0.830	1.104	0.0013(1)	9.2(6)	0.232(4)	0.479(8)
	3.0	0.002508	45.8(12)	0.854	1.097	0.0020(1)	25.7(12)	0.222(4)	0.989(21)
HF	1.5	0.0027	CF	1.0	1.0	0.0023(1)	14.8(6)	0.236(6)	0.579(15)
	1.5	0.0027	SPF	1.0	1.0	0.0025	16.1	0.262	0.571
	3.0	-0.00779	CF	1.0	1.0	0.0056(1)	72.0(12)	0.231(5)	1.185(26)
	3.0	-0.00779	SPF	1.0	1.0	0.0059	75.5	0.238	1.036

	T/T_c	m_b	$m_{\overline{MS}}[\text{MeV}]$	Z_A	Z	f_P/Z_A	$f_\pi[\text{MeV}]$	$1/Z_V f_V$	$F_V[\text{GeV}]$
W	0.55	0	0	0.804	-	0.074(1)	142(2)	-	-
	0.93	0	0	0.828	-	0.0433(17)	143(6)	-	-

	T/T_c	m_b	$m_{\overline{MS}}[\text{MeV}]$	Z_V	Z	f_P/Z	$f_\pi[\text{MeV}]$	$1/Z_V f_V$	$F_V[\text{GeV}]$
W	1.5	0.00495	30.7(52)	0.822	1.105	0.0048(3)	25.6(16)	0.211(10)	0.432(20)
	1.5	0.00092	5.7(6)	0.818	1.105	0.00088(4)	4.7(2)	0.212(21)	0.425(42)
	1.5	0	0	0.818	1.105	-0.000005	-0.02	0.212	0.425

Tab. 4.5: Hypercube (HF) and Wilson (W) fermion decay constant f_P and $1/f_V$ (F_V) above and below T_c from $48^3 \times 16$ lattices in spatial (top) and temporal direction (middle) and on a $48^3 \times 12$ lattice (bottom). For the HF we use the m_{AWI} instead of m_b .

Even at 0.93 T_c the values corresponds to the zero temperature findings, c.f. Ref. [185, 219]. Above T_c the pion decay constant comes close to or is even zero in the chiral limit as expected by its connection to the chiral condensate. The CFs of the fourth component of the axial-vector current further indicates that the pion state coupling no longer exists above T_c at the temperatures considered. All in all this documents the chiral symmetry restoration in the limit of vanishing quark masses. In contrast the modifications in the vector decay constant are, though clearly observable, not as dramatic as in the P case. This supports the assumption that mesonic like structures are still present even above the phase transition.

4.5 Spectral functions

Another way to study in-medium properties of mesons is given by investigating the behavior of the SPFs with MEM as introduced in Chapter 3. Having checked that this method works for free lattice data, we follow again the same path as in [188] but extend now the analysis to higher statistics and larger lattices, e.g., $48^3 \times 16$ below T_c for the Wilson case. For the first time SPFs of the hypercube action are shown.

Below the critical temperature the P and V SPFs for Wilson fermions are shown in Figs. 4.8 and 4.9 in the region of the ground state peak. For comparison also the corresponding screening masses are shown. As stated already their deviation from the pole masses at 0.55 T_c is only minor, but increases significantly approaching the phase transition. The figures indicate that the peak heights increase with lowering the quark mass, while they becomes broader at the same time. The broadening, however, may not imply a physics effect but simply an effect of moderate statistics. Also at low temperatures for pion, we do not see a δ -function peak but a finite width. This is understandable since with a finite statistics, it is not possible for the MEM program to resolve a δ -function peak. It was observed that the peak becomes sharper

as we increase the statistics. Since $0.55 T_c$ seems to be a rather moderate temperature, even more so for the quenched theory, it is reasonable to guess that the width is an effect of the moderate statistics. Concerning the volume dependence of these SPFs no systematic effect was observed.

Our results concerning the Wilson SPFs above T_c , see Fig. 4.10, which follow similar strategies as in Ref. [188] but use increased statistics and include larger lattices, are in agreement with Ref. [188]. In all channels the low energy parts simply scale with temperature and the ground state peak at $\omega/T \simeq 5$ even for the highest temperatures remains indicating that correlations between $q\bar{q}$ pairs still exist. This is in contradiction to Ref. [220], where the authors found significant changes between 1.4 and $1.9 T_c$ on anisotropic lattices far away from the chiral limit, a situation, which resembles findings in the charmonium sector [71, 72].

As has been mentioned in Chapter 3 lattice artifacts in the SPF of the HF action are shifted to much higher frequencies. Thus it has been speculated that also in the interacting case the infrared regime is less disturbed by cut-off effects than the Wilson case. In particular above T_c such a behavior is advantageous in order to clearly discriminate lattice artefacts from physical (bound) states. A comparison of the results we get from MEM is shown in Figs. 4.11(a) and 4.11(b). Note, that in the V channel the sum of all four contributions of γ_μ -matrices is shown, which yields twice the P CF in the free case. The figures demonstrate that for the Wilson case the possible bump at around $\omega/T \simeq 25$ is impossible to disentangle from the cut-off effects. In contrast the cut-off effects in the HF action are shifted from $\omega/T > 30$ towards $\omega/T > 80$ well separated from the infrared regime. In both models the ultraviolet regime is dominated by the default model. In order to make contact to physical values, one should bear in mind that the renormalization constants are unknown for the hypercube fermions and have been set to one.

Although the MEM error bars in Fig. 4.11(b) are large also for the Hypercube action a clear excitation close to $2\pi T$ appears. Correlations among the $\bar{q}q$ -pairs are obviously still present. Additionally two separate structures appear, which are now clearly separated from the bulk of lattice artifacts. It should be stressed that, unlike in the Wilson case for $N_\tau = 16$, no eigenvalue smearing is necessary anymore. In order to test whether we see bound states or lattice artifacts we study their N_τ dependence. Unfortunately for $N_\tau = 12$ eigenvalue smearing becomes necessary again and the Wilson two peak structure reappears (Fig. 4.11(c)). The position of the first peak is however unchanged. The picture, which arises at this point is twofold. First, it seems doubtful that smearing allows to make reliable statements about the physical nature of the second bump. In fact the SPF of the hypercube action at $N_\tau = 16$ seems to resolve the second bump as two bumps. Secondly, the physical nature of the two bumps at $N_\tau = 16$ themselves can only be analyzed by lattices with even larger N_τ . The question how many points in time are needed to determine reliable SPFs, c.g. [11, 221], remains an unsolved problem.

In Fig. 4.11(d) we show indications of an effective $U(1)_A$ as well as the $SU(N_f)_L \times SU(N_f)_R$ chiral symmetry restorations at $3 T_c$ by a degeneracy of the P-S and V-AV channels, respectively. While the first peak is almost identical for the V and AV, the P and S peak positions slightly deviate, which is due to a small entry for the S in the first bin.

In order to study how strongly the CF is affected by different energy ranges of the SPF or vice versa, we have plotted in Fig. 4.12 the ratio

$$\frac{G_V^I}{G_V}(\tau T) \equiv \int_I d\omega \sigma_V(\omega) K(\omega, \tau T) / \int_0^{\omega_{max}} d\omega \sigma_V(\omega) K(\omega, \tau T). \quad (4.35)$$

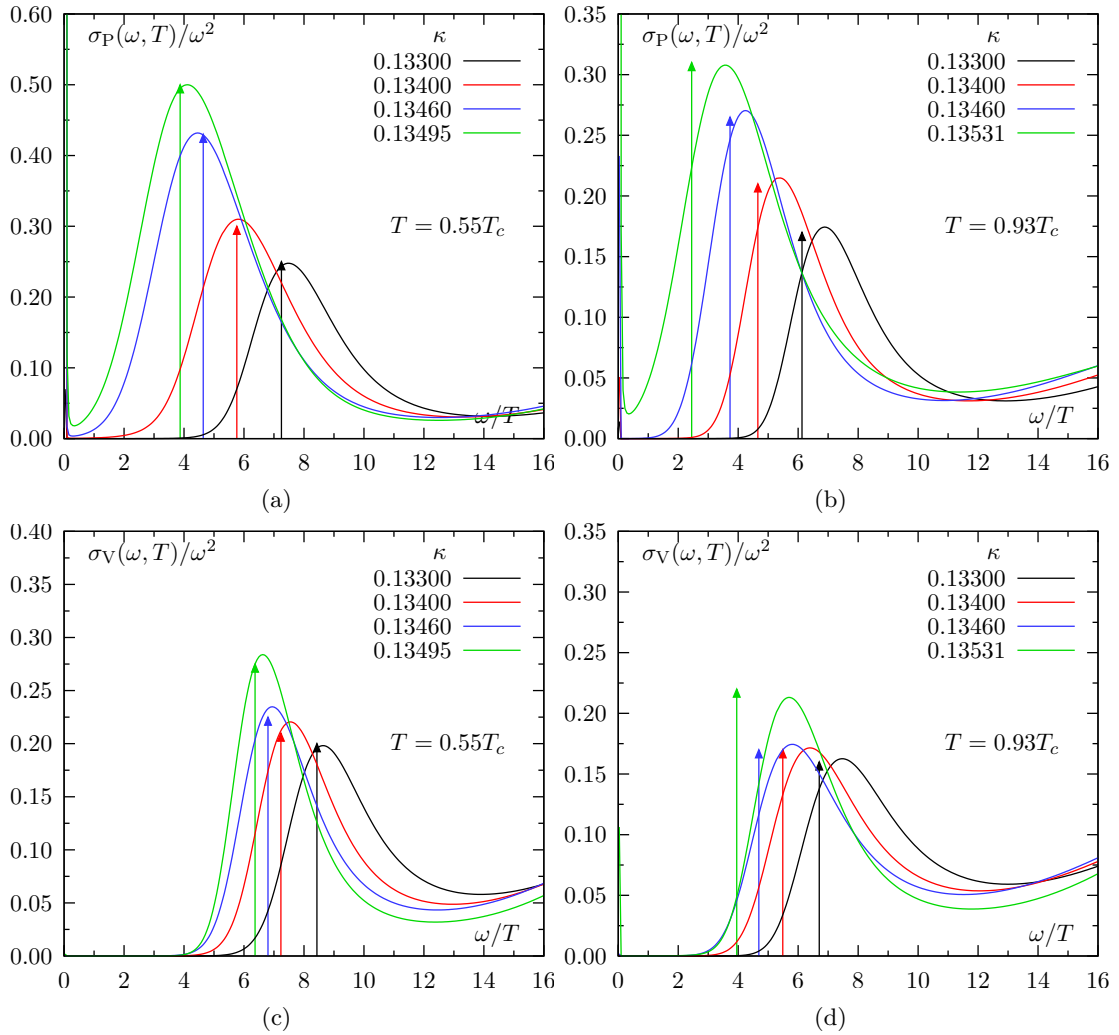


Fig. 4.8: SPF at $T=0.55 T_c$ (left) and $T=0.93 T_c$ (right) for the P (top) and the V meson (bottom), obtained from the $N_\sigma=32$ lattice. The arrows indicate the location of the screening mass.

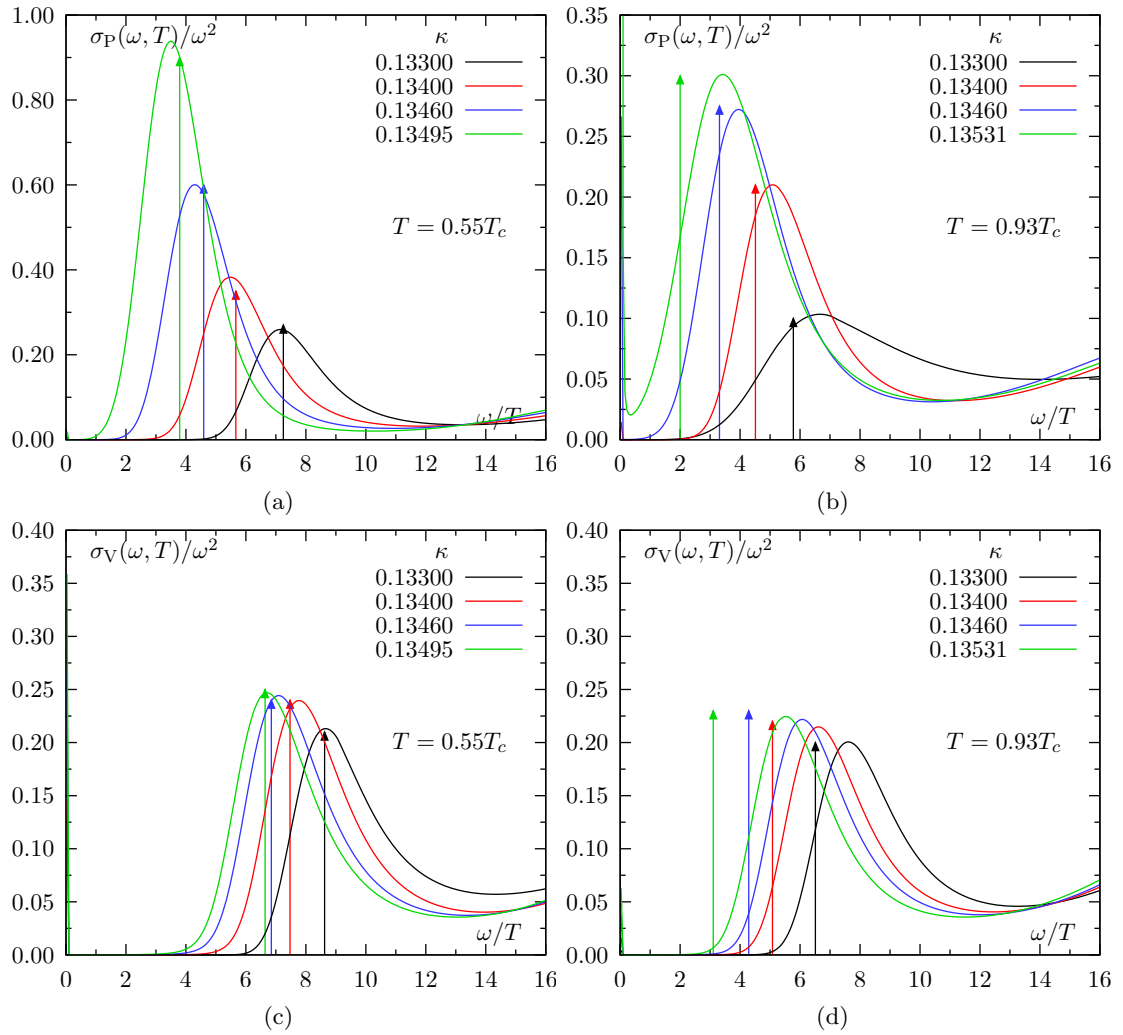


Fig. 4.9: SPFs at $T=0.55 T_c$ (left) and $T=0.93 T_c$ (right) for the P (top) and the V meson (bottom), obtained from the $N_\sigma=48$ lattice. The arrows indicate the location of the screening mass.

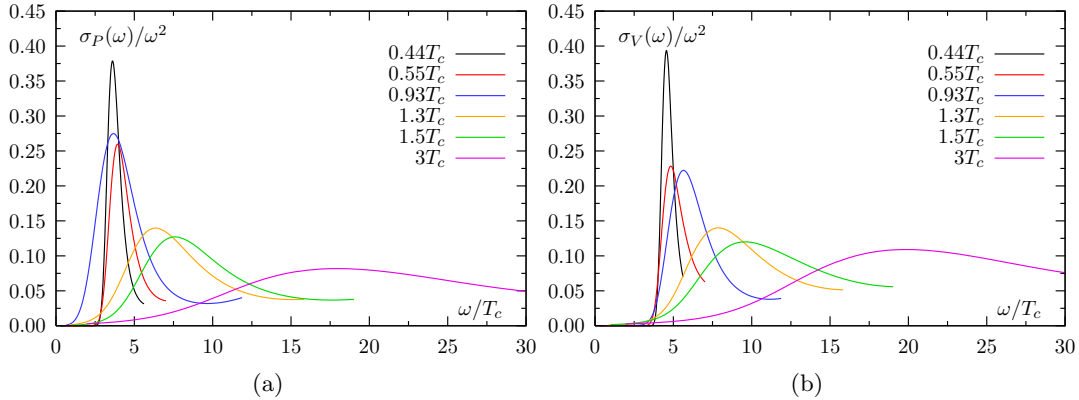


Fig. 4.10: P and V SPFs of the Wilson action at all T . Below T_c the quark masses are fixed to give the same P mass.

for the free as well as the interacting case. The intervals I are chosen to contain the peaks and lattice cut-offs in the interacting case separately. As expected the long distance part of the CF is dominated by the IR part of the SPF, while the dominant contribution for small distances up to $\tau T \lesssim 0.3$ comes from the intermediate region $10 < \omega/T < 50$. The UV, the orange, part, which represents the lattice artefacts, essentially affects only the first two points $\tau = 1-2$. Looking at the small distance part of the CF in the interacting case at $3 T_c$, one may speculate that the black line is least affected by the UV artefacts. Comparing the free and the interacting case it seems that the blue line, however, is mostly affected by UV lattice artefacts. The red line is somewhat intermediate. Thus, all in all one would say that the ground state is least affected by the lattice artefacts, the next excited state has a certain admixture of lattice artefacts and therefore its position cannot be guessed with much certainty. The second excited state is probably due to the lattice artefacts. The temperature induced changes of lattice artefacts are for the most part absorbed by the intermediate region of the SPF.

Once the V SPF is known a direct contact to the experiment can be made via the thermal dilepton production rate, see Refs. [188, 222]

$$\frac{d^8 N}{d^4 x d^4 p} = \frac{d^4 W}{dp^4} = \frac{5\alpha^2}{27\pi^3 \omega^2} \frac{1}{\exp(\omega/T) - 1} \sigma_V(\omega, \mathbf{p}, T). \quad (4.36)$$

For the free V SPF in the chiral limit and at vanishing momentum this leads to the Born rate

$$\frac{d^4 W^{\text{Born}}}{dp^4}(\omega, \mathbf{p} = \mathbf{0}) = \frac{5\alpha^2}{36\pi^2} \frac{1}{(\exp(\omega/2T) + 1)^2} \quad (4.37)$$

which is shown in Fig. 4.13. Plugging in the V SPF without using any renormalization constant we find again a suppressed dilepton production below $\omega/T \lesssim 3-4$ and an enhancement between $4 \lesssim \omega/T \lesssim 7$.

As we know how important cut-off effects are for small distances in the CF and how they might affect also the intermediate region of the reconstructed HF SPF and to further demonstrate also the possible influence of renormalization constants, we show Fig. 4.13. Here we have set Z_V such that the midpoint of the V CF matches the corresponding free HF CF. We further used the continuum default model and the full ($N_\tau = 15$) HF data at $3 T_c$. In the outcome the present cut-off effects have been completely absorbed in the three peak structure. Omitting the smallest distance point ($N_\tau = 13$) in contrast lead to an almost perfect continuum SPF and continuum Born rate for 1.5 and $3 T_c$. Such a behavior becomes clear in view of the next section. The apparent sharp peak at $\omega/T \simeq 0$ again has to be considered as a MEM artefact.

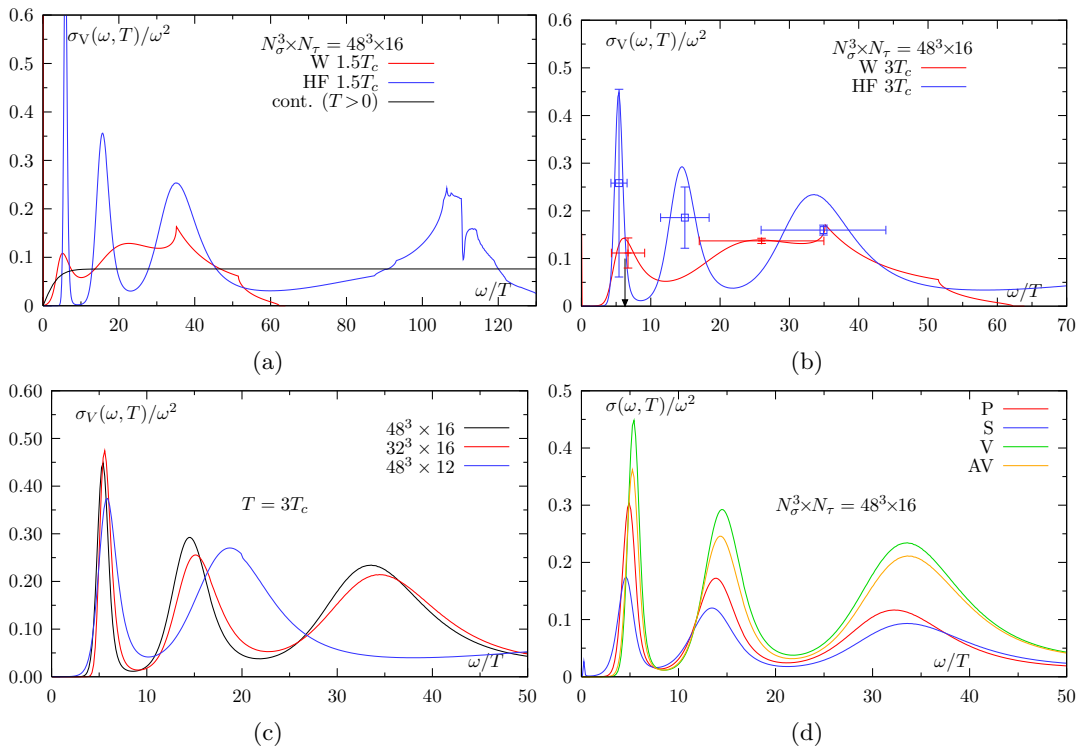


Fig. 4.11: V SPFs of the truncated fixed point and Wilson action at $1.5 T_c$ (a) and $3 T_c$ with MEM errors (b). The arrow indicates the free screening mass value $2\pi T$. Volume and N_τ dependence of the HF SPF (c). All four channels at $3 T_c$ for the hypercube action (d).

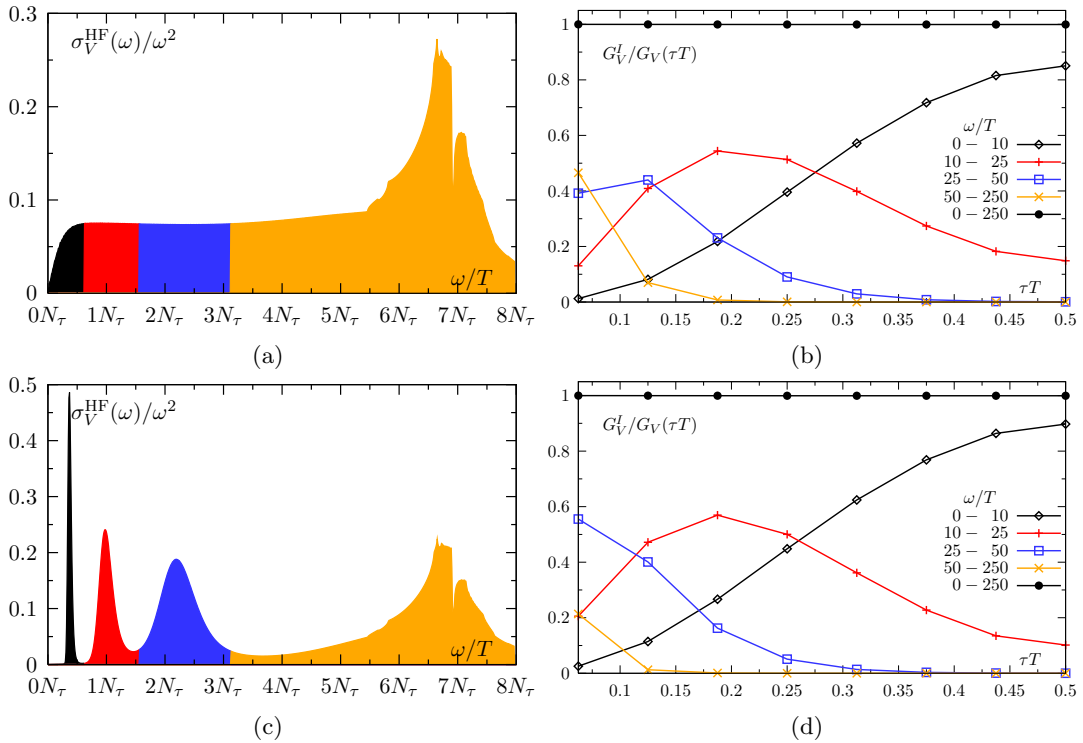


Fig. 4.12: Contributions of the different energy ranges of the HF SPF to the correlator in the free case (a,b) and at $3 T_c$ (c,d) on a $48^3 \times 16$ lattice.

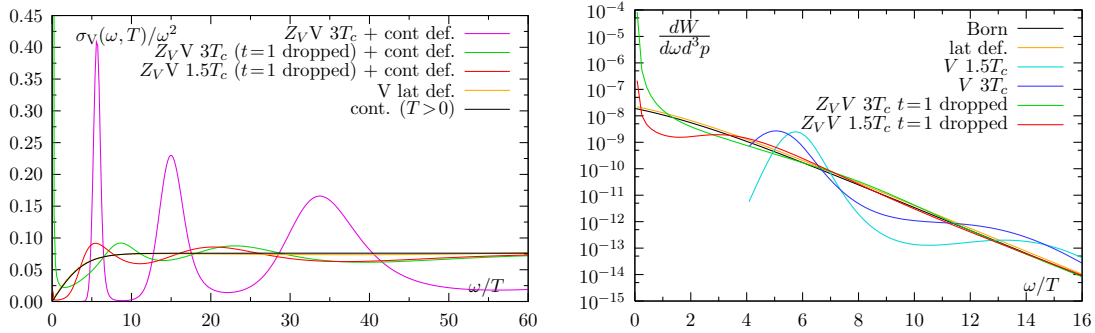


Fig. 4.13: HF V SPFs with complete CF and point at $t=1$ dropped and Z_V chosen to be 0.788 at $3 T_c$ and 0.769 at $1.5 T_c$ on a $48^3 \times 16$ lattice (left). The corresponding thermal dilepton production rate in the QGP phase using Eq. (4.36) (right).

4.6 Cut-off and thermal effects in temporal correlation functions

In this section temporal CFs above T_c are compared with the free continuum, Eq. (3.25), as well as free lattice CFs as shown in Figs. 4.14 and 4.15. This allows for a direct study of thermal modifications and the influence of possibly remaining interactions or simply cut-off effects. Since we only show results above the critical temperature⁴ and at almost vanishing quark masses, an additional discussion of the influence of non-vanishing quark masses like below T_c can be avoided. Furthermore as we have seen deviations from the free theory even at $3 T_c$ in the SPF which might come up due to MEM uncertainties through the prior default model function, one can explore how much of these deviations can already be noticed at the correlator level.

The ratio of the Wilson CF G_H and the free lattice one $G_H^{\text{W,free}}$ at the same lattice size with the known Z_H -factors included clearly indicates deviations growing with distance. These effects are much stronger in the P channel (c.f. Fig. 4.14(a)), than in the V channel (c.f. Fig. 4.14(b)), where the data lies closer to the free CF. For large distances large deviations of the order $\simeq 45-80\%$ are seen in the P channel, while they are rather small ($\lesssim 15\%$) in the V channel. Similar results have been found at the other temperatures.

Keeping the lattice spacing (N_τ) fixed at constant temperature allows us to study finite volume effects. At small τT these effects seem to be strongly absorbed by the free lattice CF as the points fall almost on top of each other. On the other hand finite a (cut-off) effects are still present in the small distance (UV) regime by comparing CFs at different N_τ and a fixed aspect ratio. They are not completely absorbed by $G_H^{\text{W,free}}$ and one can clearly observe increasing CFs with decreasing lattice spacing for the P and V. However, one should be extremely cautious in interpreting these deviations as a pure discretization effect. Ambiguities from the a , and thus the T and Z_H determination which both depend on a precise knowledge of the β -function, can play an important role for the ratio heights. Of course for the latter this should not hold for the non-perturbatively determined V renormalization constants.

The large τT behavior is somewhat different from the small distance behavior. Here cut-off effects are small or almost absent, while now the volume effects cannot be completely described by the free lattice CF. The ratios show a significant but non-systematic effect. However, all in all these effects are rather small, taken the error bars into account. This indicates that the corresponding infrared effects are only slightly different in larger volumes and supports essentially the findings of the MEM analysis in Section 4.5.

⁴for results below T_c see again [188]

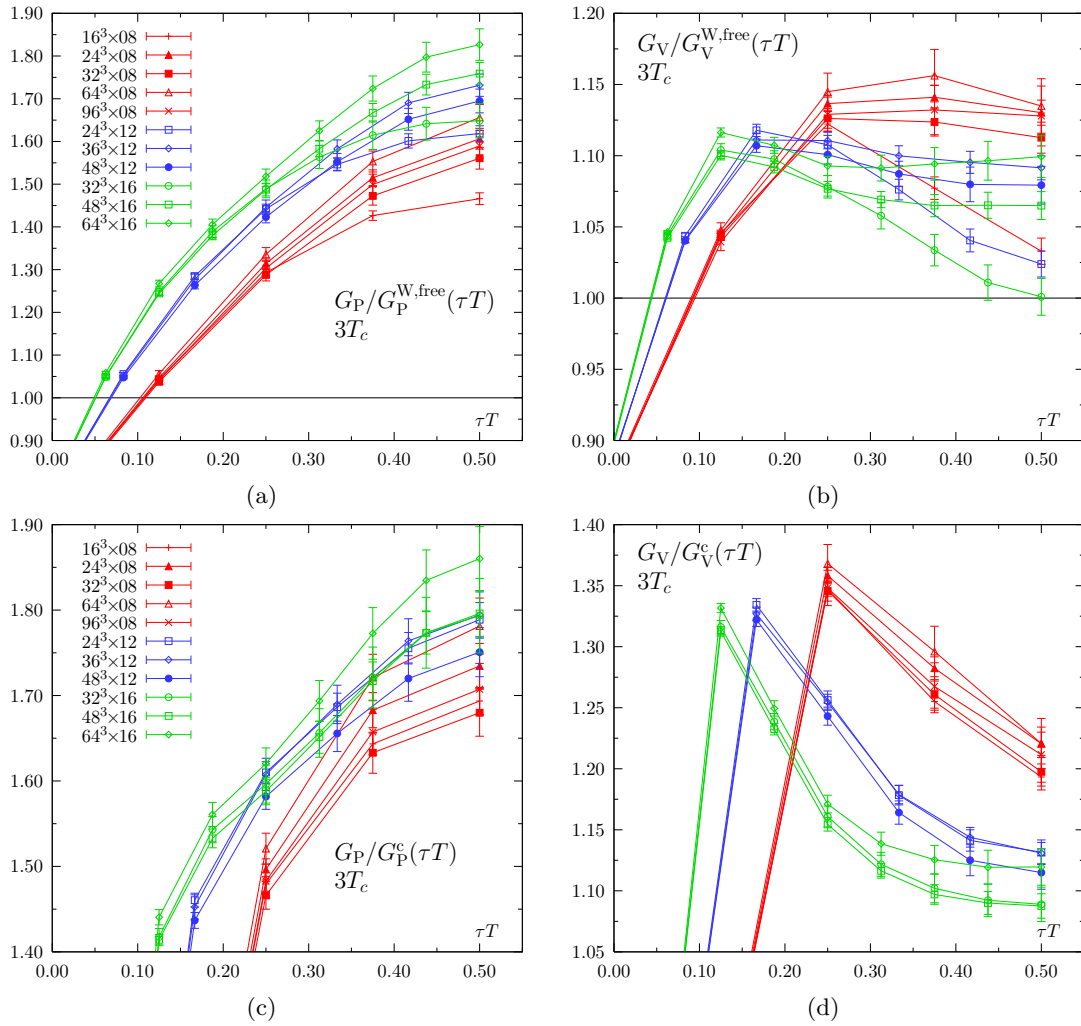


Fig. 4.14: Ratios with the temporal pseudoscalar (left) and vector (right) Wilson CFs at $3T_c$ and the free lattice CF (top) and free continuum CF (bottom) on all lattices. For the Wilson case renormalization constants Z_H have been taken into account.

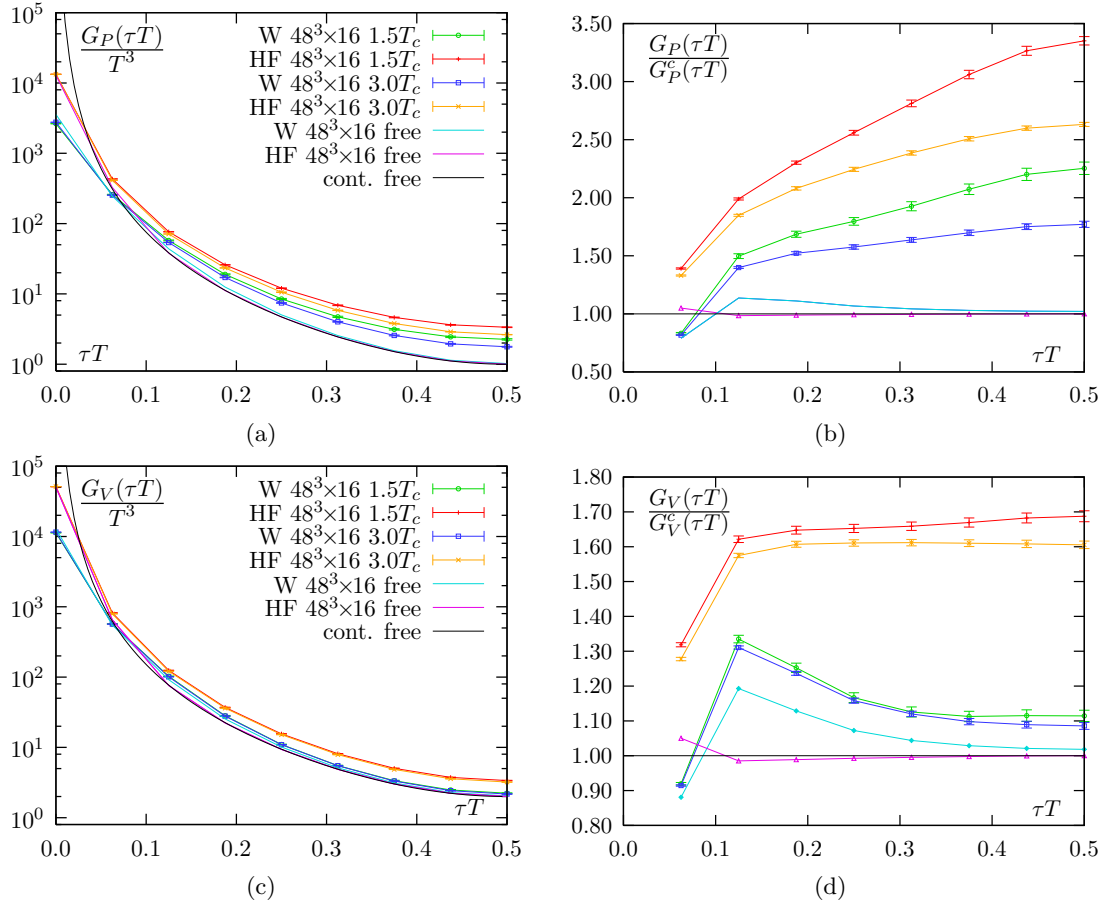


Fig. 4.15: Pseudoscalar (top) and vector (bottom) CFs in both discretizations (left) and their ratio with the free continuum CF (right) at $1.5 T_c$ and $3 T_c$. For the Wilson case renormalization constants Z_H have been taken into account.

Since finite volume effects are overestimated by the free lattice CF, it is useful to study those ratios also with the free continuum CF shown in Fig. 4.14(c,d). Indeed, finite volume effects at large τT are not so large anymore. Finite a effects are visible although, when comparing $N_\tau=8$ results with $N_\tau=12$ and 16 data. The latter are already close to each other.

On the other hand comparing both the free Wilson and HF CF above T_c normalized to their free continuum ones, Fig. 4.15, on a $48^3 \times 16$ lattice shows again the advantageous behavior of the HF formulation. Deviations are at most of order 5% for small distances, while they are much larger for Wilson fermions ($\leq 20\%$) due to the known lattice artifacts. However, by reason of the unknown HF Z_H nothing can be said at this time about their quantitative deviation in the interacting case. Especially in the V case, if one would match the ratios G_V/G_V^c at $\tau T=0.5$, their large distance behavior is similar for $1.5 T_c$ and even identical within the errors at $3 T_c$. Again the small and intermediate distance behavior lies much closer to (below) the continuum one for the HF CF.

Comparing both temperatures in Fig. 4.15 shows that in the HF and Wilson discretization the V and P CFs approach the free quark limit with rising temperature from above. However, even at $6 T_c$, not shown in the figures for clearness reasons, the Wilson V CF deviates from the free continuum CF significantly. Also, taking the cut-off effects of the free Wilson correlators into account, an enhancement of 10% remains which is in contrast to predictions obtained from HTL-resummed perturbation theory or quasiparticle models. In the former the V CF cannot be computed due to the mentioned strong (linear) divergence at low frequencies in the SPF [174], whereas the latter leads to a suppression of the correlator, as compared to the free case [223, 224]. Apart from constant factors also in this sense the HF V CFs qualitatively gives more model consistent results.

The qualitative change of CFs with momentum for Wilson fermions has also been studied in Ref. [188]. The hypercube fermions show qualitatively the same behavior. In both channels the midpoint of the CFs decreases with increasing momenta, see Fig. 4.16.

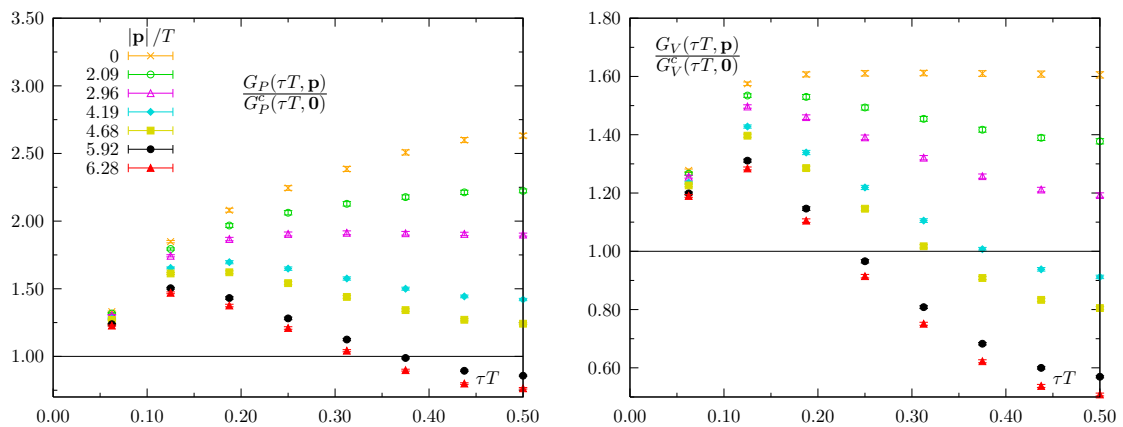


Fig. 4.16: P (left) and V (right) CFs at different momenta normalized to the free zero momentum CF at $3 T_c$ on $48^3 \times 16$ lattice for the HF action.

5 Screening masses and correlation functions in the high-temperature phase

5.1 Screening masses in infinite volume and continuum extrapolation

In this section, we will present results from a detailed investigation of the mesonic screening masses at temperatures above the deconfinement transition. In particular, we will look at the finite volume effects and finite lattice spacing effects on the screening mass. These results were presented for the first time at the *Lattice 2005* conference in Dublin, see Ref. [15].

As stated in Section 2.8.2 in the infinite temperature limit mesonic CFs are combinations of two free quark propagators. Correspondingly in the chiral limit and $\mathbf{p}_\perp = 0$ the decay of spatial correlators at large distances is dominated by twice the lowest quark Matsubara frequency $\omega_n = (2n + 1)\pi/N_\tau$, i.e.,

$$m_H^z = 2\sqrt{m_q^2 + \omega_0^2} = 2\omega_0^{quark} = 2\pi T \quad \text{for } m_q \rightarrow 0. \quad (5.1)$$

This is clearly different from the temporal mass $m_H = 0$. The distance between hadronic screening masses and the free value in the chiral limit can be considered as a measure how close the interacting system is to a system of free quarks.

This chapter now aims at comparing free spatial continuum CFs at vanishing quark masses with our findings at $m_q \simeq 0$ above T_c in order to get control over finite volume and lattice spacing effects.

The analytical study of continuum spatial CFs, here of quark-anti-quark pair with pion quantum numbers, was first addressed in Ref. [180], with the result

$$G_\pi(z) = \frac{N_c T}{2\pi z^2 \sinh(2\pi T z)} [1 + 2\pi T z \coth(2\pi T z)]. \quad (5.2)$$

From this an effective z -dependent screening mass can be defined by

$$m_P^z(z) = -\frac{1}{G(z)} \frac{\partial G(z)}{\partial z} = 2\pi T \left\{ \frac{1}{x} (2 + x \coth(x)) + \frac{1}{1 + x \coth(x)} \left(\frac{x}{\sinh^2(x)} - \coth(x) \right) \right\}, \quad (5.3)$$

where $x = 2\pi T z$. At large distances, e.g., $x \geq 5$, the exact data is reasonably well approximated by a leading behavior obtained as

$$\frac{m_P^z(z)}{T} = 2\pi \left(1 + \frac{1}{x} + \dots \right). \quad (5.4)$$

Note that the effective screening mass, which is shown in Fig. 5.1(a), does not exhibit any plateau-like behavior, which otherwise would signal the presence of a genuine pole contribution. Instead the anticipated value $2\pi T$ is reached from above, yet only at asymptotically large distances. Also in the interacting case, e.g., on $64^3 \times 16$ lattices a genuine plateau cannot be

identified at temperatures above T_c for our lattices. For definiteness we therefore will quote screening masses obtained at a certain spatial separation. The choice $z = L/4$ then leads in the free case to

$$\frac{m^z(z = L/4)}{T} = 2\pi \left(1 + \frac{2}{\pi} \frac{1}{LT} + \dots \right), \quad (5.5)$$

i.e. the leading correction to the continuum screening mass is linearly dependent, $\sim 1/(LT)$, on the (inverse) separation.

In numerical (lattice) investigation the separation is limited by the box size. In order to address finite volume effects we have calculated the free spatial lattice CFs¹ semi-analytically analogous to Ref. [187] as sums over (quark) Matsubara frequencies and momenta k_1, k_2 perpendicular to the correlation direction z

$$G_H(z) = \frac{N_c}{N_\sigma^2 N_\tau} \sum_{k_1, k_2, \omega_n} \frac{1}{(1+M)^2} \frac{1}{\sinh^2(E_1 N_\sigma/2)} \left\{ b_H \cosh \left[2E_1 \left(\frac{N_\sigma}{2} - z \right) \right] + d_H \right\}, \quad (5.6)$$

where M is given by $M = \sum_{i=1,2,4} (1 - \cos(k_i))$, $k_{1,2} = 2\pi n_{1,2}/N_\sigma$, $k_4 = \omega_n$ and

$$\cosh(E_1) = 1 + \frac{\sum_{i=1,2,4} \sin^2(k_i) + M^2}{2(1+M)}. \quad (5.7)$$

The coefficients b_H and d_H are given in Tab. 5.1.

Again the free lattice screening masses are obtained from the free lattice CFs this time via Eq. (2.184) and it turns out, Fig. 5.2, that also in this case the leading finite volume correction to the screening mass is linearly dependent on $1/(LT) = N_\tau/N_\sigma$. In the interacting case the finite volume effects are less severe. This can be understood because freely propagating quarks feel the box boundaries and the momentum cut-off more strongly than interacting quarks. In order to describe the volume effects we have therefore taken the exponent of the $1/(LT)$ term as a free parameter,

$$\frac{m_H^z(L, a)}{T} = \frac{m_H^z(a)}{T} \left(1 + \gamma \left(\frac{N_\tau}{N_\sigma} \right)^p \right). \quad (5.8)$$

We expect that p takes values between 3 as in the confined phase, e.g. [206], and 1 as in the

¹Contact terms at $z=0$ are omitted.

	b_H	d_H
P	1	0
S	d	$d - 1$
$\frac{1}{2}(V_1 + V_2)$	$1 - \frac{1}{2} \frac{\sin^2(k_1) + \sin^2(k_2)}{\sinh^2(E_1)}$	$-\frac{1}{2} \frac{\sin^2(k_1) + \sin^2(k_2)}{\sinh^2(E_1)}$
V_3	0	1
V_4	$1 - \frac{\sin^2(k_4)}{\sinh^2(E_1)}$	$-\frac{\sin^2(k_4)}{\sinh^2(E_1)}$
$\frac{1}{2}(A_1 + A_2)$	$d - \frac{1}{2} \frac{\sin^2(k_1) + \sin^2(k_2)}{\sinh^2(E_1)}$	$d - 1 - \frac{1}{2} \frac{\sin^2(k_1) + \sin^2(k_2)}{\sinh^2(E_1)}$
A_3	$d - 1$	d
A_4	$d - \frac{\sin^2(k_4)}{\sinh^2(E_1)}$	$d - 1 - \frac{\sin^2(k_4)}{\sinh^2(E_1)}$

Tab. 5.1: Coefficients b_H and d_H of the spatial free Wilson lattice meson correlation functions Eq. (5.6). Here $d = \sum_{1,2,4} \sin^2(k_i) / \sinh(E_1)$.

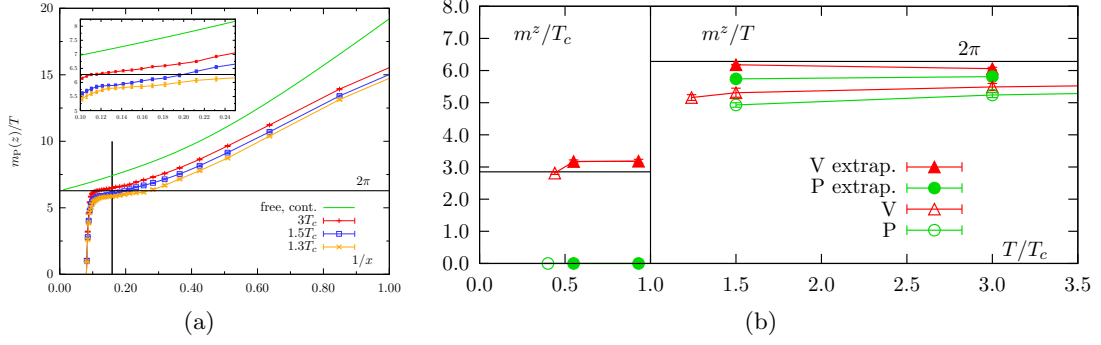


Fig. 5.1: Effective screening masses on $64^3 \times 16$ lattices compared with the free continuum one (a). Extrapolated result compared with former results [188], which have been obtained via rescaling masses determined at largest lattices with $2\pi/m_{free}^z(L, a)$. We give m^z below T_c in units of T_c from finite volume extrapolation. The physical vector mass is depicted by a black line (b).

infinite temperature limit. The fits indeed return results which decrease towards 1 with rising temperature, Tab. 5.2. To extract $m_H^z(a)$ we have fixed p at its value for $N_\tau = 8$. The remaining lattice spacing dependence can be inferred from Eq. (5.7). The leading behavior is obtained by taking into account the lowest Matsubara frequency only,

$$\cosh(E_1) \simeq 1 + \frac{\sin^2(\pi/N_\tau) + (1 + \cos(\pi/N_\tau))^2}{2(2 - \cos(\pi/N_\tau))}. \quad (5.9)$$

Further expanding in π/N_τ leads to

$$2E_1 = m_H^z(a) \simeq \frac{2\pi}{N_\tau} \left[1 - \frac{1}{3} \left(\frac{\pi}{N_\tau} \right)^2 + \dots \right], \quad (5.10)$$

m_H^z being independent of the hadron quantum numbers. Therefore, the lattice spacing dependence is expected to be quadratic in a or, equivalently in $1/N_\tau$,

$$\frac{m_H^z(a)}{T} = \frac{m_{scr}}{T} - \lambda \left(\frac{1}{N_\tau} \right)^2 + \dots \quad (5.11)$$

in the free as well as in the interacting case. Note that the continuum limit is approached from below. Thus, infinite volume and continuum limit counteract each other.

As Fig. 5.2(g) and Fig. 5.2(h) show the coefficient λ is rather small, compared to the expected value $2\pi^3/3$, and possesses large errors. Hence, finite a effects seem to play only a minor role. The final numbers are given in Tab. 5.2 and in Fig. 5.1(b). They are significantly closer to the

T	λ		T	p		T	m_{scr}/T	
	P	V_T		P	V_T		P	V_T
$1.5T_c$	4.5(26)	7.8(15)	$1.5T_c$	2.05(24)	2.21(29)	$1.5T_c$	5.74(2)	6.18(1)
$3T_c$	0.6(53)	2.5(86)	$3T_c$	1.46(15)	1.54(21)	$3T_c$	5.81(4)	6.06(4)

Tab. 5.2: Results from the data fit to Eq. (5.8) and Eq. (5.11).

free value than the fitted energy values of the largest lattices in [188] rescaled by a factor of effective screening masses at $z = N_\sigma/4$ on a free lattice divided by 2π . Due to the exceptional configurations it is difficult to analyze the data below $1.3 T_c$.

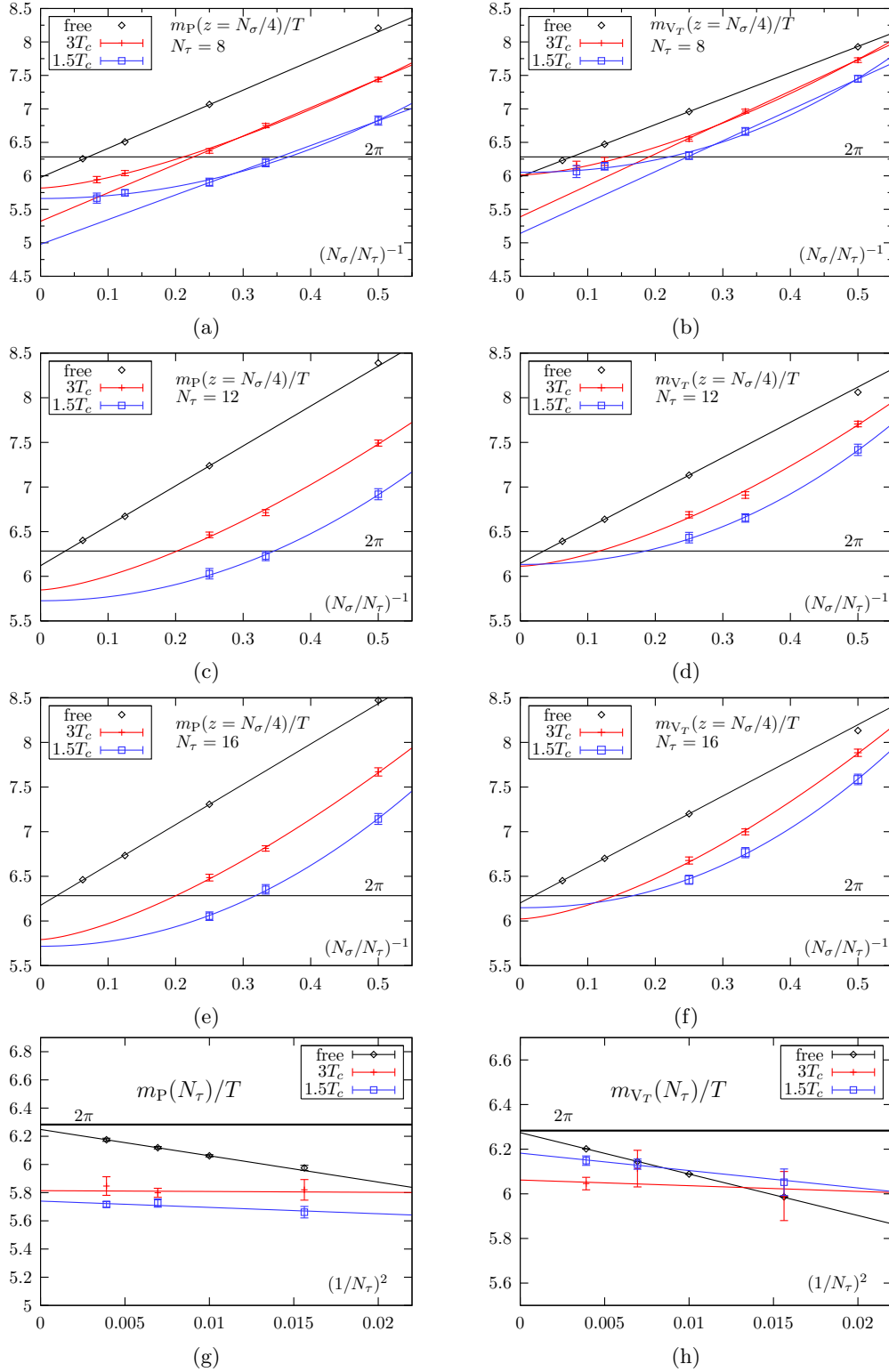


Fig. 5.2: Effective screening masses at $z = L/4$ compared to the free continuum ones as a function of aspect ratio (lattice volume) at $N_\tau = 8, 12$ and 16 (a-f) and of finite lattice spacing (g,h).

As can be seen at both temperatures the pion screening mass is about 9% smaller than in the free case while the vector meson V_T comes out close to but also below 2π . This is to be contrasted with analytical calculations by LAINE ET AL. based on dimensionally reduced screened perturbation theory and treating ω_0^{quark} as a heavy quark mass [225]. This effective high-temperature theory predicts screening masses that approach the free result from above at $T \gg T_c$

$$m^z \approx 2\pi T + 0.14083730g^2T. \quad (5.12)$$

At $T \simeq 2T_c$ the gauge coupling is estimated to be $g^2 \approx 2.7$ [226] and thus the second term corresponds to a 5% correction. Since the screening masses are expected to decrease close to the phase transition and in the light of our data it seems questionable, whether such an approach is valid at least at temperatures we observe. Additionally higher order coefficients in Eq. (5.12) equivalently to those derived in QCD pressure calculations [6] may significantly change this evolution.

The final conclusion that can be drawn out of these findings is that at least at $3 T_c$ and $1.5 T_c$ small residual bindings might still exist, which are stronger for the P than for the V_T channel. At $N_\tau = 12$ and 16 fit results need to be secured by data points from larger aspect ratios, otherwise systematic errors are larger than the final fit results imply. Furthermore one should increase the statistics and could think about using a combined fit with p held fixed at fixed T in order to improve the significance of these statements.

For our study finite size effects play a dominant role. However, once a considerably large aspect ratio $\gtrsim 12$ is reached, Fig. 5.2(a,b), they are rather small. To verify this conclusion and to show that finite a effects are still small, again larger lattices in particular for $N_\tau = 12$ and 16 are desirable. However, they are extremely costly.

5.2 Spatial correlation function in the context of chiral and Lorentz symmetry breaking

At the end of this chapter we want to have a closer look at the spatial CFs with respect to chiral symmetry. As discussed at $T = 0$ chiral symmetry $SU(N_f)_A$ is spontaneously broken in the limit of vanishing quark masses, while the $U(1)_A$ symmetry is broken anomalously. Hence, V/AV (ρ/a_1) and P/S (π/δ) respectively should be non-degenerate. Since we are unable to carry out our calculations at vanishing quark mass below T_c , we can only show these channels for finite quark mass, e.g., at $0.93 T_c$ in Fig. 5.3(a). The explicit symmetry breaking effects should be small at these fairly small pion masses in comparison to the vector masses, i.e., $m_P/m_V = 0.656$.

It has long been speculated by SHURYAK [227] that $U(1)_A$ -symmetry might be effectively restored along with the $SU(N_f)_A$ symmetry in the high temperature phase, in the sense that no $U(1)_A$ -violating effects can be found among the CFs in this phase. Moreover, it has been shown that unless there are contributions from non-topological configurations in the functional integral that form a set of measure zero in the chiral limit $U(1)_A$ -violating CFs must vanish [228].

For $N_f=3$ group theoretical arguments constrain every $SU(3)_A$ symmetric two point function to be automatically also $U(1)_A$ symmetric [229]. More generally $U(1)_A$ violation cannot occur in CFs of n quark bilinears if $n < N_f$. Hence, all two point functions are degenerate, once $SU(3)_A$ is restored.

This does not hold for $N_f=2$. Here there are two chiral ($SU(2)_A$ -)singlet two-point functions with even parity, one $U(1)_A$ -invariant and one $U(1)_A$ -variant. This opens the possibility to

study the influence of non-topological configurations on $U(1)_A$ symmetry close to the phase transition. Since V and AV are themselves $U(1)_A$ singlets their correlators can never violate $U(1)_A$ symmetry. Hence, their degeneracy, in contrast to the P and S, can serve as an indicator of $SU(N_f)_A$ symmetry, independently of any $U(1)_A$ breaking. We observe indeed that V/AV as well as P/S become degenerate above $1.5 T_c$, see Fig. 5.3(b). This is the same observation we have made by studying the corresponding SPFs, which also show a good agreement, see Fig. 4.11(d). Closer to the phase transition at $1.2 T_c$, Figs. 5.3(c) and 5.3(d), the situation is different. While the spatially transverse $V_T = 1/2(V_1 + V_2)$ and the longitudinal $V_L = V_4$ vector and axial-vector currents respectively are still degenerate, P and S are non-degenerate due to configurations with non-trivial topological charges. Thus the $U(1)_A$ symmetry for flavor non-singlet mesons at this temperature is still broken. Predictions about flavor singlet meson degeneracy, σ and η' , need disconnected propagators. However, those channels are affected by a high statistical noise and are not part of this analysis.

Finally a few words regarding Lorentz symmetry breaking. In Fig. 5.3(e) we compare V_T with $V_L = V_4$ at $0.93 T_c$ and, similarly, the corresponding AV channels. As can be seen they agree with each other as should be in case of zero temperature, where Lorentz symmetry holds - the temporal direction is indistinguishable from the spatial one. The AV CFs even at this rather high temperature are much smaller than the V CFs. At $1.2 T_c$, Fig. 5.3(f), the situation has changed and V and AV become degenerate, while at the same time the degeneracy between the transverse and the longitudinal states is lost. In this regime the former rotational symmetry $SO(3)$ on the hypertorus orthogonal to the spatial correlation direction, is broken down to $SO(2) \times Z(2)$ leading to the V_T - V_L and A_T - A_L degeneracy. At the same time chiral symmetry restoration leads to the A_L - V_L and V_T - A_T degeneracy as already discussed.

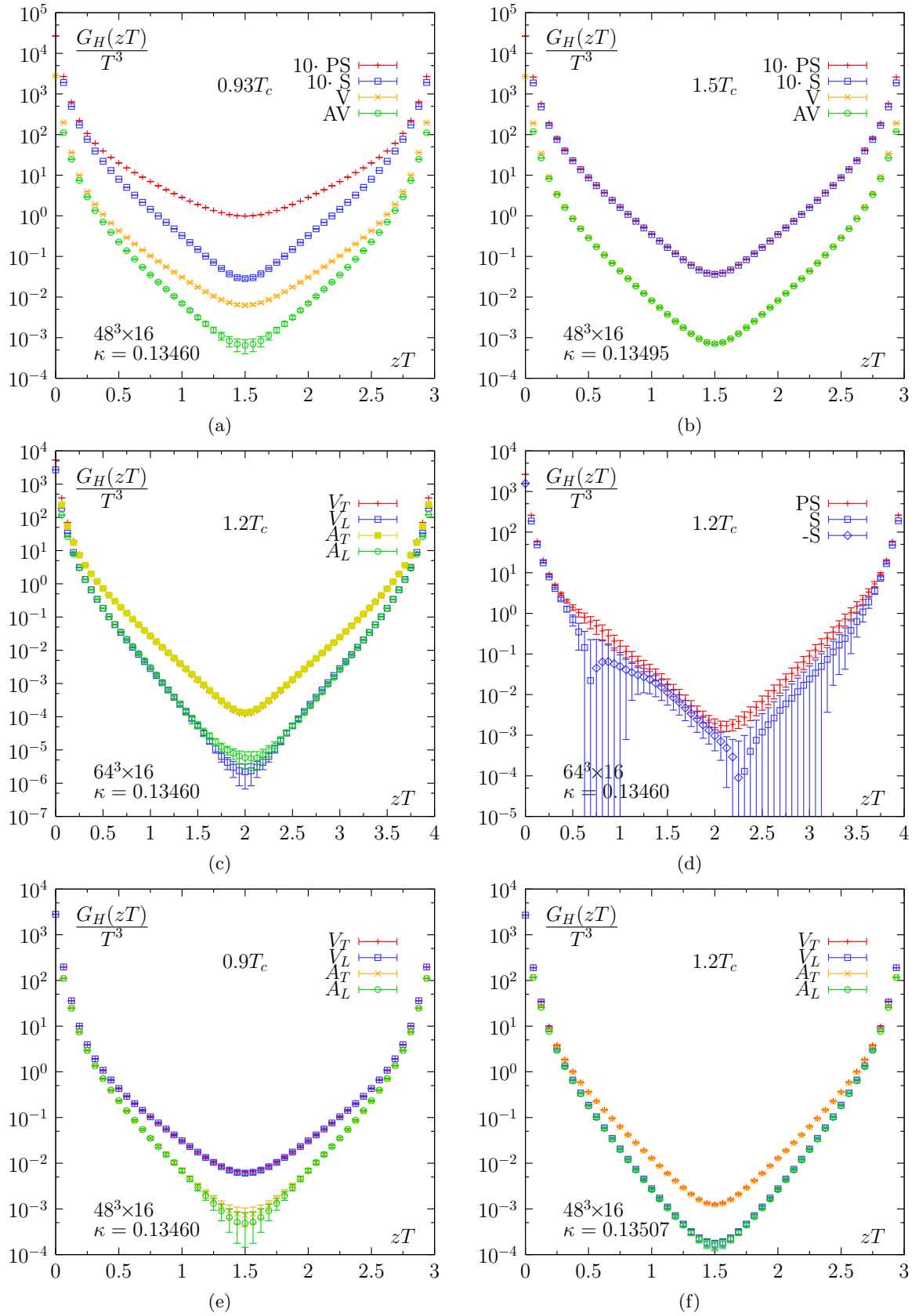


Fig. 5.3: Spatial CFs as indicator of chiral and axial symmetry breaking below and above T_c (top). $U(1)_A$ symmetry breaking effects in spatial CFs above T_c (middle). Transversal and longitudinal vector currents close to the phase transition (bottom).

Summary, conclusions and outlook

A conclusion is the place where you got tired of thinking.

ARTHUR BLOCH

In this work we have studied the properties of mesonic correlation functions built from light quarks at temperatures below, close to and well above the QCD phase transition. There are several motivations to investigate QCD under such extreme conditions. First, at temperatures of order of the QCD scale $\Lambda_{\text{QCD}} \simeq 200$ MeV, QCD is expected to undergo a transition from a hadronic phase to a deconfined phase, which is believed to be the so-called Quark Gluon Plasma (QGP). Quarks and gluons are no longer bound into hadrons, but can move (almost) freely over large distances. At the same time chiral symmetry, which at low temperatures is spontaneously broken is restored. Second, the potential QGP may be created in the ultra-relativistic heavy-ion collisions experiments at the AGS, SPS and RHIC. Likewise about 10^{-5} seconds after the big bang where the temperature was of the order $\mathcal{O}(200\text{MeV})$ the early universe probably consisted of a QGP. Thirdly, QCD simplifies under extreme conditions. At scales relevant to hadrons the QCD coupling is large, perturbative calculations fail and we have to rely on numerical simulations. However, at very high temperatures the coupling is small and therefore the perturbative treatment of QCD becomes feasible.

In order to describe processes and phenomena occurring during and right after the formation of a QGP we need to know how static and dynamical properties of hadrons are modified under changes in the environment. These properties play an important role in the evolution and the outcome of the (QGP) fireball created in heavy-ion collisions. Signatures of the QGP in the detectors need to be disentangled from those of the conventional hadronic phase. Since perturbative methods might be problematic even above the critical temperature due to the bad convergence of perturbative expansion, e.g., for the pressure, a numerical non-perturbative study like this work is mandatory.

To set the stage we have given in Chapter 1 a short introduction to QCD at finite temperature in the continuum and the latest experimental findings.

In Chapter 2 we have discussed various ways to define (thermal) QCD on the lattice. Our investigations have been done in the framework of quenched lattice QCD with the standard Wilson plaquette action for the $SU(3)$ gauge fields. For the fermion action we choose two different discretizations, the non-perturbatively $\mathcal{O}(a)$ improved Sheikholeslami-Wohlert and the hypercube truncated fixed point action. Beside the simulation techniques, we have described the phenomenologically important spectral functions and their relation to the temporal as well as spatial correlation functions for mesonic operators.

In Chapter 3 we have introduced the Maximum Entropy Method for extracting spectral functions. In order to use the free lattice spectral functions as default models we have given their derivation in both fermion formulations. Since the hypercube fermion propagator is plagued with two poles, we have used the binning procedure to do the momentum integration. The UV (lattice artefacts) have been thereby corrected compared to Ref. [188] by properly taking the various contributions of poles into account. The hypercube truncated fixed point

(HF) action shows an advantageous behavior in the IR regime in the free case, since it follows the continuum (free) dispersion relation as well as spectral function to higher energies. Further it shows a great improvement with respect to chiral symmetry compared to the Wilson action. Finally it was checked that the MEM applied to free data is capable of successfully reproducing the free spectral functions in both cases.

For our quenched simulations we have generated around 40 – 120 gauge field configurations covering a temperature range of $0.44 - 5.96 T_c$ with $N_\tau = 8, 12, 16$ and 24. In order to study finite volume effects at least three different aspect ratios of $N_\sigma/N_\tau \leq 12$ have been used. At 1.24, 1.49 and 2.98 T_c we further choose three different β values to also study remaining finite lattice spacing effects. All inversions have been done in the chiral limit above T_c and in the Wilson case at at least four different κ values below T_c , which can be used for the chiral extrapolations.

Conclusions

In this final Section we briefly summarize the main findings of Chapter 4 and Chapter 5. They contain the complete analysis of our data.

Motivated by the fact that there is no effective distinction between spatial and temporal correlators at zero temperature, we have mainly studied spatial correlators and corresponding observables. Furthermore spatial correlators can be followed to larger physical distances and can make use of more data points at finite temperature compared to the temporal ones so that we can obtain the observables more reliably. However, due to possible changes in the dispersion relation in the presence of a heat bath (see below), the general equivalence at zero temperature is lost and no simple connection to physically relevant quantities can be drawn. Nevertheless at least below T_c the findings still well agree with the zero temperature results concerning for instance critical kappa values as well as vector screening masses. The latter are only somewhat larger $\simeq 10\%$ in an infinite volume extrapolation at 0.55 and 0.9 T_c .

In Chapter 5 we have carried out a complete investigation, i.e., a finite lattice spacing and volume extrapolation, of (effective) screening masses at 1.3, 1.5 and 3.0 T_c . Guided by the infinite volume extrapolation at $T = \infty$, we find a behavior, which is apparently different from the expected behavior of free quarks. The volume extrapolations fall between those at $T = 0$ and $T = \infty$ and only small $\mathcal{O}(a^2)$ effects are present. Nevertheless the final values are close but still slightly below the expected free value of $2\pi T$. The difference from the free theory is largest for the pseudoscalar. Perturbative calculations based on dimensionally reduced effective theories, on the other hand, predict the screening masses to be above the free theory value. In comparison to our lattice results these values show a difference within $\sim 10\%$ in the temperature range 1.5-3 T_c . While our detailed investigation of lattice size dependence of screening masses indicate finite volume corrections which are in-between the confined theory behavior and free theory behavior, any interpretation of the finite volume dependence in terms of residual binding would require better control over the systematics and also studies at larger aspect ratios, e.g., at $N_\tau = 12$ and 16.

In the same manner, we have explored the axial Ward identity quark masses below and above the phase transition. Concerning the critical kappa values we find only minor deviations to the zero temperature results and small (if any) systematic finite volume effects at 1.5 and 3 T_c .

Utilizing a combined fit on correlators for extended mesonic operators the 'Bethe-Salpeter wave functions' have been extracted from spatial pion correlation functions. Their second moments, which might be interpreted as an estimate for the particle radius, decrease with increasing mass and momenta. However, these values in the chiral limit are much smaller

than the experimental ones, so that this interpretation becomes doubtful. The particle extent apparently also shrinks with rising temperature. Differences between temporal and spatial wave functions above T_c in contrast to those below T_c can presumably be explained by a strong confining potential derived from spatial Wilson-loops, i.e., a spatial string tension growing with temperature.

One of the main topics of our investigation is the analysis of spectral functions with the MEM. Below and above the critical temperature the first peak position at $\mathbf{p} = \mathbf{0}$, i.e., the pole masses, give consistent results in both discretizations. Above T_c , spectral functions and pole masses simply scale with temperature. In the free case spectral functions of the HF action, unlike those of the Wilson action, clearly disentangle physical information from lattice artefacts. However, for the time being a clear answer as to whether the additional bumps in the interacting case are lattice or MEM artefacts or possibly higher excited states cannot be given even within the hypercube formulation. The number of bumps depends on the unknown renormalization constants and the number of points in the time direction. The picture that emerges needs further studies.

By comparing the ratio of temporal correlation functions with the free continuum ones for both actions and above T_c we can clearly observe that the vector channel is much closer to being a propagation of a free $q\bar{q}$ -pair than the pion channel. Like the spectral function and the quark dispersion relation, the ratio reveals clearly a better continuum-like behavior of the HF action. In fact, besides a multiplicative difference the vector channel, unlike the pseudoscalar channel falls on top of the free continuum CF. Only the smallest distance point falls significantly below the continuum CF indicating cut-off effects. In fact, omitting the first point of the vector CF and choosing the renormalization constant such that the midpoint matches the free CF, we get an almost free continuum spectral function and hence the Born-Rate of dileptons.

A comparison of both (MEM) pole and screening masses does not indicate strong temperature deviations until $0.55 T_c$. At $0.93 T_c$ close to the phase transition, pole and screening masses as well as the corresponding dispersion relations differ. This behavior can at least for relatively heavy quarks be explained by a modified dispersion relation. In a simple model assumption changes due to a non-zero vacuum polarization tensor have been absorbed in a temperature dependent screening mass $m_H^z(T) = m(T)/A(T)$. The (mass-dependent) coefficient has been determined to be $A(0.9T_c) \simeq 1.3 - 1.5$, in agreement with the fact that pion and vector pole masses are enhanced compared to their screening counterparts. This temperature effect seems to disfavor the dropping ρ mass scenario as one of the explanations for the observed dilepton excess.

In the second part of Chapter 5 we finally explore symmetry patterns of the theory from the spatial CFs. We find a degeneration of P/S going from 1.2 to $1.5 T_c$, which is an indication of $U(1)_A$ symmetry restoration. In contrast the $SU(2)_A$ symmetry is already restored directly at $1.2 T_c$, where V/AV CFs are degenerate. The Lorentz symmetry is broken above T_c due to the heat bath. Thus for spatial correlators the former rotational symmetry in the (xyt) space is broken down as $SO(3) \rightarrow SO(2) \times Z(2)$, which becomes manifest in differences between longitudinal and transversal vector and axial-vector channels.

The pion decay constant follows the expected behavior of the chiral condensate for $SU(2)_A$ symmetry restoration and vanishes almost in the chiral limit above T_c . Below T_c we found a good agreement with the experimental values for the pion as well as for the vector decay constant. The change in the vector decay constant passing the phase transition is not as dramatic as in the pion channel, though. The pion decay constant extracted by the fourth component of the axial current in temporal direction below T_c is only slightly enhanced but essentially supports the findings by studying the spatial pion correlation functions. They

further support the notion that the pion state no longer couples to the fourth component of the axial-vector current above T_c . For the hypercube fermion action above T_c the amplitudes, i.e., the areas under the ground state peaks, are in good agreement with the results of the simple exponential fit.

Outlook

At the end of this thesis we want to give a list of improvements and open problems for future studies:

One very important remaining issue concerns the determination of the HF renormalization constants. Especially the findings of the last sections of Chapter 4 show how important their knowledge is. They are not only necessary in order to make real physical predictions but also influence the form of spectral functions by the MEM.

Concerning the MEM analyses lattices with larger N_τ are desirable and might clarify the unsatisfactory situation concerning the lattice-artifacts. Current simulations using the anisotropic formulation in the presence of dynamical (staggered) fermions might show a way out but require a simultaneous two-dimensional parameter (bare quark and gluon anisotropies) tuning. However, it is probably unavoidable to study N_τ and a dependence of spectral functions.

Further one could try to extend the calculation of free HF spectral functions within the binning procedure at non-vanishing momenta. This is especially rewarding concerning the dilepton rate.

Increasing statistics and volumes will basically and essentially improve our analyses, especially in the extrapolations of screening masses above the phase transition. However, regarding the Wilson fermions in its quenched form it seems to be hopeless to get closer to the phase transition with almost zero or physical quark masses or to lower the quark masses below T_c with conventional algorithms. In those regimes exceptional configurations will spoil every analysis in particular of spatial correlations. A dynamical study should be more appropriate, since there exceptional configurations should be more suppressed due to their almost vanishing measure. And, of course, the typical quenched artefacts for simulations in the quenched approximation are absent. Today these (finite-temperature) simulations with a proper lattice size are quite tedious and far too expensive and thus remain for further (super-)computer generations. Nonetheless dynamical simulations with chirally improved or perfect, e.g., Overlap- and Domain Wall fermions, actions and (physical) light quark flavors at zero-temperature, which are even more expensive are on their way. Secondly for current heavy ion collision at SPS and RHIC the chemical freeze-out occurs at $\mu_b \approx 100$ MeV (baryon chemical potential $\mu_B \approx 300$ MeV) and $\mu_b \approx 15$ MeV ($\mu_B \approx 45$ MeV), respectively. Thus ultimately, a finite chemical potential should be introduced to describe the quark matter created in these experiments properly.

Unavoidably one should also try get a more sophisticated control over non-trivial topological configurations whenever one wants to study mesonic properties close to the phase transition. The role of zero modes, i.e., instantons and calorons, in this regime deserves a more accurate analysis and its connection to chiral symmetry breaking should be clarified.

Altogether these options are left for future computer and theoretical physicists generations. On the experimental side CERN's new experiment, ALICE, will start soon (around 2007-2008) at the LHC and will probably give more detailed insights into the QGP and its properties.

A Conventions

A.1 $SU(N)$ generators

$SU(N)$, the special unitary group of degree N , is the group of $N \times N$ unitary matrices with unit determinant. Elements G of the group $SU(N)$ can be written as ($\Lambda \in su(N)$)

$$G = \exp \Lambda = \exp \left(\sum_{a=1}^{N^2-1} i T_a \omega^a \right) \quad (\text{A.1})$$

with the hermitian and traceless generators T_a , which generate the $su(N)$ Lie-algebra. In the fundamental representation the T_a satisfy an additional relation,

$$\{T_a, T_b\} = \frac{1}{N} \delta_{ab} + d^{abc} T_c, \quad (\text{A.2})$$

which is consistent with the normalization

$$\text{Tr} (T_a T_b) = \frac{1}{2} \delta_{ab}. \quad (\text{A.3})$$

The tensor d^{abc} is totally symmetric in a, b and c and is given by

$$d^{abc} = 2 \text{Tr} [\{T_a, T_b\}, T_c]. \quad (\text{A.4})$$

In the adjoint representation the generator is a $(N^2 - 1) \times (N^2 - 1)$ matrix and its matrix elements are given by

$$(T_a)_{bc} = -i f^{abc}. \quad (\text{A.5})$$

These generators obey the Jacobi identities

$$[T^a, [T^b, T^c]] + \text{cycl. perm.} = 0 \quad (\text{A.6})$$

$$[T^a, \{T^b, T^c\}] + \text{cycl. perm.} = 0. \quad (\text{A.7})$$

A.1.1 $SU(2)$: Pauli matrices

The generators of the $SU(2)$ group $T_i = \sigma_i/2$ are given by the three Pauli matrices

$$\sigma_1 = \begin{pmatrix} 0 & 1 \\ 1 & 0 \end{pmatrix} \quad \sigma_2 = \begin{pmatrix} 0 & -i \\ i & 0 \end{pmatrix} \quad \sigma_3 = \begin{pmatrix} 1 & 0 \\ 0 & -1 \end{pmatrix}.$$

They fulfill the (anti)commutation relation

$$[\sigma_i, \sigma_j] = 2i \epsilon_{ijk} \sigma_k \quad (\text{A.8})$$

$$\{\sigma_i, \sigma_j\} = 2\delta_{ij} \mathbb{1}_2. \quad (\text{A.9})$$

A.1.2 $SU(3)$: Gell-Mann matrices

For $SU(3)$ the generators are in general expressed in terms of the Gell-Mann matrices $T_a = \lambda_a/2$, which have the following representation

$$\begin{aligned} \lambda_1 &= \begin{pmatrix} 0 & 1 & 0 \\ 1 & 0 & 0 \\ 0 & 0 & 0 \end{pmatrix} & \lambda_2 &= \begin{pmatrix} 0 & -i & 0 \\ i & 0 & 0 \\ 0 & 0 & 0 \end{pmatrix} & \lambda_3 &= \begin{pmatrix} 1 & 0 & 0 \\ 0 & -1 & 0 \\ 0 & 0 & 0 \end{pmatrix} & \lambda_4 &= \begin{pmatrix} 0 & 0 & 1 \\ 0 & 0 & 0 \\ 1 & 0 & 0 \end{pmatrix} \\ \lambda_5 &= \begin{pmatrix} 0 & 0 & -i \\ 0 & 0 & 0 \\ i & 0 & 0 \end{pmatrix} & \lambda_6 &= \begin{pmatrix} 0 & 0 & 0 \\ 0 & 0 & 1 \\ 0 & 1 & 0 \end{pmatrix} & \lambda_7 &= \begin{pmatrix} 0 & 0 & 0 \\ 0 & 0 & -i \\ 0 & i & 0 \end{pmatrix} & \lambda_8 &= \frac{1}{\sqrt{3}} \begin{pmatrix} 1 & 0 & 0 \\ 0 & 1 & 0 \\ 0 & 0 & -2 \end{pmatrix} \end{aligned}$$

They fulfill the (anti)commutation relations

$$[\lambda_a, \lambda_b] = 2if_{abc}\lambda_c \quad (\text{A.10})$$

$$\{\lambda_a, \lambda_b\} = 2d_{abc}\lambda_c + \frac{4}{3}\mathbb{1}_{ab} \quad (\text{A.11})$$

$$\text{Tr}(\lambda_a\lambda_b) = 2\delta_{ab} \quad (\text{A.12})$$

with $a, b, c = 1, \dots, N_c^2 - 1$ and f_{abc}, d_{abc} the structure functions of the $SU(3)$.

A.1.3 (Euclidean) Dirac matrices

The Euclidian γ matrices in the non-relativistic representation are selfadjoint ($\gamma_\mu = \gamma_\mu^\dagger$) and obey the following anti-commutation relation

$$\{\gamma_\mu, \gamma_\nu\} = 2\delta_{\mu\nu}. \quad (\text{A.13})$$

They can be constructed in a non chiral representation using the Pauli matrices via

$$\gamma_i = \begin{pmatrix} 0 & i\sigma_i \\ -i\sigma_i & 0 \end{pmatrix} \quad \gamma_4 = \begin{pmatrix} \mathbb{1}_2 & 0 \\ 0 & -\mathbb{1}_2 \end{pmatrix}$$

$$\gamma_1 = \begin{pmatrix} 0 & 0 & 0 & i \\ 0 & 0 & i & 0 \\ 0 & -i & 0 & 0 \\ -i & 0 & 0 & 0 \end{pmatrix} \quad \gamma_2 = \begin{pmatrix} 0 & 0 & 0 & 1 \\ 0 & 0 & -1 & 0 \\ 0 & -1 & 0 & 0 \\ 1 & 0 & 0 & 0 \end{pmatrix} \quad \gamma_3 = \begin{pmatrix} 0 & 0 & i & 0 \\ 0 & 0 & 0 & -i \\ -i & 0 & 0 & 0 \\ 0 & i & 0 & 0 \end{pmatrix}$$

$$\gamma_4 = \begin{pmatrix} 1 & 0 & 0 & 0 \\ 0 & 1 & 0 & 0 \\ 0 & 0 & -1 & 0 \\ 0 & 0 & 0 & -1 \end{pmatrix} \quad \gamma_5 = \begin{pmatrix} 0 & 0 & 1 & 0 \\ 0 & 0 & 0 & 1 \\ 1 & 0 & 0 & 0 \\ 0 & 1 & 0 & 0 \end{pmatrix} = \gamma_1\gamma_2\gamma_3\gamma_4 = \gamma_5^\dagger$$

B Tables of results

B.1 AWI quark masses below T_c

β	T/T_c	$N_\sigma^3 \times N_\tau$	κ	$m_{AWI}^z(a)$	$m_{\overline{\text{MS}}}^z(\bar{\mu})[\text{MeV}]$
6.136	0.55	$32^3 \times 16$	0.13300	0.0771(1)	233.2(3)
		$32^3 \times 16$	0.13400	0.0494(1)	148.5(3)
		$32^3 \times 16$	0.13460	0.0326(1)	98.4(3)
		$32^3 \times 16$	0.13495	0.0226(1)	67.4(3)
		$32^3 \times 16$	0.13540	0.0097(2)	29.4(6)
		$32^3 \times 16$	0.13576(2)		
		$48^3 \times 16$	0.13300	0.0760(1)	222.1(3)
		$48^3 \times 16$	0.13400	0.0488(1)	142.6(4)
		$48^3 \times 16$	0.13460	0.0322(1)	94.1(3)
		$48^3 \times 16$	0.13495	0.0224(1)	65.5(3)
6.499	0.93	$32^3 \times 16$	0.13300	0.0761(2)	389(1)
		$32^3 \times 16$	0.13400	0.0476(2)	245(1)
		$32^3 \times 16$	0.13460	0.0302(2)	158(1)
		$32^3 \times 16$	0.13531	0.0094(3)	48(2)
		$32^3 \times 16$	0.13540	0.0066(3)	34(2)
		$32^3 \times 16$	0.13565(2)		
		$48^3 \times 16$	0.13300	0.0758(1)	387.9(2)
		$48^3 \times 16$	0.13400	0.0474(1)	241.6(3)
		$48^3 \times 16$	0.13460	0.0300(1)	153.5(4)
		$48^3 \times 16$	0.13531	0.0091(1)	46.6(4)
$48^3 \times 16$	0.13564(2)				

Tab. B.1: Quark masses as obtained from axial ward identity below T_c in the $\overline{\text{MS}}$ scheme at $\bar{\mu} \approx 2\text{GeV}$.

B.2 AWI quark masses above T_c

T/T_c	β	$N_\sigma^3 \times N_\tau$	κ	κ_c^z	$m_{AWI}^z(a)$	$m_{\overline{\text{MS}}}^z(\bar{\mu})[\text{MeV}]$	
1.2	6.205	$16^3 \times 8$	0.13599	0.13574(2)	-0.00736(64)	-23.9(21)	
		$24^3 \times 8$	0.13599	0.13573(2)	-0.00789(46)	-25.7(13)	
		$32^3 \times 8$	0.13599	0.13574(2)	-0.00723(36)	-23.5(12)	
	6.499	$24^3 \times 12$	0.13558	0.13561(1)	0.00104(22)	5.3(11)	
		$36^3 \times 12$	0.13558	0.13560(1)	0.00067(31)	3.4(16)	
		$48^3 \times 12$	0.13558	0.13561(1)	0.00097(24)	5.0(12)	
	6.721	$32^3 \times 16$	0.13507	0.13525(1)	0.00561(12)	38.0(8)	
		$48^3 \times 16$	0.13507	0.13525(1)	0.00552(11)	37.4(12)	
		$64^3 \times 16$	0.13507	0.13526(1)	0.00563(11)	38.1(8)	
1.5	6.338	$16^3 \times 8$	0.13581	0.13584(1)	0.00086(60)	3.4(24)	
		$24^3 \times 8$	0.13581	0.13582(1)	0.00033(76)	1.3(30)	
		$32^3 \times 8$	0.13581	0.13577(1)	-0.00110(41)	-4.4(26)	
		$64^3 \times 8$	0.13581	0.13579(1)	-0.00062(20)	-2.5(8)	
		$96^3 \times 8$	0.13581	0.13576(1)	-0.00155(15)	-6.2(6)	
	6.640	$24^3 \times 12$	0.13536	0.13541(1)	0.00153(21)	9.5(6)	
		$36^3 \times 12$	0.13536	0.13540(1)	0.00127(16)	7.8(10)	
		$48^3 \times 12$	0.13536	0.13539(1)	0.00092(18)	5.7(6)	
		$48^3 \times 12$	0.13525	0.13541(2)	0.00495(85)	30.7(52)	
	6.872	$32^3 \times 16$	0.13495	0.13499(1)	0.00112(11)	9.4(6)	
		$48^3 \times 16$	0.13495	0.13500(1)	0.00153(11)	12.8(9)	
		$64^3 \times 16$	0.13495	0.13499(1)	0.00133(9)	11.2(7)	
	7.192	$64^3 \times 24$	0.13440	0.13444(2)	0.00132(4)	11.0(4)	
	3.0	6.872	$16^3 \times 8$	0.13494	0.13517(1)	0.00705(34)	59.1(21)
			$24^3 \times 8$	0.13494	0.13513(1)	0.00566(28)	47.5(28)
$32^3 \times 8$			0.13494	0.13511(1)	0.00516(26)	43.3(21)	
$64^3 \times 8$			0.13494	0.13510(1)	0.00482(19)	40.4(16)	
$96^3 \times 8$			0.13494	0.13508(1)	0.00420(11)	35.2(14)	
7.192		$24^3 \times 12$	0.13440	0.13447(1)	0.00227(16)	28.6(20)	
		$36^3 \times 12$	0.13440	0.13445(1)	0.00152(12)	19.2(8)	
		$48^3 \times 12$	0.13440	0.13447(1)	0.00200(10)	25.2(13)	
7.457		$32^3 \times 16$	0.13390	0.13399(1)	0.00282(10)	49.3(17)	
		$48^3 \times 16$	0.13390	0.13399(1)	0.00262(7)	45.8(12)	
		$64^3 \times 16$	0.13390	0.13399(1)	0.00271(7)	47.4(12)	
6.0		7.457	$32^3 \times 8$	0.13390	0.13415(1)	0.00746(19)	130.4(34)

T/T_c	β	$N_\sigma^3 \times N_\tau$	$m_{AWI}^z(a)$
1.5	6.872	$32^3 \times 16$	0.00267(16)
		$48^3 \times 16$	0.00270(9)
3.0	7.457	$32^3 \times 16$	-0.00785(10)
		$48^3 \times 16$	-0.00779(5)
	7.192	$48^3 \times 12$	-0.0043(1)

Tab. B.2: Quark masses as obtained from axial ward identity above T_c in the $\overline{\text{MS}}$ scheme at $\bar{\mu} \approx 2\text{GeV}$.

B.3 Renormalization group factors

κ_c	am_q	Z	κ_c	am_q	Z	κ_c	am_q	Z	H
$\beta = 6.000$			$\beta = 6.136$			$\beta = 6.499$			
0.1324	0.080	0.79	0.1330	0.074	0.80	0.1330	0.071	0.83	S_{TI}
		0.72			0.73			0.77	P_{TI}
		0.87			0.87			0.89	V_{NP}
		0.79			0.80			0.83	AV_{NP}
0.1332	0.057	0.76	0.1340	0.046	0.77	0.1340	0.043	0.80	S_{TI}
		0.70			0.71			0.75	P_{TI}
		0.84			0.84			0.86	V_{NP}
		0.79			0.80			0.83	AV_{NP}
0.1342	0.029	0.73	0.1346	0.029	0.75	0.1346	0.027	0.78	S_{TI}
		0.67			0.69			0.73	P_{TI}
		0.81			0.82			0.84	V_{NP}
		0.79			0.80			0.83	AV_{NP}
0.1348	0.012	0.72	0.1349	0.021	0.74	0.13531	0.007	0.76	S_{TI}
		0.66			0.69			0.72	P_{TI}
		0.79			0.81			0.82	V_{NP}
		0.79			0.80			0.83	AV_{NP}
			0.1354	0.007	0.73	0.1354	0.004	0.76	S_{TI}
		0.67			0.71			P_{TI}	
		0.80			0.82			V_{NP}	
		0.80			0.83			AV_{NP}	

Tab. B.3: Current renormalization factors Z_H below T_c as obtained from Eq. (2.148) (tadpole improved, TI) and Eq. (2.150) (non-perturbatively improved, NP).

β	S_{TI}	P_{TI}	V_{TI}	V_{NP}	AV_{TI}	AV_{NP}
6.338	0.76	0.72	0.81	0.802	0.84	0.818
6.499	0.75	0.71	0.81	0.811	0.84	0.828
6.640	0.77	0.72	0.82	0.818	0.84	0.836
6.721	0.78	0.74	0.83	0.822	0.85	0.839
6.872	0.78	0.74	0.83	0.829	0.85	0.847
7.192	0.80	0.76	0.84	0.842	0.86	0.859
7.457	0.81	0.78	0.85	0.851	0.87	0.868

Tab. B.4: Current renormalization factors above T_c .

β	u^4	$g_{\text{MS}}^2(1/a)$
7.457	0.91345	1.4318
7.192	0.90890	1.5417
6.872	0.90133	1.7378
6.721	0.89928	1.7944
6.640	0.89738	1.8476
6.499	0.89383	1.9513
6.338	0.88938	2.0884
6.205	0.88528	2.2225
6.136	0.88507	2.2294
6.000	0.87779	2.4899

Tab. B.5: The calculated plaquette values and the resulting TI-couplings at $\mu=1/a$.

B.4 Screening masses

T/T_c	β	$N_\sigma^3 \times N_\tau$	m_{Pa}^z	m_{Sa}^z	m_{Va}^z	m_{Aa}^z	κ_c^z
1.24	6.205	$16^3 \times 8$	681(10)	685(7)	781(11)	779(9)	0.13599
		$24^3 \times 8$	686(6)	704(7)	760(6)	761(6)	0.13599
		$32^3 \times 8$	660(4)	751(7)	712(12)	716(10)	0.13599
1.24	6.499	$24^3 \times 12$	456(7)	460(7)	496(6)	494(4)	0.13558
		$36^3 \times 12$	425(6)	463(3)	492(6)	496(6)	0.13558
		$48^3 \times 12$	436(4)	460(7)	496(6)	494(4)	0.13558
1.24	6.721	$32^3 \times 16$	340(13)	387(20)	397(4)	383(3)	0.13507
		$48^3 \times 16$	342(4)	339(4)	371(4)	370(4)	0.13507
		$64^3 \times 16$	336(7)	358(11)	372(5)	371(4)	0.13507
1.49	6.338	$16^3 \times 8$	750(8)	760(9)	810(8)	810(7)	0.13581
		$24^3 \times 8$	705(6)	710(4)	756(7)	760(6)	0.13581
		$32^3 \times 8$	713(6)	723(9)	750(8)	749(8)	0.13581
		$64^3 \times 8$	712(8)	715(9)	730(2)	730(2)	0.13581
		$96^3 \times 8$	705(3)	712(5)	756(9)	761(8)	0.13581
1.49	6.640	$24^3 \times 12$	503(4)	505(4)	530(3)	537(3)	0.13536
		$36^3 \times 12$	450(8)	491(4)	488(6)	488(3)	0.13536
		$48^3 \times 12$	485(6)	487(4)	507(6)	506(5)	0.13536
		$48^3 \times 12$	484(5)	486(5)	507(4)	507(5)	0.13525
1.49	6.872	$32^3 \times 16$	380(5)	379(3)	396(4)	403(3)	0.13495
		$48^3 \times 16$	365(3)	365(4)	386(3)	387(3)	0.13495
		$64^3 \times 16$	350(9)	361(10)	372(6)	371(6)	0.13495
2.98	6.872	$16^3 \times 8$	775(4)	766(5)	799(4)	776(3)	0.13494
		$24^3 \times 8$	750(4)	745(4)	775(4)	770(5)	0.13494
		$32^3 \times 8$	736(3)	695(6)	755(4)	745(5)	0.13494
		$64^3 \times 8$	740(5)	741(5)	768(6)	769(6)	0.13494
		$96^3 \times 8$	732(5)	740(6)	764(4)	762(5)	0.13494
2.98	7.192	$24^3 \times 12$	523(2)	522(2)	542(2)	520(8)	0.13440
		$36^3 \times 12$	496(10)	500(5)	510(14)	510(10)	0.13440
		$48^3 \times 12$	512(3)	512(3)	526(3)	528(3)	0.13440
2.98	7.457	$32^3 \times 16$	400(6)	399(15)	412(6)	420(5)	0.13390
		$48^3 \times 16$	394(3)	394(2)	406(2)	406(2)	0.13390
		$64^3 \times 16$	383(3)	383(2)	395(2)	395(5)	0.13390
5.96	7.457	$32^3 \times 8$	768(5)	768(5)	782(6)	793(3)	0.13390

T/T_c	β	$N_\sigma^3 \times N_\tau$	m_{Pa}	m_{Sa}	m_{Va}	m_{Aa}
1.49	6.872	$32^3 \times 16$	372(4)	373(4)	397(3)	400(6)
		$48^3 \times 16$	361(3)	364(2)	382(2)	383(3)
2.98	7.457	$32^3 \times 16$	408(2)	406(2)	419(2)	417(2)
	7.192	$48^3 \times 12$	512(3)	510(3)	524(2)	524(2)

Tab. B.6: Screening masses as obtained from two exponential fits above T_c for Wilson fermions (top) and HF (bottom)

On the next page the screening masses below T_c as obtained by a two and a single state fit are shown.

κ	$m_{\mathcal{P}}^z a$		$m_{\mathcal{S}}^z a$		$m_{\mathcal{V}}^z a$		$m_{\mathcal{A}}^z a$	
$T = 0.44T_C, \beta = 6.000, 24^3 \times 16, \kappa_c^z = 0.13551(5)$ (60 configurations)								
0.13240	534(7)	534(7)	769(39)	755(46)	637(6)	638(4)	n.e.	n.e.
0.13320	457(5)	457(5)	702(44)	690(55)	576(7)	572(5)	n.e.	n.e.
0.13420	341(6)	341(6)	703(83)	-	495(14)	499(8)	n.e.	n.e.
0.13480	252(5)	252(5)	931(113)	931(108)	453(31)	456(17)	n.e.	n.e.
extra	0	0	850(30)		399(5)	399(5)	n.e.	n.e.
$T = 0.55T_C, \beta = 6.136, 24^3 \times 16, \kappa_c^z = 0.13606(5)$ (60 configurations)								
0.13300	498(4)	493(3)	716(29)	710(32)	587(3)	578(3)	n.e.	n.e.
0.13400	403(4)	398(4)	653(35)	590(21)	518(5)	506(4)	n.e.	n.e.
0.13460	344(6)	337(5)	631(38)	460(36)	479(6)	466(5)	n.e.	n.e.
0.13540	238(7)	233(9)	779(160)	-	444(13)	434(13)	n.e.	n.e.
extra	0	0	404(7)		385(8)	364(3)	n.e.	n.e.
$T = 0.55T_C, \beta = 6.136, 32^3 \times 16, \kappa_c^z = 0.13575(1)$ (120/60 configurations)								
0.13300	459(2)	453(4)	693(29)	702(41)	543(3)	527(2)	768(10)	850(77)
0.13400	360(2)	360(2)	623(50)	622(51)	470(4)	452(3)	685(32)	740(79)
0.13460	292(3)	290(3)	587(13)	591(116)	423(6)	425(6)	632(82)	649(90)
0.13495	242(2)	242(5)	552(25)	585(35)	402(8)	398(7)	614(80)	618(60)
0.13540	160(9)	163(9)	-	-	414(21)	407(21)	n.e.	n.e.
extra	0	0	531(8)		349(8)	339(10)	485(32)	
$T = 0.55T_C, \beta = 6.136, 48 \times 16, \kappa_c^z = 0.13568(2)$ (60 configurations)								
0.13300	452(2)	450(2)	-	-	540(4)	539(4)	707(54)	780(80)
0.13400	353(2)	354(3)	-	-	468(7)	467(8)	655(89)	720(80)
0.13460	287(2)	287(3)	-	-	430(8)	428(11)	670(58)	683(50)
0.13495	237(3)	232(3)	-	-	416(15)	415(14)	677(93)	691(62)
extra	0	0	-	-	361(6)	358(6)		
$T = 0.93T_C, \beta = 6.499, 24 \times 16, \kappa_c^z = 0.13582(6)$ (120 configurations)								
0.13300	438(3)	423(3)	549(10)	536(9)	452(7)	461(2)	n.e.	n.e.
0.13400	346(3)	336(3)	452(9)	440(8)	378(6)	384(3)	n.e.	n.e.
0.13460	288(4)	278(4)	388(10)	379(9)	339(9)	340(4)	n.e.	n.e.
0.13540	189(6)	186(8)	465(12)	455(11)	284(15)	281(6)	n.e.	n.e.
extra	0	0	260(8)		246(12)	248(2)	n.e.	n.e.
$T = 0.93T_C, \beta = 6.499, 32 \times 16, \kappa_c^z = 0.13549(10)$ (60 configurations)								
0.13300	387(2)	383(2)	505(13)	492(12)	432(3)	419(2)	n.e.	n.e.
0.13400	296(2)	291(2)	425(14)	403(13)	349(3)	343(3)	n.e.	n.e.
0.13460	235(4)	233(4)	422(36)	419(31)	302(3)	293(3)	n.e.	n.e.
0.13531	161(6)	153(10)	-	-	266(9)	247(8)	n.e.	n.e.
0.13540	148(7)	150(7)	-	-	258(14)	248(12)	n.e.	n.e.
extra	0	0	353(10)		219(8)	226(4)	n.e.	n.e.
$T = 0.93T_C, \beta = 6.499, 48 \times 16, \kappa_c^z = 0.13557(8)$ (60 configurations)								
0.13300	363(2)	361(2)	483(20)	484(29)	407(3)	401(2)	543(11)	530(40)
0.13400	282(2)	272(2)	392(43)	389(40)	332(3)	323(2)	465(12)	448(40)
0.13460	212(3)	207(3)	323(73)	390(5)	283(4)	284(4)	380(57)	370(70)
0.13531	126(4)	125(4)	-	-	244(11)	223(20)	242(48)	200(40)
extra	0	0	345(10)		214(4)	207(3)		

Tab. B.7: Screening masses as obtained from one and the two exponential fit. The left column represents the masses resulting from a single state fit and the right column of a combined single and double state fit. n.e. abbreviation stands for not available data.

B.5 MEM pole masses

T/T_c	β	κ	N_σ	m_{Pa}	m_{Va}	m_{Sa}		
0.44	6.000	0.13240	24	0.516(10)	0.657(5)	0.697(61)		
		0.13320	24	0.442(16)	0.601(2)	0.612(125)		
		0.13420	24	0.331(15)	0.527(3)	–		
		0.13480	24	0.250(14)	0.475(4)	–		
0.55	6.136	0.13300	48	0.459(3)	0.542(5)	0.698(37)		
			32	0.464(3)	0.561(5)	0.723(11)		
			24	0.494(3)	0.572(8)	0.716(29)		
		0.13400	48	0.342(4)	0.489(6)	0.617(24)		
			32	0.357(2)	0.494(6)	0.668(12)		
			24	0.398(3)	0.498(14)	0.653(35)		
		0.13460	48	0.284(2)	0.438(9)	0.537(50)		
			32	0.272(3)	0.453(3)	0.646(11)		
			24	0.327(6)	0.453(8)	0.631(38)		
		0.13495	48	0.214(2)	0.414(10)	0.552(91)		
			32	0.246(58)	0.431(3)	0.649(15)		
		0.93	6.499	0.13300	48	0.414(3)	0.486(20)	0.542(13)
	32			0.431(2)	0.487(1)	0.542(15)		
	24			0.438(5)	0.509(11)	0.564(14)		
0.13400	48			0.324(4)	0.424(1)	0.450(9)		
	32			0.338(2)	0.427(1)	0.457(15)		
	24			0.346(6)	0.435(3)	0.464(11)		
0.13460	48			0.252(5)	0.384(2)	0.414(11)		
	32			0.260(2)	0.361(1)	0.416(16)		
	24			0.283(8)	0.387(3)	0.394(14)		
0.13531	48			0.217(2)	0.342(3)	0.521(167)		
	32			0.224(1)	0.357(1)	0.645(38)		
T/T_c	β			N_σ	m_{Pa}	m_{Va}	m_{Sa}	m_{Aa}
1.5	6.872			32	0.265	0.296	–	0.338
				48	0.317	0.368	0.276	0.359
3.0	7.457	32	0.307	0.349	0.255	0.307		
		48	0.307	0.338	0.286	0.328		

Tab. B.8: Pole masses as obtained from the SPF by a jackknifed MEM analysis. Wilson fermions below T_c (top) and HF above T_c (bottom).

C Auxiliary Functions for the Free Lattice Field Theory

In this appendix we list various definitions and functions, needed in Section 3 in order of their appearance.

The first ones are sum rules for introducing a finite N_τ for the quark propagator in Eq. (3.35). With $f(n) = (-1)^{|n|} e^{-E|t+N_\tau n|}$ one can show that the following equations hold

$$\begin{aligned}
\sum_{n=-\infty}^{\infty} f(n) &= \frac{\sinh(2EN_\tau(t/N_\tau - 0.5))}{\cosh(EN_\tau/2)}, \\
\sum_{n=-\infty}^{\infty} \text{sgn}(t + N_\tau n) f(n) &= \frac{\cosh(2EN_\tau(t/N_\tau - 0.5))}{\cosh(EN_\tau/2)}, \\
\sum_{n=-\infty}^{\infty} (-1)^{|t+N_\tau n|} f(n) &= (-1)^t \frac{\sinh(2EN_\tau(t/N_\tau - 0.5))}{\cosh(EN_\tau/2)}, \\
\sum_{n=-\infty}^{\infty} (-1)^{|t+N_\tau n|} \text{sgn}(t + N_\tau n) f(n) &= (-1)^t \frac{\cosh(2EN_\tau(t/N_\tau - 0.5))}{\cosh(EN_\tau/2)}.
\end{aligned} \tag{C.1}$$

Note that the last two equations are true only for even N_τ .

Definitions for the fixed point action

The following functions are needed for the fermion FP-propagator, Eq. (3.44). With the shorthand notation $\hat{c}_i = \cos k_i$ and $\hat{s}_i = \sin k_i$ they are

$$\alpha_1(\mathbf{k}) = 2\hat{s}_1(\rho_1 + 2\rho_2(\hat{c}_2 + \hat{c}_3) + 4\rho_3\hat{c}_2\hat{c}_3), \tag{C.2}$$

$$\alpha_2(\mathbf{k}) = 2\hat{s}_2(\rho_1 + 2\rho_2(\hat{c}_1 + \hat{c}_3) + 4\rho_3\hat{c}_1\hat{c}_3), \tag{C.3}$$

$$\alpha_3(\mathbf{k}) = 2\hat{s}_3(\rho_1 + 2\rho_2(\hat{c}_1 + \hat{c}_2) + 4\rho_3\hat{c}_1\hat{c}_2), \tag{C.4}$$

$$\beta_1(\mathbf{k}) = 4\hat{s}_1(\rho_2 + 2\rho_3(\hat{c}_2 + \hat{c}_3) + 4\rho_4\hat{c}_2\hat{c}_3), \tag{C.5}$$

$$\beta_2(\mathbf{k}) = 4\hat{s}_2(\rho_2 + 2\rho_3(\hat{c}_1 + \hat{c}_3) + 4\rho_4\hat{c}_1\hat{c}_3), \tag{C.6}$$

$$\beta_3(\mathbf{k}) = 4\hat{s}_3(\rho_2 + 2\rho_3(\hat{c}_1 + \hat{c}_2) + 4\rho_4\hat{c}_1\hat{c}_2), \tag{C.7}$$

$$\delta(\mathbf{k}) = 2\rho_1 + 4\rho_2(\hat{c}_1 + \hat{c}_2 + \hat{c}_3) + 8\rho_3(\hat{c}_1\hat{c}_2 + \hat{c}_2\hat{c}_3 + \hat{c}_1\hat{c}_3) + 16\rho_4\hat{c}_1\hat{c}_2\hat{c}_3, \tag{C.8}$$

and

$$\kappa_1(\mathbf{k}) = \lambda_0 + 2\lambda_1(\hat{c}_1 + \hat{c}_2 + \hat{c}_3) + 4\lambda_2(\hat{c}_1\hat{c}_2 + \hat{c}_2\hat{c}_3 + \hat{c}_1\hat{c}_3) + 8\lambda_3\hat{c}_1\hat{c}_2\hat{c}_3, \tag{C.9}$$

$$\kappa_2(\mathbf{k}) = 2\lambda_1 + 4\lambda_2(\hat{c}_1 + \hat{c}_2 + \hat{c}_3) + 8\lambda_3(\hat{c}_1\hat{c}_2 + \hat{c}_2\hat{c}_3 + \hat{c}_1\hat{c}_3) + 16\lambda_4\hat{c}_1\hat{c}_2\hat{c}_3. \tag{C.10}$$

In Section 3.2.3, only the contribution of the first pole to the meson correlation function is discussed. The contribution from the second pole, appearing in Eq. (3.49), can be divided into two parts

$$\Delta G_H^{E_2}(\tau) = G_{H_2}(\tau) + G_{H_{12}}(\tau) \tag{C.11}$$

with

$$G_{H2}(\tilde{\tau}) = N_c \left(\frac{N_\tau}{N_\sigma} \right)^3 \sum_{\mathbf{k}} \frac{c_H^{FP2}(\mathbf{k}) \cosh[2E_2(\mathbf{k})N_\tau(\tilde{\tau} - 1/2)] + d_H^{FP2}(\mathbf{k})}{(P^2 - QR) \cosh^2(E_2(\mathbf{k})N_\tau/2)}, \quad (\text{C.12})$$

$$G_{H12}(\tilde{\tau}) = N_c \left(\frac{N_\tau}{N_\sigma} \right)^3 \sum_{\mathbf{k}} \frac{(-1)^{\theta(-Q)\tau+1}}{(P^2 - QR) \cosh(E_1(\mathbf{k})N_\tau/2) \cosh(E_2(\mathbf{k})N_\tau/2)} \quad (\text{C.13})$$

$$\left[g_H^{FP12}(\mathbf{k}) \{ \cosh[E_s(\mathbf{k})N_\tau(\tilde{\tau} - 1/2)] - \cosh[E_d(\mathbf{k})N_\tau(\tilde{\tau} - 1/2)] \} \right. \\ \left. + \delta^2(\mathbf{k}) \{ \cosh[E_s(\mathbf{k})N_\tau(\tilde{\tau} - 1/2)] + \cosh[E_d(\mathbf{k})N_\tau(\tilde{\tau} - 1/2)] \} \right].$$

Here the second term represents a mixed contribution from both poles with the energies $E_s = E_1 + E_2$ and $E_d = E_1 - E_2$. The functions c_H^{FP2} and d_H^{FP2} are exactly defined as c_H^{FP} and d_H^{FP} , if one replaces d^{FP} with

$$d^{FP2} \equiv d^{FP2}(\mathbf{k}) = \frac{(\mathcal{K}_1 + \mathcal{K}_2 \operatorname{sgn}(Q) \cosh E_2)^2}{\sinh^2 E_2}. \quad (\text{C.14})$$

g_H^{FP12} is defined in Table C.1 with

$$d_1^{FP12} = \frac{\mathcal{K}_1^2 \operatorname{sgn}(Q) + \mathcal{K}_2^2 \cosh E_1 \cosh E_2 + \mathcal{K}_1 \mathcal{K}_2 (\cosh E_2 + \operatorname{sgn}(Q) \cosh E_1)}{\sinh E_1 \sinh E_2}, \quad (\text{C.15})$$

$$d_2^{FP12} = \frac{\kappa_1^2 \operatorname{sgn}(Q) + \kappa_2^2 \cosh E_1 \cosh E_2 + \kappa_1 \kappa_2 (\cosh E_2 + \operatorname{sgn}(Q) \cosh E_1)}{\sinh E_1 \sinh E_2}. \quad (\text{C.16})$$

H	g_H^{FP12}	H	g_H^{FP12}
P	$d_1^{FP12} + d_2^{FP12}$	S	$-d_1^{FP12} + d_2^{FP12}$
V_0	$d_1^{FP12} + d_2^{FP12}$	A_0	$d_1^{FP12} - d_2^{FP12}$
$\sum_{i=1}^3 V_i$	$d_1^{FP12} + 3d_2^{FP12}$	$\sum_{i=1}^3 A_i$	$d_1^{FP12} - 3d_2^{FP12}$
$\sum_{\mu=0}^3 V_\mu$	$2d_1^{FP12} + 4d_2^{FP12}$	$\sum_{\mu=0}^3 A_\mu$	$2d_1^{FP12} - 4d_2^{FP12}$

Tab. C.1: The explicit form of the HF functions g_H^{FP12} appearing in Eq. (C.13). The functions $d_1^{FP12}(\mathbf{k})$ and $d_2^{FP12}(\mathbf{k})$ are defined in Eqs.(C.15) and (C.16).

D Storing data - Database SQL with MySQL

To get control over the vast amount of data regarding the CFs, we have decided to implement a database system based on SQL¹ [232]. Together with the relational database management system MySQL it is free of charge, open-source, portable and fast. Today SQL forms the backbone of most modern database systems.

Its general structure is given as follows

- data is stored in tables
- tables are subdivided in rows, containing the records (datasets), and columns
- each dataset contains various information (attributes), which is distributed over the columns of the tables

Every database table can have one or more columns designated as the primary key (PRI). It keeps all of the records straight. The other type of keys is the foreign key (FOR). These keys are used to create relationships between tables, in order to avoid redundancies and build the key concept of relational databases.

As an example of our database structure the *AZ* database is shown in Fig. D.1. It contains our Wilson data **A**bove the critical temperature in **Z** direction and consists mainly of four tables:

1. The *lattice* table stores the lattice parameter data, e.g., lattice sizes, β etc..
2. The second *momfuzz* table contains the fuzzing and smearing parameter as well as the momenta we used.
3. The configuration number of exceptionals we found in our data is stored in the third table *exceptionals*
4. CF data together with their configuration number is given in *PS* table.

A typical example of a database query is

```
SELECT * from AZ.lattice where beta=6.499;
```

or

```
USE AZ;  
SELECT * from lattice where beta=6.499;.
```

This selects all information (datasets) of table *lattice* where $\beta = 6.499$. The database selection (USE) is always assumed from now on. A somewhat more complicated query is

```
SELECT PS.value, PS.conf from PS  
INNER JOIN lattice ON (where lattice.lattice_id=PS.FK_lattice_id);
```

Here both tables —*lattice* and *PS* are linked together by a INNER JOIN to a fictive table, in which only the PS CF values together with their configuration number are selected. Other examples of join commands are, e.g., JOIN, INNER JOIN, LEFT OUTER JOIN, RIGHT OUTER JOIN. While INNER JOINS link two tables by selecting only records, which are linked by a

¹Structured Query Language, first standardized in 1986 by the American National Standards Institute (ANSI) [230]. Since then, it has been formally adopted as an international standard by the International Organization for Standardization (ISO) [231] and the International Electrotechnical Commission (IEC)

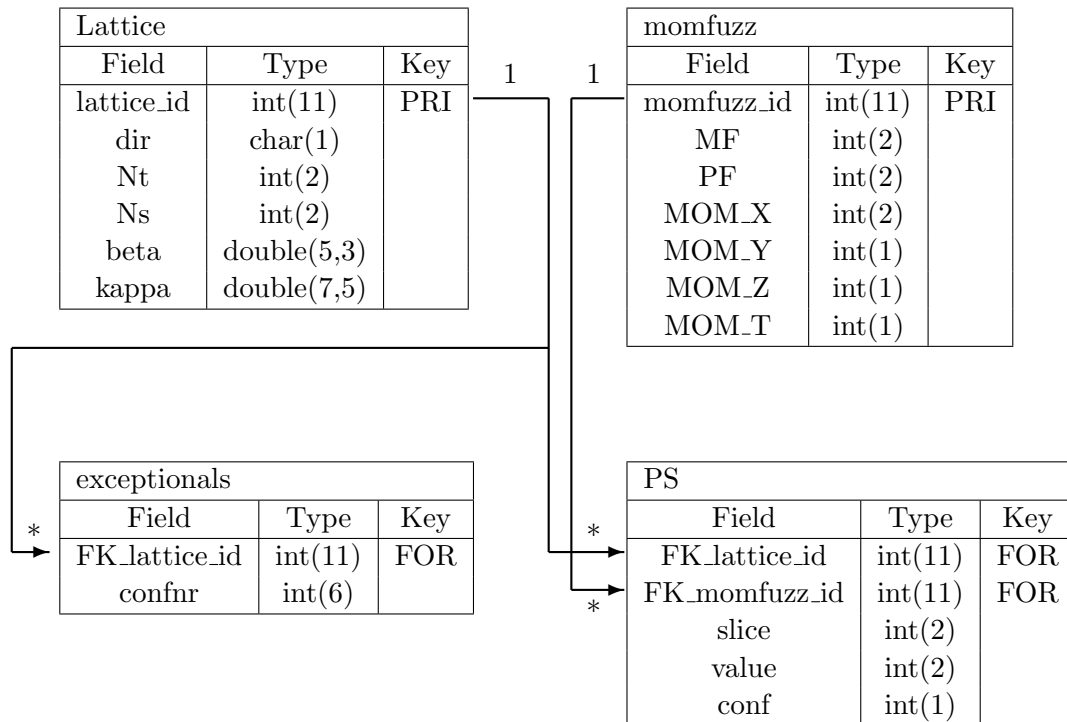


Fig. D.1: Schema of our database structure for the AZ table. 1:* denotes a one-to-many relation, e.g., one record in table momfuzz can be related to many records in PS and each record in the PS table is related to exactly one record in the momfuzz table.

foreign key, (LEFT/RIGHT) OUTER JOINS collect all entries, regardless of any connections. The queries can be send directly using the shell to the mysql-server via

```
mysql -u name -p < 'Select * ...'
```

or, e.g., by an C-API library, which allows for further data analysis by a simple C-program (see e.g., List. D.1). In the following we show, how we have created tables considering as example *PS*:

```
CREATE TABLE 'PS' (
  'slice' int(2) unsigned zerofill NOT NULL default '00',
  'value' double NOT NULL default '0',
  'conf' int(5) NOT NULL default '0',
  'FK_lattice_id' int(11) NOT NULL default '0',
  'FK_momfuzz_id' int(11) NOT NULL default '0',
  PRIMARY KEY ('slice','conf','FK_lattice_id','FK_momfuzz_id'),
  KEY 'FK_lattice_id' ('FK_lattice_id'),
  KEY 'FK_momfuzz_id' ('FK_momfuzz_id')
) TYPE=MyISAM;
```

```

1  /*****
2  /*
3  /*  PROGRAM WITH DATABASE QUERY
4  /*
5  /*
6  /*  AUTHOR Soenke Wissel
7  /*  DATE 06/29/2006
8  /*
9  /*****
10
11 #include <my_global.h>
12 #include <mysql.h>
13 #include <my_getopt.h>
14 #include <stdio.h>
15
16 char *opt_host_name=NULL;
17 char *opt_user_name=NULL;
18 char *opt_password=NULL;
19 unsigned int opt_port_num=0;
20 char *opt_socket_name=NULL;
21 char *opt_db_name=NULL;
22 unsigned int opt_flags=0;
23 int ask_password=0;
24
25 struct my_option my_opts[]=
26 {
27     {"help", '?', "Display this help and exit", NULL, NULL, NULL, GET_NO_ARG, NO_ARG,
28      0,0,0,0,0,0},
29     {"host", 'h', "Host to connect to", (gp_ptr *) &opt_host_name, NULL, NULL, GET_STR_ALLOC,
30      REQUIRED_ARG, 0,0,0,0,0,0},
31     {"password", 'p', "Password", (gp_ptr *) &opt_password, NULL, NULL, GET_STR_ALLOC, REQUIRED_ARG,
32      0,0,0,0,0,0},
33     {"port", 'P', "Port number", (gp_ptr *) &opt_port_num, NULL, NULL, GET_UINT, REQUIRED_ARG,
34      0,0,0,0,0,0},
35     {"socket", 'S', "Socket path", (gp_ptr *) &opt_socket_name, NULL, NULL, GET_STR_ALLOC,
36      REQUIRED_ARG, 0,0,0,0,0,0},
37     {"user", 'u', "user", (gp_ptr *) &opt_user_name, NULL, NULL, GET_STR_ALLOC, REQUIRED_ARG,
38      0,0,0,0,0,0},
39     {NULL, 0, NULL, NULL, NULL, NULL, GET_NO_ARG, NO_ARG, 0,0,0,0,0,0}
40 };
41
42 void
43 print_error(MYSQL *conn, char *message)
44 {
45     fprintf(stderr, "%s\n", message);
46     if (conn!=NULL)
47     {
48         fprintf(stderr, "Error %u (%s)\n", mysql_errno(conn), mysql_error(conn));
49     }
50 }
51
52 my_bool
53 get_one_option(int optid, const struct my_option *opt, char *argument){
54     switch(optid)
55     {
56     case '?':
57         my_print_help(my_opts);
58         exit(0);
59     case 'p':
60         if(!argument)
61             ask_password=1;
62         else
63         {
64             opt_password=strdup(argument);
65             if(opt_password==NULL){
66                 print_error(NULL, "could not allocate password buffer");
67                 exit(1);
68             }
69             while (*argument)
70                 *argument++='x';
71         }
72         break;
73     }
74     return(0);
75 }
76
77 int
78 main(int argc, char *argv[])
79 {
80     int n, time_step, Nset_step, N_set;
81     unsigned int i, j, *conf, num_row, N_time;
82     char query[500];
83     double **dat_mes;
84
85     char database[4]="AZ";
86     char meson[6]="PS";
87     int Ns=48;
88     int Nt=16;
89     double beta=7.457;
90     double kappa=0.13390;

```

```

86     int MF=0;
87     int PF=0;
88     int MOMX=0;
89     int MOMY=0;
90     int MOMZ=0;
91     int MOMLT=0;
92
93     const char *client_groups []={" client" ,NULL};
94     int opt_err;
95
96     MYSQL *conn;
97     MYSQL_RES *res_set;
98     MYSQL_ROW row;
99
100    my_init();
101
102    load_defaults("my2", client_groups,&argc,&argv);
103
104    if((opt_err=handle_options(&argc,&argv,my_opts,get_one_option)))
105        exit(opt_err);
106
107    conn=mysql_init(NULL);
108
109    if(conn==NULL){
110        print_error(NULL,"mysql_init() failed (probabbly out of memory\n");
111        exit(1);
112    }
113    opt_db_name=0;
114
115    if(mysql_real_connect(conn, opt_host_name , opt_user_name , opt_password , 0 , opt_port_num ,
116        opt_socket_name , opt_flags)==NULL){
117        print_error(conn, "mysql_real_connect() failed:\nError %u (%s)\n");
118        mysql_close(conn);
119        exit(1);
120    }
121
122    sprintf(query,"SELECT slice,value,conf FROM %s.%s inner join %s.lattice ON (%s.%s.
123        FK_lattice_id=%s.lattice.lattice_id) inner join %s.momfuzz ON (%s.%s.FK_momfuzz_id=%s
124        .momfuzz.momfuzz_id) WHERE beta=%g AND kappa=%g AND Ns=%lu AND Nt=%lu AND MF=%lu AND
125        PF=%lu AND MOMX=%lu AND MOMY=%lu AND MOMZ=%lu AND MOMLT=%lu ORDER BY conf,slice;",
126        database,meson,database,database,meson,database,database,database,database,meson,database,beta
127        ,kappa,Ns,Nt,MF,PF,MOMX,MOMY,MOMZ,MOMLT);
128
129    if(mysql_query(conn,query)!=0){
130        print_error(conn, "mysql_query() failed");
131    }
132    else
133    {
134        res_set=mysql_store_result(conn);
135        if(res_set==NULL){
136            print_error(conn, "mysql_store_result() failed");
137        }
138        else{
139            num_row=mysql_num_rows(res_set);
140            N_set=num_row/Ns;
141            printf("#of conf:%i\n",N_set);
142            conf=(int *) malloc( N_set * sizeof( int ) );
143            dat_mes=InitMatrix(N_set,Ns);
144            time_step=0;
145            Nset_step=-1;
146            while((row=mysql_fetch_row(res_set))!=NULL){
147                if(atoi(row[0])==0) Nset_step++;
148                n=time_step % Ns;
149                dat_mes[Nset_step][n]=atod(row[1]);
150                conf[Nset_step]=atoi(row[2]);
151                time_step++;
152            }
153        }
154
155        for (j=0;j<N_set;j++){
156            printf("\n");
157            for (i=0;i<Ns;i++){
158                printf("%i\t%e\t%u\n",i,dat_mes[j][i],conf[j]);
159            }
160        }
161
162        mysql_close(conn);
163        exit(0);
164    }

```

Listing D.1: Example of a sourcecode in C for a query to the database. User and password are defined in `~/my2.cnf`

In order to import data in our database we have used for instance for PS data into the AZ database the following script.

```

USE temp;

CREATE TABLE PS( slice int(2) unsigned zerofill NOT NULL,
value double NOT NULL,
dir char(1) NOT NULL,
Nt int(2) NOT NULL,
Ns int(2) NOT NULL,
beta double(5,3) NOT NULL,
kappa double(7,5) NOT NULL,
MF int(2) NOT NULL,
PF int(2) NOT NULL,
MOM_X int(1) NOT NULL,
MOM_Y int(1) NOT NULL,
MOM_Z int(1) NOT NULL,
MOM_T int(1) NOT NULL,
conf int(5) NOT NULL,
UNIQUE(slice,dir,Nt,Ns,beta,kappa,MF,PF,MOM_X,MOM_Y,MOM_Z,MOM_T,conf)
);

LOAD DATA INFILE '/SQL/input/AZ/PS.dat'
INTO TABLE PS FIELDS TERMINATED BY ' ';

INSERT INTO AZ.lattice (Ns,Nt,dir,beta,kappa)
SELECT DISTINCT PS.Ns,PS.Nt,PS.dir,PS.beta,PS.kappa FROM PS
LEFT OUTER JOIN AZ.lattice ON (PS.Ns=AZ.lattice.Ns AND
PS.Nt=AZ.lattice.Nt AND PS.dir=AZ.lattice.dir AND PS.beta=AZ.lattice.beta
AND PS.kappa=AZ.lattice.kappa) WHERE (AZ.lattice.Ns IS NULL);

INSERT INTO AZ.momfuzz (MF,PF,MOM_X,MOM_Y,MOM_Z,MOM_T)
SELECT DISTINCT PS.MF,PS.PF,PS.MOM_X,PS.MOM_Y,PS.MOM_Z,PS.MOM_T FROM PS
LEFT OUTER JOIN AZ.momfuzz ON (PS.MF=AZ.momfuzz.MF AND
PS.PF=AZ.momfuzz.PF AND PS.MOM_X=AZ.momfuzz.MOM_X AND
PS.MOM_Y=AZ.momfuzz.MOM_Y AND PS.MOM_Z=AZ.momfuzz.MOM_Z AND
PS.MOM_T=AZ.momfuzz.MOM_T) WHERE (AZ.momfuzz.MOM_Y IS NULL) ;

INSERT INTO AZ.PS (slice,value,conf,FK_lattice_id,FK_momfuzz_id)
SELECT PS.slice,PS.value,PS.conf,AZ.lattice.lattice_id,AZ.momfuzz.momfuzz_id
FROM PS
INNER JOIN AZ.lattice ON (PS.Ns=AZ.lattice.Ns AND PS.Nt=AZ.lattice.Nt
AND PS.dir=AZ.lattice.dir AND PS.beta=AZ.lattice.beta AND
PS.kappa=AZ.lattice.kappa)
INNER JOIN AZ.momfuzz ON (PS.PF=AZ.momfuzz.PF AND PS.MF=AZ.momfuzz.MF
AND PS.MOM_X=AZ.momfuzz.MOM_X AND PS.MOM_Y=AZ.momfuzz.MOM_Y AND
PS.MOM_Z=AZ.momfuzz.MOM_Z AND PS.MOM_T=AZ.momfuzz.MOM_T);

DROP TABLE PS;

```

It creates a temporary table *PS* in the database *temp*, reads in the data and distributes it among the various tables of the database *AZ*.

List of Abbreviations

AGS	Alternating Gradient Synchrotron, page 17
ALICE	A Large Ion Collider Experiment, page 118
AWI	Axial Ward Identity, page 28
BCS	Bardeen-Cooper-Schrieffer, page 15
BiCGStabl	Stabilized BiConjugate Gradients algorithm, page 42
BNL	Brookhaven National Laboratory, page 3
BZ	Brillouin Zone, page 27
CERN	Conseil Européen pour la Recherche Nucléaire, page 3
CF	Correlation Function, page 5
CFL	Color-Flavor-Locked, page 16
CG	Conjugate Gradient algorithm, page 42
CMS	Center of Mass System, page 3
CS	Color Superconductivity, page 15
FPA	Fixed Point Action, page 34
GMOR	Gell-Mann-Oaks-Renner, page 29
GSI	Gesellschaft für Schwerionenforschung, page 15
GUT	Grand Unified Theory, page 2
GWR	Ginsparg-Wilson Relation, page 33
HF	Hypercube truncated Fixed point (Hypercube Fermions), page 5
HTL	Hard Thermal Loop, page 21
LGT	Lattice Gauge Theory, page 4
LHC	Large Hadron Collider, page 21
LQCD	Lattice Quantum Chromo Dynamics, page 5
MEM	Maximum Entropy Method, page 4
MR	Minimal residue algorithm, page 42
MS	Minimal Subtraction, page 92
NJL	Nambu-Jona-Lasino, page 16
PCAC	Partially Conserved Axial Current, page 29
QCD	Quantum Chromodynamics, page 2
QED	Quantum Electrodynamics, page 1
QFT	Quantum Field Theory, page 1
QGP	Quark Gluon Plasma, page 3
RGE	Renormalization Group Equation, page 48
RGT	Renormalization Group Transformation, page 33
RHIC	Relativistic Heavy Ion Collider, page 3
RHMC	Rational Hybrid Monte Carlo, page 12
SI	Smearing Iterations, page 61
SIS	SchwerionenSynchrotron, page 17

SM	Standard Model, page 1
SPF	SPectral Function, page 4
SPS	Super Proton Synchroton, page 17
SQL	Structured Query Language, page 129
SW	Sheikholeslami-Wohlert, page 5
TOE	Theory Of Everything, page 2
VWI	Vector Ward Identity, page 28

List of Figures

1	The energy and pressure of lattice QCD.	3
1.1	The lightest meson multiplet of the $SU(4)_V$ flavor symmetry group.	11
1.2	Order of the phase transition for 2 + 1 sea quark flavors.	11
1.3	Collection of transition temperature results on the lattice.	12
1.4	Patterns of the $U(1)_A$ symmetry restoration.	13
1.5	First-order/crossover regime and critical surface for non-zero μ_f and the phase diagram of QCD.	16
1.6	More detailed sketch of the QCD phase diagram.	16
1.7	Cartoon of an ultra-relativistic heavy-ion collision.	17
1.8	Normalized invariant mass spectra of e^+e^- pairs from CERES	18
1.9	Space-time evolution of an A+A collision	19
2.1	Exceptional configurations close to (above) T_c	32
2.2	Impact of the twisted mass term on the (exceptional) configuration number 18800 at $1.2 T_c$	32
2.3	1-space, 2-space and 3-space hyper-links.	37
2.4	Quenched light hadron spectrum compared to the experimental values.	40
2.5	$Z(3)$ -symmetry: Polyakov loops in the complex plane.	47
2.6	The lowest eigenvalues for tuning the truncated fix point action.	52
2.7	Overlap enhancement: Fuzzing and Smearing.	61
2.8	Effective screening energy of a 'smeared' pseudoscalar.	62
3.1	Integration contour and poles for the Wilson and FP-action.	72
3.2	Dispersion relation of the Wilson and the truncated fixed point action.	73
3.3	Dependency of the SPF on the smearing level N_R	76
3.4	Reconstructed free SPF of the Wilson and the truncated FPA using the MEM.	77
3.5	The posterior probability distribution on free and interacting data.	77
4.1	Pseudoscalar and vector (MEM) pole and screening masses at $N_\tau=16$ below T_c	81
4.2	Finite volume extrapolation of vector screening masses.	82
4.3	(Screening) Dispersion relations of the P below and above T_c	85
4.4	Ground and excited state Bethe-Salpeter wave functions.	87
4.5	Bethe-Salpeter amplitudes by the ratio method at 0.55 and $3 T_c$	91
4.6	AWI quark masses below and above T_c and κ_c	92
4.7	Decay constants f_P/Z and $1/f_V Z_V$	95
4.8	SPFs at $T=0.55 T_c$ and $T=0.93 T_c$ for $N_\sigma=32$	98

4.9	SPFs at $T=0.55 T_c$ and $T=0.93 T_c$ for $N_\sigma=48$	99
4.10	P and V SPFs of the Wilson action at all T.	100
4.11	V SPFs of the truncated fixed point and Wilson action.	101
4.12	Contributions of the different energy ranges of the HF SPF to the correlator.	101
4.13	The regular and 'tuned' HF V SPF and the corresponding thermal Dilepton Production Rate in the QGP phase at $3 T_c$	102
4.14	Ratios with the temporal P and V Wilson CFs at $3 T_c$ to the free and free lattice CF.	103
4.15	P and V Wilson and HF CFs at 1.5 and $3 T_c$ and the ratios with the free continuum CF.	104
4.16	P and V CFs at different momenta for the HF action.	105
5.1	Effective screening masses compared with the free continuum one. Results of extrapolation.	109
5.2	Effective screening masses at $z = L/4$ compared to the free continuum ones.	110
5.3	Chiral and $U(1)_A$ symmetry below and above T_c	113
D.1	Schema of our database structure	130

List of Tables

1	The fundamental forces.	2
2.1	The coefficients for the fixed point action.	37
2.2	Estimated scales, temperatures and κ_c for the parameters used.	50
2.3	Lattice parameters and number of configurations for the SW-action below T_c	50
2.4	Lattice parameter and number of configurations for the SW-action above T_c	51
2.5	Parameters for the HF-action above T_c	52
2.6	The values $\Delta_H, b_h, \gamma_{H0}$	53
2.7	Correlation functions used in this thesis and their associated ground states.	59
3.1	The coefficients for the free continuum, Wilson and Fixed Point correlation functions.	72
4.1	Screening and pole masses in the chiral limit below T_c	82
4.2	Pseudoscalar Bethe-Salpeter wave functions below T_c	88
4.3	Pseudoscalar Bethe-Salpeter wave functions above T_c (Part I).	89
4.4	Pseudoscalar Bethe-Salpeter wave functions above T_c (Part II).	90
4.5	Hypercube and Wilson fermion decay constant f_P and $1/f_V$	96
5.1	Coefficients b_H and d_H of the spatial free Wilson lattice CFs.	108
5.2	Results from the data fit to Eq. (5.8) and Eq. (5.11).	109
B.1	Quark masses as obtained from axial ward identity below T_c	121
B.2	Quark masses as obtained from axial ward identity above T_c	122
B.3	Current renormalization factors Z_H below T_c	123
B.4	Current renormalization factors above T_c	123
B.5	Plaquette values and the resulting TI-couplings at $\mu=1/a$	123
B.6	Screening masses as obtained from two exponential fits above T_c for Wilson and HF action	124
B.7	Screening masses as obtained from one and two exponential fits below T_c	125
B.8	Pole masses as obtained from the SPF by a jackknifed MEM analysis	126
C.1	The explicit form of the HF functions g_H^{FP12}	128

List of Listings

D.1	Example of a sourcecode in C for a database query	131
-----	---	-----

References

- [1] S. Weinberg, *The Quantum theory of fields. Vol. 1+2: Foundations+Modern applications*. Cambridge, UK: Univ. Pr. (1995) 609 p.
- [2] T. P. Cheng and L. F. Li, *Gauge theory of elementary particle physics: Problems and solutions*. Oxford, UK: Clarendon, 2000.
- [3] J. F. Donoghue, E. Golowich, and B. R. Holstein, *Dynamics of the standard model*, vol. 2. Camb. Monogr. Part. Phys. Nucl. Phys. Cosmol., 1992.
- [4] F. Halzen and A. D. Martin, *Quarks and Leptons: An Introductory Course in Modern Particle Physics*. New York, Usa: Wiley (1984) 396p, 1984.
- [5] F. Karsch, “Lattice results on QCD thermodynamics”, *Nucl. Phys.* **A698** (2002) 199–208, hep-ph/0103314.
- [6] K. Kajantie, M. Laine, K. Rummukainen, and Y. Schroder, “The pressure of hot QCD up to $g^6 \ln(1/g)$ ”, *Phys. Rev.* **D67** (2003) 105008, hep-ph/0211321.
- [7] E. V. Shuryak and I. Zahed, “Towards a theory of binary bound states in the quark gluon plasma”, *Phys. Rev.* **D70** (2004) 054507, hep-ph/0403127.
- [8] M. Gyulassy and L. McLerran, “New forms of QCD matter discovered at RHIC”, *Nucl. Phys.* **A750** (2005) 30–63, nucl-th/0405013.
- [9] T. Matsui and H. Satz, “ J / ψ suppression by quark - gluon plasma formation”, *Phys. Lett.* **B178** (1986) 416.
- [10] E. Braaten, R. D. Pisarski, and T.-C. Yuan, “Production of soft Dileptons in the Quark - Gluon Plasma”, *Phys. Rev. Lett.* **64** (1990) 2242.
- [11] M. Asakawa, T. Hatsuda, and Y. Nakahara, “Maximum Entropy Analysis of the Spectral Functions in Lattice QCD”, *Prog. Part. Nucl. Phys.* **46** (2001) 459–508, hep-lat/0011040.
- [12] K. G. Wilson, “The renormalization group: critical phenomena and the kondo problem”, *Rev. Mod. Phys.* **47** (1975) 773.
- [13] K. Symanzik, “Continuum limit and improved action in lattice theories. 1. Principles and ϕ^4 theory”, *Nucl. Phys.* **B226** (1983) 187.
- [14] K. Symanzik, “Continuum limit and improved action in lattice theories. 2. O(N) nonlinear sigma model in perturbation theory”, *Nucl. Phys.* **B226** (1983) 205.
- [15] S. Wissel, E. Laermann, S. Shcheredin, S. Datta, and F. Karsch, “Meson correlation functions at high temperatures”, *PoS LAT2005* (2006) 164, hep-lat/0510031.
- [16] T. Matsubara, “A New approach to quantum statistical mechanics”, *Prog. Theor. Phys.* **14** (1955) 351–378.
- [17] J. Kapusta and C. Gale, *Finite-Temperature field Theory*. 2nd ed.: Principles and Applications, Cambridge, UK: Univ. Pr. (2006) 432 p. (Cambridge monographs on mathematical physics), 2006.

- [18] Y. Nambu, “Axial vector current conservation in weak interactions”, *Phys. Rev. Lett.* **4** (1960) 380–382.
- [19] J. Goldstone, “Field theories with ‘superconductor’ solutions”, *Nuovo Cim.* **19** (1961) 154–164.
- [20] S. L. Adler and W. A. Bardeen, “Absence of higher order corrections in the anomalous axial vector divergence equation”, *Phys. Rev.* **182** (1969) 1517–1536.
- [21] J. S. Bell and R. Jackiw, “A PCAC puzzle: $\pi^0 \rightarrow \gamma \gamma$ in the sigma model”, *Nuovo Cim.* **A60** (1969) 47–61.
- [22] K. Fujikawa, “Path Integral for gauge theories with fermions”, *Phys. Rev.* **D21** (1980) 2848.
- [23] G. Veneziano, “ $U(1)$ without Instantons”, *Nucl. Phys.* **B159** (1979) 213–224.
- [24] E. Witten, “Current algebra theorems for the $U(1)$ ‘Goldstone Boson’”, *Nucl. Phys.* **B156** (1979) 269.
- [25] G. ’t Hooft, “Symmetry breaking through Bell-Jackiw anomalies”, *Phys. Rev. Lett.* **37** (1976) 8–11.
- [26] G. ’t Hooft, “Computation of the quantum effects due to a four-dimensional pseudoparticle”, *Phys. Rev.* **D14** (1976) 3432–3450.
- [27] **Particle Data Group** Collaboration, W. M. Yao *et al.*, “Review of particle physics”, *J. Phys.* **G33** (2006) 1–1232.
- [28] A. Peikert, *QCD thermodynamics with 2+1 quark flavours in lattice simulations*. PhD thesis, University of Bielefeld, 2000.
- [29] M. Fukugita, M. Okawa, and A. Ukawa, “Finite size scaling study of the deconfining phase transition in pure $SU(3)$ lattice gauge theory”, *Nucl. Phys.* **B337** (1990) 181.
- [30] G. Boyd *et al.*, “Thermodynamics of $SU(3)$ Lattice Gauge Theory”, *Nucl. Phys.* **B469** (1996) 419–444, [hep-lat/9602007](#).
- [31] F. Karsch, “Lattice QCD at High Temperature and Density”, *Lect. Notes Phys.* **583** (2002) 209–249, [hep-lat/0106019](#).
- [32] F. Karsch and M. Lütgemeier, “Deconfinement and chiral symmetry restoration in an $SU(3)$ gauge theory with adjoint fermions”, *Nucl. Phys.* **B550** (1999) 449–464, [hep-lat/9812023](#).
- [33] C. Gattringer, “Linking confinement to spectral properties of the Dirac operator”, [hep-lat/0605018](#).
- [34] P. Petreczky, “Lattice QCD at finite temperature”, [hep-lat/0609040](#).
- [35] M. Cheng *et al.*, “The transition temperature in QCD”, [hep-lat/0608013](#).
- [36] R. D. Pisarski and F. Wilczek, “Remarks on the chiral phase transition in chromodynamics”, *Phys. Rev.* **D29** (1984) 338–341.
- [37] F. Karsch and E. Laermann, “Susceptibilities, the Specific Heat and a Cumulant in Two Flavor QCD”, *Phys. Rev.* **D50** (1994) 6954–6962, [hep-lat/9406008](#).
- [38] F. Karsch, E. Laermann, and A. Peikert, “Quark mass and flavor dependence of the QCD phase transition”, *Nucl. Phys.* **B605** (2001) 579–599, [hep-lat/0012023](#).
- [39] G. Boyd, F. Karsch, E. Laermann, and M. Oevers, “Two flavour QCD phase transition”, [hep-lat/9607046](#).

- [40] E. Laermann, “Chiral transition in 2 flavor staggered QCD”, *Nucl. Phys. Proc. Suppl.* **60A** (1998) 180–187.
- [41] M. F. Atiyah and I. M. Singer, “The Index of Elliptic Operators on Compact Manifolds”, *Bull. Amer. Math. Soc.* **69** (1963) 322–433.
- [42] M. F. Atiyah and I. M. Singer, “The Index of Elliptic Operators I, II, III”, *Ann. Math.* **87** (1968) 484–604.
- [43] T. Banks and A. Casher, “Chiral symmetry breaking in confining theories”, *Nucl. Phys.* **B169** (1980) 103.
- [44] D. J. Gross, R. D. Pisarski, and L. G. Yaffe, “QCD and instantons at finite temperature”, *Rev. Mod. Phys.* **53** (1981) 43.
- [45] P. de Forcrand and O. Philipsen, “The chiral critical line of $N(f) = 2+1$ QCD at zero and non-zero baryon density”, [hep-lat/0607017](#).
- [46] C. Schmidt, “The QCD phase diagram for small chemical potentials”, [hep-lat/0210037](#).
- [47] O. Kaczmarek (Private Communication).
- [48] M. G. Alford, “New possibilities for QCD at finite density”, *Nucl. Phys. Proc. Suppl.* **73** (1999) 161–166, [hep-lat/9809166](#).
- [49] D. Bailin and A. Love, “Superfluidity and Superconductivity in Relativistic Fermion Systems”, *Phys. Rept.* **107** (1984) 325.
- [50] J. Bardeen, L. N. Cooper, and J. R. Schrieffer, “Theory of superconductivity”, *Phys. Rev.* **108** (1957) 1175–1204.
- [51] M. G. Alford, K. Rajagopal, and F. Wilczek, “Color-flavor locking and chiral symmetry breaking in high density QCD”, *Nucl. Phys.* **B537** (1999) 443–458, [hep-ph/9804403](#).
- [52] T. Schafer and F. Wilczek, “Quark description of hadronic phases”, *Phys. Rev.* **D60** (1999) 074014, [hep-ph/9903503](#).
- [53] T. Schafer, “Patterns of symmetry breaking in QCD at high baryon density”, *Nucl. Phys.* **B575** (2000) 269–284, [hep-ph/9909574](#).
- [54] M. Alford and K. Rajagopal, “Color Superconductivity in Dense, but not Asymptotically Dense, Quark Matter”, [hep-ph/0606157](#).
- [55] S. Hands, “The phase diagram of QCD”, *Contemp. Phys.* **42** (2001) 209–225, [physics/0105022](#).
- [56] **CERES** Collaboration, B. Lenkeit *et al.*, “Recent results from Pb Au collisions at 158-GeV/c per nucleon obtained with the CERES spectrometer”, *Nucl. Phys.* **A661** (1999) 23–32, [nucl-ex/9910015](#).
- [57] **NA50** Collaboration, M. C. Abreu *et al.*, “Evidence for deconfinement of quarks and gluons from the J/psi suppression pattern measured in Pb Pb collisions at the CERN-SPS”, *Phys. Lett.* **B477** (2000) 28–36.
- [58] **PHENIX** Collaboration, H. Pereira Da Costa, “PHENIX results on J/psi production in Au + Au and Cu + Cu collisions at $\sqrt{s(NN)} = 200$ -GeV”, [nucl-ex/0510051](#).
- [59] **PHENIX** Collaboration, K. Adcox *et al.*, “Formation of dense partonic matter in relativistic nucleus nucleus collisions at RHIC: Experimental evaluation by the PHENIX collaboration”, *Nucl. Phys.* **A757** (2005) 184–283, [nucl-ex/0410003](#).

- [60] R. Rapp and J. Wambach, “Chiral Symmetry Restoration and Dileptons in Relativistic Heavy-Ion Collisions”, *Adv. Nucl. Phys.* **25** (2000) 1, [hep-ph/9909229](#).
- [61] S. D. Drell, D. J. Levy, and T.-M. Yan, “A Theory of Deep inelastic lepton-nucleon scattering and lepton pair annihilation processes. I”, *Phys. Rev.* **187** (1969) 2159–2171.
- [62] K. J. Eskola, “High energy nuclear collisions”, [hep-ph/9911350](#).
- [63] G. E. Brown and M. Rho, “Chiral restoration in hot and/or dense matter”, *Phys. Rept.* **269** (1996) 333–380, [hep-ph/9504250](#).
- [64] G. E. Brown and M. Rho, “Scaling effective Lagrangians in a dense medium”, *Phys. Rev. Lett.* **66** (1991) 2720–2723.
- [65] G. E. Brown and M. Rho, “Matching the QCD and hadron sectors and medium dependent meson masses: Hadronization in relativistic heavy ion collisions”, *Phys. Rept.* **398** (2004) 301–325, [nucl-th/0206021](#).
- [66] T. Hatsuda and S. H. Lee, “QCD sum rules for vector mesons in nuclear medium”, *Phys. Rev.* **C46** (1992) 34–38.
- [67] R. Rapp, G. Chanfray, and J. Wambach, “Rho meson propagation and dilepton enhancement in hot hadronic matter”, *Nucl. Phys.* **A617** (1997) 472–495, [hep-ph/9702210](#).
- [68] M. Post, S. Leupold, and U. Mosel, “The rho spectral function in a relativistic resonance model”, *Nucl. Phys.* **A689** (2001) 753–783, [nucl-th/0008027](#).
- [69] **NA60** Collaboration, S. Damjanovic *et al.*, “First measurement of the rho spectral function in nuclear collisions”, [nucl-ex/0510044](#).
- [70] **NA60** Collaboration, H. K. Woehri *et al.*, “Low mass dimuon production in proton-nucleus and indium- indium collisions”, *PoS HEP2005* (2006) 132.
- [71] M. Asakawa and T. Hatsuda, “J/psi and eta/c in the deconfined plasma from lattice QCD”, *Phys. Rev. Lett.* **92** (2004) 012001, [hep-lat/0308034](#).
- [72] S. Datta, F. Karsch, P. Petreczky, and I. Wetzorke, “Behavior of charmonium systems after deconfinement”, *Phys. Rev.* **D69** (2004) 094507, [hep-lat/0312037](#).
- [73] C.-Y. Wong, “Heavy quarkonia in quark gluon plasma”, *Phys. Rev.* **C72** (2005) 034906, [hep-ph/0408020](#).
- [74] W. M. Alberico, A. Beraudo, A. De Pace, and A. Molinari, “Heavy quark bound states above $T(c)$ ”, *Phys. Rev.* **D72** (2005) 114011, [hep-ph/0507084](#).
- [75] F. Karsch, D. Kharzeev, and H. Satz, “Sequential charmonium dissociation”, *Phys. Lett.* **B637** (2006) 75–80, [hep-ph/0512239](#).
- [76] J.-w. Qiu, J. P. Vary, and X.-f. Zhang, “J/psi suppression in nucleus nucleus collisions”, *Phys. Rev. Lett.* **88** (2002) 232301, [hep-ph/9809442](#).
- [77] L. Grandchamp, R. Rapp, and G. E. Brown, “In-medium effects on charmonium production in heavy-ion collisions”, *Phys. Rev. Lett.* **92** (2004) 212301, [hep-ph/0306077](#).
- [78] S. Datta, F. Karsch, S. Wissel, P. Petreczky, and I. Wetzorke, “Charmonia at finite momenta in a deconfined plasma”, [hep-lat/0409147](#).
- [79] M. J. Tannenbaum, “Recent results in relativistic heavy ion collisions: From ‘a new state of matter’ to ‘the perfect fluid’”, *Rept. Prog. Phys.* **69** (2006) 2005–2060, [nucl-ex/0603003](#).

- [80] F. Karsch, E. Laermann, P. Petreczky, S. Stickan, and I. Wetzorke, “A lattice calculation of thermal dilepton rates”, *Phys. Lett.* **B530** (2002) 147–152, [hep-lat/0110208](#).
- [81] P. Petreczky, “Lattice calculations of meson correlators and spectral functions at finite temperature”, *J. Phys.* **G30** (2004) S431–S440, [hep-ph/0305189](#).
- [82] J.-P. Blaizot and F. Gelis, “Photon and dilepton production in the quark-gluon plasma: Perturbation theory vs lattice QCD”, *Eur. Phys. J.* **C43** (2005) 375–380, [hep-ph/0504144](#).
- [83] G. Aarts and J. M. Martinez Resco, “Transport coefficients, spectral functions and the lattice”, *JHEP* **04** (2002) 053, [hep-ph/0203177](#).
- [84] J. P. Blaizot, E. Iancu, and A. Rebhan, “On the apparent convergence of perturbative QCD at high temperature”, *Phys. Rev.* **D68** (2003) 025011, [hep-ph/0303045](#).
- [85] J. O. Andersen, E. Braaten, E. Petitgirard, and M. Strickland, “HTL perturbation theory to two loops”, *Phys. Rev.* **D66** (2002) 085016, [hep-ph/0205085](#).
- [86] I. Montvay and G. Munster, *Quantum Fields on a Lattice*. Cambridge, UK: Univ. Pr. (1994) 491 p. (Cambridge monographs on mathematical physics), 1994.
- [87] M. Creutz, “Quarks, Gluons and lattices”, Cambridge, UK: Univ. Pr. (1983) 169 P. (Cambridge Monographs On Mathematical Physics).
- [88] R. Gupta, “Introduction to lattice QCD”, [hep-lat/9807028](#).
- [89] R. P. Feynman, “Space-time approach to nonrelativistic quantum mechanics”, *Rev. Mod. Phys.* **20** (1948) 367–387.
- [90] K. G. Wilson, “Quarks and strings on a lattice”, *New Phenomena In Subnuclear Physics. Part A. Proceedings of the First Half of the 1975 International School of Subnuclear Physics, Erice, Sicily, July 11 - August 1, 1975*, ed. A. Zichichi, Plenum Press, New York, 1977, p. 69, CLNS-321.
- [91] H. J. Rothe, “Lattice gauge theories: An Introduction”, *World Sci. Lect. Notes Phys.* **74** (2005) 1–605.
- [92] K. G. Wilson, “Confinement of quarks”, *Phys. Rev.* **D10** (1974) 2445–2459.
- [93] M. Lüscher and P. Weisz, “On-shell improved lattice gauge theories”, *Commun. Math. Phys.* **97** (1985) 59.
- [94] K. Symanzik, “Mathematical Problems in Theoretical Physics”, *Lecture notes in Physics*. Springer-Verlag, Berlin (1982) 153.
- [95] M. Lüscher and P. Weisz, “Computation of the action for on-shell improved lattice gauge theories at weak coupling”, *Phys. Lett.* **B158** (1985) 250.
- [96] H. B. Nielsen and M. Ninomiya, “No go theorem for regularizing chiral fermions”, *Phys. Lett.* **B105** (1981) 219.
- [97] C. Itzykson and J. M. Drouffe, *Statistical Field theory. Vol. 1: From Brownian motion to renormalization and lattice gauge theory*. Cambridge, UK: Univ. Pr. 1-403, 1989.
- [98] M. Bochicchio, L. Maiani, G. Martinelli, G. C. Rossi, and M. Testa, “Chiral symmetry on the lattice with Wilson fermions”, *Nucl. Phys.* **B262** (1985) 331.
- [99] G. M. de Divitiis and R. Petronzio, “Non-perturbative renormalization constants on the lattice from flavour non-singlet Ward identities”, *Phys. Lett.* **B419** (1998) 311–316, [hep-lat/9710071](#).
- [100] M. Gell-Mann, R. J. Oakes, and B. Renner, “Behavior of current divergences under $SU(3) \times SU(3)$ ”, *Phys. Rev.* **175** (1968) 2195–2199.

- [101] M. E. Peskin and D. V. Schroeder, *An Introduction to quantum field theory*. Reading, USA: Addison-Wesley 842p, 1995.
- [102] B. Sheikholeslami and R. Wohlert, “Improved continuum limit lattice action for QCD with Wilson fermions”, *Nucl. Phys.* **B259** (1985) 572.
- [103] M. Lüscher, S. Sint, R. Sommer, P. Weisz, and U. Wolff, “Non-perturbative $O(a)$ improvement of lattice QCD”, *Nucl. Phys.* **B491** (1997) 323–343, [hep-lat/9609035](#).
- [104] M. Guagnelli and R. Sommer, “Non-perturbative $O(a)$ improvement of the vector current”, *Nucl. Phys. Proc. Suppl.* **63** (1998) 886–888, [hep-lat/9709088](#).
- [105] M. Creutz, “Fun with Dirac eigenvalues”, [hep-lat/0511052](#).
- [106] W. Söldner (Private Communication).
- [107] **CP-PACS** Collaboration, K. Kanaya *et al.*, “Quenched light hadron spectrum with the Wilson quark action: Final results from CP-PACS”, *Nucl. Phys. Proc. Suppl.* **73** (1999) 189–191, [hep-lat/9809146](#).
- [108] A. Shindler, “Twisted mass lattice QCD: Recent developments and results”, *PoS LAT2005* (2006) 014, [hep-lat/0511002](#).
- [109] S. Aoki and O. Bar, “Twisted-mass QCD, $O(a)$ improvement and Wilson chiral perturbation theory”, *Phys. Rev.* **D70** (2004) 116011, [hep-lat/0409006](#).
- [110] R. Frezzotti and G. C. Rossi, “Chirally improving Wilson fermions. I: $O(a)$ improvement”, *JHEP* **08** (2004) 007, [hep-lat/0306014](#).
- [111] C. Gattringer and S. Solbrig, “Low-lying spectrum for lattice Dirac operators with twisted mass”, *PoS LAT2005* (2006) 127, [hep-lat/0509079](#).
- [112] S. Aoki and O. Bar, “Automatic $O(a)$ improvement for twisted-mass QCD”, [hep-lat/0610098](#).
- [113] J. B. Kogut and L. Susskind, “Hamiltonian of Wilson’s lattice gauge theories”, *Phys. Rev.* **D11** (1975) 395.
- [114] L. Susskind, “Lattice fermions”, *Phys. Rev.* **D16** (1977) 3031–3039.
- [115] M. Creutz, “Flavor extrapolations and staggered fermions”, [hep-lat/0603020](#).
- [116] S. R. Sharpe, *Rooted staggered fermions: good, bad, or ugly?* Talk given at The XXIV International Symposium on Lattice Field Theory Tucson, Arizona, July 23-28 2006.
- [117] P. H. Ginsparg and K. G. Wilson, “A remnant of chiral symmetry on the lattice”, *Phys. Rev.* **D25** (1982) 2649.
- [118] D. B. Kaplan, “A Method for Simulating Chiral Fermions on the Lattice”, *Phys. Lett.* **B288** (1992) 342–347, [hep-lat/9206013](#).
- [119] Y. Shamir, “Chiral fermions from lattice boundaries”, *Nucl. Phys.* **B406** (1993) 90–106, [hep-lat/9303005](#).
- [120] P. Hasenfratz, V. Laliena, and F. Niedermayer, “The index theorem in QCD with a finite cut-off”, *Phys. Lett.* **B427** (1998) 125–131, [hep-lat/9801021](#).
- [121] M. Luscher, “Exact chiral symmetry on the lattice and the Ginsparg- Wilson relation”, *Phys. Lett.* **B428** (1998) 342–345, [hep-lat/9802011](#).
- [122] W. Bietenholz *et al.*, “Preconditioning of improved and *perfect* fermion actions”, *Comput. Phys. Commun.* **119** (1999) 1–18, [hep-lat/9807013](#).

- [123] S. Shcheredin, “Simulations of lattice fermions with chiral symmetry in quantum chromodynamics”, [hep-lat/0502001](#).
- [124] K. G. Wilson and J. B. Kogut, “The Renormalization group and the epsilon expansion”, *Phys. Rept.* **12** (1974) 75–200.
- [125] L. P. Kadanoff, “Lectures on the application of renormalization group techniques to quarks and strings”, *Rev. Mod. Phys.* **49** (1977) 267–296.
- [126] W. Bietenholz and U. J. Wiese, “Perfect Lattice Actions for Quarks and Gluons”, *Nucl. Phys.* **B464** (1996) 319–352, [hep-lat/9510026](#).
- [127] W. Bietenholz, “Chiral symmetry, renormalization group and fixed points for lattice fermions”, [hep-lat/9402005](#).
- [128] W. Bietenholz, R. Brower, S. Chandrasekharan, and U. J. Wiese, “Progress on Perfect Lattice Actions for QCD”, *Nucl. Phys. Proc. Suppl.* **53** (1997) 921–934, [hep-lat/9608068](#).
- [129] K. Orginos, W. Bietenholz, R. Brower, S. Chandrasekharan, and U. J. Wiese, “The Perfect Quark-Gluon Vertex Function”, *Nucl. Phys. Proc. Suppl.* **63** (1998) 904–906, [hep-lat/9709100](#).
- [130] D. H. Weingarten and D. N. Petcher, “Monte Carlo Integration for Lattice Gauge Theories with fermions”, *Phys. Lett.* **B99** (1981) 333.
- [131] H. Hamber and G. Parisi, “Numerical Estimates of Hadronic masses in a pure $SU(3)$ Gauge theory”, *Phys. Rev. Lett.* **47** (1981) 1792.
- [132] P. Schmidt, *Hadronic properties in the vicinity of the critical temperature*. PhD thesis, University of Bielefeld, 2000.
- [133] P. Schmidt, “QCD bei endlichen Temperaturen mit quenched Wilson Fermion”, Master’s thesis, University of Bielefeld, 1996.
- [134] **CP-PACS** Collaboration, S. Aoki *et al.*, “Light hadron spectrum and quark masses from quenched lattice QCD”, *Phys. Rev.* **D67** (2003) 034503, [hep-lat/0206009](#).
- [135] T. Yoshie, “Light hadron spectroscopy”, *Nucl. Phys. Proc. Suppl.* **63** (1998) 3–15, [hep-lat/9711017](#).
- [136] **HPQCD** Collaboration, C. T. H. Davies *et al.*, “High-precision lattice QCD confronts experiment”, *Phys. Rev. Lett.* **92** (2004) 022001, [hep-lat/0304004](#).
- [137] N. Metropolis, A. W. Rosenbluth, M. N. Rosenbluth, A. H. Teller, and E. Teller, “Equation of state calculations by fast computing machines”, *J. Chem. Phys.* **21** (1953) 1087–1092.
- [138] N. Cabibbo and E. Marinari, “A new method for updating $SU(N)$ matrices in computer simulations of gauge theories”, *Phys. Lett.* **B119** (1982) 387.
- [139] A. D. Kennedy and B. J. Pendleton, “Improved heat bath method for Monte Carlo calculations in lattice gauge theories”, *Phys. Lett.* **B156** (1985) 393.
- [140] E. Pietarinen, “String tension in $SU(3)$ lattice gauge theory”, *Nucl. Phys.* **B190** (1981) 349.
- [141] K. Fabricius and O. Haan, “Heat bath method for the twisted Eguchi-Kawai model”, *Phys. Lett.* **B143** (1984) 459.
- [142] S. L. Adler, “Overrelaxation method for the Monte Carlo evaluation of the partition function for multiquadratic actions”, *Phys. Rev.* **D23** (1981) 2901.
- [143] M. Creutz, “Overrelaxation and Monte Carlo Simulation”, *Phys. Rev.* **D36** (1987) 515.

- [144] S. L. Eisenstadt *et al.*, “Variational iterative methods for nonsymmetric systems of linear equations.”, *SIAM J. Num. Anal.* **20** (1983) 345.
- [145] M. R. Hestenes and E. Stiefel, “Conjugate Gradient”, *J. Res. Nat. Bur. Standards* **49** (1952) 409.
- [146] H. van der Vorst, “A Fast and Smoothly Converging Variant of Bi-CG for the Solution of Nonsymmetric Linear Systems”, *SIAM J. Sc. Stat. Comp.* **13** (1992) 631.
- [147] G. Cella, A. Hoferichter, V. K. Mitrjushkin, M. Muller-Preussker, and A. Vicere, “Efficiency of different matrix inversion methods applied to Wilson fermions”, *Int. J. Mod. Phys. C* **7** (1996) 787–809, [hep-lat/9606003](#).
- [148] T. A. DeGrand and P. Rossi, “Conditioning techniques for dynamical fermions”, *Comput. Phys. Commun.* **60** (1990) 211.
- [149] N. Stanford. PhD thesis, University of Edinburgh, 1994.
- [150] M. H. Quenouille, “Approximate Tests of Correlation in Time-Series”, *J. Roy. Statist. Soc. B* **11** (1949) 18.
- [151] F. James and M. Roos, “‘minuit’ A system for function minimization and analysis of the parameter errors and correlations”, *Comput. Phys. Commun.* **10** (1975) 343–367.
- [152] C. Michael and A. McKerrell, “Fitting Correlated Hadron Mass Spectrum Data”, *Phys. Rev.* **D51** (1995) 3745–3750, [hep-lat/9412087](#).
- [153] G. ’t Hooft, “On the phase transition towards permanent quark confinement”, *Nucl. Phys.* **B138** (1978) 1.
- [154] G. ’t Hooft, “A property of electric and magnetic flux in nonabelian gauge theories”, *Nucl. Phys.* **B153** (1979) 141.
- [155] A. M. Polyakov, “Thermal properties of gauge fields and quark liberation”, *Phys. Lett.* **B72** (1978) 477–480.
- [156] C. Schmidt, *The Phase Diagram and Equation of State of Improved Lattice QCD for High Temperatures and small Chemical Potential*. PhD thesis, University of Bielefeld, 2003.
- [157] L. D. McLerran and B. Svetitsky, “Quark liberation at high temperature: A Monte Carlo study of $SU(2)$ gauge theory”, *Phys. Rev.* **D24** (1981) 450.
- [158] J. B. Kogut *et al.*, “Deconfinement and chiral symmetry restoration at finite temperature in $SU(2)$ and $SU(3)$ gauge theories”, *Phys. Rev. Lett.* **50** (1983) 393.
- [159] S. Chandrasekharan and N. H. Christ, “Dirac Spectrum, Axial Anomaly and the QCD Chiral Phase Transition”, *Nucl. Phys. Proc. Suppl.* **47** (1996) 527–534, [hep-lat/9509095](#).
- [160] M. A. Stephanov, “Chiral symmetry at finite T, the phase of the Polyakov loop and the spectrum of the Dirac operator”, *Phys. Lett.* **B375** (1996) 249–254, [hep-lat/9601001](#).
- [161] W. Bietenholz, “Convergence rate and locality of improved overlap fermions”, *Nucl. Phys.* **B644** (2002) 223–247, [hep-lat/0204016](#).
- [162] S. Shcheredin (Private Communication).
- [163] R. G. Edwards, U. M. Heller, and T. R. Klassen, “Accurate Scale Determinations for the Wilson Gauge Action”, *Nucl. Phys.* **B517** (1998) 377–392, [hep-lat/9711003](#).
- [164] C. R. Allton, “Lattice Monte Carlo data versus perturbation theory”, [hep-lat/9610016](#).

- [165] B. Beinlich, F. Karsch, E. Laermann, and A. Peikert, “String Tension and Thermodynamics with Tree Level and Tadpole Improved Actions”, *Eur. Phys. J.* **C6** (1999) 133–140, [hep-lat/9707023](#).
- [166] R. Sommer, “A New way to set the energy scale in lattice gauge theories and its applications to the static force and alpha-s in $SU(2)$ Yang-Mills theory”, *Nucl. Phys.* **B411** (1994) 839–854, [hep-lat/9310022](#).
- [167] **ALPHA** Collaboration, M. Guagnelli, R. Sommer, and H. Wittig, “Precision computation of a low-energy reference scale in quenched lattice QCD”, *Nucl. Phys.* **B535** (1998) 389–402, [hep-lat/9806005](#).
- [168] M. Göckeler *et al.*, “Perturbative renormalisation of bilinear quark and gluon operators”, *Nucl. Phys. Proc. Suppl.* **53** (1997) 896–898, [hep-lat/9608033](#).
- [169] G. P. Lepage and P. B. Mackenzie, “On the Viability of Lattice Perturbation Theory”, *Phys. Rev.* **D48** (1993) 2250–2264, [hep-lat/9209022](#).
- [170] S. Sint and P. Weisz, “Further results on $O(a)$ improved lattice QCD to one-loop order of perturbation theory”, *Nucl. Phys.* **B502** (1997) 251–268, [hep-lat/9704001](#).
- [171] G. Parisi, “Recent progresses in gauge theories”, Presented at 20th Int. Conf. on High Energy Physics, Madison, Wis., Jul 17-23, 1980.
- [172] T. R. Klassen, “The (Lattice) QCD potential and coupling: How to accurately interpolate between multiloop QCD and the string picture”, *Phys. Rev.* **D51** (1995) 5130–5152.
- [173] M. Lüscher, S. Sint, R. Sommer, and H. Wittig, “Non-perturbative determination of the axial current normalization constant in $O(a)$ improved lattice QCD”, *Nucl. Phys.* **B491** (1997) 344–364, [hep-lat/9611015](#).
- [174] F. Karsch, M. G. Mustafa, and M. H. Thoma, “Finite Temperature Meson Correlation Functions in HTL Approximation”, *Phys. Lett.* **B497** (2001) 249–258, [hep-ph/0007093](#).
- [175] M. le Bellac, *Thermal Field Theory*. Cambridge University Press, 1996.
- [176] M. A. Shifman, A. I. Vainshtein, and V. I. Zakharov, “QCD and resonance physics. Sum rules”, *Nucl. Phys.* **B147** (1979) 385–447.
- [177] E. V. Shuryak, “Correlation functions in the QCD vacuum”, *Rev. Mod. Phys.* **65** (1993) 1–46.
- [178] V. Koch, E. V. Shuryak, G. E. Brown, and A. D. Jackson, “The Propagation of quarks in the spatial direction in hot QCD”, *Phys. Rev.* **D46** (1992) 3169–3179, [hep-ph/9204236](#).
- [179] T. Hashimoto, A. Nakamura, and I. O. Stamatescu, “Temperature dependent structure in the mesonic channels of QCD”, *Nucl. Phys.* **B400** (1993) 267–308.
- [180] W. Florkowski and B. L. Friman, “Spatial dependence of meson correlation functions at high temperature”, *Z. Phys.* **A347** (1994) 271–276.
- [181] R. Gupta, D. Daniel, and J. Grandy, “Bethe-Salpeter amplitudes and density correlations for mesons with Wilson fermions”, *Phys. Rev.* **D48** (1993) 3330–3339, [hep-lat/9304009](#).
- [182] **UKQCD** Collaboration, P. Lacock, A. McKerrell, C. Michael, I. M. Stopher, and P. W. Stephenson, “Efficient Hadronic Operators in Lattice Gauge Theory”, *Phys. Rev.* **D51** (1995) 6403–6410, [hep-lat/9412079](#).
- [183] **Ape** Collaboration, M. Albanese *et al.*, “Glueball masses and the loop loop correlation functions”, *Phys. Lett.* **B197** (1987) 400.
- [184] N. Ishii, H. Suganuma, and H. Matsufuru, “Scalar glueball mass reduction at finite temperature in $SU(3)$ anisotropic lattice QCD”, *Phys. Rev.* **D66** (2002) 014507, [hep-lat/0109011](#).

- [185] **CP-PACS** Collaboration, T. Yamazaki *et al.*, “Spectral function and excited states in lattice QCD with maximum entropy method”, *Phys. Rev.* **D65** (2002) 014501, [hep-lat/0105030](#).
- [186] I. Wetzorke, *Lattice QCD Calculations of Hadron Spectra and Spectral Functions in the Vacuum and in a Thermal Heat Bath*. PhD thesis, University of Bielefeld, 2001.
- [187] F. Karsch, E. Laermann, P. Petreczky, and S. Stickan, “Infinite temperature limit of meson spectral functions calculated on the lattice”, *Phys. Rev.* **D68** (2003) 014504, [hep-lat/0303017](#).
- [188] S. Stickan, *Thermal Meson Properties from Correlation Functions and their Spectral Representation*. PhD thesis, University of Bielefeld, 2003.
- [189] T. Bayes, “An essay towards solving a problem in the doctrine of chances”, *Philosophical Transactions of the Royal Society of London* **53** (1763) 370–418.
- [190] J. Skilling, “Maximum Entropy and Bayesian Methods”, *Kluwer, Academic Publishers, London* **74** (1989) 45–52.
- [191] S. F. Gull and G. J. Daniell, “Maximum Entropy and Bayesian Methods”, *Nature* **272** (1978) 686.
- [192] E. T. Jaynes, “Maximum Entropy and Bayesian Methods in Applied Statistics”, *Cambridge Univ. Press, Cambridge* **272** (1986) 26–58.
- [193] T. Umeda and H. Matsufuru, “Remarks on the maximum entropy method applied to finite temperature lattice QCD”, *PoS LAT2005* (2006) 154, [hep-lat/0510026](#).
- [194] R. K. Bryan, “Maximum entropy analysis of oversampled data problems”, *Eur. Biophys.* **J18** (1990) 165–174.
- [195] H. Jeffreys, *Theory of Probability*. Oxford Univ. Press., 1998.
- [196] M. Jarrell and J. E. Gubernatis, “Bayesian inference and the analytic continuation of imaginary-time quantum Monte Carlo data”, *Phys. Rep.* **269** (1996) 133–195.
- [197] S. Stickan, “In medium hadron properties”, [hep-lat/0301009](#).
- [198] S. Datta (Private Communication).
- [199] G. Aarts and J. M. Martinez Resco, “Continuum and lattice meson spectral functions at nonzero momentum and high temperature”, *Nucl. Phys.* **B726** (2005) 93–108, [hep-lat/0507004](#).
- [200] D. B. Carpenter and C. F. Baillie, “Free fermion propagators and lattice finite size effects”, *Nucl. Phys.* **B260** (1985) 103.
- [201] I. Wetzorke, F. Karsch, E. Laermann, P. Petreczky, and S. Stickan, “Meson Spectral Functions at finite Temperature”, *Nucl. Phys. Proc. Suppl.* **106** (2002) 510–512, [hep-lat/0110132](#).
- [202] P. Petreczky, F. Karsch, E. Laermann, S. Stickan, and I. Wetzorke, “Temporal quark and gluon propagators: Measuring the quasiparticle masses”, *Nucl. Phys. Proc. Suppl.* **106** (2002) 513–515, [hep-lat/0110111](#).
- [203] S. R. Sharpe, “Quenched chiral logarithms”, *Phys. Rev.* **D46** (1992) 3146–3168, [hep-lat/9205020](#).
- [204] M. Göckeler *et al.*, “Scaling of non-perturbatively $O(a)$ improved Wilson fermions: Hadron spectrum, quark masses and decay constants”, *Phys. Rev.* **D57** (1998) 5562–5580, [hep-lat/9707021](#).
- [205] T. Blum *et al.*, “Quenched lattice QCD with domain wall fermions and the chiral limit”, *Phys. Rev.* **D69** (2004) 074502, [hep-lat/0007038](#).

- [206] M. Fukugita, H. Mino, M. Okawa, G. Parisi, and A. Ukawa, “Finite size effect for hadron masses in lattice QCD”, *Phys. Lett.* **B294** (1992) 380–384.
- [207] M. Luscher, “Volume dependence of the energy spectrum in massive quantum field theory. 1. Stable particle states”, *Commun. Math. Phys.* **104** (1986) 177.
- [208] T. Bhattacharya, R. Gupta, G. Kilcup, and S. R. Sharpe, “Hadron Spectrum with Wilson fermions”, *Phys. Rev.* **D53** (1996) 6486–6508, [hep-lat/9512021](#).
- [209] D. Becirevic *et al.*, “Light hadron spectroscopy on the lattice with the non-perturbatively improved Wilson action”, [hep-lat/9809129](#).
- [210] B. Velikson and D. Weingarten, “Hadron wave functions in Lattice QCD”, *Nucl. Phys.* **B249** (1985) 433.
- [211] J. van der Heide, *The pion form factor from lattice QCD: A non-perturbative study at zero and finite temperature*. PhD thesis, 2004.
- [212] M. W. Hecht and T. A. DeGrand, “Wave functions of S wave hadrons in the quenched approximation to lattice QCD”, *Phys. Rev.* **D46** (1992) 2155–2168.
- [213] E. Laermann and P. Schmidt, “Meson Screening Masses at high Temperature in quenched QCD with improved Wilson quarks”, *Eur. Phys. J.* **C20** (2001) 541–552, [hep-lat/0103037](#).
- [214] M. C. Chu, M. Lissia, and J. W. Negele, “Hadron structure in lattice QCD. 1. Correlation functions and wave functions”, *Nucl. Phys.* **B360** (1991) 31–66.
- [215] **NA7** Collaboration, S. R. Amendolia *et al.*, “A Measurement of the space-like Pion electromagnetic Form-Factor”, *Nucl. Phys.* **B277** (1986) 168.
- [216] **ALPHA** Collaboration, M. Guagnelli *et al.*, “Non-perturbative results for the coefficients $b(m)$ and $b(A)$ - $b(P)$ in $O(a)$ improved lattice QCD”, *Nucl. Phys.* **B595** (2001) 44–62, [hep-lat/0009021](#).
- [217] **ALPHA** Collaboration, S. Capitani, M. Lüscher, R. Sommer, and H. Wittig, “Non-perturbative quark mass renormalization in quenched lattice QCD”, *Nucl. Phys.* **B544** (1999) 669–698, [hep-lat/9810063](#).
- [218] O. Dumbrajs *et al.*, “Compilation of coupling constants and low-energy parameters. 1982 Edition”, *Nucl. Phys.* **B216** (1983) 277–335.
- [219] D. Pleiter, *Quantum Chromodynamics with Improved Fermion Actions*. PhD thesis, Freie Universität Berlin, 2000.
- [220] M. Asakawa, T. Hatsuda, and Y. Nakahara, “Hadronic spectral functions above the QCD phase transition”, *Nucl. Phys.* **A715** (2003) 863–866, [hep-lat/0208059](#).
- [221] T. Umeda, K. Nomura, and H. Matsufuru, “Charmonium at finite temperature in quenched lattice QCD”, *Eur. Phys. J.* **C39S1** (2005) 9–26, [hep-lat/0211003](#).
- [222] L. D. McLerran and T. Toimela, “Photon and Dilepton Emission from the Quark - Gluon Plasma: some general Considerations”, *Phys. Rev.* **D31** (1985) 545.
- [223] M. G. Mustafa, A. Schafer, and M. H. Thoma, “Non-perturbative dilepton production from a quark-gluon plasma”, *Phys. Rev.* **C61** (2000) 024902, [hep-ph/9908461](#).
- [224] J. Kapusta, “Electron Positron Pair Production as a probe of Chiral Symmetry in a hot QCD Plasma”, *Phys. Lett.* **B136** (1984) 201–203.
- [225] M. Laine and M. Vepsäläinen, “Mesonic correlation lengths in high-temperature QCD”, *JHEP* **02** (2004) 004, [hep-ph/0311268](#).

-
- [226] K. Kajantie, M. Laine, K. Rummukainen, and M. E. Shaposhnikov, “3d $SU(N)$ + adjoint Higgs theory and finite-temperature QCD”, *Nucl. Phys.* **B503** (1997) 357–384, [hep-ph/9704416](#).
- [227] E. V. Shuryak, “Which chiral symmetry is restored in hot QCD?”, *Comments Nucl. Part. Phys.* **21** (1994) 235–248, [hep-ph/9310253](#).
- [228] T. D. Cohen, “The High Temperature Phase of QCD and $U(1)_A$ Symmetry”, *Phys. Rev.* **D54** (1996) 1867–1870, [hep-ph/9601216](#).
- [229] M. C. Birse, T. D. Cohen, and J. A. McGovern, “ $U(1)_A$ symmetry and correlation functions in the high temperature phase of QCD”, *Phys. Lett.* **B388** (1996) 137–140, [hep-ph/9608255](#).
- [230] American National Standards Institute, *American national standard for information systems: database language — SQL: ANSI X3.135-1992*. American National Standards Institute, 1430 Broadway, New York, NY 10018, USA, 1992. Revision and consolidation of ANSI X3.135-1989 and ANSI X3.168-1989, Approved October 3, 1989.
- [231] International Organization for Standardization, *ISO/IEC 9075:1992: Title: Information technology — Database languages — SQL*. International Organization for Standardization, Geneva, Switzerland, 1992. Available in English only.
- [232] J. R. Groff and P. N. Weinberg, *SQL, the complete reference*. Osborne/McGraw-Hill, Berkeley, CA, USA, 1999.

Acknowledgments

Feeling gratitude and not expressing it is like wrapping a present and not giving it.

WILLIAM ARTHUR WARD

I would like to take the opportunity to offer thanks to all the people, who accompanied me during my four years time in Bielefeld and made this work possible, especially

- my advisor Prof. Dr. Edwin Laermann for proposing such an interesting project. His continuous support and encouragement, the many interesting and enlightening discussions and the pleasant atmosphere were essential ingredients to this thesis.
- Prof. Dr. Frithjof Karsch for giving me the opportunity to work in the
International Graduate School
Quantum Fields and Strongly Interacting Matter:
From Vacuum to Extreme Density and Temperature Conditions
in collaboration with Université Paris-Sud XI (Paris VI, Paris VII, Saclay).
- Prof. Dr. Mikko Laine for being so kind to referee my thesis.
- concerning our project, special thanks go to the think tank Dr. Sven Stickan, Ph.D. Saumen Datta, Dr. Wolfgang Söldner, Dr. Stanislav Shcheredin, Dr. Olaf Kaczmarek and Dr. Jan van der Heide. Dr. Norbert Attig and Wolfgang Frings from Forschungs-zentrum Jülich for giving me help and computational advises for the JUMP.
- my (former) office mates Dr. Felix Zantow, Sodbileg Chagdaa and Chuan Miao for providing me the pleasant and thought-provoking working environment.
- all those, who have provided me the opportunity for research stays and participations on conferences in Paris, Moscow (thank you, David), Dublin and Brookhaven (NY). I will never forget this time.
- of course to my former colleagues and now dear friends Jörg Erdmann, Dr. Matthias Döring, Dr. Lars Fromme, Dr. Kay Hübner, Dr. Michael Seniuch, Tim Stockamp, Aleksandar Rakić and Oliver Vogt for all discussions about physical and non-physical issues and this wonderful regular 15.30h tea-break, 16.00h soccer plays and barbecues.
- the secretaries Gudrun Eickmeyer and Susi von Reder for helping me with all the administration stuff from the beginning on and organizing our annual excursions.
- all members and alumni of the Fakultät für Physik (E5/E6).
- last but not least to my parents, Elsi Wissel-Jütter and Dr. Helmut Wissel for giving me unconditional and continuous (financial:)) support during my studies. Vielen Dank!

Sönke Wissel,

Bielefeld, October 30th 2006

Selbstständigkeitserklärung

Hiermit erkläre ich, die vorliegende Arbeit selbstständig ohne fremde Hilfe verfasst und nur die angegebene Literatur und Hilfsmittel verwendet zu haben.

Sönke Wissel,
Bielefeld, 30. Oktober 2006

Curriculum vitæ

Personal Data

Name Sönke Wissel
Date of birth 16th August 1976
Place of birth Hannover
Nationality German
Marital status single
Present address Fakultät für Physik
Universität Bielefeld
D-33501 Bielefeld
E-mail: wissel@physik.uni-bielefeld.de

Schools

1982-1986 Grundschule Berge
1986-1995 Gymnasium Leoninum, Handrup
1995 Abitur

University

1996-2002 Münster University, Studies in Physics
2002 Münster University, Diplom in Theoretical Physics
*Die graphische Charakter- und Hoppingparameterentwicklung
der $N=1$ $SU(2)$ -Super-Yang-Mills-Theorie in d Dimensionen*
(supervised by Prof. Dr. G. Münster)
2003-2006 Bielefeld University, scholarship holder of the IGS
*Quantum Fields and Strongly Interacting Matter:
From Vacuum to Extreme Density and Temperature Conditions*
2006 Bielefeld University, Doktor in Theoretical Physics
*Mesonic Correlation Functions from Light Quarks and
Their Spectral Representation in Hot Quenched Lattice QCD*
(supervised by Prof. Dr. E. Laermann)

Other Activities

2005 XXIII International Symposium on Lattice Field Theory, Dublin, Ireland
2005 International Advanced School of Theoretical Physics, Dubna, Russia
2003-2005 Miscellaneous Courses, Colloquia and Workshops
in Paris, Brookhaven and Bielefeld

